The effect of surfactants, enzymes and temperature on soils investigated using electrochemical and crystallisation techniques for detergency applications

CHOWDHURY, MEHRIN

The effect of surfactants, enzymes and temperature on soils investigated using electrochemical and crystallisation techniques for detergency applications

Mehrin Chowdhury

A thesis submitted for the degree of Doctor of Philosophy at the University of Durham

Department of Chemistry

November 2015

Abstract

The behaviour of surfactant at an oil-water interface is of fundamental importance across a range of application, one of which is detergency. For the characterisation of various anionic and non-ionic surfactants, which make up commercial detergent solution, at the aqueous-organic interface, electrochemical methods combined with conductivity, electrocapillary curves and optical microscopy were employed. The findings have revealed that the adsorption and partitioning of the anionic surface active ions at the interface between two immiscible electrolyte solutions can cause reproducible chaotic effects at the region of transfer potentials of the surfactant ions. Factors such as the Marangoni effect and spontaneous emulsification at the phase boundary, as well as the presence of micelles, micellar emulsification and transfer of emulsion droplets across the interface have been found to contribute to these chaotic currents at the organic-water interface. By applying cyclic voltammetry and chronoamperometry techniques, it was established that the irregular oscillations became more pronounced as the concentration of sodium dodecylbenzene sulphonate (SDBS) was increased from 1.5 mM -13.4 mM and the current spikes dissipated as the concentration of triton- x- 114 was increased from 8.6 mM - 114 mM in the aqueous phase consisting of 13.4 mM of SDBS. Similar results were obtained using P&G's Y and N surfactants. The rise in current instability due to enhanced concentration of the SDBS, which was used as the standard surfactant, was confirmed using chronoamperometry, conductivity measurements and electrocapillary curves. The interfacial instability was prominent in the presence of electrolytes at the aqueous-1,2-DCE/oil phase boundaries which was visually evident in the optical microscopic images obtained. Furthermore, needle-like crystals were identified at the aqueous-1,2-DCE interface with electrolytes, with and without the addition of anionic/non-ionic surfactants. This suggests that a crystallisation process was initiated by the presence of dehydrated salt ions at the phase boundary, which is likely to be promoted by the surfactant ions.

Lard has been used as the fat 'model' for washing experiments since it is composed of more problematic high melting point components compared to other sources of fat. Lard was deposited onto fabrics and left to age over a period of 4 hours at 20 ^{o}C and also, at the temperatures of -10 ^{o}C, 10 ^{o}C, 20 ^{o}C and 30 ^{o}C for 5 days. These samples, when analysed using the small angle X-ray scattering (SAXS) technique, revealed peaks at 2θ values of 2^{o} and 2.6 ^{o} with d-spacing values of 43.2 Å - 44.3 Å, indicating the existence of the most thermodynamically stable β' and β polymorphs. This was confirmed using the wide angle X-

ray scattering (WAXS) technique, which showed presence of β' crystals on soiled fabrics left to age overnight and also, for 30 days with and without the application of detergent at 20 ^{o}C. Soiled fabrics washed with a low concentration (0.7 mg/mL), a high concentration (50 mg/mL) and no C24E3S surfactant when analysed using SAXS displayed formation of only the β' and β polymorphs. It was observed that the most effective method for lard removal was via emulsification and roll-up mechanisms along with agitation generated by the propeller, in the presence of a low C24E3S surfactant concentration. Polyester swatches were found to exhibit greater lard removal at low and no surfactant concentration while cotton fabric showed better lard removal comparing to other types of fabrics used, when a high surfactant concentration was applied.

The effectiveness of enzymes such as NAD^{+}-dependent diaphorase (DP) and glycerol dehydrogenase (GDH), which are required for the breakdown of glycerol (a product generated by lipolysis of triglycerides in the presence of lipase enzymes), were investigated using immobilised sol-gel/FcAuNP/enzymatic carbon macro- and screen printed electrodes. The sol-gel/FcAuNP/enzymatic biosensors have demonstrated low K_m values of 4.9 $\pm$ 0.01 mM and 5.4 $\pm$ 0.01 mM, respectively, compared to the literature value of 9.9 mM. This indicates enhanced electron mediation between the re-dox centre of the GDH enzyme and the electrode surface and, the attainment of higher affinity for the glycerol substrate. The immobilised sol-gel/FcAuNP/ NAD^{+} - dependent DP and GDH enzymatic SPE is capable of detecting a wide range of glycerol concentrations from 0.2 mM to 24.8 mM, exhibit a fast response time and a correlation coefficient of 0.9988 was also attained. The inexpensive, simple to use and easily disposable miniature biosensor has displayed other desirable characteristics such as reusability, reproducibility, real-time monitoring, high sensitivity and selectivity for glycerol.

Acknowledgements

Firstly, I would like to thank my main supervisor, Dr Ritu Kataky, for all her help, support and encouragement she has provided me with during my PhD study. I am grateful to Dr. Ritu Kataky for providing me the chance to do a PhD in electrochemistry at Durham University and for giving me the chance to participate in numerous national and international conferences and encouraging me to work with others from different areas of Chemistry. All of this has allowed me to expand my scientific knowledge and experience. Thank you once again Dr. Ritu Kataky for all your help, support and guidance.

I would like to thank Dr. Sharon Cooper for all her help and guidance that she has provided me with and for allowing me to undertake my soiled fabric wash experiments in her laboratory. Thank you to Janet Berry and Reduwan for their help with the wash experiments. I would like to extend my thanks to Dr. Richard Thompson, Dr. Paul Hodgkinson and Professor John Girkin for their help and advice at the beginning of my PhD. Also, thank you to Eric Robles and Neil Lant from P&G for all their help and allowing me to use their equipments at the Newcastle Innovation Centre. Thanks to Euan Magennis from P&G for all his valuable advice.

Many thanks to all the past and present group members and friends from the Chemistry department for all their support and encouragement which has helped me get through the difficult moments during my PhD. Also, thank you to Helen Riggs for providing me with technical assistance for SAXS, WAXS and ESEM, to Doug Carswell for his assistance with DSC and MS and to Budhika Mendis for his help with running the TEM. Thank you to P&G and the Chemistry department, Durham University for sponsoring my PhD.

Lastly, I would like to say thank you to my family especially to my mum and dad for their help and support and to my sister and brother for their encouragement.

Declaration

The work described in this thesis was carried out in the Department of Chemistry at Durham University between October 2011 and October 2015, under the supervision of Dr. Ritu Kataky. All the work is my own, unless otherwise stated. Any part of this thesis work has not been submitted previously for a degree at this or any other university.

Statement of Copyright

Publications

The following publications are in the process of submission/to be submitted and they are based on the work undertaken for chapters 4 & 5 in this thesis:

- Emulsification at the liquid-liquid interfaces: effects of potential, electrolytes and surfactants (accepted on the 6th of November 2015).
- Ferrocenated gold nanoparticles and enzymes in sol-gel matrices enhance electron mediation and the rate of enzyme activity (submitted).
- Formation of needle-like crystals at the aqueous-1,2-DCE interface with electrolytes in the absence and presence of surfactants (submitted).

Table of Contents

List of symbols and abbreviations

Abbreviations	Meaning
ITIES	Interface between two immiscible electrolyte solutions
SAXS	Small-Angle X-ray Scattering
WAXS	Wide-Angle X-ray Scattering
FcAuNP	Ferrocenated gold nanoparticles
C	Carbon
GOx	Glucose oxidase
GTO	Glycerol trioleate
TEM	Transmission electron microscopy
SPEs	Screen Printed Electrodes
NAD^+/NADH	Nicotinamide Adenine Dinucleotide
GDH	Glycerol Dehydrogenase
DP	Diaphorase
CV	Cyclic Voltammetry
CA	Chronoamperometry
C24E3S	Sodium Lauryl Ethoxy Sulphate
Y surfactant	Linear Alkylbenzene Sulphonate
N surfactant	Alcohol Ethoxylate
SDBS	Sodium dodecylbenzene sulphonate
CMC	Critical Micelle Concentration
1,2-DCE	1,2-dichloroethane
MVN	Modified Verwey-Niessen model
Ox	Oxidised species
Red	Reduced species
RE	Reference electrode
WE	Working electrode

CE	Counter electrode
SE	Sensor electrode
NaCl	Sodium chloride
Pt	Platinum flag
TBA^+	Tetrabutylammonium cation
TPB^-	Tetraphenylborate anion
Cl^-	Chloride anion
Li^+	Lithium cation
KCl	Potassium Chloride
TBACl	Tetrabutylammonium chloride
MgCl2	Magnesium chloride
MS	Mass Spectroscopy
DSC	Differential Scanning Calorimetry
ESEM	Environmental scanning electron microscope
EDX	Energy-dispersive X-ray spectroscopy
TAG	Triacylglycerides
FTIR	Fourier transform infrared spectroscopy
AFM	Atomic force microscopy

Symbol	Meaning	units
$\Delta\phi$	Inner potential difference	V
$\Delta_{o}^{w}\phi$	Phase-boundary potential	V
$\Delta_{o}^{w}\phi_{i}^{\emptyset,}$	Standard ion-transfer potential of ion *i*	V
R	Gas constant	$JK^{-1}mol^{-1}$
T	Absolute temperature	K
z_i	Charge of the ion i	-
F	Faraday constant	$C\ mol^{-1}$
c	Concentration of ion	M
$\Delta_{o}^{w}\phi^{1/2}$	Half-wave potential	V
D	Diffusion coefficient	cm^2s^{-1}
A	Electrode surface area	cm^2
J_e	Electron flux density for the electron transfer reaction	$mol\ cm^{-2}s^{-1}$
x	Length	m
t	Time	s
λ	Wavelength of X-rays	nm
n	Integer	-
d	Spacing between the planes of the atomic lattice	Å
θ	Contact angle	degrees
q	Length of the scattering vector	nm
h	Planck's constant	m^2kgs^{-1}
m_e	Mass of an electron	kg
v	Velocity	ms^{-1}
θ_i	Surface coverage of i	-
μ_i	chemical potential of a chemical species i	$J\ mol^{-1}$
p	Pressure	Pascal
q^w	Excess surface charge density	C/m^2
C_{dl}	Double layer capacitance	Farad

Γ_m	Maximum adsorption of the surface active ions	-
$G^o_{ads,i}$	Standard Gibbs energy of adsorption	J mol^{-1}
$\Delta G^o_{tr,j}$	Gibbs energy for the transfer	J mol^{-1}
$\Delta\phi^{\emptyset}_{dp}$	Standard potential of desorption	V
$\Delta\phi^{\emptyset}_{ad}$	Standard potential of adsorption	V
k_a	rate constant of micellar assembly	-
k_d	rate constant of micellar disassembly	-
K_m	Michaelis -Menten constant	M
α	Alpha polymorph	-
β	Beta polymorph	-
β’	Beta prime polymorph	-
T_m	Melting temperature	^{o}C
ΔG*	Gibbs energy barrier	J mol^{-1}
γ	Interfacial tension	mN/m

List of figures

biosensor for glycerol detection

List of tables

Appendix

THESIS OUTLINE:

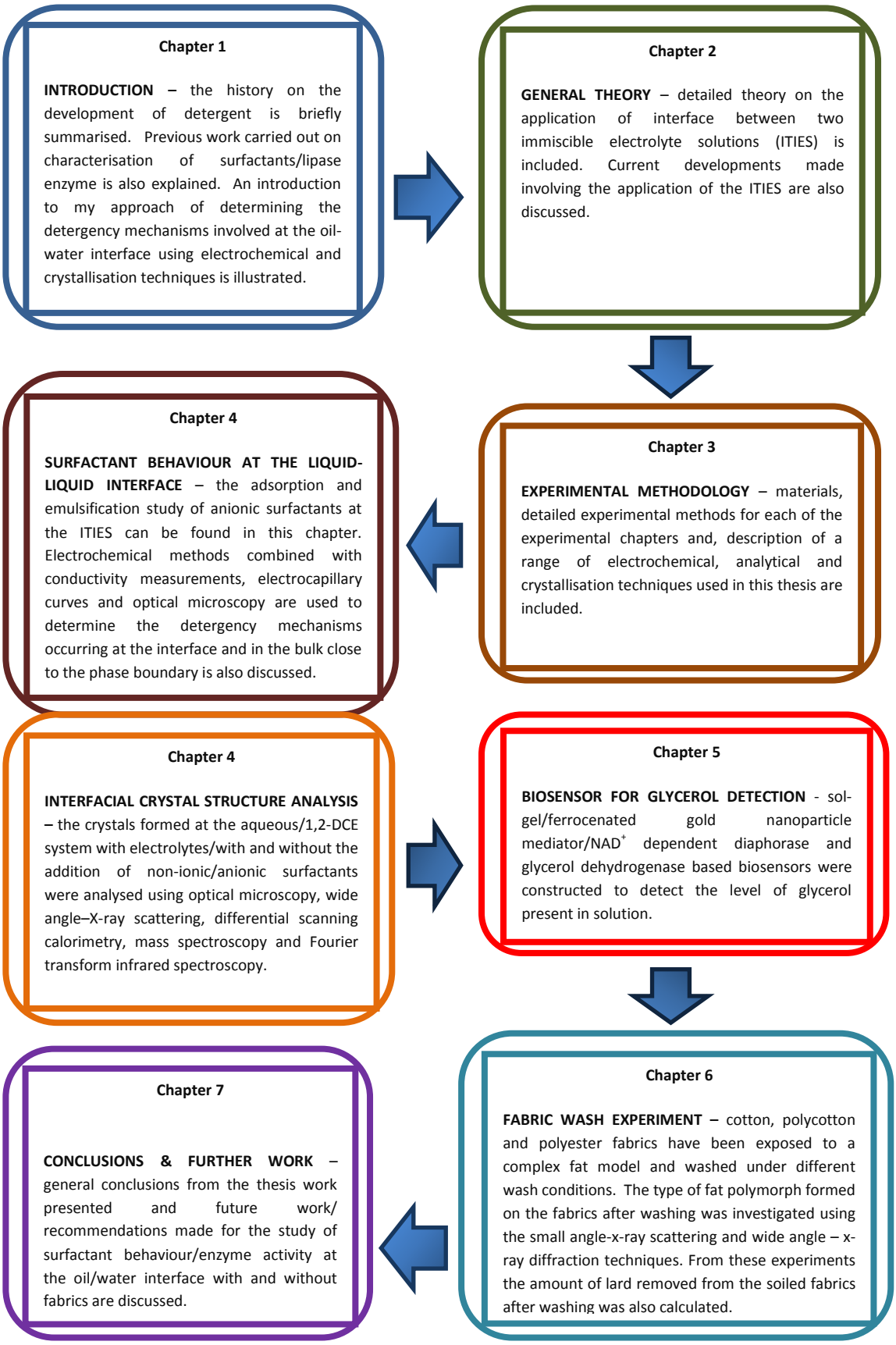

CHAPTER 1

Introduction

1.1 Introduction to laundry detergent

Over the years, the detergent industry has contributed immensely towards improving the health of the human race via averting the spread of diseases and infections. By continuous improvement of hygiene conditions, the quality of life of the consumers has also enhanced with time. Archaeological evidence shows that soap was first invented and used around 2800 BC[1]. In Europe, by the seventh century manufacturing soaps was well-established. The first ever synthetic detergent was developed in 1916 by the Germans as result of fat shortage during World War I[2]. However, it was only in the early 1940s when the revolution in detergency-making was initially acknowledged due to the discovery of built detergents which were then made available in the markets, in the United States[3]. Following this, a variety of other detergent-based products appeared on the market, which was designed for cleaning floors, dishes and laundry. The demand for these types of new products in the market even to this date is extremely high and the detergency industry is still expanding especially in the developing world as more people are able to afford these "luxurious" products. In the developed world such as in the North America and Europe on the other hand, the market for the household/personal care products is still growing, however at a much slower pace [4].

The household/personal care products can be categorised according to: (1) the type of product i.e. powders, liquids, gels or tablets, (2) the cleaning functionality such as fine/coloured/non-coloured fabrics, woollens or kitchen cleaners, (3) product-added values for instance, cleans and softens or disinfects and (4) aesthetics like colours and fragrances which enhances the desirability of the substance [5,6,7,8]. The compositions of these products have become more complex over time as technology is continuously developing and much improved/automatic appliances like washing machines, dishwashers, self-cleaning ovens and microwaves are manufactured. Other essential points which need to be considered when developing the household/personal care goods include the requirement of minimum effort and shortest time for application and also, to ensure that the products are environmentally friendly/safe to use as well as biodegradable[9]. At the same time, the detergent must be able to display better performance in terms of removing a wider range of soils and substrates from

various types of fabrics (like cotton, polycotton polyester or wool) under different cleaning conditions (i.e. different wash temperature and varying level of water hardness depending on the amount of calcium or magnesium present in the water) [10]. The wash conditions and the method for cleaning clothes vary from country to country and at each home [11]. Additional aspects for example, fibre content, colour, dye-fastness, type of fabric, sturdiness and fragility as well as the economical factor at different countries, availability of raw materials and skilled formulator can also have an impact on the way the products are formulated [6].

A laundry detergent is usually composed of a mixture of raw materials which includes surfactants, builders, bleaching agent, softeners, enzymes, brighteners and fragrances which are required for example, to improve detergency and prevent soil redisposition[12]. Detergency can be described as the process of removal of unwanted substances like soils from solid surfaces of textiles when brought into contact with a liquid. The removal of soils depends on a number of factors and these include mechanical action of the washing machine, the type of detergent and substrate involved[13]. Detergency testing is important for developing detergent formulation, improving the design of washing machines and textile fibres and finishes. The effectiveness of detergency is therefore determined by chemical analysis, physical measurements, toxicological and ecological examination and functional ability of the detergent. The functionality of a detergent is based on how efficiently it can remove soil and lead to soil degradation in the presence of enzymes or bleach. Factors like the level of water consumption and energy input are also considered when developing personal care products such as laundry detergents [14].

1.2 PhD objectives

The objective of this work is to understand the physical chemistry behind the swelling of solid fatty soil to enable the development of new detergent technologies for cold water cleaning (sustainability). Removal of solid fatty soils remains extremely challenging despite decades of research in industry as the environmental drive for lower washing temperatures means that the fat deposits often exist in solid form at these low temperatures. This is further exacerbated by the fact that fats crystallise into different polymorphs and their influence on fat removal remains not fully understood. This PhD work mainly focuses on how the fats/oils behave at low temperature and also investigates the effect of two widely used ingredients in the detergent formulation which are the surfactants and the lipase enzymes, at the oil/water phase boundary. The key mechanisms via which surfactants function at the oil/water

interface are emulsification, roll-up or solubilisation[15]. Emulsification involves reduction of the interfacial tension at the oil-water interface[16] while the fabric surface-water interfacial tension is lowered by the deposition of surfactant molecules at the interface as a result of roll-up mechanism[16]. Another effective mechanism via which soils are removed from fabrics is solubilisation. This involves micelles breaking down the soils into smaller fragments held within the micellar core when there are excess amounts of surfactant relative to oil present [17]. The lipase enzymes on the other hand mainly act by catalysing the cleavage of carboxyl ester bonds in tri-, di- and monoacylglycerols which are major constituents of animal, plant and microbial fats and oils. Consequently, hydrolysis of the triglycerides leads to generation of products such as carboxylic acids, glycerols and alcohols [18].

In recent years, various techniques such as the dynamic interfacial tension [19,20],sum frequency scattering[21], neutron reflectometry[22], phase contrast microscopy[23,24,25], fluorescence microscopy[25] and Brewster angle microscopy[26] have been used to characterise surfactants at the oil/water phase boundary. Whereas, the lipase activity has been investigated using a range of methods which include volumetry[27], colorimetry and spectrophotometric measurements [27,28,29], cryogenic transmission electron microscopy[30], Infrared spectroscopy [31,32], fluorometry [33], and chromatography [34,35,36]. However, all of the above methods/techniques reported require extensive sample preparation and were found to be much more time-consuming compared to methods at the liquid-liquid interface which have been used in this study to obtain in depth information on surfactant mechanisms (i.e. surfactant adsorption, Marangoni effect and micellar emulsification) that occur at the oil and water interface. Furthermore, quick and non-destructive X-ray diffraction (i.e. small-angle X-ray scattering (SAXS) and wide-angle X-ray scattering (WAXS)) techniques were used to investigate the change in the polymorphic state of fats whilst varying the temperature and to examine the effectiveness of the surfactants on removing different kinds of fat polymorphs from various types of fabrics, under cold water wash conditions where the wash temperature was kept constant at 20, 30 and 40 ^{o}C. On the other hand, for the rapid detection of lipase enzyme activity, sol-gel/ FcAuNP (ferrocenated gold nanoparticles)/NAD^{+} (Nicotinamide adenine dinucleotide) - dependent DP (diaphorase) and GDH (glycerol dehydrogenase) based macro- and screen printed electrodes (SPEs) has been developed. The modified enzymatic SPEs are simple yet cost-effective and easily disposable after use while simultaneously the biosensors were found to display additional desirable characteristics such as higher sensitivity, selectivity and specificity when compared to other methods available.

1.3 References

1. Castleden, R. *Inventions that Changed the World*. (Little Brown Books Group, 2007).
2. Toedt, J., Koza, D. & Cleef-Toedt, K. V. *Chemical Composition of Everyday Products*. (Greenwood Publishing Group, 2005).
3. Operations, U. S. C. H. C. on G. *Phosphates in Detergents and the Eutrophication of America's Waters: Twenty-third Report*. (U.S. Government Printing Office, 1970).
4. Broze, G. *Handbook of Detergents: Properties*. (CRC Press, 1999).
5. Zoller, U. & Sosis, P. *Handbook of Detergents, Part F: Production*. (CRC Press, 2008).
6. Mendelson, C. *Laundry: The Home Comforts Book of Caring for Clothes and Linens*. (Simon and Schuster, 2009).
7. Muller, P. M. & Lamparsky, D. *Perfumes: Art, Science and Technology*. (Springer Science & Business Media, 2012).
8. Showell, M. *Handbook of Detergents, Part D: Formulation*. (CRC Press, 2005).
9. Corporation, M. C. *How it Works: Science and Technology*. (Marshall Cavendish, 2003).
10. Aehle, W. *Enzymes in Industry*. (John Wiley & Sons, 2008).
11. Falbe, J. *Surfactants in Consumer Products: Theory, Technology and Application*. (Springer Science & Business Media, 2012).
12. OECD. *Series on Emission Scenario Documents Water Based Washing Operations at Industrial and Institutional Laundries*. (OECD Publishing, 2014).
13. Lai, K.-Y. *Liquid Detergents*. (CRC Press, 2005).
14. Cutler, G. *Detergency: Theory and Technology*. (CRC Press, 1986).
15. Miller, C. A. & Raney, K. H. Solubilization—emulsification mechanisms of detergency. *Colloids Surf. Physicochem. Eng. Asp.* **74,** 169–215 (1993).
16. Dillan, K. W., Goddard, E. D. & McKenzie, D. A. Oily soil removal from a polyester substrate by aqueous nonionic surfactant systems. *J. Am. Oil Chem. Soc.* **56,** 59–70 (1979).
17. Rosen, M. J. *Surfactants and Interfacial Phenomena*. (John Wiley & Sons, 2004).
18. Paiva, A. L., Balcão, V. M. & Malcata, F. X. Kinetics and mechanisms of reactions catalyzed by immobilized lipases. *Enzyme Microb. Technol.* **27,** 187–204 (2000).
19. Li, G., Prasad, S. & Dhinojwala, A. Dynamic interfacial tension at the oil/surfactant-water interface. *Langmuir ACS J. Surf. Colloids* **23,** 9929–9932 (2007).

20. Reichert, M. D. & Walker, L. M. Interfacial Tension Dynamics, Interfacial Mechanics, and Response to Rapid Dilution of Bulk Surfactant of a Model Oil–Water-Dispersant System. *Langmuir* **29,** 1857–1867 (2013).
21. de Aguiar, H. B., Strader, M. L., de Beer, A. G. F. & Roke, S. Surface Structure of Sodium Dodecyl Sulfate Surfactant and Oil at the Oil-in-Water Droplet Liquid/Liquid Interface: A Manifestation of a Nonequilibrium Surface State. *J. Phys. Chem. B* **115,** 2970–2978 (2011).
22. Zarbakhsh, A., Webster, J. R. P. & Eames, J. Structural Studies of Surfactants at the Oil−Water Interface by Neutron Reflectometery. *Langmuir* **25,** 3953–3956 (2009).
23. Sjoblom, J. *Emulsions and Emulsion Stability: Surfactant Science Series/61*. (CRC Press, 2005).
24. Shahidzadeh, N., Bonn, D. & Meunier, J. A new mechanism of spontaneous emulsification: Relation to surfactant properties. *EPL Europhys. Lett.* **40,** 459 (1997).
25. Hanczyc, M. M., Toyota, T., Ikegami, T., Packard, N. & Sugawara, T. Fatty Acid Chemistry at the Oil−Water Interface: Self-Propelled Oil Droplets. *J. Am. Chem. Soc.* **129,** 9386–9391 (2007).
26. Binks, B. & Furlong, D. *Modern Characterization Methods of Surfactant Systems*. (CRC Press, 1999).
27. Stoytcheva, M., Montero, G., Zlatev, R., A. Leon, J. & Gochev, V. Analytical Methods for Lipases Activity Determination: A Review. *Curr. Anal. Chem.* **8,** 400–407 (2012).
28. Gomes, N., Gonçalves, C., García-Román, M., Teixeira, J. A. & Belo, I. Optimization of a colorimetric assay for yeast lipase activity in complex systems. *Anal. Methods* **3,** 1008 (2011).
29. Abd-Elhakeem, M. A., Elsayed, A. M. & Alkhulaqi, T. A. New Colorimetric Method for Lipases Activity Assay in Microbial Media. *Am. J. Anal. Chem.* **04,** 442–444 (2013).
30. Brennan, J. L. *et al.* Enzymatic Activity of Lipase−Nanoparticle Conjugates and the Digestion of Lipid Liquid Crystalline Assemblies. *Langmuir* **26,** 13590–13599 (2010).
31. Snabe, T. & Petersen, S. B. Application of infrared spectroscopy (attenuated total reflection) for monitoring enzymatic activity on substrate films. *J. Biotechnol.* **95,** 145–155 (2002).
32. Farias, R. N., Chehin, R. N. & Canela, R. Fourier-transformed infrared assay for the determination of the positional specificity of non-specific and 1,3-specific lipases. *Biotechnol. Lett.* **22,** 905–908 (2000).
33. Hammond, R. C. & Gotfredsen, S. *Applications of Lipases as Biocatalysts*. (CRC Press, 1990).

34. Li, T.-Y., Deng, K.-G., Chen, B. & Yao, S.-Z. [Determination of lipase activity by gas chromatography]. *Yao Xue Xue Bao* **44,** 628–631 (2009).

35. Kulkarni, N. & Gadre, R. V. Simple gas chromatography method for lipase assay. *Biotechnol. Tech.* **12,** 627–628 (1998).

36. Nollet, L. M. L. & Toldra, F. *Handbook of Dairy Foods Analysis*. (CRC Press, 2009).

CHAPTER 2

Fundamental of electrochemistry

2.1 Review of liquid-liquid interface between two immiscible electrolyte solutions

The application of electrochemistry at the liquid-liquid interface between two immiscible electrolyte solutions (ITIES) have advanced significantly over the last three decades although it has been established since the end of 19th century. Ion partition equilibria at the interface were first studied by Walther Nernst in 1892. Nernst derived the fundamental relationship relating potential difference of the inner potentials to the ratio of ion concentrations in the aqueous and organic phases[1]. Following this, the first ITIES experiment was performed by Nernst and Riesenfeld in 1902, which involved investigating the current change due to transfer of iodide ion at a water-phenol interface[2]. Other interfacial characteristics such as the theoretical model of the diffuse double layer at the liquid-liquid interface was then proposed by Verwey and Niessen in 1953 [3].

The initial electrochemistry experiments were initiated by Claude Gavach using the 4-electrode system methodology in order to examine the transfer of tetraalkylammonium cations across the ITIES, in 1968[4]. The next major development in the field of electrochemistry was proposed by Koryta *et al.* in 1977, who suggested that the ITIES had similarities to that of a biological membrane surface and also, it can behave as a polarised electrode under specific conditions. Kortya's research led to the realisation that the transfer of ions across the ITIES resembles the redox reactions at the electrode surface[5]. These remarkable findings and the theoretical concepts developed led to in depth understanding about the structure of the interface and charge transfer mechanisms between the two immiscible solutions. Furthermore, based on the theory and the experimental work performed on the liquid -liquid interface, Osakai *et al*. and Sanchez *et al.* produced an ITIES model for determining the Gibbs free energy transfer of hydrated ions across the interface formed between the water and organic phases[6].

Another major breakthrough in the field of electrochemistry was made by Samec *et al*., using a 4-electrode potentiostat viable results was obtained for the Cesium (Cs^+) ion transfer from water to the nitrobenzene phase without ohmic potential drop interference at the interface[7]. The potentiostat system involved use of two counter electrodes and two reference electrodes, one for each phase and, a feedback correction to eliminate the potential drop[8].

Further to this, Baruzzi and Uhlken successfully developed a method involving use of a 4-electrode potentiostat with current interruption technique for the eradication of ohmic potential drop and to allow sampling of real interfacial voltage[9]. In 1986, Taylor, Girault and Senda *et al.* eliminated the potential drop from the electrochemical system by introducing liquid-liquid micro-ITIES, which is either supported at the tip of a pulled glass micro-pipette or within a micropore array[10]. The asymmetry in ion transfer, as a result of the ions being transported from the micro-pipette to the surface and from the outside of the pipette to the surface was used to study charge transfer at the micro-ITIES. An alternative approach was developed by Albery *et al*. using a rotating diffusion cell which was later modified by Mazanares *et al*. to study the rate constant of ion transfer kinetics across the liquid-liquid ITIES[11]. Further to this, Wilke *et al.* derived a method for the determination of ion transfer mechanism across the liquid-liquid interface, which involved stirring the aqueous and organic phase during the potential sweep [12].

The wide variety of applications has made the use of ITIES one of the most popular methods for studying numerous electrochemical reactions at the interface. For example, ITIES can be used as chemical sensors[13], for ion-selective electrodes[14,15], for electrochemical extraction procedures such as selective ion separation from a mixture depending on the potential applied[16], for controlling mass transport in a system, for catalysis processes and biological reactions, to monitor ion transfer across the liquid-liquid interface and also, to quantify metals ions in the contaminated water[17].

2.2 Electrochemistry at the liquid-liquid interface between two immiscible electrolyte solutions

In an ITIES system, an interface is referred to as the formation of a phase boundary between two immiscible and ion conductive solutions with different physiochemical properties[18]. A polarisable interface is formed by two immiscible solutions at equilibrium; a large potential change is produced at the interface upon the passage of extremely small amount of current. For such system, the potential range is also known as the potential window which is in turn controlled with an external circuit/potential source such as a potentiostat and there are no transferrable ions present between the aqueous and the organic phases[19]. For ion exchange to take place at a maximum rate, the interface has to be non-polarisable. This means that a fixed or a small potential difference can be established across the interface upon the passage of high current. As a result, at least one common ion is shared between the aqueous and the organic solutions[20]. A non-polarisable phase boundary is achieved by applying an external

potential between two reference electrodes placed in the vicinity of the interface[21]. The desired potential between the tips of the reference electrodes is maintained using a 4-electrode potentiostat whereas the current is measured between the two counter electrodes. This ensures that the reference electrodes remain unaffected by the current and a constant potential is achieved at all time (figure 2.1)[22].

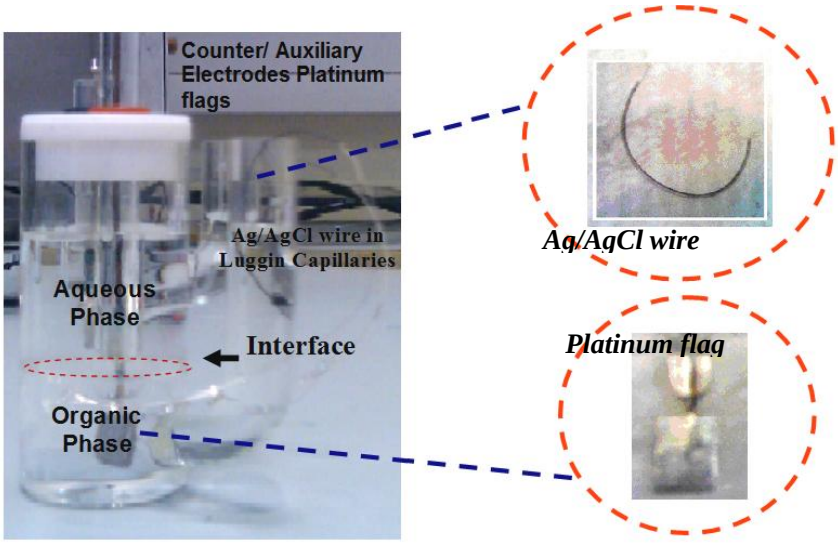

Figure 2.1: Electrochemical cell setup showing water|1, 2 -DCE interface.

The 4-electrode system consists of two platinum counter electrodes which are fully immersed into each of the two liquid/liquid phases. The reference silver/silver chloride (Ag/AgCl) electrodes on the other hand are connected to the two immiscible liquid-liquid layers using Luggin capillaries. One of the reference electrodes is placed in the organic solution via which it is linked to the organic phase within a Luggin capillary. The function of the capillaries is to minimise the voltage drop between the two reference electrodes and there is usually a distance of about 1 mm between the tips and the interface[23]. When a current flows through the ITIES, a potential difference develops between the tips of the Luggin capillaries and the interface due to solution resistance and ohmic potential drop. The ohmic potential is compensated by the positive feedback mechanism of the potentiostat used[24].

The immiscible electrolyte solutions are composed of an aqueous phase consisting of water and hydrophilic salt (i.e. Lithium chloride (LiCl)) and, an organic phase consisting of an apolar solvent (such as 1, 2-dichloroethane (1,2-DCE)) and hydrophobic salt (i.e. tetrabutylammonium tetraphenylborate (TBATPB)). The degree of miscibility between the two phases and the width of the potential window domain is vastly influenced by the hydrophobicity of the salt in the organic phase[25]. The organic solvent used in the liquid-liquid ITIES system has a high

dielectric constant which means it can weaken the forces of attraction between the electrolyte ions and allow maximum dissociation of the electrolytes to form ions. The analyte solution usually contains the ion species of interest in addition to the water soluble electrolyte. The electrolyte salts ensure that a balanced ionic strength is established, which is required for minimising the junction potential[26].

When strongly soluble hydrophilic and hydrophobic electrolyte salts are dissolved in the specific phases and an external potential is applied, the interface becomes polarisable. A potential window is then established, which is limited by the electrolytes. The outsides of the potential window are affected by the background ions. When a positive transfer potential is applied, a hydrophilic cation and a hydrophobic anion moves across the interface into the adjacent phases. Following this, when a negative potential is applied a lipophilic cation and a hydrophilic anion is transferred across the interface into the adjoining phases. The transfer of the ions across the interface is indicative by the two sharp extremes produced on the voltammogram (figure 2.2)[27]. There are no common species between the two phases in an ideally polarised system and the polarisability of the ITIES is dependent on the Gibbs energy of transfer of the electrolytes.

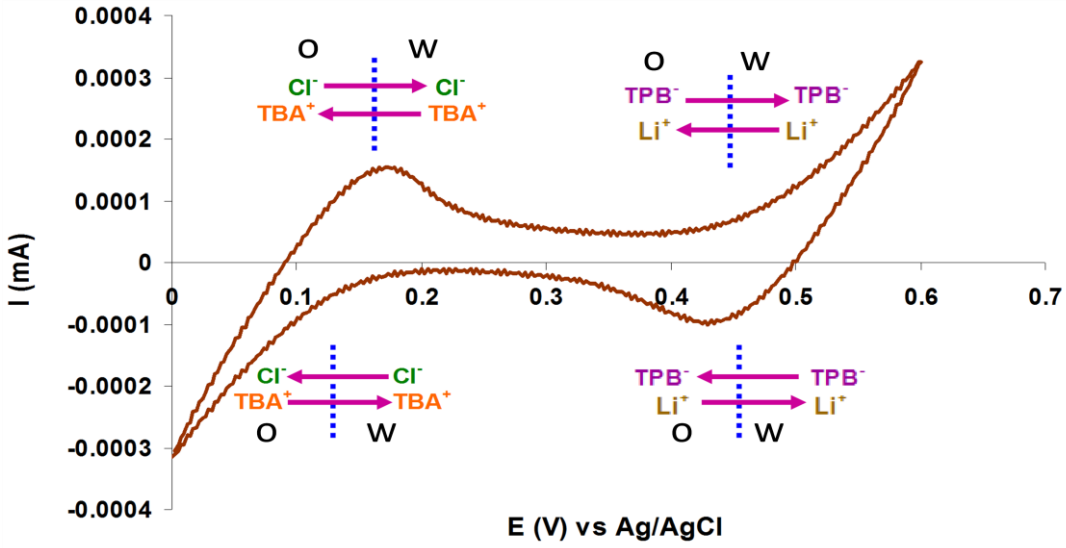

Figure 2.2: A typical voltammogram of polarised ITIES[27] .

When an ion is added with a formal potential in-between that of the electrolytes added to one of the liquid-liquid phases, a potential difference is attained and consequently, the transfer of ion leads to flux of charges across the aqueous/organic interface. This is measured as current against the function of applied potential (see chapter 4 results and discussion for exemplary CV of tetraethylammonium chloride (TEACl)).

2.3 Factors affecting the liquid-liquid interface

Factors such as the macro interface (figure 2.3), low concentrations of electrolyte ions, less conductive electrolyte solutions i.e. oily immiscible layer and the current can lead to an increase in the resistance and the ohmic potential drop[28].

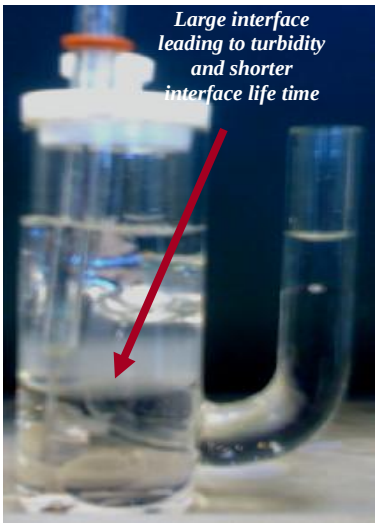

Figure 2.3: Electrochemical cell with large turbid interface, after a potential of 50 mV/s was applied.

Additional drawbacks which could lead to distortion in the voltammogram include a rise in interfacial tension, an increase in the interface capacitance, a small polarisability of the organic phase and an increase in the surface charge density[29]. Such flaws in the ITIES system can be eliminated for example, by creating micro interfaces, reducing the distance between the tip and the organic solution or by converting one of the two phases into a polymer gel. The organic phase can be jellified by the addition of poly (vinyl chloride) and the aqueous phase can be solidified by inserting an agar[30,31].

Other methods include the use of a 4-electrode potentiostat for reducing the electric resistance and preventing the polarisation of the reference electrodes. Polar solvents with a larger polarisiability phase for ion transfer and higher dissociating strength can reduce the potential drop[32]. Alternatively, a mechanically stable liquid-liquid interface can be established by placing an unreactive and thin porous membrane between two immiscible electrolyte solutions[33].

2.4 Charge transfer reactions at the liquid-liquid/the electrolyte solution-electrode interfaces

There are 3 types of charge transfer reactions that could occur at an interface when a potential difference is applied. These are ion, facilitated ion and electron transfer processes[34].

2.4.1 Ion transfer reaction at the liquid-liquid interface

When two immiscible solutions are brought in contact with one another and a potential is achieved from the molecules situated close to the interface and in the presence of excess free charges. The transfer of an ion between the aqueous and the organic phase can be defined by equation 2.1[35].

$$x_{i\,(w)}^{z_i} = x_{i\,(o)}^{z_i} \qquad \text{(eq. 2.1)}$$

Where, $x_{i\,(w)}^{z_i}$ is the ion transfer from the aqueous to the organic phase and the $x_{i\,(o)}^{z_i}$ is the ion transfer from organic to the aqueous phase. The Galvani potential difference between the two conductive media at equilibrium can be related to the aqueous and the organic phases sharing a common ion. The ion transfer process can be therefore expressed in the form of Nernst equation (equation 2.2), which administrates the ion distribution at equilibrium between the two electrified liquid solutions[36].

$$\Delta_o^w \phi = \Delta_o^w \phi_i^{\emptyset} + \frac{RT}{z_i F}\, In\, \frac{c_i^o}{c_i^w} \qquad \text{(eq. 2.2)}$$

Where, $\Delta_{\mathrm{o}}^{\mathrm{w}}\phi$ *i*s the phase-boundary potential or the difference in the inner potentials of the organic and the water phases, $\Delta_{\mathrm{o}}^{\mathrm{w}}\,\phi_{\mathrm{i}}^{\emptyset}$ is the standard ion-transfer potential of ion *i*, which can be replaced by the formal potential of transfer $\Delta_{\mathrm{o}}^{\mathrm{w}}\,\phi_{\mathrm{i}}^{\emptyset\,\prime}$, *R* is the gas constant (J mol K^{-1}), *T* is the absolute temperature (K), z_i is the charge of the ions, *F* is the Faraday constant (C mol^{-1}) and *c* is the concentration of ion *i* in the organic and water phase(mol cm^{-3}). The Nernst equation above is also applicable for the ion transfer process at the electrolyte-electrode solution interface.

2.4.2 Assisted or facilitated ion transfer reaction at the liquid-liquid interface

An ion with higher Gibbs energy of transfer are usually observed to move across the interface just outside or close to the positive/negative ends of the potential window in the presence of

electrolytes. The Gibbs energy of ion transfer however can be reduced enough for the transfer process to occur within the potential window by combining the charged species with a ligand. The complexation process at the interface is outlined below (equation 2.3)[37].

$$x_{i_{(aq)}} + L_{(o)} \leftrightarrow x_i L_{(o)} \qquad \text{(eq. 2.3)}$$

Where, x_i is the ion species and *L* is the ligand that forms a complex with the ion. In 1991, Girault *et al.* proposed possible reaction mechanisms for the facilitated ion transfer process which in turn depends on the solubility of the ligands in the aqueous or the organic phases. These are transfer by interfacial complexation (TIC), transfer by interfacial dissociation (TID), transfer followed by organic phase complexation (TOC) and aqueous complexation followed by the transfer of the complex (ACT)[38]. During the same time, theoretical equations (equations 2.4 and 2.5) for current-potential relationship demonstrating TIC for 1:1 complexation was developed by Matsuda *et al.*, given that the bulk concentration of the ions is greater than the bulk concentration of ligands[39]:

$$\Delta_o^w \phi = \Delta_o^w \phi^{1/2} + \frac{RT}{zF} In \left(\frac{I}{I_1 - I}\right) \qquad \text{(eq. 2.4)}$$

$$\Delta_o^w \phi^{1/2} = \Delta_o^w \phi^{\emptyset} - \frac{RT}{zF} In\, \xi + \frac{RT}{zF} In \left(\frac{1 + \xi K_{P,L} + K_a^w c_m^w}{K_{P,L} + K_a^o c_m^o}\right) \qquad \text{(eq. 2.5)}$$

Where, $\Delta_o^w \phi^{1/2}$ is the half-wave potential, $I_1$is the diffusion limited current, ξ is equal to $(\mathrm{D_o}/\mathrm{D_w})^{1/2}$ where, D_w and D_o are the diffusion coefficients for all of the transferred species in the aqueous and organic phases respectively, c_m^w / c_m^o are the concentrations of the ions in the aqueous/organic phases , $K_{P,L}$ and k_a^w / k_a^o are the distribution coefficients of the ligand and the complexion constants in both the water and the organic phases. The facilitated ion transfer reaction leads to a reduction in the solvation energy which in turn allows the ion to be transported without any complications.

2.4.3 Electron transfer reaction at liquid-liquid interface

At the liquid-liquid interface when a potential is applied, the electrons are transferred between the redox species present in the aqueous and the organic phases. This can be represented by equations 2.6 (for the oxidation reaction), 2.7 (for the reduction reaction) and 2.8 (for the redox reaction) below[40].

$$Ox_1^{z,01}{}_{(w)} + e^- \leftrightarrow Red_1^{z,R1}{}_{(w)} \qquad \text{(eq. 2.6)}$$

$$Red_2^{z,R2}{}_{(o)} \leftrightarrow Ox_2^{z,02}{}_{(o)} + e^- \qquad \text{(eq. 2.7)}$$

$$Ox_1^{z,01}{}_{(w)} + Red_2^{z,R2}{}_{(o)} \leftrightarrow Red_1^{z,R1}{}_{(w)} + Ox_2^{z,02}{}_{(o)} \qquad \text{(eq. 2.8)}$$

Where, $Ox_1^{z,01}$and $Red_2^{z,R2}$ are the reactants, $Red_1^{z,R1}$ and $Ox_2^{z,02}$ are the products of the reaction and n is the number of electrons involved in the reaction. The electron transfer reaction can be defined in terms of the concentrations of the redox species using the Nernst equation (equation 2.9) as stated below[41].

$$\Delta_o^w \phi = \Delta_o^w \phi_e^{\emptyset} + \frac{RT}{n_1 n_2 F} In \left(\left(\frac{c_{Red_1}^w}{c_{Ox_1}^w}\right)^{n^2} \left(\frac{c_{Ox_2}^o}{c_{Red_2}^o}\right)^{n^1}\right) \qquad \text{(eq. 2.9)}$$

Where, $c_{Red_1}^w$and $c_{Red_2}^o$ are the concentrations of the reduced species in the liquid phase 1 and the liquid phase 2, respectively. The $c_{Ox_1}^w$ and $c_{Ox_2}^o$ terms on the other hand are the concentrations of the oxidised species in the liquid phase 1 and the liquid phase 2, respectively. The liquid-liquid interface can be used to determine the kinetic properties such as the rate of ion or electron transfer, the standard Gibbs energy and the standard potentials of the ions/electrons as well as the diffusion coefficient and the rate constant values of the charged particles can be also evaluated.

2.4.3.1 The rate of electron transfer at liquid-liquid interface

From a kinetic prospect, a single electron transfer process across the liquid-liquid interface can be defined by the second order rate law (equation 2.10) below[42].

$$J_e = -\frac{j}{F} = k_f c_{Red_1}^w(x=0) c_{Ox_2}^o(x=0) - k_r c_{ox_1}^w(x=0) c_{Red_2}^o(x=0) \qquad \text{(eq. 2.10)}$$

Where, $J_e$is the electron flux density for the electron transfer reaction in the direction of water to organic phase, j is the electric current density, k_f and k_r are the forward and reverse reaction rate constants, $c^w$and $c^o$are the concentrations of the reactant at the aqueous and the organic side of the ITIES, respectively. The heterogeneous rate constants for the forward and the backward electron transfer process can be related to one another by the principle of microscopic reversibility as expressed in the form of equation 2.11[42].

$$\frac{k_f}{k_r} = \exp[-F\,(\Delta_o^w \phi - \Delta_o^w\, \phi_e^{\emptyset})RT] \qquad \text{(eq. 2.11)}$$

For an equilibrium distribution of the reactant or the products to positions (x) denoted by letters a and b close to the interface in the aqueous and organic phases respectively, the k_f rate constant can be given by equation 2.12[42].

$$k_f = k_{ft}\,\rho(a,b) = k_{ft}\exp[-z_{Red_1}\ F\phi_2^w + \ z_{Ox_2}F\phi_2^{wo})/RT] \qquad \text{(eq. 2.12)}$$

Where, k_{ft} is the true rate constant, $\rho(a,b)$ is the probability of the redox species reaching the positions a and b which are close to the interface. Beyond these points, the electrons are driven by the local potential gradients across the phase boundary. Given that the interface between the aqueous and the organic phase is plane and sharp, the k_{ft} term can be represented by the expression stated below (equation 2.13)[42,43].

$$k_{ft} = Z\exp(\frac{\Delta G^{\neq}}{RT}) \qquad \text{(eq. 2.13)}$$

$$\text{Where, } \Delta G^{\neq} = (\lambda+\Delta G^{\Theta})^2/4\lambda \qquad \text{(eq. 2.14)}$$

Where, Z is a pre-exponential term, $\Delta G^{\neq}$is the Gibbs activation energy, $G^{\Theta}$is the standard electrochemical Gibbs energy of electron transfer from x = a to x = b and λ_r is the total reorganisation energy (gained from the solvent and reactant/product conformational changes) of the electron transfer process.

2.4.4 Electron transfer reaction at the electrolyte-electrode interface

There are two types of electron transfer reactions that can occur at the electrolyte-electrode interface and these are faradaic and non-faradaic processes[44]. The Faradaic reaction involves transfer of electrons or charges across an interface in a potential region which is thermodynamically and kinetically favourable for the process to occur. If the transfer process occurs in solution than the reaction is classed as homogeneous and if the process takes place at the electrode surface then the reaction is referred to as heterogeneous[45]. The Faradaic current in turn leads to a change in the highest level of electronic energy necessary for an

oxidation or reduction reaction to occur at the charge-transfer electrode. This can be signified by the expression below (equation 2.15)[46]:

$$O + ne^- \leftrightharpoons R \qquad \text{(eq. 2.15)}$$

Where, *O* and *R* are the oxidised (loses electrons) and reduced (gains electrons) species. In this process, when a potential is applied to the working electrode, the electrons are transferred between the metal-solution phase boundary. At equilibrium, the potential applied at the electrode (E) depends on the concentration of the electroactive species and can be described by the Nernst equation (equation 2.16)[47].

$$E = E^o + \frac{RT}{nF} ln \frac{[Ox]_0}{[Red]_0} \qquad \text{(eq. 2.16)}$$

Where, $[Ox]_0$ and $[Red]_0$ are the concentrations of the oxidised and reduced species in the solution, $E^o$is the formal potential, R is the universal gas constant (8.314 $JK^{-1}mol^{-1}$), *T* is the temperature, n is the number of electrons transferred during the reaction and F is the Faraday constant (96,485 A/mol). The Faradaic current can be used to determine the kinetic properties such as the rate of ion or electron transfer, the standard Gibbs energy, the standard potentials of the ion or electron transfer, the diffusion coefficient and the rate constant values of the charged ions.

The Faradaic reaction can be defined in terms of Fermi level, E_F^α, which represents the available average energy of electrons in phase α and it is the level up to which the highest energy electrons can occupy a partially filled band[48]. For an inert metal electrode in contact with a solution under equilibrium condition, it can be assumed that the Fermi levels of both phases are equal, $E_F^S = E_F^M$, and it can be therefore assumed that the average energies of the electrons are equivalent in both phases as the electrons are transferred from higher Fermi level to the lower level. This can be represented by the model below[49] (figure 2.4).

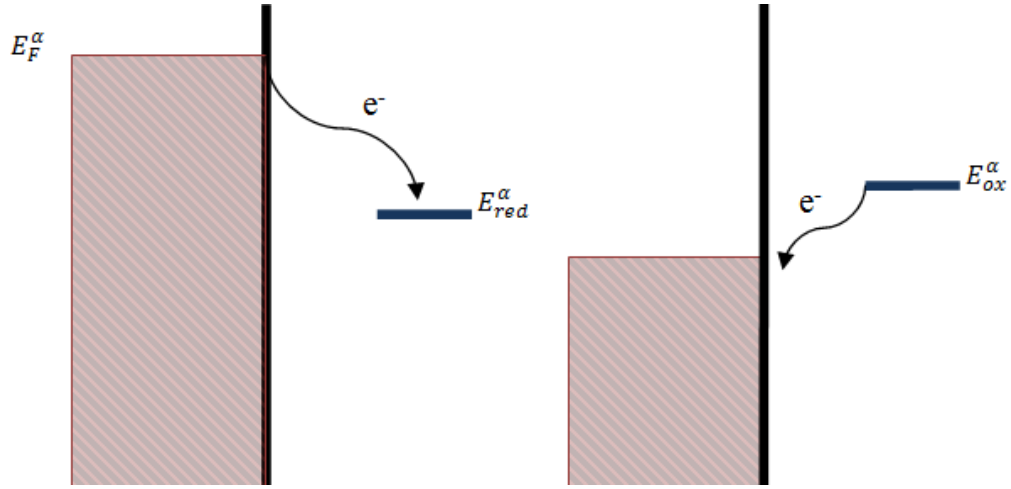

Figure 2.4: A model showing the change in E_F^α upon applying a potential leading to (a) reduction ($(E_{red}^\alpha)\ and$ (b) oxidation (E_{ox}^α) reaction.

A simple reaction involves mass transport of the electroactive species to the electrode surface followed by electron transfer to the interface and finally, mass transport of the redox species into the bulk solution. This is illustrated in the schematic diagram below (figure 2.5) [50].

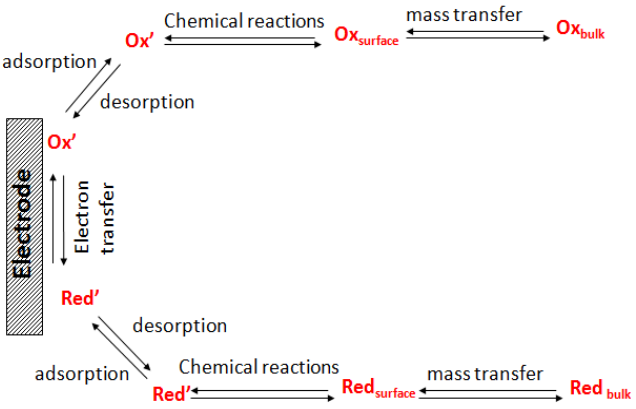

Figure 2.5: Schematic representation of a general electrode process.

Non-faradaic reaction on the other hand is where the adsorption and the desorption processes take place at the electrode-solution interface and no charge-transfer reaction occurs as it is thermodynamically or kinetically unfavourable[51]. This can lead to change in the electrode structure, the electrode area or the solution constituent with the varying potential applied. The non-faradaic current can influence the electrochemical data obtained for the faradaic processes occurring at the metal-electrode and the solution interface. Such processes therefore should be considered when evaluating the faradaic reaction results[52]. In non-Faradaic process, the electrode-solution interface mimics a capacitor as the potential applied causes the charging current to flow while the currents build up on the electrode surface[53]. For

an ideal capacitor, the charge (q) stored is directly proportional to the potential difference and can be defined by equation 2.17[54].

$$q = CE \qquad \text{(eq. 2.17)}$$

Where C is capacitance (in Farads, F) and E is the potential of the capacitor (in Volts, V).

2.4.4.1 The rate of electron transfer reaction at the electrolyte- electrode interface

The rate of forward (V_f) and backward (V_r) electron transfer processes can be expressed in terms of the first order reaction (equations 2.18 and 2.19)[55] :

$$V_{f=} k_f c_o(0,t) \qquad \text{(eq. 2.18)}$$

$$\text{And, } V_{r=} k_r c_R(0,t) \qquad \text{(eq. 2.19)}$$

Where, $c_o$and c_R are the concentrations of the electroactive species in the forward and reverse processes and k_f and k_r are the forward and reverse reaction rate constants, respectively. The overall reaction rate ($V_{overall}$) can be represented in the form of following expression (equation 2.20)[55]:

$$V_{overall} = V_f - V_r = k_f c_o(0,t) - k_r c_o(0,t) \qquad \text{(eq. 2.20)}$$

The rate constants (k_f and k_r) are in turn dependent on the potential applied and therefore, can be defined in terms of equations 2.21 and 2.22.

$$k_f = k^o \exp\left[-\alpha n F \frac{E-E^o}{RT}\right] \qquad \text{(eq. 2.21)}$$

$$\text{And, } k_r = k^o \exp\left[-\alpha n F \frac{E-E^o}{RT}\right] \qquad \text{(eq. 2.22)}$$

Where, k^o is the standard heterogeneous rate constant that represents the reaction occurring between the reactant and the electrode, α is the electron transfer coefficient that mirrors the change in free energy with respect to the reactants and the products in the reaction. Since, the forward (i_f) and reverse (i_r) currents are proportional to the rate of reactions in both ways (V_f and V_r), the overall current can be expressed by the difference in the currents of the forward and reverse reactions (equation 2.23)[55].

$$i_{overall} = i_f - i_r = nFA[k_f c_o(0,t) - k_r c_R(0,t)] \qquad \text{(eq. 2.23)}$$

By substituting the k_f and k_r expressions (equations 21 and 22) into the above equation generates the Butler-Volmer equation (equation 2.24), which in turn shows that the current-potential relationship for the reactions are dependent on the rate of electron transfer[55].

$$i = nFA\,k^o\{c_O(0,t)\exp\,[-\frac{\alpha nF(E-E^O)}{RT}] - c_R(0,t)\exp\,[\frac{(1-\alpha)nF(E-E^O)}{RT}]\} \qquad \text{(eq. 2.24)}$$

Where, E^o is the potential at which both the forward and reverse rate constants have the same value. When the interface is at equilibrium with a solution where c_o is equal to c_R, $E = E^o$ and the $k_f c_O$ is equal to $k_r c_R$. Consequently, k_f = k_r. The movement of the charges is therefore constant in both forward and reverse directions and with equal anodic and cathodic currents. This can be expressed in terms of the exchange current, i_o, at E^o which in turn is directly proportional to k^o(equation 2.25)[56].

$$i_o = i_a = i_c = nFAk^o\mathrm{c} \qquad \text{(eq. 2.25)}$$

Therefore, the Butler-Volmer equation can be defined by i_o, at equilibrium using equation 2.26 below[56].

$$i = i_o[\exp\,(-\frac{\alpha nF\eta}{RT}] - \exp\,(\frac{(1-\alpha)nF\eta}{RT})] \qquad \text{(eq. 2.26)}$$

Where, η is the overvoltage, which is the extra potential outside the equilibration potential leading to current, i, and also, equal to E (potential applied) - E_{eq} (potential at equilibrium).

2.5 Double layer at the liquid-liquid interface

The electric double layer formed at the ITIES was first proposed by Verwey and Niessen in 1939 as mentioned earlier. The layer is composed of two adjoining space-charge regions with surplus of cations on one side whilst excess of anions is distributed on the other side. However, a mixture of positively and negatively charged ions can exist on both sides. This in turn causes the interface between the two phases to be electrically neutral[57]. The space charge distribution was referred to as two back-to back layers by Gouy-Chapman[58]. Following which, Gavach e*t al.* in 1977 proposed a new modified Verwey-Niessen (MVN) model by taking into account of the assumption that the electrical regions are separated by an ion free layer of solvent molecules which is also referred to as an inner layer (figure 2.6)[59].

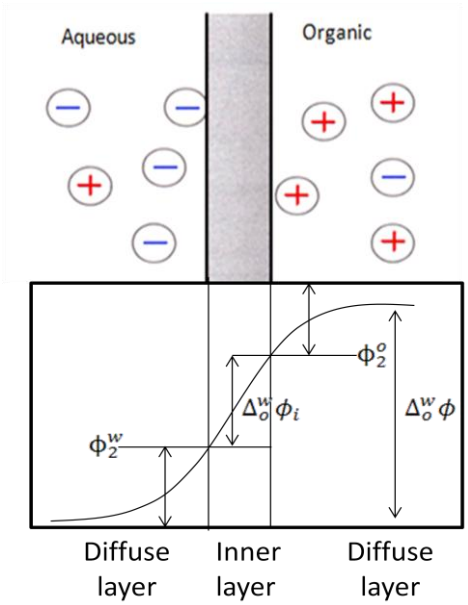

Figure 2.6: Model of ITIES with an inner layer separating the two-space charge regions[59].

In the MVN model, the Galvani potential difference, $\Delta_o^w\phi$, between the two immiscible phases can be defined by equation 2.27[38].

$$\Delta_o^w\phi = \phi^w - \phi^o = \Delta_o^w\phi_i + \phi_2^o - \phi_2^w \qquad \text{(eq. 2.27)}$$

Where, the $\Delta_o^w\phi_i$ term is the potential difference across the inner layer, ϕ_2^o and ϕ_2^w represent the potential differences across the diffuse layers in the organic and the water phases, respectively.

The excess charge densities of the aqueous (Q_S^w) and the organic (Q_S^o) phases in the part of the electrically neutral double layer can be defined by equation 2.28[60].

$$Q_S^w + Q_S^o = 0 \qquad \text{(eq. 2.28)}$$

Given that the space charge regions are separated by a layer of solvent molecules, it can be related to the Galvani potential difference, $\Delta_o^w\phi$, between the aqueous and the organic phases by equation 2.29.

$$\Delta_o^w\phi = \phi_{in}^{w,o} + \phi_2^o - \phi_2^w \qquad \text{(eq. 2.29)}$$

Where, $\phi_{in}^{w,o}$, $\phi_2^o$and ϕ_2^w are the potential differences across the inner layer and the space charge regions in the organic and the aqueous phases. The double layer at the liquid-liquid interface is composed of a Helmhotz plane similar to that of the Gouy-Chapman-stern

electrical double layer model. The inner Helmholtz plane (IHP) is considered to pass through the centre of the specifically adsorbed ions whereas the distance of closest approach to the interface for the non-specifically adsorbed ions is referred to as the outer Helmholtz plane (OHP) [61]. The OHP plane is considered as the approximate site for ion transfer. The inner layer leads to separation of the OHP for the aqueous and the organic phases at the ITIES[62].

Following the development of the MVN model, Girault and Schiffrin introduced the mixed solvent layer for illustrating the ITIES which proposed that a constant variation in the constituent of one phase to the other was a suitable representation comparing to the modified Verwey-niessen model suggested by Gavach et al[63]. This was due to the interfacial tension measurements of the non-polarisable ITIES, which revealed that there is a surface excess of water at the phase boundary between the organic solvent and the aqueous electrolyte, causing the ions to infiltrate the interfacial region and form a mixed solvent layer. The Galvani potential difference was found to spread within the aqueous and the organic diffusion layers with a reduced potential drop and the mixed solvent layer. The diffusion of the ions at the interface is highly dependent on the hydrophilicity of the ions[63].

2.6 Electrical double layer at the electrode-solution interface

When an electrode is placed in an electrolyte solution, a potential is produced at the electrode-electrolyte interface which permits the electronic charge on the electrode to attract ions with opposite charge and also, adjust the solvent dipoles. If the electrode is positively charged it will attract negative ions from the solution while a negatively charged electrode will pull positive ions towards it[64]. The separation of charge at the electrode-electrolyte solution interface can be described in terms of an electrical double layer which in turn consists of two layers of charge. One of these layers is located at the electrode surface and the other in the aqueous electrolyte solution[64].

The concept of the electrical double layer was first defined by Helmholtz in 1879[65]. However, the potential applied and the electrolyte concentration used has been found to alter the double layer capacity. Following this, both Gouy and Chapman have developed a double layer model separately, taking into account of the fact that the double layer thickness varies with the movement of ions via diffusion[66]. The model was then further expanded by Stern in 1924 who integrated both Helmholtz and Gouy- Chapman's models into a simple double layer model, demonstrating that it is made up of a Stern/compact layer, which is composed of ions close to the electrode surface, and a diffusion layer next to it, situated in the bulk solution[67].

The complexity of the double layer can be illustrated by the model representation below (figure 2.7) [68].

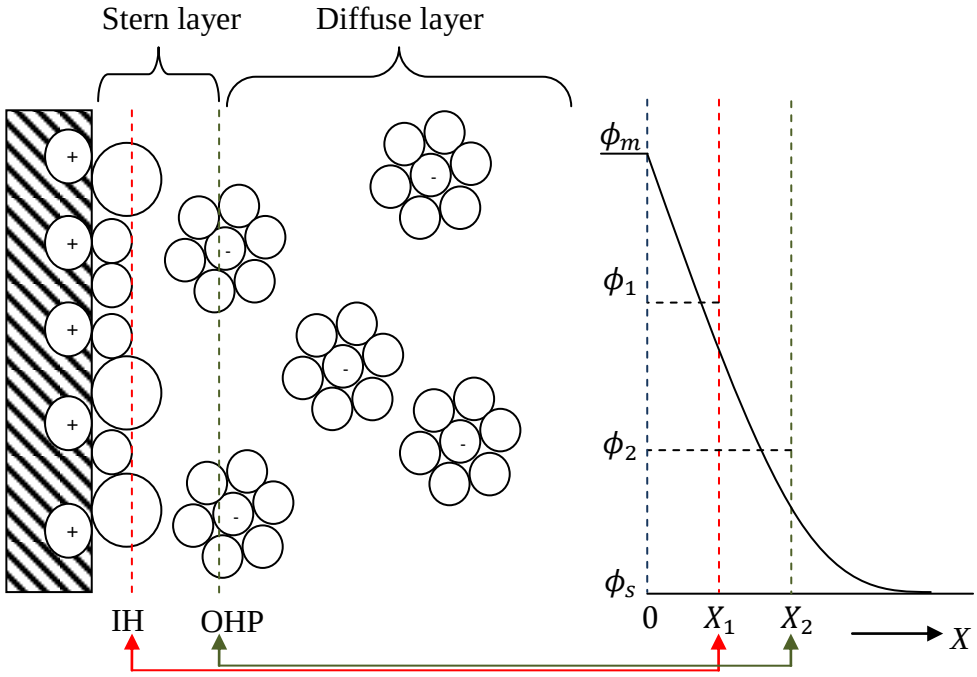

Figure 2.7: Schematic representation of the double layer model.

Where, ϕ_m is the maximum potential, ϕ_1 is the potential at which specific ion adsorption occurs, ϕ_2 is the potential at which non-specific adsorption takes place and ϕ_s is the minimum potential, X is the distance from the electrode, X_1 is the distance from the electrode at which specific ion adsorption occurs, X_2 is the distance from the electrode at which solvated ions are non-specifically adsorbed, IHP is the inner Helmholtz Plane and OHP is the outer Helmholtz plane. Based on the above double layer model, it can be deduced that the interface is neutral due to the total charge density of the bulk solution (σ^S) side of the double layer being equal to that of both the stern (σ^i) and diffuse (σ^d) layers. This can be expressed by equation 2.30 below[69].

$$\sigma^S = \sigma^i + \sigma^d \qquad \text{(eq. 2.30)}$$

The IHP of the double layer was first pioneered by Grahame in 1947. It is the inner layer adjoining the electrode, consisting of solvent molecules and the specifically adsorbed ions. The OHP on the other hand is composed of the solvated and the non-specifically adsorbed ions that are bound to the electrode via long-range electrostatic forces[70]. Both of these planes make up the Stern layer. Beyond this, there is a diffuse layer which expands from the OHP layer to the bulk solution and it can be defined as a three-dimensional region of scattered

ions[71]. The thickness of the diffuse layer is dependent on the total ionic concentration of the solution and it can be expressed by the Boltzmann equation stated below (equation 2.31)[72].

$$c(x) = c(0)\exp(-zF\phi)/RT \qquad \text{(eq. 2.31)}$$

Where, $c(x)$ is the concentration of the ionic species from a fixed distance (x) away from the surface which exponentially decays with the ratio between the $zF\phi$ (electrostatic energy) and RT (thermal energy) terms. Variation in the double layer structure, double layer capacitance and the charging current can affect the rate of electrode reaction.

In 1963, a new double layer model was proposed by Bockris, Devanathan and Muller which took into consideration the predominant role and re-orientation of the solvent molecules at the interface. However, the distribution of the electronic charges at the electrode is not completely elucidated in this model[73].

2.7 Factors affecting the rate of reaction

Electrochemical methods can be used to measure the ion and the electron transfer. The behaviour of an electrochemical reaction can be controlled by changing certain variables whilst keeping the other factors constant (figure 2.8)[74].

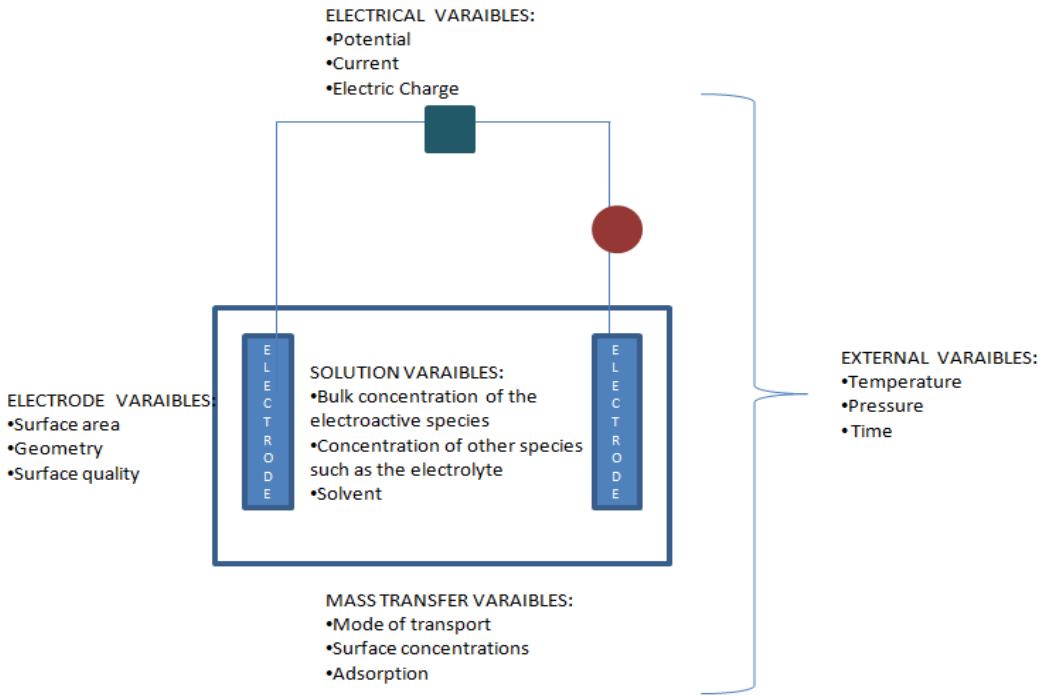

Figure 2.8: Variables affecting the rate of reaction[74].

The rate of reaction at an electrode-solution interface is influenced by the parameters shown in figure 2.8. The solid-liquid interface can be affected by variables such as the bulk concentration of the electroactive species, the concentration of the electrolytes, the solvents used and the pH of the solution. These factors can also have an influence on the liquid-liquid interface[75].

2.8 Mass transfer reactions at the solid-liquid and the liquid-liquid interfaces

The ion transfer process across the ITIES is restricted by the mass transfer of ions at the interface similar to that occurring for the transfer of electroactive species at the electrolyte-electrode interface. There are three types of mass transfer processes that can take place in an electrochemical reaction at the interface between the electrode and the solution and it is also applicable to the ITIES. These are diffusion, convection and migration[76]. The rate of mass transport of the electroactive species/ions at a fixed point is referred to as the flux, $J_{(x,t)}$, which in turn is defined as the number of molecules flowing through a unit area of an imaginary place in a unit of time[77]. This can be represented by the Nernst-Planck equation (equation 2.32) below[38].

$$\underbrace{J_{(x,t)} = -D}_{\text{Diffusion}} \underbrace{\frac{\partial c_{(x,t)}}{\partial x} - \frac{zFDc}{RT} \frac{\partial \phi_{(x,t)}}{\partial x}}_{\text{Migration}} + \underbrace{c_{(x,t)} \mathrm{V}_{(x,t)}}_{\text{Convection}} \qquad \text{(eq. 2.32)}$$

Where, D is the diffusion coefficient (m^2s^{-1}), $\frac{\partial c_{(x,t)}}{\partial x}$ is the concentration gradient at distance x and time t, $\frac{\partial \phi_{(x,t)}}{\partial x}$ is the potential gradient, $c_{(x,t)}\mathrm{V}_{(x,t)}$ is the hydrodynamic velocity (ms^{-1}) in the x direction, z and c are the charge and the concentration of the electroactive species ($molm^{-3}$), respectively. For a diffusion process, when the current flows through the electrolyte solution, the concentration of the reactant decreases at the interface in relative to the bulk concentration as the electrochemical reaction takes place. This leads to a diffusion flux due to the formation of a concentration gradient. Consequently, the ion species in the solution linearly diffuse across from a high to a low concentration region. Since both, the migration and the convection processes are negligible in most ITIES/electrolyte-electrode investigations; the movement of the charged species is limited to the diffusion process. The diffusion phenomenon across a macro-interface can be defined by Fick's first law (equation 2.33), which shows that the rate of the diffusion flux is directly proportional to the slope of the concentration gradient, given that the system is at a steady state[78]. The change in the concentration of the electroactive/ionic species at the electrolyte-electrode interface and in

the aqueous and organic phases respectively, can be expressed as a function of time and therefore, defined by Fick's second law (equation 2.34) [79].

$$J_{(x,t)} = -D \frac{\partial C_{(x,t)}}{\partial x} \quad \text{(eq. 2.33)}$$

$$\left(\frac{\partial c}{\partial t}\right) = D \frac{\partial^2 c}{\partial x^2} \quad \text{(eq. 2.34)}$$

Where, J is the flux ($molm^{-2}s^{-1}$), the minus sign in equation 2.33 indicates that the substances are moving down the concentration gradient, D is the diffusion coefficient (m^2s^{-1}), c is the concentration of the ionic/electroactive species ($molm^{-3}$), x is the length (meters) and t is the time (seconds). Furthermore, the current, i, is directly proportional to the flux and the surface area (A), which can be defined by equation 2.35 below[80].

$$i = -nFAJ \quad \text{(eq. 2.35)}$$

By substituting equation 2.33 into equation 2.35 generates equation 2.36, which demonstrates that the current at a particular time is directly proportional to the concentration of the electroactive/the ionic species.

$$i = nFAD \frac{\partial c_{(x,t)}}{\partial x} \quad \text{(eq. 2.36)}$$

Migration on the other involves movement of the charged particles due to a potential gradient[81]. During this process, the charge is carried by an ionic particle in the solution. Contrary to this, convection can be defined as the movement of the electroactive species/the ions within a volume upon application of an external mechanical energy force produced via stirring, pumping or sonicating. Natural convection can also take place as a result of vibration or formation of a density/thermal gradient in the bulk solution[82].

The simultaneous occurrence of all three modes of mass transport however can lead to difficulties in the analysis of the results obtained. Consequently, the electrochemical systems are modified to eliminate one or more of these mass transport factors. For instance, the migration process is minimised by restraining electromigration via adding higher concentration of the supporting electrolyte than the concentration of the electroactive species present, which in turn enhances the conductivity of the solution and allows a constant ionic strength to be established[83]. As a result, the term $\frac{zFDc}{RT} \frac{\partial \phi_{(x,t)}}{\partial x}$ in equation 2.32 becomes insignificant and it is neglected. Furthermore, at the liquid-liquid and the electrode-electrolyte interfaces, the solutions generally remain unstirred and the electrodes are inert. This

therefore implies that there are no vibrations or convection in the electrochemical cells. Hence, in this case the term $c_{(x,t)}\mathrm{V}_{(x,t)}$ in equation 2.32 can be ignored[84].

2.9 Macro-ITIES

A macro-ITIES can be considered as a plane interface between two semi-infinite liquid phases. A macro-ITIES can be used for the study of charge transfer processes and various chemical reactions, in the form of current flow. This type of ITIES also allows precise monitor and control of both, the potential between two liquid-liquid phases as well as the structure and the properties of the interface[85]. The diffusion process across the macro-ITIES is linear. The change in the rate of the diffusion flux across the macro interface and the change in the concentrations of the charged species in the different phases can be expressed by Fick's first law (equation 2.33) and Fick's second law (equation 2.34) respectively, as mentioned in section 2.8. Furthermore, for a macro-interface the current is directly proportional to the flux and this can be defined by equation 2.36. Based on the Nernst equation (equation 2.2), the boundary conditions for a macro interface and the equality of the flux in both phases generates equation 2.37[86].

$$-D^w \left(\frac{\partial c^w}{\partial x}\right)_{x=0} + D^o \left(\frac{\partial c^o}{\partial x}\right)_{x=0} = 0 \qquad \text{(eq. 2.37)}$$

Where, D^w and D^o are the diffusion coefficient values of the charged species in the aqueous and the organic phases and $c^w$and c^o are the concentrations of the charged species in the aqueous and the organic solutions.

2.10 Micro-ITIES

Micro-ITIES is useful for the study of ion transfer processes because the diffusion fields can be controlled by the geometry of the system and also, the ohmic potential drop can be minimised using this method. Additionally, a low charging current and a high mass transfer rate can be attained using a micro ITIES which makes it ideal for fast kinetic measurements. Micro-ITIES supported on a micro-pipette tip, with a diameter less than a micrometer, is used to provide spherical diffusion effect similar to that of a solid microelectrode as the charged species enters the pipette which in turn increases mass transport and generates a steady – state current[87]. However, when the ions transfer from the micro-pipette to the phase boundary, it follows a linear diffusion regime due to limitation arising from the walls of the micro-pipette. In the case of micro-holes in supporting polymer films, the transport of ions is controlled by a

spherical diffusion field. Based on this, if the micro-interface is considered to be spherical it can be defined by Fick's first law (equation 2.38) and for the distribution of the charged species near the micro interface for a reversible charge transfer reaction, Fick's second law (equation 2.39) can be applied in spherical coordinates[54].

$$J = -D\left(\frac{\partial c}{\partial r}\right) \qquad \text{(eq. 2.38)}$$

$$\left(\frac{\partial c}{\partial t}\right) = D\left(\frac{\partial^2 c}{\partial r^2}\right) + \frac{2D}{r}\left(\frac{\partial c}{\partial r}\right) \qquad \text{(eq. 2.39)}$$

Where, J is the flux ($molm^{-2}s^{-1}$), r is the radial distance of the interface from the centre of the sphere (meters), D is the diffusion coefficient (m^2s^{-1}), c is the concentration of the ionic species ($molm^{-3}$) and t is the time (seconds). The asymmetrical diffusion pattern produced using a micro-pipette can be used for example, to study the charge transfer processes occurring at the micro-ITIES[88] and to determine the charged species which are responsible for limiting the potential window[89].

2.11 References

1. Ling, G. *In Search of the Physical Basis of Life*. (Springer Science & Business Media, 2012).
2. Volkov, A. G., Deamer, D. W., Tanelian, D. L. & Markin, V. S. Electrical double layers at the oil/water interface. *Prog. Surf. Sci.* **53,** 1–134 (1996).
3. Petrović, M., Kaštelan-Macan, M. & Horvat, A. J. M. Thin-layer chromatographic behaviour of substituted phenolic compounds on silica gel layers impregnated with Al(III) and Cu(II). *J. Chromatogr. A* **607,** 163–167 (1992).
4. Koryta, J. Theory and applications of ion-selective electrodes part 4. *Anal. Chim. Acta* **139,** 1–51 (1982).
5. Vanysek, P. *Charge Transfer Processes on Liquid/Liquid Interfaces: The First Hundred Years.* (NORTHERN ILLINOIS UNIV DE KALB DEPT OF CHEMISTRY, NORTHERN ILLINOIS UNIV DE KALB DEPT OF CHEMISTRY, 1992). at <http://www.dtic.mil/docs/citations/ADA260421>
6. Osakai, T., Kakutani, T. & Senda, M. A Novel Amperometric Ammonia Sensor. *Anal. Sci.* **3,** 521–526 (1987).
7. Samec, Z., Mareček, V. & Weber, J. Charge transfer between two immiscible electrolyte solutions: Part II. The investigation of Cs+ ion transfer across the nitrobenzene/water interface by cyclic voltammetry with IR drop compensation. *J. Electroanal. Chem. Interfacial Electrochem.* **100,** 841–852 (1979).

8. Koryta, J. *et al.* A new model of membrane transport: Electrolysis at the interface of two immiscible electrolyte solutions. *J. Electroanal. Chem. Interfacial Electrochem.* **116,** 61–68 (1980).
9. Harrington, M. S., Anderson, L. B., Robbins, J. A. & Karweik, D. H. Multiple electrode potentiostat. *Rev. Sci. Instrum.* **60,** 3323 (1989).
10. Zazpe, R., Hibert, C., O'Brien, J., Lanyon, Y. H. & Arrigan, D. W. M. Ion-transfer voltammetry at silicon membrane-based arrays of micro-liquid–liquid interfaces. *Lab. Chip* **7,** 1732 (2007).
11. Manzanares, J. A., Lahtinen, R., Quinn, B., Kontturi, K. & Schiffrin, D. J. Determination of rate constants of ion transfer kinetics across immiscible electrolyte solutions. *Electrochimica Acta* **44,** 59–71 (1998).
12. N, W., R, I., S, C., S, D. & A, B. Ion-Transfer Processes across Liquid/Liquid Interfaces Promoted by a Convective Flux. *Bull Chem Soc Jpn* **75,** 235–240 (2002).
13. Bakker, E. & Qin, Y. Electrochemical Sensors. *Anal. Chem.* **78,** 3965–3984 (2006).
14. Zhang, X., Ju, H. & Wang, J. *Electrochemical Sensors, Biosensors and Their Biomedical Applications*. (Academic Press, 2007).
15. Wang, J., Du, Z., Wang, W. & Xue, W. Ion-Selective Electrode for Anionic Surfactants Using Hexadecyl Trimethyl Ammonium Bromide-Sodium Dodecylsulfate as an Active Ionophore. *Int. J. Electrochem.* **2011,** 1–7 (2011).
16. *The Interface Structure and Electrochemical: Interface Structure and Electrochemical Processes at the Boundary between Two Immiscible Liquids*. (Springer-Verlag Berlin and Heidelberg GmbH & Co. KG, 1987).
17. Sisk, G. D., Herzog, G., Glennon, J. D. & Arrigan, D. W. M. Assessment of ion transfer amperometry at liquid-liquid interfaces for detection in CE. *Electrophoresis* **30,** 3366–3371 (2009).
18. Kazarinov, V. E. *The Interface Structure and Electrochemical Processes at the Boundary Between Two Immiscible Liquids*. (Springer Science & Business Media, 2012).
19. Volkov, A. G., Deamer, D. W. & Tanelian, D. L. *Liquid interfaces in chemistry and biology*. (Wiley, 1998).
20. Petsev, D. N. *Emulsions: Structure, Stability and Interactions*. (Academic Press, 2004).
21. Bockris, J. O. & Reddy, A. K. N. *Modern Electrochemistry: An Introduction to an Interdisciplinary Area*. (Springer Science & Business Media, 1973).

22. Osakai, T., Komatsu, H. & Goto, M. Cationic-surfactant transfer facilitated by DNA adsorbed on a polarized 1,2-dichloroethane/water interface. *J. Phys. Condens. Matter* **19,** 375103 (2007).
23. Bockris, J. O., Reddy, A. K. N. & Gamboa-Aldeco, M. *Modern Electrochemistry*. (Springer, 2000).
24. Gamburg, Y. D. & Zangari, G. *Theory and Practice of Metal Electrodeposition*. (Springer, 2011).
25. Kontturi, A.-K., Kontturi, K., Murtomäki, L. & Schiffrin, D. J. Application of scaled particle theory to the salting out of single hydrophobic ions. *J. Chem. Soc. Faraday Trans.* **86,** 931–936 (1990).
26. Zhurov, K., Dickinson, E. J. F. & Compton, R. G. Dynamics of Ion Transfer Potentials at Liquid–Liquid Interfaces. *J Phys Chem B* **115,** 6909–6921 (2011).
27. Edwards, R., Vignali, M. & Cunnane, V. Derivation of the explicit equation relating mass-transport-limited-current to voltage at the interface between two immiscible electrolyte solutions (ITIES). *J. Appl. Electrochem.* **39,** 205–211 (2009).
28. Liu, S., Li, Q. & Shao, Y. Electrochemistry at micro- and nanoscopic liquid/liquid interfaces. *Chem. Soc. Rev.* **40,** 2236 (2011).
29. Santos, H. A., García-Morales, V. & Pereira, C. M. Electrochemical Properties of Phospholipid Monolayers at Liquid–Liquid Interfaces. *ChemPhysChem* **11,** 28–41 (2010).
30. Berduque, A., Sherburn, A., Ghita, M., Dryfe, R. A. W. & Arrigan, D. W. M. Electrochemically Modulated Liquid−Liquid Extraction of Ions. *Anal Chem* **77,** 7310–7318 (2005).
31. Fantini, S. *et al.* Influence of the presence of a gel in the water phase on the electrochemical transfer of ionic forms of β-blockers across a large water|1,2-dichloroethane interface. *Eur. J. Pharm. Sci.* **18,** 251–257 (2003).
32. Kakiuchi, T. Limiting Behavior in Equilibrium Partitioning of Ionic Components in Liquid−Liquid Two-Phase Systems. *Anal Chem* **68,** 3658–3664 (1996).
33. Amemiya, S., Kim, Y., Ishimatsu, R. & Kabagambe, B. Electrochemical heparin sensing at liquid/liquid interfaces and polymeric membranes. *Anal. Bioanal. Chem.* **399,** 571–579 (2011).
34. Laforge, F. *Nanoelectrochemistry at Liquid/liquid Interfaces and Biomembranes*. (ProQuest, 2008).
35. Iglesias, R. A. & Dassie, S. A. *Ion Transfer at Liquid/Liquid Interfaces*. (Nova Science Pub Incorporated, 2010).

36. Gobry, V. *et al.* Generalization of Ionic Partition Diagrams to Lipophilic Compounds and to Biphasic Systems with Variable Phase Volume Ratios. *J Am Chem Soc* **123,** 10684–10690 (2001).
37. Nishizawa, S. *et al.* Facilitated Sulfate Transfer across the Nitrobenzene-Water Interface as Mediated by Hydrogen-Bonding Ionophores. *Anal. Sci.* **20,** 1559–1565 (2004).
38. Zoski, C. G. *Handbook of Electrochemistry*. (Elsevier, 2006).
39. Zoski, C. G. *Handbook of Electrochemistry*. (Elsevier, 2007).
40. Izutsu, K. *Electrochemistry in Nonaqueous Solutions*. (Wiley-VCH Verlag GmbH & Co. KGaA, 2009). at <http://doi.wiley.com/10.1002/9783527629152>
41. Bockris, J. O., Conway, B. E. & White, R. E. *Modern Aspects of Electrochemistry*. (Springer Science & Business Media, 2012).
42. Bard, A. J., Inzelt, G. & Scholz, F. *Electrochemical Dictionary*. (Springer Science & Business Media, 2012).
43. Laforge, F. Nanoelectrochemistry at liquid/liquid interfaces and biomembranes. (CITY UNIVERSITY OF NEW YORK, 2008). at <http://gradworks.umi.com/32/96/3296956.html>
44. Zhou, D. & Greenbaum, E. *Implantable Neural Prostheses 2: Techniques and Engineering Approaches*. (Springer Science & Business Media, 2010).
45. Zoski, C. G. *Handbook of Electrochemistry*. (Elsevier, 2007).
46. Grimnes, S. & Martinsen, O. G. *Bioimpedance and Bioelectricity Basics*. (Academic Press, 2014).
47. Bard, A. J., Inzelt, G. & Scholz, F. *Electrochemical Dictionary*. (Springer Science & Business Media, 2012).
48. Quimby, R. S. *Photonics and Lasers: An Introduction*. (John Wiley & Sons, 2006).
49. Fuchigami, T., Atobe, M. & Inagi, S. *Fundamentals and Applications of Organic Electrochemistry: Synthesis, Materials, Devices*. (John Wiley & Sons, 2014).
50. Bard, A. J. & Faulkner, L. R. *Electrochemical Methods: Fundamentals and Applications*. (Wiley, 2000).
51. Bond, A. M. *Modern Polarographic Methods in Analytical Chemistry*. (CRC Press, 1980).
52. Vittorio, M. D., Martiradonna, L. & Assad, J. *Nanotechnology and Neuroscience: Nano-electronic, Photonic and Mechanical Neuronal Interfacing*. (Springer, 2014).
53. Conway, B. E. *Electrochemical Supercapacitors: Scientific Fundamentals and Technological Applications*. (Springer Science & Business Media, 2013).
54. Zutshi, K. *Introduction to Polarography and Allied Techniques*. (New Age International, 2006).

55. Wang, J. *Analytical Electrochemistry*. (John Wiley & Sons, 2006).
56. Wang, J. *Analytical Electrochemistry*. (John Wiley & Sons, 2006).
57. Volkov, A. G. *Liquid interfaces in chemistry and biology*. (Wiley, 1998).
58. Volkov, A. G. *Liquid Interfaces In Chemical, Biological And Pharmaceutical Applications*. (CRC Press, 2001).
59. Bagotsky, V. S. *Fundamentals of Electrochemistry*. (Wiley-Interscience, 2011).
60. Bagotsky, V. S. *Fundamentals of Electrochemistry*. (John Wiley & Sons, 2005).
61. Kim, J. U. Electrical double layer : revisit based on boundary conditions. *Computer* 1–12 (2005).
62. Webster, J. G. *The Measurement, Instrumentation, and Sensors Handbook*. (Springer, 1999).
63. Girault, H. H. in *Modern Aspects of Electrochemistry* (eds. Bockris, J. O., Conway, B. E. & White, R. E.) **25,** 1–62 (Springer US, 1993).
64. Revankar, S. T. & Majumdar, P. *Fuel Cells: Principles, Design, and Analysis*. (CRC Press, 2014).
65. Goel, A. *Colloidal Chemistry*. (Discovery Publishing House, 2006).
66. Paunovic, M. & Schlesinger, M. *Fundamentals of Electrochemical Deposition*. (John Wiley & Sons, 2006).
67. Rieger, P. H. *Electrochemistry*. (Springer Science & Business Media, 1994).
68. Zhang, L. L. & Zhao, X. S. Carbon-based materials as supercapacitor electrodes. *Chem. Soc. Rev.* **38,** 2520 (2009).
69. Pessarakli, M. *Handbook of Plant and Crop Stress, Second Edition*. (CRC Press, 1999).
70. Krauskopf, K. B. & Ernst, W. G. *Frontiers in Geochemistry: Organic, Solution, and Ore Deposit Geochemistry*. (Geological Society of America, 2002).
71. Oh, C. H. *Hazardous and Radioactive Waste Treatment Technologies Handbook*. (CRC Press, 2001).
72. Wang, J. *Analytical Electrochemistry*. (John Wiley & Sons, 2004).
73. Bockris, J. O., Devanathan, M. A. V. & Muller, K. On the Structure of Charged Interfaces. *Proc. R. Soc. Math. Phys. Eng. Sci.* **274,** 55–79 (1963).
74. Bard, A. J. & Faulkner, L. R. *Electrochemical Methods: Fundamentals and Applications*. (Wiley, 2001).
75. Pletcher, D. & Walsh, F. *Industrial Electrochemistry*. (Springer, 1990).
76. Plambeck, J. A. *Electroanalytical chemistry: basic principles and applications*. (Wiley, 1982).

77. Monk, P., Mortimer, R. & Rosseinsky, D. *Electrochromism and Electrochromic Devices*. (Cambridge University Press, 2007).
78. Irene, E. A. *Electronic Materials Science*. (John Wiley & Sons, 2005).
79. Campbell, F. C. *Elements of Metallurgy and Engineering Alloys*. (ASM International, 2008).
80. Yacoub, M. & Yang, G.-Z. *Body Sensor Networks*. (Springer Science & Business Media, 2007).
81. Singh, R. P. & Heldman, D. R. *Introduction to Food Engineering*. (Academic Press, 2008).
82. Oldham, K., Myland, J. & Bond, A. *Electrochemical Science and Technology: Fundamentals and Applications*. (John Wiley & Sons, 2011).
83. Inzelt, G. *Conducting Polymers: A New Era in Electrochemistry*. (Springer Science & Business Media, 2012).
84. *Effect of Scale During Electrochemical Degradation of Naphthalene and Salicylic Acid*. (ProQuest, 2008).
85. Volkov, A. G. & Deamer, D. W. *Liquid-Liquid InterfacesTheory and Methods*. (CRC Press, 1996).
86. Möbius, D., Miller, R. & Fainerman, V. B. *Surfactants: Chemistry, Interfacial Properties, Applications: Chemistry, Interfacial Properties, Applications*. (Elsevier, 2001).
87. Sanchez Vallejo, L. J., Ovejero, J. M., Fernández, R. A. & Dassie, S. A. Simple Ion Transfer at Liquid|Liquid Interfaces. *Int. J. Electrochem.* **2012,** 1–34 (2012).
88. Beattie, P. D., Delay, A. & Girault, H. H. Investigation of the kinetics of assisted potassium ion transfer by dibenzo-18-crown-6 at the micro-ITIES by means of steady-state voltammetry. *J. Electroanal. Chem.* **380,** 167–175 (1995).
89. Stewart, A. A., Shao, Y., Pereira, C. M. & Girault, H. H. Micropipette as a tool for the determination of the ionic species limiting the potential window at liquid/liquid interfaces. *J. Electroanal. Chem. Interfacial Electrochem.* **305,** 135–139 (1991).

CHAPTER 3

Experimental methodology

3.1 4-electrode set-up for the study of surfactant behaviour at the ITIES

The electrochemical measurements for the study of surfactant ion transfer, adsorption and micellar formation was conducted at a macro liquid-liquid interface which in turn mimicked the oil and water phase boundary using a 4-electrode system. A 4 –electrode configuration with a positive feedback (figure 3.1) was employed because it: (1) allows Ohmic compensation, (2) minimises the resistance in the organic and aqueous solutions, (3) reduces the current capacitance and (4) maintains the desired potential between the tips of the reference electrodes throughout the experiments[1].

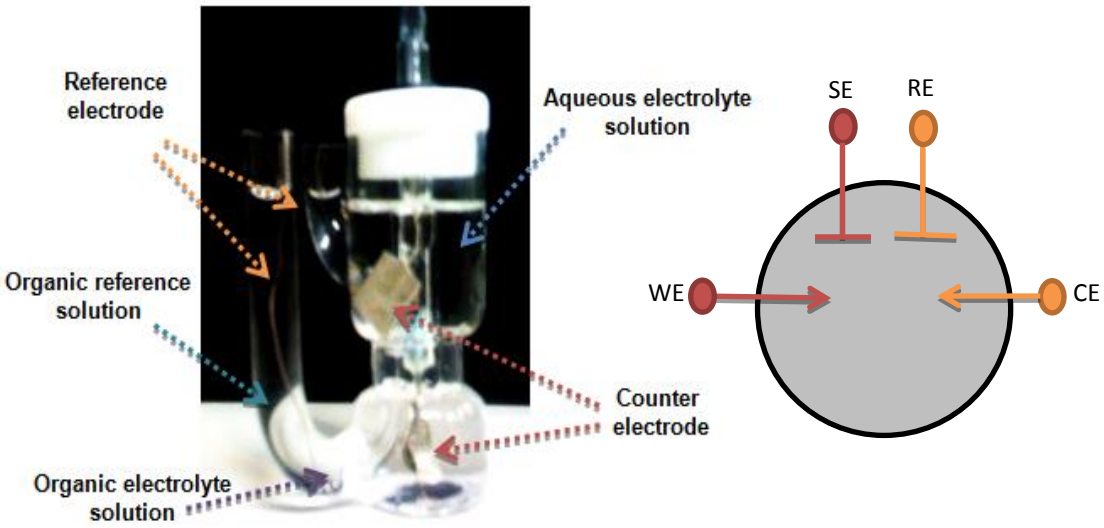

Figure 3.1: (a) set-up for the 4-electrode electrochemical cell system and (b) schematic representation of the 4-electrode system. The analyte of interest was added to the aqueous electrolyte solution and the silver-silver chloride (Ag/AgCl) wires were used as the reference electrodes whilst the platinum (Pt) flags acted as the working electrodes.

The 4-electrode system consists of two Pt flags that serve as working electrodes in each of the two immiscible electrolyte solutions and two reference electrodes (3M potassium chloride (KCl), E= 0.208 V vs. standard hydrogen electrode) which are made up of two high-

purity silver wires with a diameter of 0.25 mm and coated with silver chloride (via the potentiostatic oxidation process - more information on the method for preparing Ag/AgCl electrodes can be found under the reference electrode section 3.1.4). In this study, one of the Ag/AgCl electrodes was placed into a luggin capillary containing the organic reference solution which in turn is in contact with the organic solvent whilst the other one was inserted into another luggin capillary consisting of the aqueous electrolyte solution. The reference electrodes were positioned as close as possible to the tip of the luggin capillaries and nearer to the interface in order to reduce the potential drop[2]. The current flow was measured between the two Pt electrodes and this ensured that the reference electrodes remained unaffected by the current and a constant potential was achieved at all time. The potential applied between the two reference Ag/AgCl electrodes was controlled using a Potentiostat-Galvanostat Model PGSTAT12 Autolab (Metrohm Applikon B.V, Netherlands).

The area of the polarised interface was measured to be 3.64 cm^2 for the larger electrochemical cell and 2.2 cm^2 for the smaller cell used for the electrochemical measurements. All of the experiments were undertaken at room temperature of 22 $\pm$ 2^{o}C and inside a Faraday cage to reduce the interference from the external electromagnetic field/ background noise.

3.1.1 3-electrode set-up for the study of surfactant behaviour at the ITIES

In a 3-electrode set-up the potential difference (ΔE) between the working electrode and the reference electrode is controlled using the potentiostat. The current drawn through the reference electrode with well-defined potential at the same time via the potentiostat is negligible. This process can be represented by the equation stated (eq. 3.1) below[3].

$$\Delta E = (\phi_M - \phi_S)_{working} - (\phi_M - \phi_S)_{reference} \qquad \text{(eq. 3.1)}$$

Where, ϕ_M is the potential at the metal electrode and ϕ_S is the potential of the solution. In a 3-electrode system, the potential drop $(\phi_M - \phi_S)_{working}$ on the working electrode – solution interface leads a current to flow. This in turn causes the counter electrode to be driven via the potentiostat to the appropriate voltage required to pass the same current as induced through the working electrode, as a function of a controlled applied potential[4]. The set-up for 3-electrode system (figure 3.2) can be seen below.

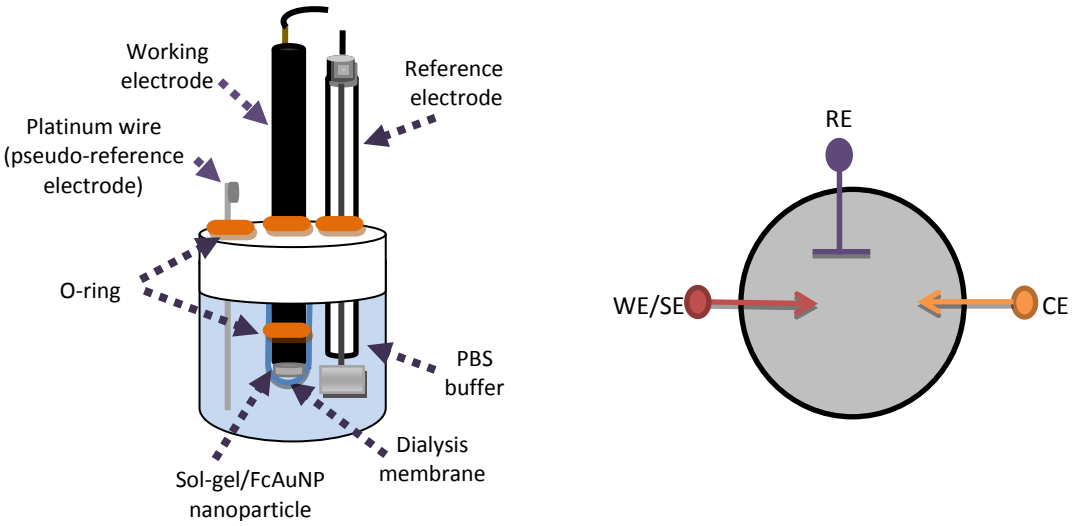

Figure 3.2: (a) set-up for 3-electrode electrochemical cell system and (b) schematic representation of the 3-electrode system. Where, the Ag/AgCl electrode was used as the reference electrode (RE), the platinum (Pt) flag acted as the counter electrode (CE) and the glassy carbon electrode served as the working electrode (WE). The electrochemical leads for the working electrode (WE) /the sensor electrode (SE) were coupled together.

3.1.2 2-electrode set-up for the study of surfactant behaviour at the ITIES

The 2-electrode system is composed of a reference electrode and a working electrode (figure 3.3). A potential is applied to the electrochemical cell and the current is then measured as a function of the potential.

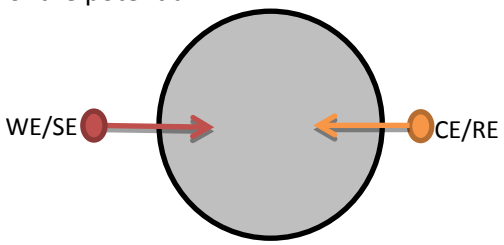

Figure 3.3: Schematic representation of the 2-electrode system. Where, the electrochemical connections for Ag/AgCl electrodes/platinum (Pt) flags were connected together and the Ag/AgCl electrodes acted as a reference electrode (CE/RE). The working (WE) /sensor (SE) electrode connections on the other hand were attached together and the glassy carbon electrode served as the working electrode (WE).

For this system, the current generated flows through the working electrode which in turn passes through the reference electrode[5]. The 2-electrode system usually involves use of a reference electrode which does not alter its electrode potential throughout the detection process[6].

3.1.3 The working electrode

The working electrode in an electrochemical system is where the reaction processes occur. The types of electrodes usually used are gold (Au), platinum (Pt) and carbon (C, in the form of graphite or glassy carbon). Depending on the available potential window a suitable electrode is chosen for each investigation undertaken. A solid electrode normally requires a careful pre-treatment where the electrode surface is cleaned and polished using alumina suspensions of various particle sizes before drying and using it. The use of Au, Pt or C electrodes are preferable for identifying analytes in the range of positive potentials and in aprotic solvents in both negative and positive ranges of potential. On the other hand, in the negative range of potential and in protic solvents, the use of mercury electrodes is desirable because of high overpotential of the reduction of hydrogen. Noble metal i.e. Iridium and silver based electrodes have been reported although less commonly used as working electrodes[7].

3.1.4 Reference electrodes

The SHE is the prime reference electrode and its potential is found to be zero at all temperatures. The saturated calomel electrode (SCE) and the Ag/AgCl electrodes are more commonly employed as the reference electrodes for practical measurements[8]. However, the Ag/AgCl electrode is most frequently manipulated because it is simple to use, can be easily constructed and requires only KCl electrolyte for preparation. The reference electrode can be defined as an electrode for which the Galvani potential difference between the metal electrode and the solution is consistent and to ensure that it remains stable at equilibrium only an insignificant amount of current can pass through the reference electrode. The redox process for the Ag/AgCl electrode is expressed by equation 3.2 and the potential of the reference electrode can be determined by the Nernst equation (equation 3.3) stated below [9,10].

$$AgCl_{(s)} + e^{-} \leftrightarrow Ag_{(s)} + Cl^{-} \quad \text{(eq. 3.2)}$$

$$E_{Ag|AgCl} = E^{o}{}_{Ag|AgCl} - \frac{RT}{F} \ln a_{Cl-} \quad \text{(eq. 3.3)}$$

Where, E^{o} is the standard potential, *R* is universal the gas constant, *T* in the absolute temperature, *F* is the Faraday constant and a is the chemical activity for the relevant species.

The Ag/AgCl reference electrodes were prepared by placing two pieces of silver wires in a solution of 3 M KCl and applying a potential of 2 V for 20 minutes using a potentiostat. The potentiostatic oxidation process in turn led to formation of an insoluble brown layer on the wires. The Ag/AgCl wires were then rinsed with deionised water before use or was fixed inside glass tubing consisting of 3M KCl and sealed with a porous frit for macro liquid-liquid interface investigations. The glass tube based Ag/AgCl reference electrodes were washed with deionised water and then immersed in the aqueous solution containing KCl to maintain the potential of the electrodes and to enhance the conductivity when not in use [11].

3.1.5 Counter electrode

The current flows between the working electrode and the counter electrode[12]. A Pt foil/wire or titanium wire is usually manipulated as the counter or auxiliary electrode and these electrodes are only used in a 3-electrode system. The area of the counter electrode is significantly larger than the working electrode and this is to ensure that the current measurement is not affected by passivation, deactivation or blocking[13].

3.1.6 Pseudo reference electrode

Pseudo reference electrodes are usually used as part of three electrode arrangements and are manipulated when using techniques such as polarography and in cyclic voltammetry. The electrodes consist of platinum[14] or silver wires submerged in the sample solution or even in the form of activated carbon dipped into the electrolyte. Pseudo electrodes have low impedance and are capable of exhibiting constant potential when the reference potential is not known. The electrodes functionality is dependent on the sample solution

composition[15]. These types of electrodes are calibrated using a reference redox system such as ferrocene or cobaltocane by introducing it as an internal reference into the electrolyte during an experiment or by measuring the potential after the experiment using the reference redox system or a conventional reference electrode[16].

3.2 Electrochemical cell used for the characterisation of surfactants

The electrochemical cells referred to as scheme 1 (for the background) and scheme 2 (for the addition of surfactants) below were used for the electrochemical, conductivity and electrocapillary curve measurements. The schemes show that 1,2-dichloroethane (DCE) was used as the organic solvent whilst lithium chloride (LiCl) and tetrabutylammonium tetraphenylborate (TBATPB) were used as the supporting electrolytes in the aqueous and organic phases, respectively. Both, tetrabutylammonium chloride (TBACl) and magnesium chloride ($MgCl_2$) were used to prepare the organic reference solution which was in contact with the organic phase. In this study, the reference solution consisted of a common ion which is the TBA^+ cation that can be also found in the organic phase. Once the concentration of the TBA^+ ion reaches equilibrium between the two phases, it generates an interfacial potential. Thus, the overall potential applied by the potentiostat represents the sum of interfacial potential, the potential of the two reference electrodes and the potential of the reference interface.

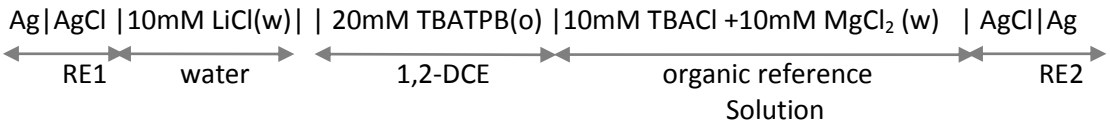

Scheme 3.1 Electrochemical cell used to obtain background data for the ion transfer analysis.

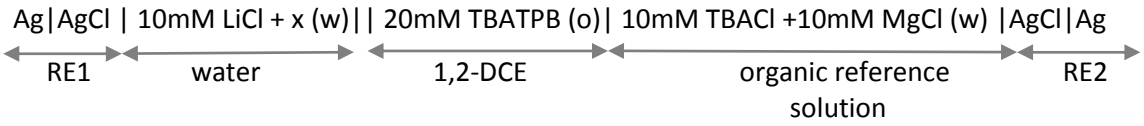

Scheme 3.2 Electrochemical cell used for ion transfer analysis.

Where, x is the analyte/surfactants added to the aqueous phase. For conductivity and electrocapilary curve measurements, the 1, 2-DCE phase was replaced with glycerol trioleate as the organic phase.

3.3 Sol-gel modified carbon electrode used as the biosensor for determination of the enzymatic activity

The glucose oxidase (GOx) and glycerol dehydrogenase (GDH) enzymes along with the ferrocenated gold nanoparticles (FcAuNPs) were immobilised to the surface of glassy carbon electrodes for the analysis of enzyme activity using the sol-gel method.

Sol and gels have naturally existed in various types of materials such as ink, clay, blood, serum and milk[17]. Sols are stable dispersion of colloidal particles in a solution which were first discovered with gold by Faraday, in 1853. The insight into colloidal science was first initiated by Graham in 1861 and since then the concept of ceramic colloidal sols has been explored to understand the nature and behaviours of the particle dispersions [18]. Gels on the other hand are cross-linked polymeric chains with length greater than micrometer and submicrometer pores. The gel-like substances was first synthesised by Ebelmen in the form of silica gels in 1846 where hydrolysis of tetraethyl orthosilicate under acidic conditions led to formation of glass-like material known as silicon dioxide[19]. Further to this, it was Roy and co-workers who discovered that extensive chemical homogeneity can be accomplished in colloidal gels. This idea of sol-gel method was then applied in the 1950s-1960s to produce a range of ceramic oxide components involving aluminium, silicon and titanium which could not be made via the conventional ceramic powder technique. Glass and polycrystalline ceramic fibers to coatings and films for improving insulation characteristics are just a few examples of the products which have been developed via this sol-gel technique[20]. Sol-gel can be prepared via three different ways which include gelation of colloidal particles in solution, hydrolysis and polycondensation of alkoxide or nitrate based precursors followed by drying under over critical temperature/aging and drying at room temperature (figure 3.4)[21] .

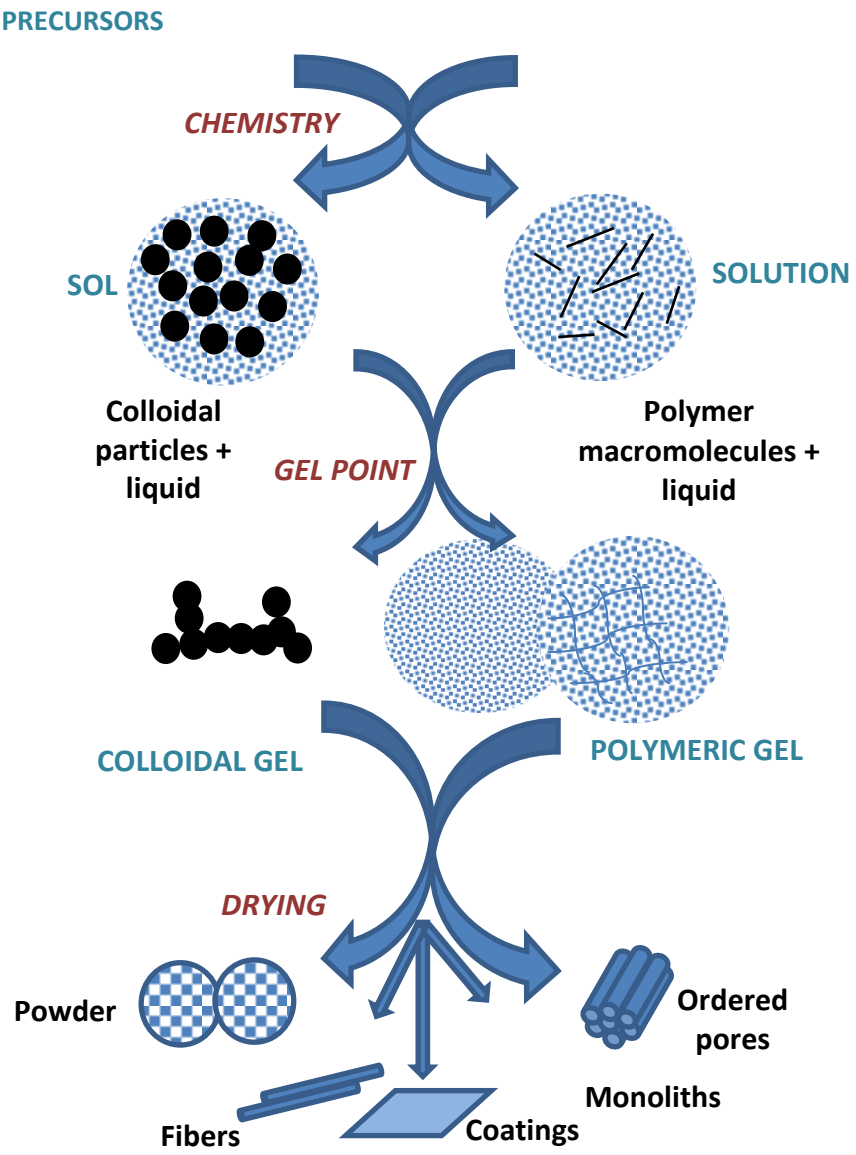

Figure 3.4: Simplified schematic presentation of sol-gel processes [21].

The sol-gel for the biosensor work was initially prepared by mixing tetramethyl orthosilicate (1.5 Ml, TMOS), 1-butyl-3-methylimidozolium octyl sulphate (2.0 mL), 6M hydrochloric acid (0.02 mL, HCl) and deionised water (4.5 mL) using a vortex mixer for 2 minutes. The mixture was then sonicated further for 15 minutes to allow hydrolysis of the TMOS precursor before heating it up to 70 ^{o}C for 30 minutes to ensure all the alcohol was removed. Following this, the solution was cooled and neutralised to pH7 using HCl (0.1 M). A 0.5 mL of sol-gel solution was then mixed with the and 10% GOx/a mixture of DP and GDH (0.15 mL, prepared in 0.1 M phosphate buffer solution (PBS)) and, left for several hours to gel. The GC electrode was thoroughly cleaned using the alumina powder solution for approximately two

minutes before ringing it with deionised water and drying it with a lens tissue. The sol-gel mix (0.4 µL) was then mixed with FcAuNPs (0.3 µL) and drop-casted on to the surface of the working electrode. The sol-gel immobilised bioelectrode was left to gel on the electrode surface overnight before a thin layer of dialysis membrane was used to cover and hold the sol-gel mixture firmly in a fixed position, making it suitable for analysis in the PBS solution.

A background for just the sol-gel and FcAuNP based biosensor without enzyme(s) in pH7 PBS (used for GOx) and pH8 PBS (used for GDH and liapse) was obtained using the 3-electrode configuration. Where, the GC electrode (with a surface area of 0.07 cm^2) was used as the working electrode, a platinum wire was utilised as the pseudo reference electrode and a platinum flag acted as the counter electrode. Electrochemical measurements were performed at room temperature using a computer controlled Autolab Potentiostat (Metrohm Autolab B.V. Netherlands) with *iR* compensation which acted as the power supply (figure 3.5).

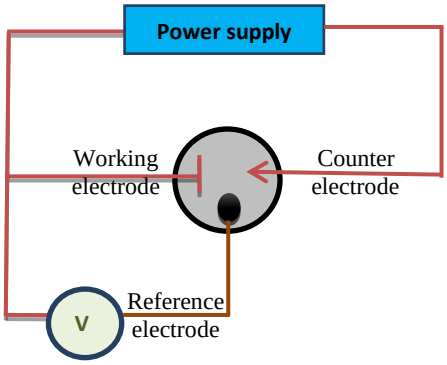

Figure 3.5: Schematic representation of a three electrode electrochemical cell set up used for sol-gel based bioelectrode analysis.

The immobilised sol-gel/FcAuNP/ enzymatic biosensors were examined using the cyclic voltammetry (CV, with a potential window of -1 V to 1 V) and chronoamperometry (CA, constant potentials of 0.01V (for GOx), -0.3 V (for GDH) and 0.04 V (for lipase) was applied) techniques. All the sol-gel based biosensors with/without enzymes when not in use were kept in pH7/ pH8 PBS (depending on the type of enzyme (s) used at one time) at 4 ^{o}C in the fridge. After checking the activation of the modified glassy carbon electrode using the standard GOx enzyme, the activity of GDH was investigated with and without the lipase enzyme in solution by following the same procedure. The whole process for inspecting enzymatic activities was repeated using the sol-gel based screen printed electrodes. A series

of Lineweaver-Burk graphs were then plotted for both the sol-gel/FcAuNP/enzymatic macro- and SPE-based biosensors. From the graphs, the k_m value for each of the enzymes was determined and compared to the literature in order to establish whether the macro- or SPE based biosensor was most sensitive in demonstrating enzyme effectiveness.

3.4 Preparation of FcAuNPs

The FcAuNPs were prepared by mixing equal volumes of gold nanoparticles (AuNP) which was purchased from Sigma Aldrich as citrate-stabilised colloids in water and 5 mM of 6-(ferrocenyl)-hexanethiol (FHT) as received from Sigma in hexane, using a vortex stirrer overnight. The resultant red aqueous layer consisting of the modified gold nanoparticles was then rinsed with hexane 3 times to remove any impurities that might be present. The top solvent layer was then disposed of using a pipette. After the final rinse, the aqueous phase composed of the FcAuNPs were extracted by evaporating the small amount of hexane solvent layer left over using a rotary evaporator. Following this, the FcAuNPs were characterised using the ultraviolet spectroscopy which revealed a small shift in wavelength from 519 (for unmodified AuNPs) to 520 nm (for modified AuNPs) and also, by using the transmission electron microscopy (TEM) the exact average core diameter of the FcAuNPs stabilised in the citrate buffer (figure 3.6) were determined to be 5.74 nM (more information on TEM can be found in this chapter in section 3.17 below).

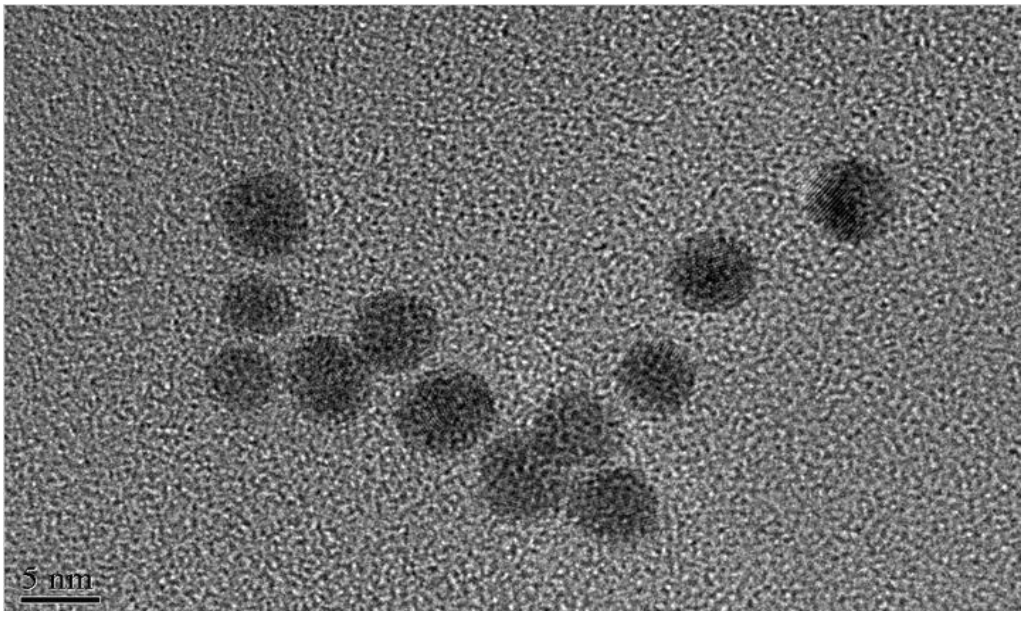

Figure 3.6: TEM image of the FcAuNPs.

3.5 Screen printed electrodes

Screen printed electrodes (SPEs) are electrochemical substrates which have various applications ranging from detecting pollutants[22], textiles[23], advertising to acting as enzymatic biosensors for biomedical applications[24]. These electrodes have been produced and used worldwide since over a thousand years ago and within the last few decades, new developed format and printing material properties such as enhanced response, ease of handling and disposing of after use has made the SPEs ideal i.e. for analysis of environmental pollutants[25]. SPEs are also the most desired electrochemical sensors for in situ analysis due to other advantageous properties like high sensitivity, linear output and low power requirement [25]. The real breakthrough for the use of SPEs was accomplished in 1987 when MediSense introduced these electrodes as glucose biosensors for medical applications. Such electrodes can be easily modified using substrates such as metals, inorganic nanomaterials, enzymes or DNA sequences to serve multiple purposes[26]. Below is a schematic diagram of a SPE (figure 3.7).

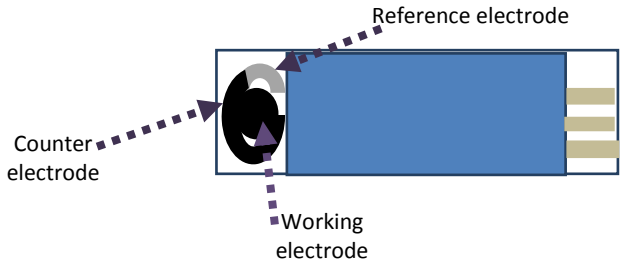

Figure 3.7: Schematic diagram of a SPE.

The preparation of SPEs involves use of a woven mesh to support an ink-blocking stencil [27]. A roller is then moved across the stencil to force the ink/printable substrates such as silver or carbon ink pastes mixed with mineral binders or insulating polymers, which are used to increase the adhesion of the inks onto the electrodes, through the woven mesh into open spaces on the electrochemical substrates [28]. A series of woven meshes have been developed and used to print different sections of the electrode in the similar manner as stated above.

The disadvantage associated with using polymers is that it enhances the electron transfer resistance and slows down the kinetics of processes such as heterogeneous, irreversible and

quasi-reversible redox reactions occurring at the surfaces of SPEs. In order to overcome this barrier and to increase the electrocatalytic performance, noble metals were added to the ink/polymer paste. The only impediment is that the noble metals are highly expensive[29]. However, in recent years inexpensive materials such as manganese oxide and Bismuth oxide/nanoparticles have been used and proven to be an effective replacement for metals. Pretreatment of SPEs by removing contaminants such as organic ink components has also been found to be a useful method for intensifying the electrochemical characteristics of SPEs and enhancing the electrodes surface roughness and functionalities [30].

The ink, once it passes the meshes, is then dried and solidified via a thermal process between two ink layers on the electrochemical substrate. An ink coating is then used to protect the silver ink printed conductive tracks from the remaining parts of the electrode. The working electrodes on the other hand are mainly composed of carbon or gold ink. However, carbon ink paste is generally the most preferable printable material compared to gold as it is relatively cheap, chemically inert and can be easily modified for use in different systems [31]. SPEs in different forms such as a disc, ring or band can be easily generated in small batches using screen printed machines or mass produced as arrays. These electrodes can be used to easily achieve reproducibility, stability, rapidity and high standard chemical performance[32]. SPE arrays can be also manipulated to calibrate and analyse a range of unknown samples simultaneously. These types of electrodes behave as microelectrodes for example, by enhancing the signal to noise ratios, allowing a low ohmic drop to be achieved and increasing the mass transport rate[33]. Other benefits associated with this technique are it is portable and therefore can be transported and used in the laboratory or hospitals. It is also an inexpensive method compared to other analytical methods available for the applications stated above.

3.6 Chemicals

All of the chemicals used were of analytical grade and used without further purification and as purchased from Sigma Aldrich Corporation, Dorset or provided by P&G, Newcastle. The material safety data sheet (MSDS) for each of the compounds was read before use and appropriate steps were followed accordingly. All of the aqueous based solutions were prepared using deionised water (with resistivity of $\geq$ 18 MΩ cm) from Sartorius Arium 611 ultrapure water system/Millie-Q system (Watford, UK).

3.6.1 Aqueous and organic supporting electrolytes

The electrolyte that has been used for the aqueous phase was lithium chloride (10 mM, 99% LiCl, Sigma-Aldrich, UK) and for the organic phase the electrolyte manipulated was tetrabutylammonium tetraphenylborate (20 mM, 99% TBATPB, Fluka, UK). The organic reference solution was composed of tetrabutylammonium chloride (5 mM, 97% TBACl, Sigma-Aldrich, UK) and magnesium chloride (10 mM, 99% $MgCl_2$, Sigma-Aldrich, UK) (scheme 3). For the enzymatic biosensor work, 1-butyl-3-methylimidozolium octyl sulphate (95%, Sigma-Aldrich, UK) was incorporated in the sol-gel and used as the electrolyte. The function of the electrolytes used is to enhance the conductivity of the solution, prevent the transport of electroactive species by ion migration, establish a potential window by setting limits for the polarisable range and to maintain constant ionic strength and pH. The increase in the potential window is dependent on the increase in hydrophobicity of the organic electrolyte.

3.6.2 Other chemicals and solvents used

Sodium dodecylbenzene sulphonate (SDBS, Sigma-Aldrich, UK), triton-X-114 (Sigma-Aldrich, UK), 1,2-DCE (99%, Sigma-Aldrich, UK), GOx enzyme (Sigma-Aldrich, UK), GDH enzyme (Sigma-Aldrich, UK), diaphorase (DP, Sigma-Aldrich, UK), lipase (Sigma-Aldrich, UK), 6-(ferrocenyl)-hexanethiol (6-FHT, Sigma-Aldrich, UK), 5 nanometer unmodified gold nanoparticles in citrate stabilised colloid form (AuNP, Sigma-Aldrich, UK), glycerol trioleate (GTO, P&G, UK), surfactants Y (anionic) and N (non-ionic) (P&G, UK), lard (ASDA and Tesco, UK), tetramethyl orthosilicate (TMOS) (1.5 mL, Sigma- Aldrich, UK), HCl (6 M, Sigma-Aldrich, UK), potassium phosphate monobasic (99% Sigma-Aldrich, UK), potassium phosphate dibasic (99%, Sigma-Aldrich, UK), nicotinamide adenine dinucleotide (NAD, 99%, Sigma-Aldrich, UK), glucose oxidase (GOx, Sigma-Aldrich, UK), glycerol dehydrogenase (GDH, Sigma-Aldrich, UK), monobasic potassium phosphate (Sigma, UK) and dibasic potassium phosphate (Sigma, UK). For my surfactant study of the ITIES, the solvent chosen was 1,2-DCE. This is because 1,2-DCE is:

- Immiscible with water.
- A polar solvent which allows disassociation of the supporting electrolytes and hence, enhances conductivity.

- A solvent with different density to water which in turn allows a stable liquid-liquid phase boundary to be achieved for interfacial study.

Although 1,2-DCE is an ideal solvent and capable of producing the suitable potential window range required for investigating the surfactant ion transfer, adsorption and emulsification process, there are also some disadvantages such as it is toxic and carcinogenic. However, necessary precautions have been undertaken when handling 1,2-DCE in order to minimise exposure and prevent inhalation or skin contact. The glycerol trioleate (GTO) has been chosen as the alternative organic phase to 1,2-DCE because it is one of the main triglycerides found in the vegetable and olive oil which are often used for cooking. As an electrolyte sufficiently soluble in GTO was not found, electrochemical studies were not conducted using the aqueous-GTO system. However, conductivity and surface tension measurements were undertaken and compared for both the aqueous (with LiCl) -1,2-DCE (with TBATPB) and aqueous (with LiCl)-GTO systems.

3.7 Electrochemical techniques established using potentiostat

All electrochemical data were obtained using a computer-controlled potentiostat. For the cyclic voltammetry, the initial potential range used was from 0 to 600 mV. A positive current was generated due to anionic ions transferring across the interface from the aqueous to the organic phase as the potential was scanned forward and lower concentrations of each of the anionic surfactants was added to the aqueous phase of the water/1,2-DCE system. Vice versa, as the potential was reversed the cationic head groups of the surfactants were transported from the organic to the aqueous phase. This was represented in the form of a negative current.

Electrochemical techniques function on the basis of that either a constant current between two electrodes needs to be applied and the potential as a function of time is measured or alternatively, a potential is applied and the current response as a function of time is determined. Coulometry is an example of a technique which requires the current to flow to the electrodes at a fixed pace and it is controlled by a galvanostat device. For other methods such as chronopotentiometry, cyclic voltammetry and differential pulse voltammerty the current is measured as a function of electrode potential, using a potentiostat[11].

3.7.1 Cyclic Voltammetry

Cyclic voltammetry (CV) is one of the most widely used voltammetric techniques for quantitative analysis. It has various applications for example, it can be used to determine the reversible and non-reversible characteristics of a redox species and also, to identify the mechanisms of adsorption and transfer of ion or electron processes. Kinetic and thermodynamic data such as the formal potential, the rate constant values, the diffusion coefficients and the number of electrons transferred in a redox reaction can be determined using this method[34]. CV is an example of a potential-sweep technique, where the applied electrode potential is varied as a function of time and the resultant current is measured[35]. This technique involves application of an increasing voltage (forward scan) followed by a decreasing linear voltage (reverse scan) to a working electrode via a potentiostat, over a period of time. During this, the reaction of interest takes place which is dependent on the electroactive species in solution. The response can be identified on the voltammogram by the change in current within the potential window, as voltage is applied. A second potential sweep is usually carried out for detailed study of the electrochemical reactivity of the charged species. The variation in the potential applied can be represented as a triangular potential waveform (figure 3.8) [3,36].

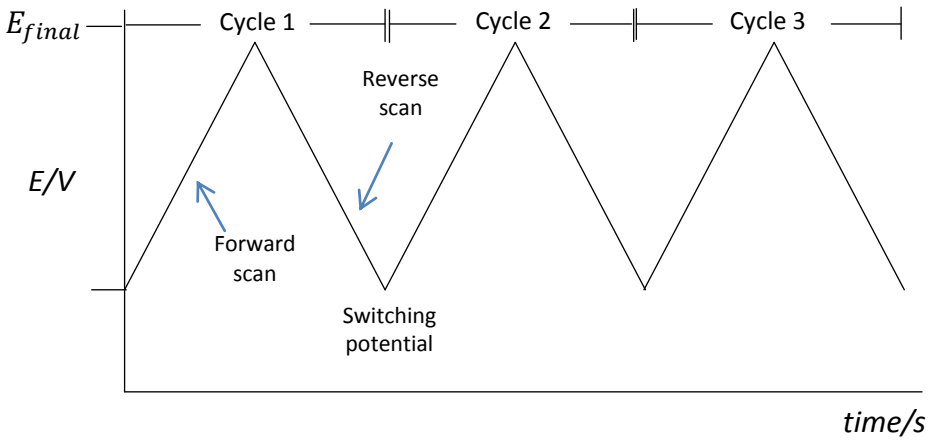

Figure 3.8: Triangular potential waveform measured as a function of time[3].

The current flow at the working electrode is measured using CV and plotted as a current-potential voltammogram. There are two types of voltamograms that can be obtained as a result of charge transfer which are reversible and irreversible[37]. The characterisation of

surfactants using cyclic voltammetry has shown a reversible reaction. For a reversible process, when a potential applied reaches the formal transfer potential of the ionic species it leads to an increase in ion transfer and a maximum rate of mass transfer of species is also attained across the electrode-electrolyte or liquid-liquid interface. This is turn causes the current to enhance as observed using the CV (figure 3.9).

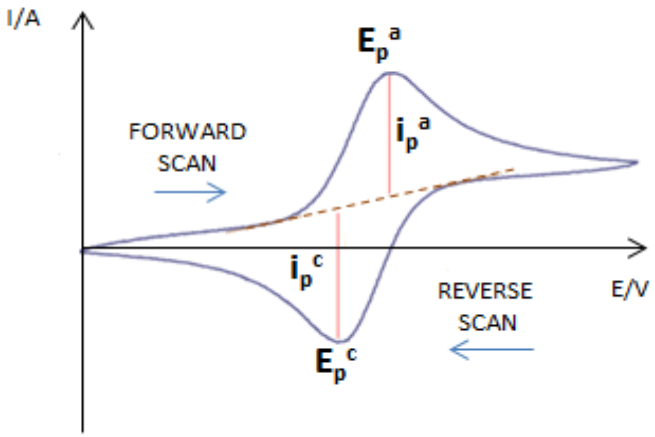

Figure 3.9: Cyclic voltammogram for a reversible reaction showing the transfer of charged ion/redox species across a liquid-liquid macro interface. Where, E_{pa} is the anodic peak potential, E_{pc} is the cathodic peak potential, i_{pa} is the anodic peak current and i_{pc} is the cathodic peak current.

However, as the potential was continuously increased above the formal potential, the concentration of the ionic species decreased due to the depletion effect. This was evident by the reduction in current. As the scan was reversed, the direction of the ion transfer was also observed to change. A rise in the negative current was identified in the reverse scan as the potential applied approached the formal potential. The peak current ratio (i_p^a/i_p^c) as well as the formal potential (E^o) and the voltage separation between the current peaks (ΔE) can be determined from the voltammogram obtained for a reversible process and expressed by the equations below (equations 3.4 and 3.5)[38].

$$E^O = \frac{E_p^a + E_p^c}{2} \qquad \text{(eq. 3.4)}$$

$$\Delta E = E_p^a - E_p^c = \frac{57}{n}\, mV \qquad \text{(eq. 3.5)}$$

The change in the peak current for the ion transfer reactions with change in scan rate (figure 3.10) can be expressed using the Randles-Sevcik equation (equation 3.6).

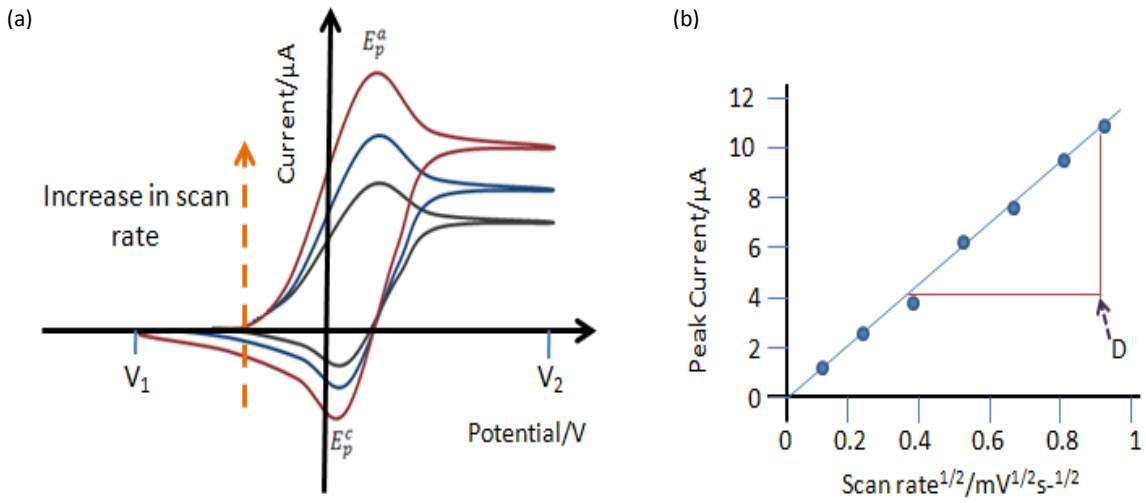

Figure 3.10: (a) Change in scan rate as a function of applied potential and, (b) peak current versus scan rate$^{1/2}$. Where, D is the diffusion coefficient value of the electroactive species (cm^2/sec).

According to Randles -Sevcik equation, it can be stated that i_p is linearly proportional to $v^{1/2}$and the concentration of the active species (equation 3.6)[39].

$$i_p = 269\, n^{3/2} A D^{1/2} v^{1/2} c^b \qquad \text{(eq. 3.6)}$$

Where, *ip* is the peak height (amp), *n* is the number of electrons, *A* is the electrode active surface area (cm^2), v is the scan rate (V/sec) and c^b is the bulk concentration of solution. By applying the above equation to the plot of i_p versus $v^{1/2}$ (figure 3.10b) and ensuring all the other parameters are kept constant, kinetic data such as the diffusion coefficient *(D)* of the transferring ion/electroactive species can be determined[40]. Prior to investigating the surfactant mechanisms, tetraethylammonium chloride was used as an internal reference to determine the standard ion transfer potential and reversible half-wave potential from the cyclic voltammograms.

3.7.2 Chronoamperometry

Chronoamperometry (CA) is one of the most widely used step techniques for studying various electrode mechanisms. During the initial potential step no faradaic current occurs however, as the potential is stepped to a potential at which the reaction of interest takes place a change in current can be observed[41]. This technique involves stepping the potential of the working electrode and measuring the faradaic current, as a function of time. CA also produces high capacitive current however it decays exponentially and faster than the current of interest. Therefore, the faradaic current can be evaluated after the charging current has dropped to zero (figure 3.11)[42].

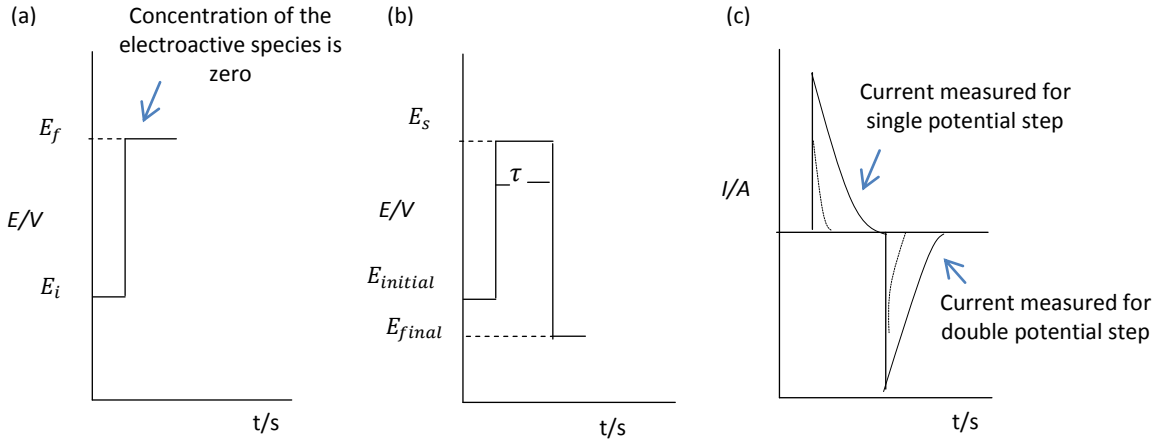

Figure 3.11: (a) Single-potential (b) Double-potential step & (c) current versus time plot obtained using Chronoamperometry technique [42].

Where, *Ei* is the initial potential, *Es* is the step potential, E_f is the final potential and *t* is the period of time before final potential is applied. The dashed line in figure 3.11c shows an excitation signal produced only in the presence of background electrolytes and the solid line represents current due to electrolysis of the charged species. It can be evaluated from figure 3.11c that the current decreases over time as the concentration of the analyte reduces at the electrode surface. The current eventually reaches zero as a steady state for the concentration of electroactive species is established. The current can be defined as the rate of charge flow (*Q*) across the interface at time, *t*, and it can be expressed in the form of equation 3.7 [42].

$$i_t = \left(\frac{dQ}{dt}\right)_t = nF\ \left(\frac{dN}{dt}\right)_t \qquad \text{(eq. 3.7)}$$

Where, *n* is the number of electrons (eq/mol), *F* is the Faraday's constant (96,500 C mol^{-1}) (C/eq) and *N* is the number of moles of the species. The rate of conversion of the electroactive species (*dN/dt*) is directly related to the area of the electrode and the flow of material to the electrode. Since, the analyte transports across to the electrode by diffusion the rate of conversion can be defined by the modified Fick's first law, equation 3.8 [43].

$$i_t = nF\ AD_o\ \left(\frac{\partial C_o}{\partial X}\right)_{X=0,t} \qquad \text{(eq. 3.8)}$$

Where, *i* is the current (A) at time, *t*, *A* is the electrode area (cm^2), *c* is the concentration (mol cm^{-3}) and *D* is the diffusion coefficient of the electroactive species, *t* is the time (s) and, *x* (cm) is the distance from the electrode. By applying the Cottrell equation (equation 3.9), kinetic data such as number of electrons transferred and diffusion coefficient values as well as reaction mechanisms can be determined from the current, *i,* as a function of inverse $t^{½}$ [44].

$$i = nFACD^{1/2}\pi^{-1/2}t^{-1/2} \qquad \text{(eq. 3.9)}$$

3.7.3 Differential Pulse Voltammetry

There are various types of step and pulse techniques which can be used to determine the concentration of the active species. These methods involve application of a potential pulse in the form of linear or pulse waveforms or a combination of both. The pulse voltammetric techniques involve measurement of the current after a potential pulse is applied. Such techniques lower the detection limits of the voltammetric measurements by significantly enhancing the ratio between the faradaic and the non-faradaic currents[45]. Examples of pulse techniques are normal pulse voltammetry (NPV), square wave voltammetry (SWV), stripping voltammetry (SV) and differential pulse voltammetry (DPV) [46]. DPV is one of the numerous potential step voltammetric techniques that have been developed to improve sensitivity of the Faradaic current response relative to the capacitive current. Due to its high sensitivity and resolving power it is widely used for quantitative analysis such as for the determination of the standard ion transfer potential of the

system [47]. This specific technique involves applying a series of small voltage pulses with constant amplitude to the electrochemical system and superimposing it on the staircase wave form (figure 3.12a). The current is measured before the application of a pulse (τ_1) and again at the end of the pulse (τ_2). The difference between the individual currents, ΔI, measured at these two points (τ_1 and τ_2) is then plotted against the function of applied voltage. This results in the formation a peak-shaped signal (figure 3.12b) [48].

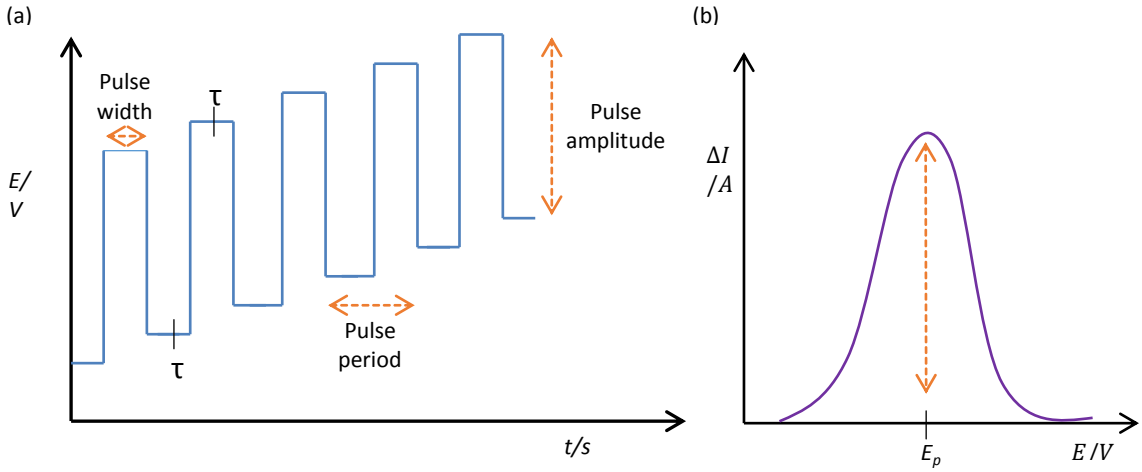

Figure 3.12: (a) Waveform of pulses applied superimposed on a staircase for a typical DPV experiment and (b) Peak shaped profile of difference in current against the potential applied from a DPV scan.

The pulse is measured twice to ensure that the capacitive current due to double layer charging (I_c) decays and does not interfere with the faradaic current (I_f). Since I_f follows diffusion controlled conditions, in terms of the Cottrell equation it can be expressed in the form of $I_f \propto t^{1/2}$ (figure 3.13) and the charge $Q \propto t^{1/2}$ [3].

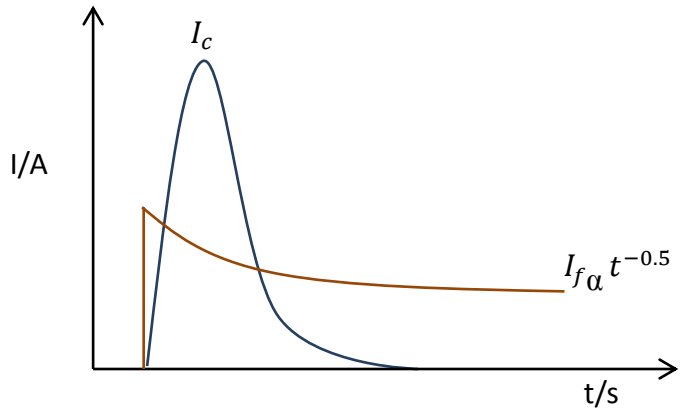

Figure 3.13: Exponential decrease of capacitive current and decay of Faradaic current as a function of $1/\ time^{1/2}$ after application of a potential step.

The peak current, i_p, for a reversible faradaic reaction can be determined according to equation 3.10 [49].

$$i_p = nFAc\ (\frac{D}{\pi t_p})^{\frac{1}{2}}\ \frac{1-\sigma}{1+\sigma} \qquad \text{(eq. 3.10)}$$

$$\text{Where,}\quad \sigma = exp\ (\frac{nF\Delta_p E}{2RT}) \qquad \text{(eq. 3.11)}$$

Where, *n* is the number of electrons, *F* is the Faraday's constant, *A* is the area of the electrode (cm^{-1}), *c* is the concentration of the analyte (mol cm^{-3}), *D* is the diffusion coefficient value (cm s^{-1}), t_p is the pulse width, $\Delta_p E$ is the pulse amplitude, *R* is the gas constant (J mol^{-1} K^{-1}) and *T* is the temperature (K). The DPV peaks are usually symmetrical for a reversible process and asymmetrical for irreversible reactions [49].

3.8 Conductivity measurements of the liquid-liquid interface

Conductivity is a physical quantity which can be measured with good reproducibility and high sensitivity. It is an inexpensive technique frequently used for determining the critical micellar concentration (CMC) of an ionic surfactant however the slope of the differential conductivity below and above the CMC point can be used to evaluate the degree of counter-ion dissociation of micelles and their aggregation number [50]. In this study, a series of conductivity experiments on the water and organic phase with and without electrolytes were undertaken at room temperature using a 4310 conductivity meter (Jenway, UK) (figure 3.14).

Figure 3.14: Image of 4310 conductivity meter.

The conductivity probe was placed in the aqueous phase and was brought as close as possible to the aqueous (with/without 10 mM LiCl)– 1,2-DCE (with/without 20 mM TBATPB)/GTO interface using an optical microscope before measurements were taken, as different volumes of the 33 mM stock solution of SDBS surfactant were added to the aqueous phase in order to achieve overall concentrations of 1.5 mM, 8 mM and 13.4 mM. The differential conductivity (μS)/ differential concentration (mM) against concentration (mM) of surfactant with and without electrolytes were plotted to determine the points at which the critical micellar concentration is attained and the surfactant adsorption/emulsification processes occur. The graph was also manipulated to identify if the electrolytes had an effect on the CMC or the adsorption/emulsification processes of the SDBS surfactant.

3.9 Fourier Transform infrared Spectroscopy

Fourier Transform infrared Spectroscopy (FTIR) is one of the simplest, most rapid and highly sensitive analytical methods and is also non-destructive. It uses vibrational characteristics at resonance frequencies to fingerprint different types of functional groups. The chemical bonds of a specific structure vibrate at a characteristic frequency corresponding to the discrete energy levels. When the sample is irradiated with light, resonant frequencies are

absorbed which in turn increases the amplitude of vibration. This gives information about the chemical components of the sample examined in the form of infrared transmission or an absorption spectrum. It is dependent on factors such as molecular shape, potential energy, bond angle and length of the molecules. Other advantages associated with such a technique include use of only a small quantity (< 1 mg) of the sample for analysis [51,52].

The FTIR data for the crystal samples were obtained using a single-bounce Thunderdome (Spectra- Tech) ATR accessory, which was situated in the sample chamber of a Nicolet Nexus spectrometer attached to a liquid nitrogen cooled HgCdTe detector. A golden-gate diamond internal reflection accesory with a fixed incident angle of 45^{o} and a contact area of around 1 mm was used for sample analysis (figure 3.15).

Figure 3.15: Image of Nicolet Nexus ATR-FTIR spectrometer.

All the spectra (for the background and the crystal samples) were scanned 128 times at 4 cm^{-1} spectral resolution. Each spectrum was run between 4000 to 650 cm^{-1}. The spectra for all of the crystal samples were then ratioed against the background spectrum which was aquired prior to sample analysis. The spectra obtained can be plotted in absorbance (A) or percent transmission (% T) against wavenumbers measured in cm^{-1}.

3.10 Optical microscopy

An inverted microscope is composed of a light source and condenser positioned above the stage and pointing down whilst four to six objective lens of different magnifications fitted to a revolving nosepiece are situated below the stage pointing upwards. The stage of the

inverted microscope is usually fixed in one position and the focus is adjusted by moving the objective lens across the vertical axis. The focus mechanism consists of a dual concentric knob for coarse and fine adjustment (figure 3.16).

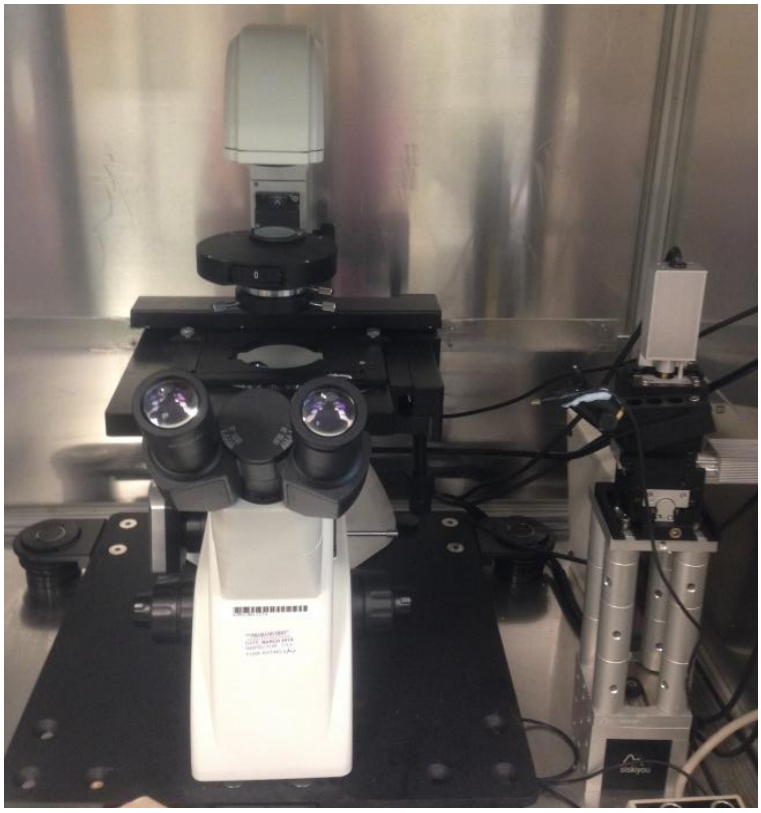

Figure 3.16: image of Olympus CKX31 inverted optical microscope.

This type of microscope is advantageous for observing living cells or organisms and also, it is used for micromanipulation applications[53]. The optical microscopic images of the interface between the aqueous phase with and without electrolytes containing SDBS and the organic phase containing 1,2-DCE with and without electrolytes / pure GTO were obtained using an Olympus CKX31 inverted optical microscope (GT Vision, UK) with a GXCAM-5 camera attached to it and a 4x objective lens was also manipulated. All the images captured were then analysed using the GX Capture software. For each concentration of SDBS, a volume of 200 µL of the surfactant solution and 200 µL of the 1,2-DCE/GTO were deposited on a glass slide before examining the aqueous-1,2-DCE/GTO interfaces using the optical microscope.

Furthermore, emulsion droplets were produced by adding 0.1 µL of the 1,2-DCE with and without electrolytes /GTO to 2 mL of deionised water containing 1.5 mM – 13.4 mM of the

SDBS surfactant. The images of the droplets were then obtained using the Olympus CKX31 inverted optical microscope in a similar manner as mentioned above for the examination of the interfaces. For each surfactant concentration, the images were analysed using Image J software to determine the average size of the emulsion droplets.

3.11 Differential Scanning Calorimeter

The thermal transitions of the crystal samples were determined using the Differential Scanning Caorimeter (DSC, Perkin Elmer Pyris1 DSC Q1000, TA instruments) (figure 3.17). DSC is a thermoanalytical technique which measures the difference in heat flow between the sample and a reference used whilst the material is heated or cooled. There are two types of DSC instruments and these are the heat flux and the power compensation DSCs. The DSCs can transform the temperature difference into a measurement of energy per unit mass related to the phase change which initially led to the difference in temperature. Therefore, any change in the material which causes the heat capacity of the material to alter is detected using the DSC [54].

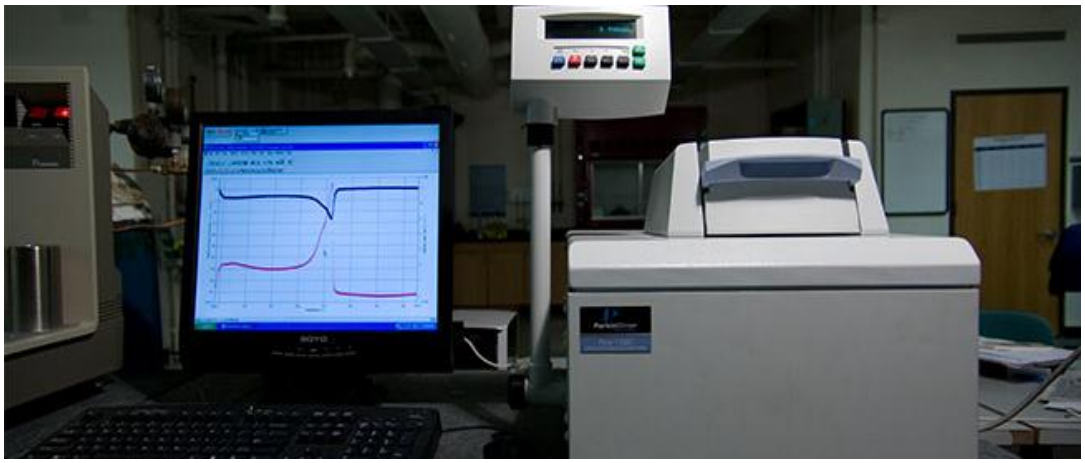

Figure 3.17: image of the Perkin Elmer Pyris1 DSC Q1000.

The DSC used was initially calibrated with indium (the standard calibration reference material) before analysing the crystalline samples [55]. In each case, the crystal samples were weighed into a 40 µL aluminium pan and then heated up from room temperature (RT) to 250 °C followed by cooling from 250 °C to RT, at a rate of 5°C/min. A 500 amu mass spectrometer (MS, Hiden Analytical Limited, UK) was also employed to identify the components of the interfacial crystals while heating up the samples from RT to 250 °C and

then cooling them down from 250 °C to RT. In MS, the crystallite samples in vaporised form were initially ionised in the ionisation chamber under vacuum. The resultant positive ions were then accelerated into a finely focused beam. Following this, depending on the mass-to-charge ratio (*m/z*) of the ions, the charged particles were separated and deflected on to the detector by adjusting the magnetic field from the mass analyser. Finally, the streams of ions pass from the analyser to the detector and are detected as an electric current from which the relative abundance of each ion type with their respective *m/z* is recorded[56].

3.12 Electrocapillary curve and interfacial tension measurements

For electrocapillary curves and the interfacial tension measurements, a Wilhelmy plate ST9000 surface tensiometer (NIMA, UK) at 22 $\pm$ 0.5 ^{o}C was calibrated and used (figure 3.18).

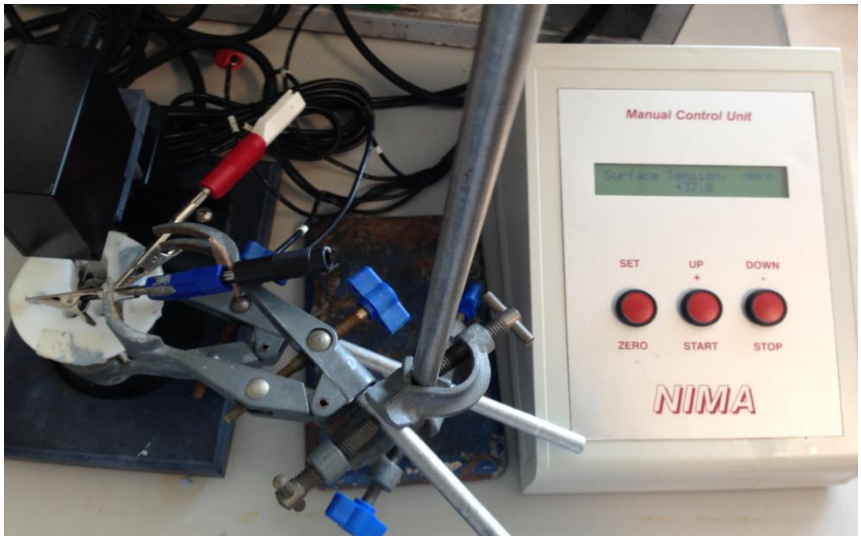

Figure 3.18: image of a Wilhelmy plate ST9000 surface tensiometer.

The 2-electrode electrochemical cell arrangement was applied to investigate the effect of voltage and concentration on the chaotic behaviour at the liquid-liquid interfaces. The interfacial tension measurements were performed simultaneously with voltage changes on a polarised flat surface. The potential was increased from 0 V – 0.8 V at an interval of 0.2 V. For each SDBS concentration, in both, the aqueous (with LiCl)- 1,2-DCE (with TBATPB) and aqueous (with LiCl)- GTO systems, the potential was kept constant for 100 seconds before measuring the surface tension at equilibrium. All measurements were performed at ambient temperature.

A series of electrocapillary curves showing the difference in the interfacial tension, $\Delta\gamma$, against the potential change expressed in the form of $\left(\frac{F}{RT}\right)(\phi - \phi_{pzc})$ were plotted for both the aqueous with and without electrolytes - 1,2-DCE with and without electrolytes /GTO systems, as the SDBS concentration was varied between 0 mM – 13.4 mM.

3.13 Laser diffraction particle sizing analyser

The laser diffraction technique is used to measure particle size distribution for a wide range of materials with submicron to millimetre size range. The advantages of using this method are attainment of rapid measurements, reliability, repeatability and a high sample throughput with great precision [57]. The technique is composed of a beam of polarised light with known fixed wavelength of 0.63 μm which, when it impinges on the particles dispersed in the carrier solution or gas, causes the light to scatter. The angle and the intensity of the diffracted light are measured using an array of photosensitive detectors (figure 3.19) [58].

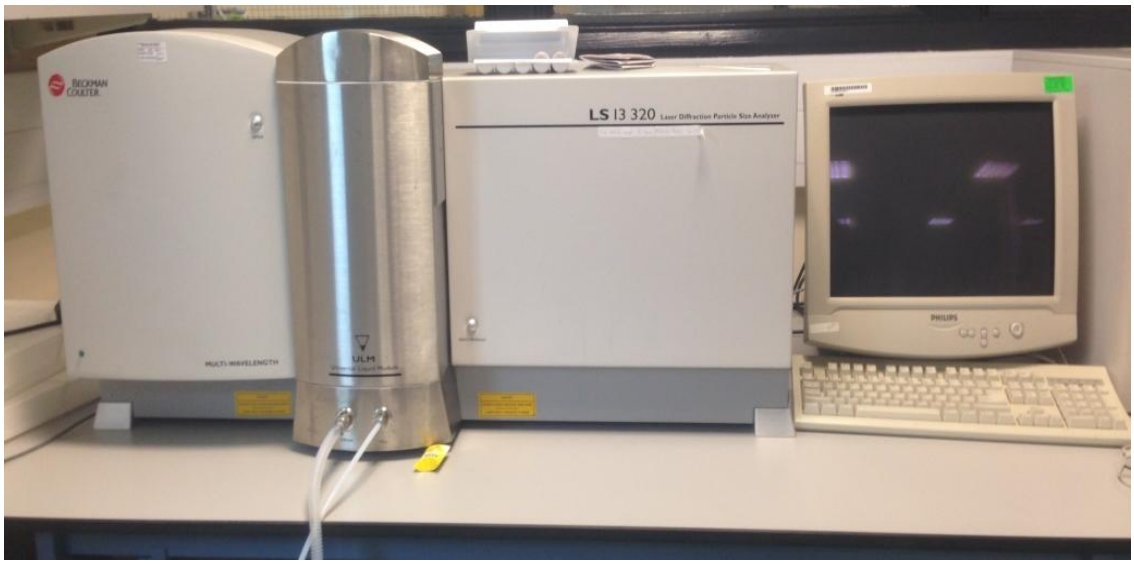

Figure 3.19: image of laser diffraction particle sizing analyser.

Following this, by applying mathematical algorithms, the signals detected are then converted into particle size distributions. The basic scattering equation (equation 3.12) of light by a single particle given that the scattering object is spherical and the refractive index of the material (both the real and imaginary components) is known, is stated below [59].

$$I(\theta) = \frac{I_o}{2\kappa^2 a^2} \{[S_1(\theta)]^2 + [S_2(\theta)]^2\} \qquad \text{(eq. 3.12)}$$

Where, $I(\theta)$ is the intensity of the scattered light as a function of angle, θ; I_o is the intensity of the incident light beam; κ is the wave number; a is the distance from the scattering particle to the detector; $S_1(\theta)$ and $S_2(\theta)$ are the complex scattering functions which defines the scattering of light in a 360° surface. The type of light source and the position of the detectors are governed by the size of particles investigated. In modern light diffraction instruments however there are several light sources and detectors available which in turn allow a dynamic range of particles to be detected using this method. The laser diffraction is usually calibrated to align the instrument using standard garnet powder particles with an average size of 35 µm. After calibrating it just once, the laser diffraction technique can be used multiple times without further requirement for calibration. This means that an accurate size distribution can be derived as the particle size is inversely proportional to the diffraction angle, given that the light passes through the suspension [59].

3.14 X-ray diffraction techniques

X-ray diffraction methods are non-destructive analytical techniques used to identify the structures of crystalline materials and are also employed for quantitative determination of crystal substances by analysing the diffraction pattern. The structures of the crystals can be related to the diffraction configuration using Bragg's Law (equation 3.13)[60].

$$n\lambda = 2d \sin\theta \qquad \text{(eq. 3.13)}$$

In Bragg's Law, n is an integer, λ is the wavelength of X-rays, d is the spacing between the planes of the atomic lattice and θ is the angle between the incident ray and the surface of the planes. The Bragg's Law can be illustrated using the diagram below (figure 3.20).

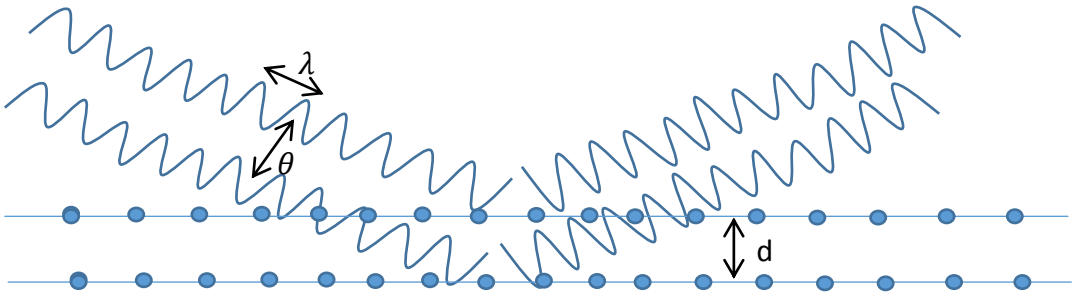

Figure 3.20: Diagram illustrating Bragg's Law [60].

There are two different diffraction techniques which have been used in this study and these are wide angle X-ray scattering (WAXS) and small angle X-ray scattering (SAXS). The distinguishable characteristics which separate the two techniques are the scattering angles. WAXS is used to investigate samples with 2θ > 5° whereas, SAXS can be manipulated to examine samples with lower 2θ ranging between 0.1 to 10°.

3.14.1 Small Angle X-ray Scattering

A Bruker Nanostar Small Angle X-ray Scattering (SAXS) instrument along with cross-coupled Göebel mirrors and pin-hole collimation was used for SAXS measurements. CuKα radiation of 1.54 Å was produced using an X-ray tube with a voltage of 40 kV and a current of 35 mA, which scatters upon contact with the sample in the capillary. The SAXS camera was fitted with a Hi-star 2D detector (pixel size 100 µm) which displays direct electronic imaging of the X-ray pattern. A vacuum pump was used to reduce air scattering in the sample chamber.

The background was subtracted from the scattering files which were then integrated to give one-dimensional scattering function *I(q),* where *q* is the length of the scattering vector and can be defined by the equation 3.14.

$$q = (4\pi/\lambda)sin\theta \qquad \text{(eq. 3.14)}$$

Where, λ = is the wavelength and 2θ is the scattering angle. The sample distance used was 650 mm which gave a q range from 0.2 to 30.6 nm^{-1}.

3.14.1.1 Solid fat analysis using SAXS

A small quantity of lard was carefully deposited on to the aluminium foil and tightly sealed in a cuvette before SAXS analysis was conducted in order to determine any polymorphic changes occurring with change in temperature. Since lard is the most complex fat it was used as the model for problematic fat removal. An equal amount of lard was then smeared across each swatches of fabric and examined using SAXS in a similar manner as stated above. The temperature range applied to the soiled samples varied between 5 °C to 60 °C using an XYZ temperature controller which was connected to the SAXS.

3.14.1.2 Liquid surfactant analysis

SAXS analysis was conducted on soiled solutions (before/after washing). Approximately 0.05 mL of the solutions was injected into a capillary tube before sealing both ends of the cuvette firmly for SAXS measurements. This method was used to identify the presence of micelles with increase in concentration of the surfactants/detergents.

3.14.2 Wide Angle X-ray Scattering

A Bruker GADDS D8 Wide Angle X-ray Scattering (WAXS) instrument with cross-coupled Göebel mirrors and pin-hole collimation was used to obtain information on the packing of the surfactant nolecules, 1,2-DCE - TBATPB/surfactant based crystal samples and polymorphic crystal structures of soils (with and without the deposition of it on different types of fabrics). A tube X-ray source was used with a voltage of 40 kV and a current of 40 mA, which produced a CuKα radiation of 1.54 Å. The WAXS camera was fitted with a Hi-star 2D detector (pixel size 100 μm) (figure 3.21).

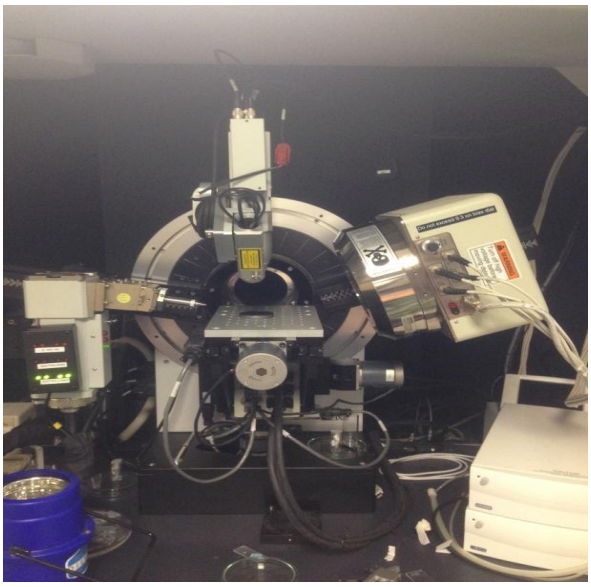

Figure 3.21: Image of Bruker D8 diffractometer.

The scattering files collected were integrated to give the one-dimensional scattering function *I(q)*. The sample detector distance used was 150 mm which gave a 2θ range of 10^{o} to 45^{o}. The WAXS data was processed using the GADDS software from which the 2θ, d-

spacings and peak intensities of all the samples investigated were determined. The samples were placed on a silica wafer before WAXS analysis was commenced, in order to minimise the background scattering.

3.15 Environmental scanning electron microscope

In Environmental scanning electron microscope (ESEM), with its specialised electron detectors and pumping systems, the electron beam is emitted from an electron gun under high vacuum to a sample chamber, where either the pressure or temperature can be altered to adjust the humidity level, which in turn allows imaging of the specimens in it natural form[61].

Figure 3.22: Image of the Philips XL30 ESEM used.

The Philips XL30 ESEM (figure 3.22) was used to characterise the sol-gel/FcAuNP mixture used to make the enzymatic biosensors. A 0.3 µL of the sol-gel/FcAuNP mixture was gently sonicated for 30 minutes before depositing the solution onto a silica wafer for ESEM analysis. The accelerated voltage applied was 24 kV and the electron beam spot size was 4.3 nm. The magnification in the ESEM was an order of magnitude of 8000x. The gaseous

secondary electron detector (GSED) was applied which used gas to amplify the electron signal.

3.16 Atomic Force Microscopy (AFM)

AFM has been proven to be a useful technique for measuring the physical and surface properties of a material at the nanometer scale. This method involves use of a probe or tip which is situated at the apex of a silicon cantilever. The cantilever or the sample surface is mounted on the piezocrystal which allows the sharp probe to be positioned in relation to the surface so that it can scan across the surface of interest. This in turn causes deflection of the cantilever arm which is monitored by the change in the path of a laser light. The beam of the laser light is reflected from the upper side of the cantilever on to a position-sensitive photodetector. The forces of interaction between the probe and the surface due to deflection are then measured, as a function of distance[62]. A Veeco Multimode Atomic Force Microscope along with Nanoscope IV controller was used for analysis of lard samples (figure 3.23).

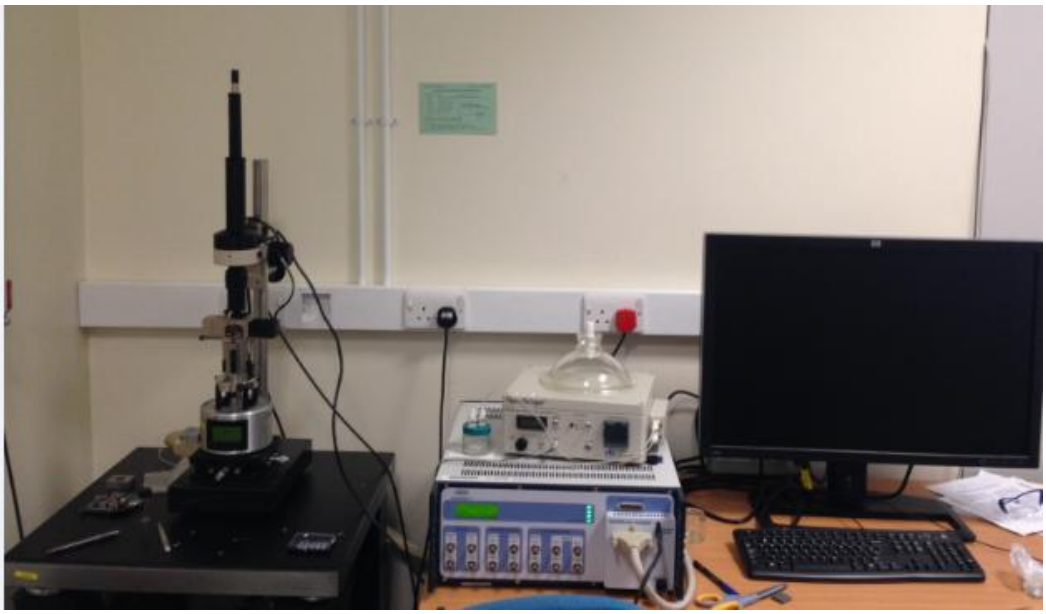

Figure 3.23: Image of a Veeco Multimode Atomic Force Microscope.

The lard specimen in solid form was deposited on to a silicon wafer which was then placed into the AFM. For the AFM, the imaging mode of operation used was the contact mode.

From this, the deflection signal was recorded and displayed in the form of a topograph. The temperature was increased from 10 ^{o}C- 60 ^{o}C using a temperature controller which is connected to the AFM.

3.17 Transmission Electron Microscopy

Transmission Electron Microscopy (TEM) is a microscopy technique, which is capable of generating high resolution images of a material up to an atomic level compared to other microscopic methods such as the light microscope. In TEM, a beam of electrons is transmitted through the sample where it interacts with the specimen. An image is then produced, magnified and focused before detecting it using an imaging device such as fluorescent screen, photographic film or CCD camera[63]. The high resolution generated due to the small de Broglie wavelength of the electrons (equation 3.15) allows fine details such as the shape, size and structure of small materials that are thousands of times smaller than the objects detected using a light microscope to be identified[64].

$$\lambda = \frac{h}{\sqrt{2m_e V}} \qquad \text{(eq. 3.15)}$$

Where, λ is the wavelength, h is the Planck's constant and equals to 6.6 x 10^{-34} Js, m_e is the mass of an electron which is 9.11 x 10^{-31} kg and v is the velocity of the beam. The electron wavelength is typically around 0.02 Å compared to a few Å for X-rays. The overall resolution is affected by the diffraction limit (δ_1) and the spherical aberration (δ_2). By taking into account of all the above factors and that the semi-angle of collection of magnifying lens is 0.1 radians/ 5^{o}, the theoretical resolution limit can be determined using equation 3.16 below[65,66].

$$\delta_1 = \frac{d_{s1}}{2} = \frac{0.61\lambda}{\varepsilon \sin\varphi} \qquad \text{(eq. 3.16)}$$

Where, d_{s1} is the diffraction limited spot size, ε is the refractive index of the viewing medium, φ is the semi-angle of collection of magnifying lens and ε is equal to 1 for air, at small angles. The $\varepsilon \sin\varphi$ value also known as numerical aperture can be approximated to unity assuming that the resolution is equal to half the wavelength of light. The theoretical

value however is not attainable due to lens deviation. To reduce this effect, a small aperture can be employed to ensure that the electrons can pass through the centre of the lens[65].

The JEOL 2100F Schottky field emission gun TEM used in this study has a point resolution of 2.3 Å and 1.0 Å information limit (figure 3.24), operating at 200 kV. The sample was prepared by depositing a drop of the sol-gel/FcAuNP solution onto a special glass grid before analysing it using the TEM.

Figure 3.24: Image of JEOL 2100F field emission gun TEM.

The phase contrast, high resolution electron microscopy and diffraction patterns were processed by a Gatan Orius Camera. The sample images captured were analysed via Digital Micrograph platform software. The chemical composition of the sol-gel/FcAuNP sample investigated was determined using the Energy-dispersive X-ray Spectroscopy (EDX) and an Oxford INCAx-Sight Si(Li) detector.

3.18 The soiling and ageing process

5 cm x 5 cm pieces of fabrics i.e. polyester, polycotton and cotton were initially cut out for the soiling, washing and ageing process. Each fabric swatch was then weighed before depositing and spreading the melted (at 55 ^{o}C for 10 minutes) lard across the surface evenly. Lard was used as the fat model as it consists of a mixture of fatty acids therefore making its removal more problematic compared to other fats. The soiled fabrics were then weighed

and stored at -10 °C (on dry ice), 10 °C (in a water bath), 20 °C and 30 °C (in ovens) before washing. After washing the soiled swatches of fabrics, the samples were dried at the appropriate temperatures for one day, three days and five days before SAXS and WAXS analyses were conducted to determine the polymorphic state of the fat crystals. Overall, 24 pieces of fabrics were required to conduct the experiments. Each experiment was repeated twice for accuracy. Alongside the above experiments, two sets of soiled fabric swatches were also exposed to 10 °C by placing the pieces of fabrics on ice and another two sets of fabrics were kept on dry ice at a temperature of -10 °C for 1 day. Throughout the day the soiled fabric samples were analysed after 1 hour, 4 hours and 16 hours using SAXS (table 3.1). Any significant differences in the results obtained from the experiments with and without ice/dry ice were then evaluated. Each experiment was conducted twice for accuracy.

Table 3.1: the number of fabrics required for the ageing process for day 1 (per technique).

Fabrics	polyester	polycotton	cotton
-10 °C	2	2	2
10 °C	2	2	2
20 °C	2	2	2
30 °C	2	2	2
-10 °C (dry ice)	6 (analysed after 1 hour, 4 hours and 8 hours)	6 (analysed after 1 hour, 4 hours and 8 hours)	6 (analysed after 1 hour, 4 hours and 8 hours)
10 °C (ice)	6 (analysed after 1 hour, 4 hours and 8 hours)	6 (analysed after 1 hour, 4 hours and 8 hours)	6 (analysed after 1 hour, 4 hours and 8 hours)

In total, 60 swatches of fabrics were required for the one day ageing experiments (table 3.1). For analysis of the washed soiled fabrics by either one of the specific techniques such as SAXS or WAXS after 3 days (24 swatches of fabrics) and 5 days (24 swatches of fabrics) of ageing at different temperatures required a total of 48 pieces of fabrics.

3.19 The Washing Process

The above procedure as used for the ageing process (days 1 -5) was repeated for preparing samples for the washing cycle. As before, the fabric swatches were exposed to a range of temperature (i.e. -10 °C, 10 °C, 20 °C and 30 °C) and stored overnight (on dry ice, in water bath and ovens) before washing was carried out in Newcastle Innovation Centre, Newcastle.

The wash process was undertaken without the use of surfactant as a control experiment. A low concentration of 0.7 mg/ml, a high concentration of 50 mg/ml of C24E3S surfactant and no surfactant was applied for the washing process. The C24E3S surfactant was used because it showed micellar formation at a range of concentrations and was easily detectable using SAXS. The surfactant concentrations were scaled up to make up a volume of 800 mL which is the maximum a tergotometer wash pot can hold (figure 3.25).

Figure 3.25: Schematic diagram of the tergotometer setup used for the washing process.

The temperatures used for cold water wash were set at 20 ^{o}C, 30 ^{o}C and 40 ^{o}C. Overall, for each wash water temperature a total of 24 soiled fabric swatches were used. Due to time limitation, repeats for only the soiled fabrics exposed and dried after wash at temperatures of 10 ^{o}C and 20 ^{o}C were undertaken (experiments 2, 3 and 5 as stated in table 3.2).

Table 3.2: the number of soiled fabrics required for one specific wash temperature/ per technique (such as SAXS, WAXS or NMR) used.

Experiment No.	Soiled fabrics	polyester	polycotton	cotton
1	Exposed to -10 ^{o}C (for drying overnight at -10 ^{o}C)	1	1	1
2	Exposed to 10 ^{o}C (for drying overnight at 10 ^{o}C)	2	2	2
3	Exposed to 20 ^{o}C (for drying overnight at 20 ^{o}C)	2	2	2
4	Exposed to 30 ^{o}C (for drying overnight at 30 ^{o}C)	1	1	1
5	Exposed to 10 ^{o}C (for drying overnight at 20 ^{o}C)	2	2	2
Total number of fabrics		8	8	8

For all of the wash temperatures (20 ^{o}C, 30 ^{o}C and 40 ^{o}C) and analysis of the washed soiled fabrics by one specific technique i.e. SAXS or WAXS, a total of 72 pieces of fabrics were needed (table 3.3).

Table 3.3: shows the number of fabric swatches required for the different wash temperatures and for analysis of the washed fabrics by one specific technique.

Fabric type / **Wash temperature /^{o}C**	**polyester**	**polycotton**	**cotton**
20	8	8	8
30	8	8	8
40	8	8	8
Total number of fabric swatches	24	24	24

The soiled fabric swatches in the absence and presence of C24E3S surfactant were washed using a tergotometer and by applying mechanical agitation at a constant speed of 200 rpm for 20 minutes. All the samples were then further rinsed with clean water for 8 minutes to remove excess surfactant from the fabrics. After washing and rinsing was carried out, the fabric swatches were exposed to and dried at appropriate temperatures of 10 ^{o}C, 20 ^{o}C and 30 ^{o}C before cutting out 1 cm x 1 cm sized pieces of fabrics for SAXS and WAXS analysis. Each sample analysis was undertaken for a period of 1 hour using SAXS/ WAXS. The data obtained was then integrated and intensity versus 2θ plots was produced. The amount of lard removed from the washed soiled fabrics was also evaluated (see section 3.20).

In this washing process, factors such as fabrics, washing and thermal exposure temperature were the variables. The type of fat, fabric and surfactant used as well as the speed of the tergotometer were kept constant throughout the experiments outlined above.

3.20 Quantification of lard removed after washing

The level of lard removed after washing at wash temperatures of 20, 30 and 40 ^{o}C was determined quantitatively using equation 3.17 below.

$$\text{soil removal} = \left(\frac{\text{weight of sample aged} - \text{weight of sample washed}}{\text{weight of sample aged}} \right) x\ 100 \qquad \text{(eq. 3.17)}$$

3.21 References

1. Ryan, T. *Electrochemical Detectors: Fundamental Aspects and Analytical Applications*. (Springer Science & Business Media, 2012).
2. Bagotsky, V. S. *Fundamentals of Electrochemistry*. (John Wiley & Sons, 2005).
3. Compton, R. G. & Banks, C. E. *Understanding Voltammetry*. (World Scientific, 2011).
4. Girault, H. H. *Analytical and Physical Electrochemistry*. (CRC Press, 2004).
5. Lambrechts, M. & Sansen, W. *Biosensors: Microelectrochemical Devices*. (CRC Press, 1992).
6. Zhou, D. & Greenbaum, E. *Implantable Neural Prostheses 2: Techniques and Engineering Approaches*. (Springer Science & Business Media, 2010).
7. Scholz, F. *Electroanalytical Methods: Guide to Experiments and Applications*. (Springer, 2013).
8. Fuchigami, T., Atobe, M. & Inagi, S. *Fundamentals and Applications of Organic Electrochemistry: Synthesis, Materials, Devices*. (John Wiley & Sons, 2014).
9. Palanna, O. G. *Engineering Chemistry*. (Tata McGraw-Hill Education, 2009).
10. Gellings, P. J. & Bouwmeester, H. J. *Handbook of Solid State Electrochemistry*. (CRC Press, 1997).
11. Kaifer, A. E. & Gómez-Kaifer, M. *Supramolecular Electrochemistry*. (John Wiley & Sons, 2008).
12. Scott, R. A. *Applications of Physical Methods to Inorganic and Bioinorganic Chemistry*. (John Wiley & Sons, 2007).
13. Karunakaran, C., Bhargava, K. & Benjamin, R. *Biosensors and Bioelectronics*. (Elsevier, 2015).
14. Kasem, K. K. & Jones, S. Platinum as a Reference Electrode in Electrochemical Measurements. *Platin. Met. Rev.* **52,** 100–106 (2008).
15. Inzelt, G., Lewenstam, A. & Scholz, F. *Handbook of Reference Electrodes*. (Springer Science & Business Media, 2013).
16. Inzelt, G. in *Handbook of Reference Electrodes* (eds. Inzelt, G., Lewenstam, A. & Scholz, F.) 331–332 (Springer Berlin Heidelberg, 2013). at <http://link.springer.com/10.1007/978-3-642-36188-3_14>
17. Livage, J. & Lemerle, J. Transition Metal Oxide Gels and Colloids. *Annu. Rev. Mater. Sci.* **12,** 103–122 (1982).

18. Bergna, H. E. & Roberts, W. O. *Colloidal Silica: Fundamentals and Applications*. (CRC Press, 2005).
19. Pierre, A. C. *Introduction to Sol-Gel Processing*. (Springer Science & Business Media, 2013).
20. Hench, L. L., Ulrich, D. R., Engineering, U. of F. D. of M. S. and & Engineering, U. of F. C. of. *Ultrastructure processing of ceramics, glasses, and composites*. (Wiley, 1984).
21. Ju, H., Zhang, X. & Wang, J. *NanoBiosensing: Principles, Development and Application*. (Springer Science & Business Media, 2011).
22. Hayat, A. & Marty, J. Disposable Screen Printed Electrochemical Sensors: Tools for Environmental Monitoring. *Sensors* **14,** 10432–10453 (2014).
23. Gorton, L. *Biosensors and Modern Biospecific Analytical Techniques*. (Elsevier, 2005).
24. Honeychurch, K. C. & Hart, J. P. Screen-printed electrochemical sensors for monitoring metal pollutants. *TrAC Trends Anal. Chem.* **22,** 456–469 (2003).
25. Nikolelis, D. *Biosensors for Direct Monitoring of Environmental Pollutants in Field*. (Springer Science & Business Media, 1997).
26. Svancara, I., Kalcher, K., Walcarius, A. & Vytras, K. *Electroanalysis with Carbon Paste Electrodes*. (CRC Press, 2012).
27. Moretto, L. & Kalcher, K. *Environmental Analysis by Electrochemical Sensors and Biosensors: Fundamentals*. (Springer, 2014).
28. Cooper, J. & Cass, T. *Biosensors*. (Oxford University Press, USA, 2004).
29. Bartlett, P. N. *Bioelectrochemistry: Fundamentals, Experimental Techniques and Applications*. (John Wiley & Sons, 2008).
30. Schlesinger, M. *Applications of Electrochemistry in Medicine*. (Springer Science & Business Media, 2013).
31. Ozkan, S. A., Kauffmann, J.-M. & Zuman, P. *Electroanalysis in Biomedical and Pharmaceutical Sciences: Voltammetry, Amperometry, Biosensors, Applications*. (Springer, 2015).
32. Parkash, O., Yean, C. & Shueb, R. Screen Printed Carbon Electrode Based Electrochemical Immunosensor for the Detection of Dengue NS1 Antigen. *Diagnostics* **4,** 165–180 (2014).
33. Honeychurch, K. C. Screen-printed Electrochemical Sensors and Biosensors for Monitoring Metal Pollutants. *Insciences J.* 1–51 (2012). doi:10.5640/insc.020101
34. Wang, J. *Analytical Electrochemistry*. (John Wiley & Sons, 2006).

35. Scott, R. A. & Lukehart, C. M. *Applications of Physical Methods to Inorganic and Bioinorganic Chemistry*. (John Wiley & Sons, 2013).

36. Cazes, J. *Analytical Instrumentation Handbook, Third Edition*. (CRC Press, 2004).

37. Balzani, V. *Electron Transfer in Chemistry*. (Wiley-VCH Verlag GmbH, 2001).

38. Oldham, K., Myland, J. & Bond, A. *Electrochemical Science and Technology: Fundamentals and Applications*. (John Wiley & Sons, 2011).

39. Monk, P. M. S. *Fundamentals of Electro-Analytical Chemistry*. (John Wiley & Sons, 2008).

40. Monk, P. M. S., Mortimer, R. J. & Rosseinsky, D. R. *Electrochromism: Fundamentals and Applications*. (John Wiley & Sons, 2008).

41. Hammerich, O. & Lund, H. *Organic Electrochemistry, Fourth Edition,*. (CRC Press, 2000).

42. Zutshi, K. *Introduction to Polarography and Allied Techniques*. (New Age International, 2006).

43. Zanello, P. *Inorganic Electrochemistry: Theory, Practice and Applications*. (Royal Society of Chemistry, 2003).

44. Montenegro, I. *Microelectrodes: Theory and Applications: Theory and Applications*. (Springer Science & Business Media, 1991).

45. Wang, J. *Analytical Electrochemistry*. (John Wiley & Sons, 2004).

46. Schalley, C. A. *Analytical Methods in Supramolecular Chemistry*. (John Wiley & Sons, 2012).

47. Molina, A. *et al.* Differential Pulse Voltammetry for Ion Transfer at Liquid Membranes with Two Polarized Interfaces. *Anal. Chem.* **81,** 4220–4225 (2009).

48. Dahmen, E. A. M. F. *Electroanalysis: Theory and Applications in Aqueous and Non-Aqueous Media and in Automated Chemical Control*. (Elsevier, 1986).

49. Heumann, K. G. *Handbook of Elemental Speciation: Techniques and Methodology*. (John Wiley & Sons, 2004).

50. Abe, M. *Mixed Surfactant Systems, Second Edition*. (CRC Press, 2004).

51. Swann, G. E. A. & Patwardhan, S. V. Application of Fourier Transform Infrared Spectroscopy (FTIR) for assessing biogenic silica sample purity in geochemical analyses and palaeoenvironmental research. *Clim. Past* **7,** 65–74 (2011).

52. Stuart, B. H. *Infrared Spectroscopy: Fundamentals and Applications*. (John Wiley & Sons, 2004).

53. VSM, L. C. P. T. *Manual of Assisted Reproductive Technologies and Clinical Embryology*. (Jaypee Brothers Medical Publishers Pvt. Ltd., 2014).

54. Sepe, M. P. *Thermal Analysis of Polymers*. (iSmithers Rapra Publishing, 1997).

55. Höhne, G. W. H., Hemminger, W. & Flammersheim, H.-J. *Differential Scanning Calorimetry: An Introduction for Practitioners*. (Springer Science & Business Media, 2013).

56. Gross, J. H. *Mass Spectrometry: A Textbook*. (Springer Science & Business Media, 2011).

57. Syvitski, J. P. M. *Principles, Methods and Application of Particle Size Analysis*. (Cambridge University Press, 2007).

58. Rhodes, M. J. *Introduction to Particle Technology*. (John Wiley & Sons, 2008).

59. Zheng, J. *Formulation and Analytical Development for Low-Dose Oral Drug Products*. (John Wiley & Sons, 2009).

60. Lou, L. *Introduction to Phonons and Electrons*. (World Scientific, 2003).

61. Goodhew, P. J., Humphreys, J. & Beanland, R. *Electron Microscopy and Analysis, Third Edition*. (CRC Press, 2000).

62. Bowen, W. R. & Hilal, N. *Atomic Force Microscopy in Process Engineering: An Introduction to AFM for Improved Processes and Products*. (Butterworth-Heinemann, 2009).

63. Kumar, C. S. S. R. *Transmission Electron Microscopy Characterization of Nanomaterials*. (Springer Science & Business Media, 2013).

64. Atkins, P., Paula, J. de & Friedman, R. *Quanta, Matter, and Change: A Molecular Approach to Physical Chemistry*. (OUP Oxford, 2009).

65. Williams, D. B. & Carter, C. B. *Transmission Electron Microscopy: A Textbook for Materials Science*. (Springer Science & Business Media, 2009).

66. CHEN, C. Crystallisation of glycine and dipicolinic acid (DPA) from microemulsions. (Durham University, 2013). at <http://etheses.dur.ac.uk/6984/>

CHAPTER 4

Surfactant characterisation at the liquid-liquid interface

4.1 Surfactant behavior at the liquid-liquid interface

The behaviour of surfactant at an oil/water interphase is of fundamental importance across a range of application, which includes detergency[1], oil processing[2,3], agrochemicals[4], medicine[5], water treatment[6] and food production[7,8]. The first study on ion transfer across the liquid-liquid interface was undertaken in the 1970s by the pioneer Claude Gavach in the field of electrochemistry at the interface between two immiscible electrolyte solutions (ITIES), using various electrochemical methods such as chronoamperometry and impedance spectroscopy[9]. The methods were used to determine parameters related to the ionic transfer kinetics i.e. the transfer coefficients, rate constants and interfacial double layer capacitance[10,11]. The work on the ion transfer across the ITIES was further explored by professor Koryta and co-workers in Heyrovsky institute, Prague between the late 70s and the late 80s using various systems including the water-nitrobenzene and metal-electrolyte solutions [12,13,14,15]. At the same time, the concept of ideally polarised ITIES based on the standard Gibbs energy of ion transfer was also introduced by Koryta et al[16]. The fundamental studies carried out on ion transfer across the ITIES has permitted deeper understanding of : (1) the influence that charge transfer kinetics have on the interfacial structure and (2) how the ion exchange process at the phase boundary can be used for electrochemical sensing of ionic analytes which are difficult to detect by redox electrochemistry[17]. The advances in the electrochemistry of charge transfer in liquid-liquid systems have allowed determination of various essential properties of ion transfer such as the standard Gibbs energy of transfer of different types of simple ionic species which can be easily established using voltammetric techniques[18,19]. The interactions between ions or redox species on charged interface have been found to play a fundamental role in interfacial instability[20]. Current experimental work performed by Kakiuchi *et al*, on transfer of anionic surfactants, alkanesulphonate sodium salts and alkyl sulphate ions, across the water (with 10 mM LiCl) -1,2 DCE (with 20 mM TPnATPB) interface has shown evidence for the presence of instability region in the polarised potential range of the phase-boundary potential, using cyclic voltammetry[21]. Kakiuchi's research showed as the half-wave potential for interfacial transfer of the surface active ions was approached, irregular oscillations and chaotic behaviour of the current were identified as a result of electrochemical instability within the potential region around the mid-

point potential[22]. These findings were then further confirmed by using potential-step chronoamperometry (CA) which also demonstrated the existence of instability range due to potential dependent adsorption and partitioning of the surface active ions on the phase-boundary potential. The irregular current was found to be more pronounced with increase in surfactant concentration, decrease in the scan rate using CV and increase in potential when applying the CA[23]. The chaotic currents occur as a result of Marongoni-type movements and the spontaneous emulsification occurring at the interface due to the driving forces produced by the difference in the chemical potentials of the reactant species present in both the aqueous and organic phases. The spontaneous emulsification results in formation of emulsion particles to reinstate the system to its stable state however the avalanche-type transfer of these particles across the liquid-liquid phase boundary has also been found to give rise to chaotic currents as detected electrochemically[24]. All of these attributes indicate that the electrochemical instability is both time- and concentration-dependent phenomenon. It has also been established by Kakiuchi and co-workers that cations such as Na^+ and Li^+ from surfactants/electrolytes in solution can be entrapped in the process of emulsion particle formation. This was evident from the consecutive current spikes observed using the CV technique[25].

Similar instability results as obtained for the anionic surfactants was also reported by Kakiuchi *et al.* for the transfer of cationic surfactants i.e. the decylammonium ions (DA^+, 0.5 - 1 mmol dm^{-3}) and, the nonyl- and octyl-ammonium ions (2 mmol dm^{-3}) across the 1,2-DCE (100 mM TPnATPB)/water (with 0.1 M LiCl and 10 mM HCl) interface[26]. The current augmentations observed however was seen to disappear after a 10 mmol dm^{-3} of sorbitan monooleate (non-ionic surfactant) was added to the doedecylsulphonate (anionic) surfactant based system and also, when a 3 mmol dm^{-3} of sorbitan monooleate was mixed with the 1,2-DCE phase of the decylammonium (cationic) surfactant based liquid-liquid system. This is due to the sorbitan monooleate acting as a stabiliser and strongly adsorbing at the interface, repressing the convection motion of the solutions which was reflected in the shape of the voltammogram resembling an electrochemically reversible reaction. Thus, reducing the surface tension (γ) in the entire potential region and also, decreasing the dependency of the γ on the potential applied[21,26,27].

Further studies on surfactant at the ITIES showed that the maximum adsorption of the ions take place when the interfacial potential reaches the standard ion transfer potential of the surface active molecules. As a result, the double layer capacitance becomes negative and the interfacial tension with respect to phase boundary potential becomes positive[28]. The interface overcomes the unstable state by bringing the phase boundary potential outside of the instability

potential range and also, via releasing energy through processes such as spontaneous emulsification and movement of the interface due to Marangoni effect (which is caused by the mass transfer along the interface as a result of surface tension gradient)[29]. By understanding the electrochemical instability caused by the transfer and adsorption of the surfactant ions, various instability related problems such as fluctuations at the water and organic phase systems can be solved and also, mechanisms involved in spontaneous emulsification and digestion of fat can be determined.

4.2 Stability and instability of the electrified liquid-liquid interface

The adsorption of surfactant at the liquid-liquid interface system has been known to cause electrochemical instability. In electrochemistry, the oscillation of phase-boundary potential ($\Delta_o^w\phi$) at the oil-water interface has been described in terms of forming and breaking the surfactant layers and, the adsorption and desorption of ion-pair at the interface[30,31]. The early work conducted by Arai *et al.* in 1995 demonstrated presence of interfacial oscillations and instability caused by the adsorption of sodium dodecylsulphate at the water-octanol phase boundary, using potentiometry[30]. Following this, Maeda *et al.* showed self-sustained oscillations for a system consisting of water phase with cetrylmethylammonium and nitrobenzene phase with picric acid[31]. In most recent years, the process of surface active ion transfer and the instability due to adsorption of surfactant at the liquid-liquid interface has been extensively studied by Kakiuchi using techniques such as cyclic voltammetry and chronoamperometry[32]. Kakiuchi's research revealed that the width and location of the instability range is influenced by a number of factors which include change in surface tension ($\Delta\gamma$) due to adsorption of ion, absorbability and concentration of the ion, curvature of electrocapillary curve, the potential difference between the two immiscible phases at the interface, the amount of electrolyte salt used, the relative location of $\Delta_{\mathrm{o}}^{\mathrm{w}}\phi_{pzc}$ (potential difference at point of zero charge i.e. the highest point of the capillary curve)[33] *and* $\Delta_{\mathrm{o}}^{\mathrm{w}}\phi_i^{\emptyset\prime}$ (standard ion transfer potential) as well as factors such $B_i^{o,\emptyset}m_i$ (the adsorption coefficient) and $\Delta G_{ads,i}^{\emptyset}$ (standard adsorption Gibbs energy at $\Delta_{\mathrm{o}}^{\mathrm{w}}\phi_i^{\emptyset\prime}$) [34, 35, 36].

Kakiuchi initially established that the criterion for attaining a stable electrified liquid-liquid interface require the γ with respect to the phase-boundary potential ($\Delta_o^w\phi$) to be negative. This can be defined in terms of $(\partial^2\gamma/\partial\Delta_o^w\phi^2)_{T,P,\mu_j} < 0$ and the first derivative of the Lippmann equation (equation 4.1) [37,38].

$$q^w = -\left(\frac{\partial \gamma}{\partial \Delta \phi}\right)_{T,P,\mu_i} = -\frac{1}{A}\left(\frac{\partial \Delta G^\sigma}{\partial \Delta \phi}\right)_{T,P,\mu_i} \quad \text{(eq. 4.1)}$$

Where, q^w is the excess surface charge density in water, ΔG^σ is the surface excess Gibbs energy, $\Delta\phi$ is the inner potential difference or Galvani potential between the water and 1,2-DCE phase, *A* is the area of the interface (cm^2), *T* is the temperature, μ_i is the chemical potential of a chemical species, i, and *p* is the pressure. According to the lippmann equation (equation 4.1), the slope of an electrocapillary curve (see section 4.3) represents the excess surface charge density on the water phase side of the interface. Differentiation of the above expression for stable phase boundary condition relates the γ to the potential difference and the capacitance. This can be represented in the form of second derivative of Lippmann equation (equation 4.2) below [39,40].

$$C_{dl} = \left(\frac{\partial q^w}{\partial \Delta \phi}\right)_{T,P,\mu_i} = -\left(\frac{\partial^2 \gamma}{\partial \Delta \phi^2}\right)_{T,P,\mu_i} = -\frac{1}{A}\left(\frac{\partial^2 \Delta G^\sigma}{\partial \Delta \phi^2}\right)_{T,P,\mu_i} \geq 0 \quad \text{(eq 4.2)}$$

Where, C_{dl} is the double layer capacitance. For fixed condition at a constant temperature and pressure, the high level of entropy is converted to minimum Gibbs energy of the system and this in turn leads to a decrease in the γ and a positive double layer capacitance is achieved[41]. However, when a surfactant is introduced into the above equilibrium system, the polarised interface becomes unstable due to phase boundary potential-dependent partitioning and adsorption of the surface active molecules in the two electrolyte solutions, organic and water[42]. The criterion for an unstable system can be expressed as $(\partial^2\gamma/\partial\Delta_o^w\phi^2)_{T,P,\mu_j} > 0$. The term is violated due to an instability potential range within the $\Delta_o^w\phi$ values and this in turn generates a positive finite value of γ as a result of spontaneous emulsification in the liquid-liquid two phase system which is evident by the clouding effect at the vicinity of the interface[43,44,45]. The emulsification process is initiated by the hydrodynamic movement of the interface which is Marangoni-driven and caused by the formation of surface tension gradients[46,47,48]. The energy required for such reaction to take place is obtained from just simple rearrangement of the components within the system[49]. The Marangoni instability in a liquid-liquid system caused by the transfer of solute ions was first discovered by Sternling and Scriven[50] and the emulsification phenomenon was initially observed by Johannes Gad in 1878, who discovered that a solution of lauric acid in oil instantly emulsified when coming into contact with an aqueous alkali solution, in a surfactant based system[51]. Brücke in 1879 later confirmed Gad's findings and also, demonstrated that high concentrations of alkali prevent the emulsification process[52]. Following

this, various self-emulsification processes occurring in oil-water-alcohol, fatty acid-warm aqueous alkali solution and a range of oil-water two phase systems in the presence of non-surface active salts[53], anionic[25,54], non-ionic[55,56] and cationic[57] surfactants, due to uneven lowering of surface tension in the interface have been reported[56,57,58]. The emulsification process have been proven useful for a variety of surface chemistry and related applications such as dispersion of chemicals in industrial and agricultural processes[59,60], formulating drug delivery systems[60,61] and digestion of food[62].

It can be therefore suggested from the term $(\partial^2\gamma/\partial\Delta_o^w\phi^2)_{T,P,\mu_j} > 0$, that the adsorption and partition processes for surfactant ions in two immiscible media i.e. the water and organic phase, is mainly affected by the phase potential difference, $\Delta_o^w\phi$, at the interface which can be defined by equation 4.3 [63].

$$\Delta_o^w\phi = \phi^w - \phi^o \qquad \text{(eq. 4.3)}$$

Where, ϕ^w and ϕ^o are the inner potentials of water and organic phase. As the partitioning effect of the surface active ions is dependent on the $\Delta_o^w\phi$, it can be expressed by the Nernst equation (equation 4.4)[64]:

$$\Delta_o^w\phi = \Delta_o^w\phi_i^\emptyset + \frac{RT}{z_iF}\, In\, \frac{c_i^o}{c_i^w} \qquad \text{(eq. 4.4)}$$

Where, *R* is the gas constant, *T* is the absolute temperature, *z* is the valency of the surfactant ions, F is the Faraday constant, c_i^o and c_i^w are the concentrations of the surfactant ions in the water and organic phases. The Δγ due to surfactant adsorption as well as the adsorption Gibbs energy are both also dependent on the potential difference between the two phases. This can be expressed in terms of equations 4.5-4.7[65].

$$\Delta\gamma = \left(\frac{4RT}{zF}\right)(8RTx)^{1/2}cosh\left(\frac{zF}{4RT}\Delta\phi\right) + RT\Gamma_m[In(1-\theta_i) + a\theta_i^2] \qquad \text{(eq. 4.5)}$$

$$\Delta G_{ads,i}^{o,0} = \Delta G_{ads,i}^\emptyset + z_iF\,\beta_i\,[\Delta_o^w\phi - \Delta_o^w\,\phi_i^\emptyset] \qquad \text{(eq. 4.6)}$$

$$\Delta G_{ads,i}^{w,0} = \Delta G_{ads,i}^\emptyset - z_iF\,(1-\beta_i)[\Delta_o^w\phi - \Delta_o^w\,\phi_i^\emptyset] \qquad \text{(eq. 4.7)}$$

Where, *R* is the gas constant, *T* is the absolute temperature, x is the product of permittivity and the concentration of electrolytes in both 1,2-DCE and water, Γ_m is the maximum adsorption of the surface active ions (the value is assumed to be the same in both phases), z is the valency of the surfactant ions, F is the Faraday constant, $\Delta G_{ads,i}^{o,0}$ is the standard Gibbs energy of adsorption from the organic phase, $\Delta G_{ads,i}^{w,0}$ is the standard Gibbs energy of adsorption from water phase, $\Delta_o^w \phi$ is the potential difference between the 2 phases, $\Delta G_{ads,i}^{\emptyset}$ is the standard Gibbs energy at $\Delta_o^w \phi_i^{\emptyset}$, which in turn is the reference point of the potential dependent $\Delta G_{ads,i}^{o,0}$ and $\Delta G_{ads,i}^{w,0}$ (Standard Gibbs energy of adsorption from O and W phases) and β_i is a constant independent of $\Delta_o^w \phi$. When an anionic surfactant is adsorbed from the water to the organic phase and the bulk concentration of the surface active ions in the water solution decreases, $\Delta G_{ads,i}^{w,0}$ becomes more positive with negative $\Delta_o^w \phi$, between the two immiscible phases[66]. The difference in the adsorption Gibbs energy represents the relative affinity of the adsorbed molecules to the adjacent phases and this in turn is dependent on the hydrophilic-lipophilic balance of the surfactant[67].

4.3 Electrocapillary curve for surfactants at the liquid-liquid interface

The adsorption of the surface active ions reaches the highest when the potential is close to the $\Delta_o^w \phi_i^{\emptyset\prime}$ of the ions and decreases with the potential away from the $\Delta_o^w \phi_i^{\emptyset\prime}$, giving rise to a bell-shaped peak. This leads to instability which can be observed within the potential range established for a series of the phase-boundary potentials applied[68]. When plotting electrocapillary curves showing the presence of instability range for a system where the concentration of the surfactant is small and adequate amount of supporting electrolytes are present in both (water and organic) phases, it is assumed that the $\Delta\gamma$ because of specific ion adsorption and the diffuse part of the double layer are additive. The total variation in γ is then plotted as a function of $y = \left(\frac{F}{RT}\right)\left(\Delta_o^w \phi - \Delta_o^w \phi_{pzc}\right)$, representing an electrocapillary curve (figures 4.1a and 4.1b). The $\Delta_o^w \phi_{pzc}$ is normally located in the middle of the potential range for a polarised interface between the two immiscible electrolyte solutions and the $\Delta_o^w \phi_i^{\emptyset}$ of the surfactant is usually close to the $\Delta_o^w \phi_{pzc}$ for an unstable system[69]. A dip in the middle of the electrocapillary curve can be identified due to surfactant adsorption (figures 4.1a and 4.1b) indicating a decrease in the interfacial tension which however remains positive despite the instability. Thus, a positive curvature in the electrocapillary curve and a negative capacitance is attained in the range of $\Delta_o^w \phi$ where the system in unstable[70].

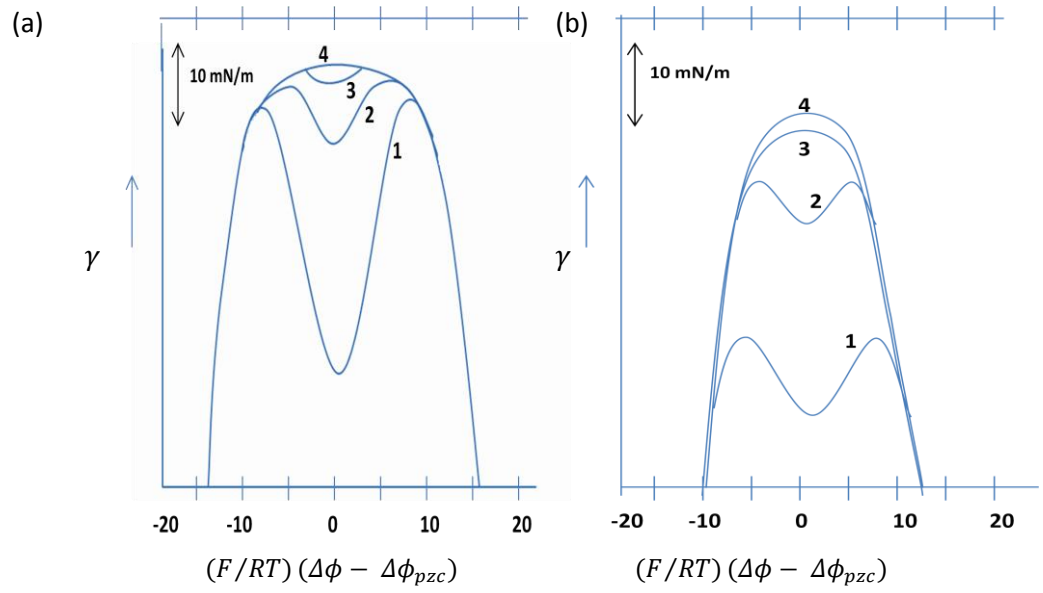

Figure 4.1: Electrocapillary curves for different concentrations of surfactant (labeled 1 (high)-4 (low)) added to the aqueous phase with electrolyte concentration of (a) 0.8 and (b) 80 mol dm^{-3} [23].

From figures 4.1a and 4.1b, it can be also deduced that the instability potential range increases with an increase in surfactant concentration and it decreases with an increase in the electrolyte concentration indicated by the narrowing of the electrocapillary curve. Enhancing the electrolyte concentration therefore stabilises the electrochemical system [71,72].

4.4 The adsorption process of surfactant molecules defined in terms of adsorption isotherm models

The amount of surfactant adsorbed at the interface is usually determined using the simplest method of interfacial tension measurements. For solutions, below the critical micelle concentration (CMC) point a decline in the equilibrium surface tension (γ_{eq}) is normally achieved with an increase in the concentration of the surfactant. As the surfactant concentration is continuously increased, a sudden change in the γ_{eq} signifying the attainment of the CMC point is observed. Enhancing the surfactant concentration just above the CMC level, causes the γ_{eq} to remain constant, indicating formation of micelles[73].

The Gibbs adsorption isotherm (equation 4.10) is another method for quantitative determination of the surfactant level adsorbed at the interface. This particular isotherm is fundamental to all the adsorption reactions and used to develop models such as the Van der Waals and Volmer isotherms corresponding to non-localised adsorption as well as Langmuir and

Frumkin isotherms which illustrate the localised adsorption process of the surfactant molecules[74,75]. The Gibbs adsorption equation (equation 4.10) below is for a system consisting of only one surface active constituent, species i. The adsorbed amount of surfactant at the interface is expressed in terms of the surface excess, Γ_i, which is defined as the excess of solute per unit area of the interface comparing to the bulk concentration. For dilute solutions, the surface excess and concentration is likely to be equivalent as the bulk concentration is small[76].

$$\Gamma_i = -\frac{1}{nRT}\frac{d\gamma}{d\ In\ c} \qquad \text{(eq. 4.10)}$$

Where, *n* is a constant depending on the number of species which makes up the surfactant and adsorb at the interface, *R* is the gas constant, *T* is the absolute temperature, *c* is the concentration of the surfactant and γ is the surface tension.

The isotherm models (Langmuir and Frumkin adsorption isotherms) relevant to localised adsorption and appropriate for the liquid-liquid system investigated are explained further. The Langmuir adsorption isotherm (equation 4.11.1) derived by Langmuir in 1918 is the simplest adsorption isotherm. The model defines surfactant adsorption by taking into account of the salinity, surfactant concentration and permeability. The adsorption is irretrievable with surfactant concentration and reversible with level of salt[77]. The isotherm is based on the assumption that there are finite numbers of adsorption sites and that each site is occupied by a single adsrobate molecule. During adsorption, a point of saturation is achieved when all of the available sites are taken up by the adsorbate molecules and complete monolayer coverage is attained. The Langmuir model presumes that intermolecular interaction does not exist between the surfactant molecules in either the bulk solution or at the interface[78]. Hence, the activation energies of the molecules are independent of the surface concentration of the surface active molecules. However, according to the Langmuir Isotherm (equation 4.11.1), the Γ_i is related to the surfactant concentration in the bulk solution or at the phase boundary [79,80]:

$$\Gamma_i = \frac{\Gamma_m c_1}{c_1 + a} \qquad \text{(eq. 4.11.1)}$$

Where, Γ_m is the adsorption capacity, $c_1$is the surfactant concentration and a is the surfactant activity. The Frumkin isotherm on the other hand was developed by Frumkin in 1925 and in contrast to the Langmuir isotherm it takes into account of all the forces which exists between the adsorbed surfactant molecules i.e. the intermolecular and repulsive interactions[81]. It also assumes that there is a strong relationship between the activation energies and the surface

concentration. The adsorption of the surfactant can be therefore accurately defined by the Frumkin adsorption isotherm equation 4.11.2[82].

$$B_i^{\alpha} c_i^{\alpha} = \frac{\theta_i}{1-\theta_i} \exp(-2a\theta_i) \qquad \text{(eq. 4.11.2)}$$

Where, B_i^{α} is the adsorption coefficient, C_i^{α} is the concentration of the ions (i) in the water or 1,2-DCE phase and θ_i is the surface coverage of i and α is the interaction parameter. The first part of the equation 4.8 represents the diffuse component of the double layer for an unstable interface and, the second term signifies specific adsorption of i and potential-dependent through θ_i.

4.5 The mechanism of surfactant adsorption process at the interface

As the surfactant molecules are introduced into the liquid-liquid ITIES system, the surface active ions are extensively adsorbed at the water and organic interface. The adsorption process involves interface-seeking surface active molecules to arrange in a specific manner so that it allows the surfactant molecules to diffuse from the bulk of a solution to the interface and replace the solvent molecules which in turn leads to formation of a monolayer at the phase boundary[83]. During adsorption, the hydrophilic moieties of the surfactant molecules face the water phase whilst the hydrophobic part immerses in the organic phase. As the concentration of the surfactant is continuously increased, the interface eventually becomes saturated due to accumulation of surfactant molecules. This leads to an increase in the unfavourable interaction between the hydrophobic tail of the surface active molecules and the polar water molecules. The phenomenon causes surfactant molecules to polymerise and form micelles, which are held together by the Van der Waals interaction, as the critical micelle concentration (CMC) is reached with enhanced concentration of the surface active molecules. Consequently, hydrophobic substances like fats are emulsified inside these micelles and this in turn allows the system to overcome instability via loss of energy[84].

Simultaneously, due to weak adsorption, the surfactant ions can diffuse across from the phase boundary to the bulk via weak diffusion and convection flow (figure 4.2)[85]. In the bulk phase, both micelles and monomers of the surfactant molecules exist in equilibrium. Micelles are however unstable species which means that they can release monomers and decompose in order to balance the number of monomers adsorbed at the interface. The whole cycle of surfactant adsorption and desorption as well as micellar assembly and demicellisation ensures

that the surfactant concentration remains constant at the phase boundary as well as in the subsurface layer and bulk solution (figure 4.2)[86].

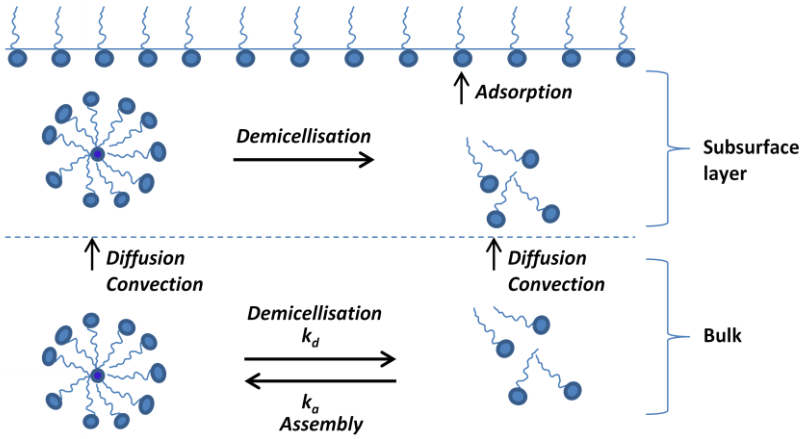

Figure 4.2: Role of the micelles and monomers in the kinetics of surfactant adsorption[52].

Where, k_a is the rate constant of assembly of micelles and k_d is the rate constant of micellar disassembly. The first models of micellar kinetics for homogeneous solutions were developed by Kresheck *et al*[88] and Aniansson and wall[89]. The models are based on fast and slow reactions of the micellar dynamics. The fast process involves exchange of monomers between the micelles and the surrounding solutions whereas the slow process encompass complete decomposition of the micelles to monomers[90]. From figure 4.2, it can be observed that the monomer concentration of the surfactant molecules in the bulk follows convective diffusion and therefore can be represented by equation 4.12[91].

$$\frac{\partial c_1}{\partial t} + V_X \left(\frac{\partial c_1}{\partial X}\right) = D \left(\frac{\partial^2 c}{\partial X^2}\right) + mk_d c_m - mk_a c_1^m \qquad \text{(eq. 4.12)}$$

Where, c_1 is the concentration of the monomer, X represent the solution surface, V_X is the *X* component of the mean mass velocity, c_m is the concentration of micelles, *m* is the aggregation number. On the other hand, micellar diffusion can be defined in term of the diffusion equation stated below (equation 4.13)[91].

$$\frac{\partial c_m}{\partial t} + V_X \left(\frac{\partial c_m}{\partial X}\right) = D_m \left(\frac{\partial^2 c_m}{\partial X^2}\right) + k_a c_1^m - k_d c_m \qquad \text{(eq. 4.13)}$$

Where, D_m is the diffusion coefficient of the micelles. During desorption, it is the charged hydrated part of the molecules which transfers across the interface from the aqueous to the

organic phase. This means that the Gibbs energy for the transfer of the hydrated moiety from water to the organic phase ($\Delta G^{o}_{tr,j}$) mainly influences the standard potential of desorption, ($\Delta\phi^{\emptyset}_{dp}$). The difference in the standard potential of adsorption ($\Delta\phi^{\emptyset}_{ad}$) and $\Delta\phi^{\emptyset}_{dp}$ is equivalent with the Gibbs energy for the adsorption of surfactant molecules from water to the interface ($\Delta G^{o}_{ad,W,j}$). The Gibbs energy for the processes of surfactant transfer, adsorption and desorption can be expressed in terms of equation 4.14[92].

$$\Delta G^{o}_{tr,j} = \Delta G^{o}_{ad,W,j} + \Delta G^{o}_{dp,Org,j} \qquad \text{(eq. 4.14)}$$

Where, $\Delta G^{o}_{dp,Org,j}$ is the Gibbs energy for desorption of the surface active ions from the interface to the organic phase. The $\Delta G^{o}_{dp,Org,j}$ term defines the Gibbs energy for the transfer of a hydrophilic head group which include a spacer chain and a segment of the long side chains from the water to the organic phase. The $\Delta G^{o}_{ad,W,j}$ term corresponds to the Gibbs energy for the transfer of the remaining side chains from the water to the organic phase of the phase boundary[92].

4.6 The effect of electrolytes on the surfactant/water and organic phase interface

The precipitation of ionic surfactants caused by the presence of salts such as the use of builders has been found to reduce the effectiveness of the detergent solution. This can be problematic for a wide range of applications including enhanced oil recovery process from high salinity reservoirs. In order to overcome this problem and to improve the salinity tolerance, mixtures of both non-ionic and anionic surfactants have been used in detergent formulations[93]. Kolev *et al.* however have shown that the addition of sodium chloride (NaCl) electrolyte to the solutions consisting of ionic surfactants such as sodium dodecyl sulphate (SDS) led to binding of the counterions to the oppositely charged head groups of the surfactant molecules. The counterions therefore act as a second surface active constituent which results in a significant decrease in the total surface electric charge[94]. Similar findings were also reported by Stellner and Scamehorn[95], both of whom observed crystal formation as a result of NaCl electrolyte cations and SDS ions (used above its CMC level) interacting and precipitating out in salt form in an equilibrated surfactant system. Although, a non-ionic surfactant, [$NP(EO)_{10}$] surfactant was also added above its CMC level to the solution consisting of the electrolyte and the anionic surfactant, the non-ionic surfactant was not integrated in the crystal structures[95]. Furthermore, the electrolyte and

the anionic surfactant was found to exist either as a monomer, in mixed micelles (for surfactant)/attached to the micelle surface (for electrolytes) or as a precipitate. The precipitation of the anionic surfactant-electrolyte counterion complex can be expressed by the following concentration based solubility product equation (equation 4.15):[95]

$$K_{SP} = [A^-]_{mon}\,[c^+]_u \qquad \text{(eq. 4.15)}$$

Where, K_{SP} is the concentration-based solubility product, $[A^-]_{mon}$ is the concentration of anionic surfactant monomer and $[c^+]_u$ is the concentration of the free electrolyte counterion. The above expression can be used to determine the amount of electrolyte required for the precipitation of a fixed concentration of surfactant. The equilibrium state of a system where the anionic surfactant molecules adsorb at the interface and subsequently, the electrolyte counterions interact with the anionic head-groups regardless of non-ionic surfactant adsorbing/not adsorbing at the phase boundary can be presented by the Stern isotherm (equation 4.17)[96].

$$\frac{\Gamma_2}{\Gamma_1} = \frac{K_{St}c_{2s}}{1+K_{St}c_{2s}} \qquad \text{(eq. 4.17)}$$

$$\text{and, } K_{St} = \frac{1}{Q_{12}} \qquad \text{(eq. 4.18)}$$

Where, Γ_1 is the total surface concentration of both anionic and non-ionic surfactants, Γ_2 is the surface concentration of the bound counterions, c_{2s} is the subsurface concentration of the counterions, K_{St} is the Stern constant and Q_{12} is the equilibrium constant of the reaction, demonstrating the association-dissociation equilibrium of the surfactant and the counterion in the bulk solution. as stated in equation 4.19[97].

$$c_1c_2 = Q_{12}c_{12} \qquad \text{(eq. 4.19)}$$

In the above equation, c_1 and c_2 are the concentrations of the surfactant ions and counterions, respectively. Following the work of Kolev *et al.* and Stellner *et al*, Mortada and co-workers reported that when a range of salts including NaCl, $NaNO_3$ (Sodium Nitrate) and Na_2SO_4 (Sodium Sulphate) at concentrations between 0.05-1 mol L^{-1} were added to the aqueous phase consisting of 0.05% (w/v) triton-x-114, it led to a decrease in the in the solubility and reduction in the cloud

point of the non-ionic surfactant due to competition for water between the poly(oxyethylene) chain and the hydrated salt ions. This in turn was found to cause precipitation of the dehydrated surface active and salt ions at the phase boundary as well as promote interaction between the precipitated interfacial electrolyte and surfactant ions, forming insoluble complexes[98]. This phenomenon is referred to as the 'salting-out effect' which can also occur as a result of desorption of ions from the hydrophilic segments of the micelles that consecutively enhances the interaction between micelles and thus, leads to precipitation of the surfactant molecules at the interface [98,99]. Nascentes *et al.* have further shown that the addition of > 9% m/v of NaCl to the Triton-X-100/SDS system significantly decreases the cloud point, even in the presence of an anionic surfactant. The triton-x-114/SDS surfactant system with NaCl salt was also found to endorse the secondary 'salting- out' effect of the electrolytes which was evident by the formation of precipitated electrolyte-surfactant complex at the interface[100]. The findings were reflected in the results obtained by *Gu et al.* for various surfactant systems including the triton-x-100/SDS system in the presence of salts such as NaCl and NaSCN (sodium thiocyanate) as well as the SDS/triton-x114 and CTAB (cetrimonium bromide)/triton-x114 systems with lanthanum (III) chloride ($LaCl_3$), magnesium chloride ($MgCl_2$), NaCl, potassium ferricyanide ($K_3Fe(CN)_6$), potassium sulphate (K_2SO_4) or potassium nitrate (KNO_3) electrolytes [101,102].

For two liquid phase system with electrolytes, where the organic solvent such as 1,2-DCE is partially miscible in water, solvent diffusion between the aqueous phase and the organic solution is likely to occur[103]. Consequently, this phenomenon can trigger the formation of a concentration gradient of water at the vicinity of the interface and lead to a decrease in the water coordination of the solute ions and, dehydrate the hydrate ions over a prolonged period of time. The electrostatic interaction between the dehydrated ions in turn can produce ion clusters/aggregates near the phase boundary which can promote the initiation of interfacial heterogeneous nucleation process and crystal growth[104,105]. This type of liquid-liquid crystallisation reaction was observed by Kitayama *et al*. using water/1-butanol system in the presence of salts such as NaCl and potassium chloride (KCl) and, by applying non-equilibrium molecular dynamics simulations[106]. It was also established that the crystallisation process initiated as a result of mutual diffusion between the water phase and the 1-butanol solution in turn provides the liquid-liquid system with the necessary motive force required for transforming the non-equilibrium system into its equilibrium state[107]. Furthermore, Hundhammer *et al.* demonstrated that the organic electrolyte tetraphenylborate (TPB^-) ions can react with silver ions (Ag^+) and form ion-pairs while both the metals ions and the hydrophobic electrolyte ions are electrochemically transferred across the water/nitrobenzene interface. The electrolyte-metal

ion complexes generated were then found to precipitate out and trigger interfacial nucleation process and film growth[108]. Cacote *et al.* also obtained similar findings when examining the transfer of Ag^+ by complex formation with tetrakis(4-chlorophenylborate ($TPBCl^-$) across the water/1,2-DCE interface using voltammetry technique at the micro-ITIES. Precipitation of $Ag^+/TPBCl^-$ complexes were detected in the form of a new peak using CV at a scan rate of 50 mV/s and within a potential range of -200 mV to 400 mV[109]. Kontturi *et al*, further established that the insoluble ion-pair formation and salting out effect of the hydrophobic ions at the ITIES can lead to a reduction in the polarisable potential range and thus, lower the formal potential of a variety of monovalent cations[110,111]. Moreover, ion pair association between the hydrophilic electrolyte cations i.e. K^+/Na^+ and the hydrophobic anions i.e. TPB^- ions at the interface, leading to rapid heterogeneous nucleation and crystallisation processes was initially observed by Barry in 2013 for various liquid-liquid systems, including the aqueous (0.1 M KCl)-1,2-DCE (20 mM TBATPB) and aqueous (3% NaCl (w/v))-1,2-DCE (10 mM TBATPB) systems with and without the addition of 10% (v/v) NH_4OH and 10% (v/v) NH_4OH with 15 mM Hydrazine[112]. The nucleation and the crystallisation reactions was reported to only occur in the presence of nuclei/precipitate at the interface and when high potentials of +0.6 V and +1 V were applied constantly to the above systems, respectively. It was also established that the whisker-like K^+TPB^- crystals were formed after applying potential for just 25 seconds whereas the N^+TPB^- crystallites were visible within 15 minutes after the potential was implemented. The whisker-like morphology of the crystals was seen to vary according to the type of cation present in the aqueous phase, which indicates that the crystallite form generated at the phase boundary may follow a cation-dependent growth mechanism. Moreover, using the H-NMR and SEM-EDX analysis it was identified that the crystals were mainly composed of TBATPB electrolyte as a result of interaction between excess the TBA^+ and TPB^- ions. Contrary to this, the CV and the potentiostatic measurements revealed that the crystallites are produced because of K^+/Na^+ and TPB^- ion interaction at the interface. The results therefore suggest that possibly a mixture of both K^+TPB^- /Na^+TPB^- crystal aggregates and TBA^+TPB^- complexes at the phase boundary are likely to trigger the heterogeneous nucleation and crystallisation processes[112].

4.7 Sodium dodecylbenzene sulphonate

Surfactant adsorption at the oil/water interface and the lowering of the interfacial tension plays an important role in controlling the desired interfacial properties in many practical applications. These range from large-scale industrial operations to small-scale household uses, such as

enhanced oil recovery, detergency and stabilisation of emulsions in food and cosmetic products. Sodium dodecylbenzene sulphonate (SDBS) can be represented generally by the following formula: $RC_6H_4SO_3H$, where, R is a long branched or straight chain fatty acid radical mainly dodecyl (figure 4.3)[113].

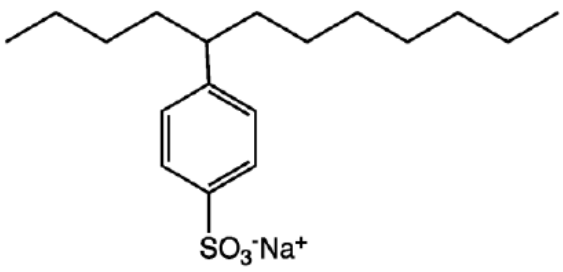

Figure 4.3: Chemical structure of SDBS[114].

It is the principal active ingredient in most household laundry detergents. The advantage of using this particular alkyl aryl sulphonate is that the ions are less subjected to hydrolysis and precipitation in the presence of multivalent ions in hard water. It acts as an excellent foaming agent and has a low order of toxicity[115,116].

4.8 Triton-x-114

Triton-x-114 is a non-ionic octylphenol ethoxylated surfactant with excellent wetting and detergency characteristics (figure 4.4)[117]. It is also less toxic, cost effective and commercially available at highly purified form. At low detergent concentrations, the non-ionic surfactant exists as monomers whereas at high concentrations both monomers and micelles are present in equilibrium. It has a cloud point of 23-26 ^oC[118].

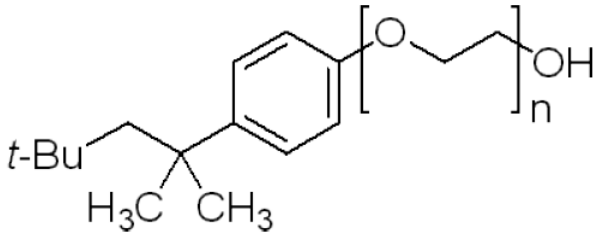

Figure 4.4: Chemical structure of Triton-x-114[118].

Triton-x-114 is homogeneous at cold temperatures however above a critical/cloud temperature it can undergo temperature induced phase separation and form an aqueous based two phase system with a surfactant depleted top phase and a surfactant enriched bottom phase[119].

4.9 Glycerol trioleate

Glycerol trioleate (GTO) has been chosen as the preferred oil in this study because it is one of the main triglycerides found in the vegetable and olive oil which are often used for cooking. GTO is a triester consisting of a trihydric alcohol, glycerol and three long chain fatty acids. The fatty acid in the oil is primarily oleic acid which is an 18-carbon unsaturated compound. The double bond in oleic acid has a cis configuration which makes the molecule bent in the center and therefore, it is unable to pack well into a crystal lattice (figure 4.5). Hence, oils such as GTO are a liquid at room temperature[120].

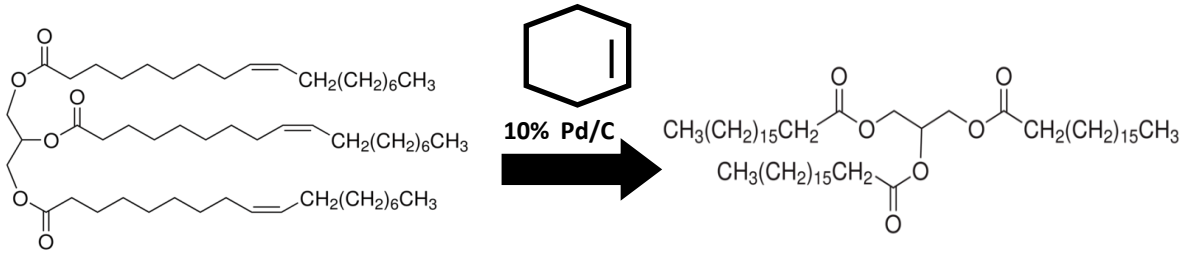

Glycerol trioleate
MW 885.47

Glycerol tristearate
MW 891.52

Figure 4.5: conversion of glycerol trioleate to glycerol tristearate via hydrogenation process[121].

This specific type of oil can exist in 3 types of polymorphic forms: α (melting point of -32 ^{o}C), β' (melting point of -12 ^{o}C) and β (melting point of -4.9 ^{o}C)[122]. GTO can be hydrogenated to a solid fat such as glycerol tristearate which is composed of trans double bonds and it tends to melt around the temperature of 70 – 75 ^{o}C[123].

Since a suitable electrolyte was not found to be soluble in GTO, 1,2-DCE was used as the alternative organic phase for electrochemical analysis. More information on 1,2-DCE can be found in the experimental methodology chapter.

4.10 Method/Techniques used

Below are a list of techniques and methods used for investigating the surfactant behaviour at the liquid-liquid interface.

4.10.1 Cyclic voltammery CV)

The CV in this study has been used to investigate the transfer and adsorption behaviour of the surface active ions at the interface. Scan rates from 10-100 mV/s was applied and a potential range from 0 – 0.5 V was used to detect the analyte. More information on this technique can be found in the experimental methodology chapter.

4.10.2 Chronoamperometry

The Chronoamperometry (CA) method was applied to confirm the transfer and adsorption behaviour of the surface active ions at the interface as detected using the CV technique. The potential was stepped up from 0 mV to 200 mV, 300 mV and 400 mV. More information on CA is included in the experimental methodology chapter.

4.10.3 Electrocapillary curve

The effect of voltage and surfactant concentration on the liquid-liquid interfaces as observed with CV and CA was also investigated using interfacial tension measurements, which was performed while simultaneously increasing the voltage from 0 V – 0.8 V at an interval of 0.2 V. The potential was kept constant for 100 seconds before the interfacial tension was obtained at equilibrium for each voltage applied. All measurements were performed at ambient temperature. More information on the electrocapillary curve measurements can be found in the experimental methodology chapter.

4.10.4 Conductivity

Conductivity measurements were obtained for the water-1,2-DCE/oil phase with and without electrolyte and with the addition of different concentrations of SDBS surfactant, to determine the mechanisms occurring at the interface. More information on conductivity is comprised in the experimental methodology chapter.

4.10.5 Optical microscopy

The optical microscopy technique has been applied to visually observe the increase in instability with increase in surfactant concentration at the oil/1,2-DCE-water interphase, with and without the addition of electrolyte. More information on optical microscopy can be located in the experimental methodology chapter.

4.11. Results and Discussion

4.11.1 Background electrolyte and reference ion transfer studies

Initial experiment was aimed to establish a potential range between 0 V-0.6 V. This was limited by the background electrolytes which are lithium chloride (LiCl) and tetrabutylammonium tetraphenylborate (TBATPB), transferring across from one phase to the other at the two extremes of the potentials (figure 4.6).

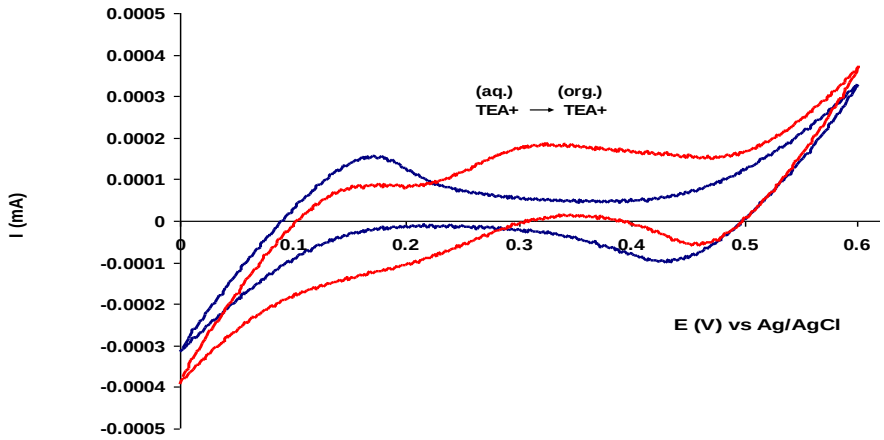

Figure 4.6: current versus potential graphs produced using CV for aqueous/LiCl – 1,2-DCE/TBATPB (blue coloured CV) and aqueous/LiCl/TEACl (tetraethylammonium chloride) – 1,2-DCE/TBATPB (red coloured CV) systems.[124]

From figure 4.6 – blue coloured CV (the LiCl and TBATPB system), it can be observed that when a forward potential was applied, a positive peak was formed within the potential range between 0.15 – 0.2 V indicating that the Cl^- ions were transferred to the aqueous phase while the TBA^+ ions were transported across the interface into the organic phase. As the potential was increased further to 0.6 V, the TPB^- ions were transferred from the 1, 2 – DCE phase to the aqueous phase and the Li^+ ions moved across from the aqueous to the organic solution. Following this, as the scan was reversed, TPB^- anions returned to the organic phase and Li^+ cations crossed back to the water phase which was specified by a negative peak at 0.45 V. In order to restore the charge balance, Cl^- ions were transferred from the aqueous phase to the organic phase and TBA^+ ions crossed over to the water phase as the potential was brought back to 0 V. The degree of interface polarisation is dependent on the potential differences of the ions in both the aqueous and organic phases[124]. The ion exchange between the two immiscible phases can only take place if the external potential applied provides the ions with the necessary Gibbs energy of transfer which is required for the charged species to move from one phase to

another. This transfer potential which leads to ion transfer across the interface is dependent on the charge, lipophilicity and diffusion coefficient values of the ions.

Furthermore, when a 2 mM of the TEACl was introduced into the aqueous phase of the water/LiCl – 1,2-DCE/TBATPB system, a current offset around 0.3-0.35 V was observed on the forward scan (figure 4.6 – red coloured CV). From the CV data, the standard transfer potential ($\Delta_o^w \phi_{TEA^+}^{\emptyset}$) for the TEA^+ ions transferring across from the water to the 1,2-DCE phase was determined to be 0.35 V. The Gibbs energy of transfer, $G_{tr}^{o',w\rightarrow DCE}$, for this system was estimated to be 2.7 KJ mol^{-1} using equation 4.20 stated below which is slightly higher than the literature value of 1.8 KJ mol^{-1} [125].

$$\Delta_o^w G_{tr}^{o',w\rightarrow DCE} = -z_i F \, \Delta_o^w \phi_i^{\emptyset} \qquad \text{(eq. 4.20)}$$

Where, z_i is the charge number, *F* is the Faraday constant (96,500 c / mol) and $\Delta_o^w \phi_i^{\emptyset}$ is the standard ion-transfer potential of ion, i. The standard ion transfer potential was determined to be 0.35 V from the voltammogram above (figure 4.6 - red coloured CV). The Gibbs energy of transfer is calculated based on the TATB and TPTB assumption which means that the standard potential for the transfer of one ion is related to another and all the ions involved have equal values, given that the ions have similar sizes[126].

4.11.2 Characterisation of anionic and non-ionic surfactants at the liquid-liquid interface

4.11.2.1 Cyclic voltammetry

The cyclic voltammograms (CVs) for the transfer of 0.5 mM – 17.97 mM of SDBS, 8.6 mM - 114 mM of triton-x-114 surfactant, 4.2 mM – 9.7 mM of P&G's Y (anionic) surfactant and 17 mM – 51 mM of P&G's N (non-ionic) surfactant across the 1,2-DCE-water interface with electrolytes were recorded using a potentiostat, at varying scan rates. For SDBS, an increase in current was observed with an increase in concentration below 1.5 mM. However, significant changes indicated by the presence of more prominent current spikes were observed when the SDBS concentration was increased to 1.5 mM (CMC point for SDBS), 8 mM (surfactant adsorption) and 13.4 mM (micellar emulsification). The changes in current at these concentrations were therefore discussed in this chapter. The current oscillations as observed with an increase in concentration of SDBS were found to completely disappear as the concentration of Triton-X-114 was enhanced to and above 8.6 mM. The current dissipation was clearly identified in the CVs for Triton-X-114 at concentrations of 48.1 mM, 83 mM and 114 mM, which have been included in

this chapter. Similar results as SDBS was also obtained using P&G's Y surfactant at concentrations of 4.2 mM (CMC point), 5.8 mM (surfactant adsorption), 6.2 mM (surfactant adsorption) and 9.7 mM (micellar emulsification). The current fluctuations disappeared when concentration of P&G's N surfactant was increased to and above 17 mM. A clear indication of the current augmentations disappearing was observed at 17 mM, 35 mM and 51 mM of P&G's N surfactant, which are discussed in this chapter.

4.11.2.2 SDBS

The CVs for the transfer of 0.5 mM – 17.97 mM of SDBS across the 1,2-DCE-water interface with electrolytes were recorded, at varying scan rates. It was observed that there was an increase in the current around 0.32 V with an increase in SDBS concentration from 0.5 mM – 0.8 mM when a scan rate of 50 mVs^{-1} was applied, indicating the transfer of SDBS ions across the 1,2-DCE-water phase boundary (figure 4.7).

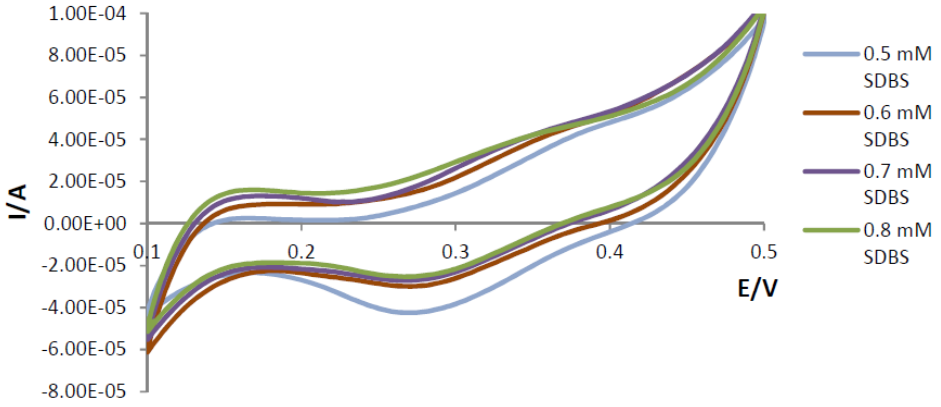

Figure 4.7: Cyclic voltammograms for 0.5 - 0.8 mM of SDBS added to the aqueous phase of the water-1,2-dce system with electrolytes, at a scan rate of 50 mVs^{-1}.

In this study, it was observed that as the concentration of SDBS was increased to and above the CMC level of 1.5 mM, an increase in current instability was identified using CV. From figure 4.8a, it can be seen that there is a dip around the 0.2 V region, in the positive scan, as 1.5 mM of SDBS was added to the aqueous phase and the potential applied approached the half wave potential of 150 mV for the transferring surfactant ions which is comparable to the $E_{1/2}$ value of 150 mV for sodium dodecylsulphonate (a similar surfactant)[21,22]. This suggests that the surfactant molecules are being adsorbed and accumulated at the interface leading to commencement of micellar formation. At 1.5 mM, the CMC point for SDBS is achieved so the onset of micellisation is very

feasible. Since the current instability was more pronounced at 1.5 mM, 8 mM and 13.4 mM of SDBS, the CVs for these specific concentrations are discussed in terms of the possible detergency mechanisms that might be occurring at the interface, in this chapter.

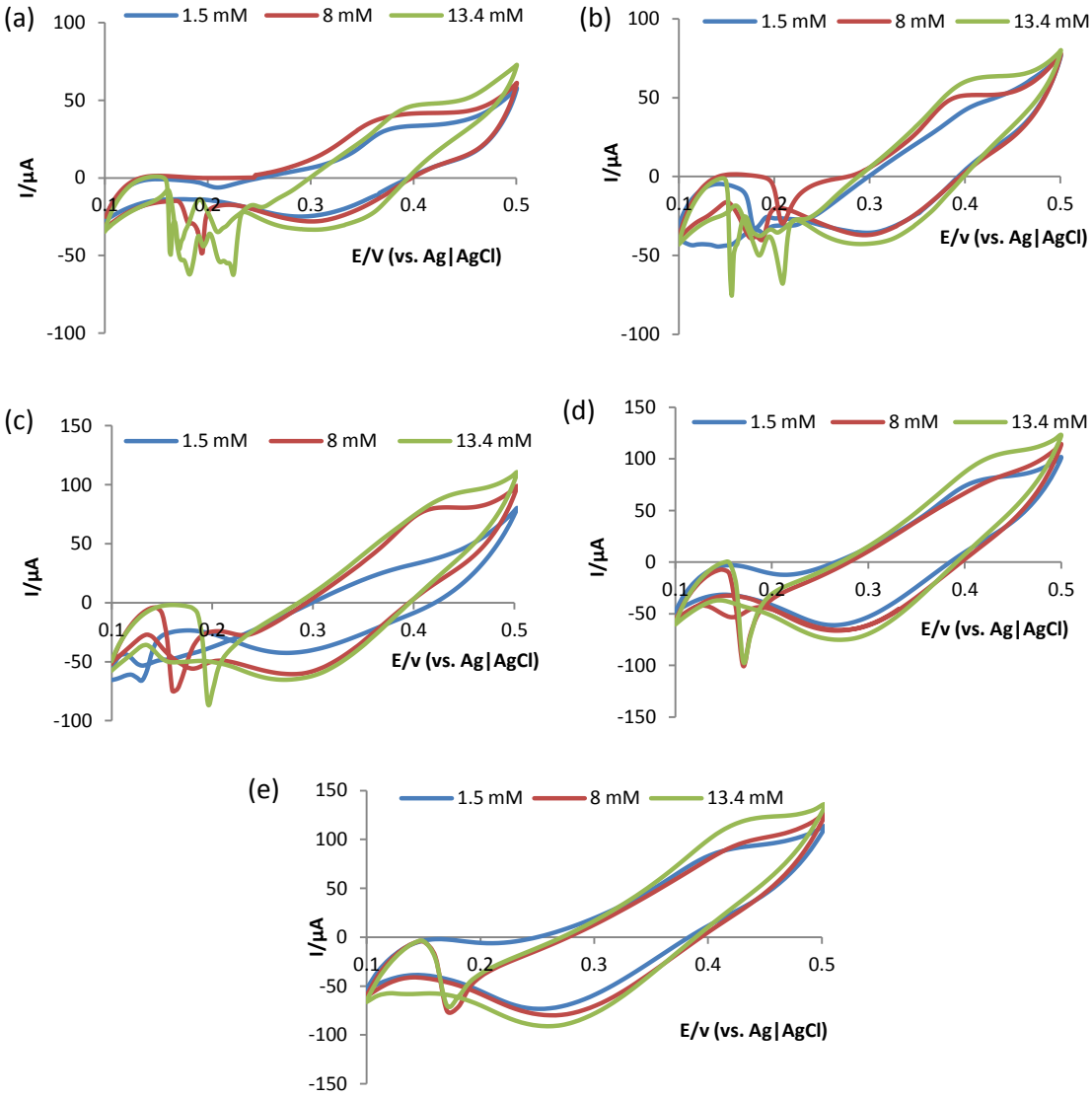

Figure 4.8: CVs showing the transfer and adsorption of 1.5 mM- 13.4 mM of SDBS surfactant, at the aqueous (with LiCl) and 1,2-DCE (with TBATPB) interface at a scan rate of (a) 10 mVs^{-1} , (b) 20 mVs^{-1}, (c) 50 mVs^{-1}, (d) 70 mVs^{-1} and (e) 100 mVs^{-1}.

Furthermore, a split peak was observed approximately at a potential of 0.18 – 0.19 V in the reverse scan for SDBS concentration of 8 mM, which possibly indicates aggregation of micellar droplets and onset of micellar emulsification at the phase boundary. On increasing the concentration of SDBS above 8 mM to 13.4 mM, it was observed that the split peaks were converted to chaotic oscillations. This signifies that further emulsification at the interface has

taken place. From the CVs, it can be observed that with an increase in concentration of the anionic surfactants, there is a potential and concentration - dependent adsorption and partitioning of the surface active ions at the liquid-liquid interface. Similar results were also observed for other scan rates ranging between 20 -100 mVs^{-1} (figures 4.8b-4.8e). The results obtained using CV were also found to be dependent on the scan rate. The oscillatory behaviour was more pronounced at lower scan rates (10 and 20 mVs^{-1}) whereas at higher scan rates (70 and 100 mVs^{-1}) the current spikes shifted towards the more negative potentials (less than 300 mV). A narrowing of the potential range from around 100 mV (at 10 mVs^{-1}) to 37 mV (at 100 mVs^{-1}) within which the irregular current occurred was also observed with increase in scan rate (figures 4.8a-4.8e). This scan rate dependency is clearly indicative of a time dependent surfactant adsorption and emulsification process at the interface. Furthermore, apart from the transfer, adsorption and partitioning behavior of the surfactant, other factors such as electrochemical instability and convective movement of the solution due to the Marangoni effect have been found to contribute to the current augmentations identified[127]. It can be also stated from the CVs that the unstable system overcomes the state as the phase boundary potential is brought outside the instability potential range.

4.11.2.3 P&G's Y Surfactant

An increase in interfacial instability with an increase in concentration was also identified when investigating the behaviour of P&G's Y surfactant at the aqueous (with LiCl) - 1,2-DCE (with TBATPB) interface. From figure 4.9, an increase in the current instability indicated by a large dip in the current at the forward scan and at a potential of 0.2 V was seen as the concentration of the surfactant was enhanced to 9.7 mM (above the CMC level). Two small irregular current oscillations were spotted at the potentials of 0.16 V and 0.21 V as the scan was reversed. The difference in the CV results obtained for SDBS and P&G's anionic surfactant is probably due to the Y surfactant consisting of a mixture of carbon chain lengths (ranging between C12-C14) as opposed to SDBS which is composed of a carbon chain length of C12.

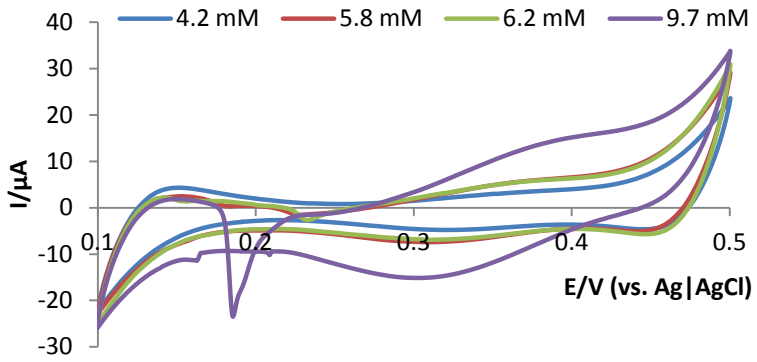

Figure 4.9: CVs obtained at a scan rate of 10 mV/s show the transfer and adsorption of 4.2 mM, 5.8 mM, 6.2 mM and 9.7 mM of P&G's Y (anionic) surfactant across the aqueous (with LiCl) and 1,2-DCE (with TBATPB) interface.

All of the data collected for the anionic surfactants using CV are similar to the results which were previously reported by Kakiuchi, who ascribed the chaotic behaviour to electrochemical instability, spontaneous emulsification and Marangoni effect, when a concentration of 0.5 mmol dm^{-3} of sodium dodecylsulphonate (similar surfactant to SDBS) was added to the aqueous phase of the water-1,2-DCE system with electrolytes[21]. However, in this study the anionic surfactants were added above the CMC point which demonstrated that micellar emulsification can also lead to irregular oscillations. The instability as identified in the results obtained is overcome when the potential excursion is scanned outside the instability range. Thus, confirming that the instability exists within a potential range (of approximately 100 mV width for the SDBS system and 25 mV for the Y surfactant system), in the region of the electrocapillary maximum and the standard ion transfer potential ($\Delta_O^W\phi$) of the surface active ions[128]. The mechanism of micellar emulsification occurring at the oil-water interface in the presence of anionic surfactants, which has not been reported to this date, is explored more in depth using other techniques such as conductivity, interfacial tension measurements and optical microscopy and the findings are discussed below.

4.11.2.4 Triton – X - 114

The addition of the non-ionic surfactant, triton-x-114, was found to suppress the chaotic behaviour observed with the SDBS anionic surfactant. It was seen that by gradually increasing the concentration of triton-x-114 from 8.6 mM to 114 mM in the water phase containing 13.4 mM of SDBS led to disappearance of the irregular current spikes (figure 4.10).

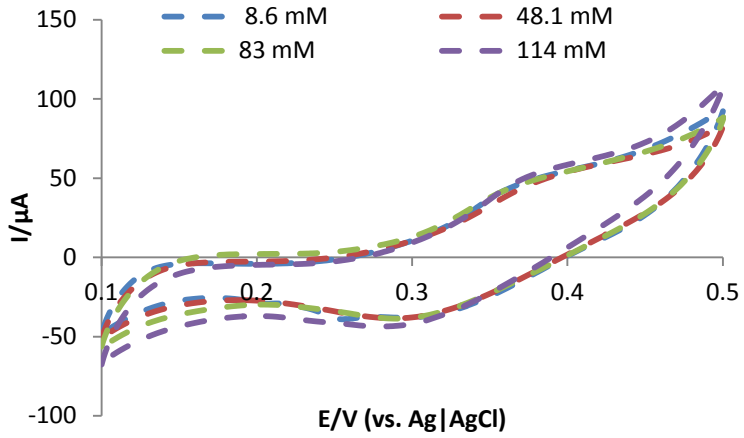

Figure 4.10: CVs for 8.6 mM- 114 mM of triton -x-114 obtained at a scan rate of 10 mVs^{-1}.

The shape of the CVs resembling that of expected for a reversible ion transfer reaction was clearly evident at the concentrations of 48.1 mM, 83 mM and 114 mM of triton-x-114 , at the scan rates ranging between 10-100 mVs^{-1} (figure 4.11a – 4.11e)[29].

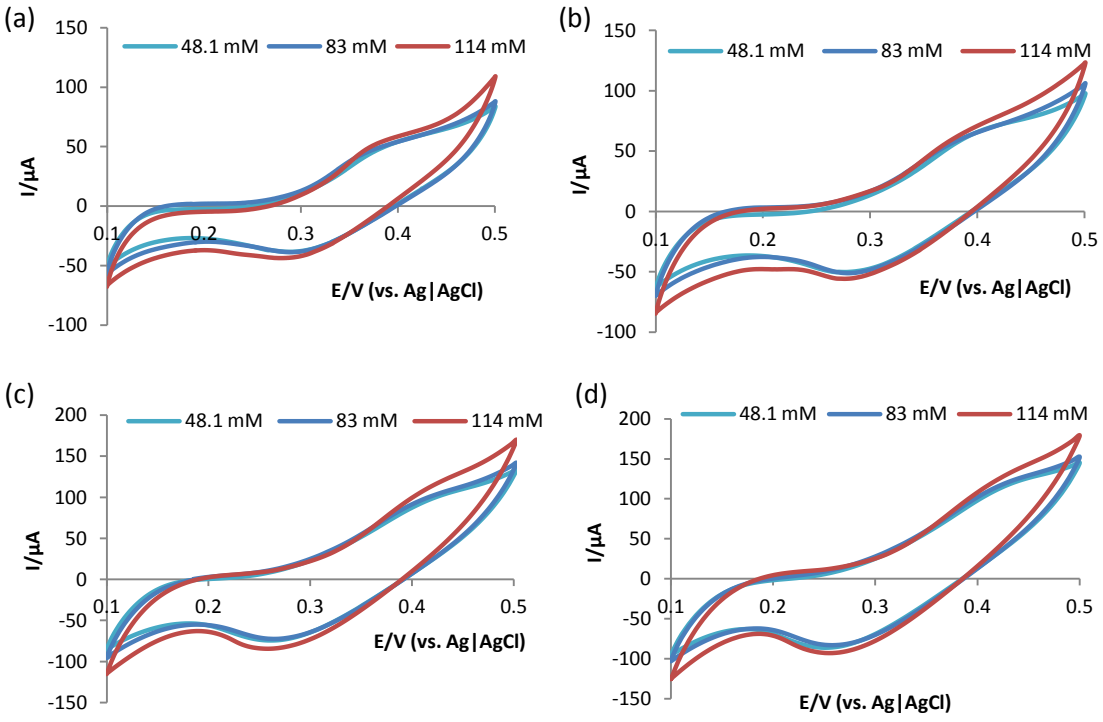

(e)

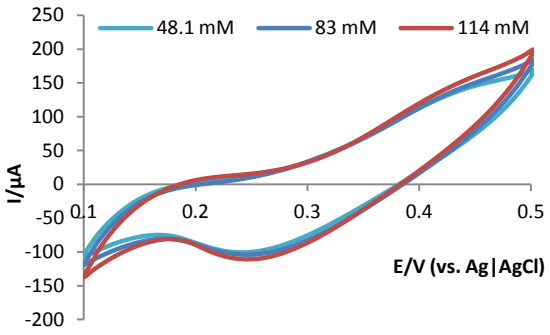

Figure 4.11: CVs for 48.1 mM, 83 mM and 114 mM of triton-x-114 obtained at a scan rate of (a) 10 mVs^{-1}, (b) 20 mVs^{-1}, (c) 50 mVs^{-1}, (d) 70 mVs^{-1} and (e) 100 mVs^{-1}.

4.11.2.5 P&G's N surfactant

A P&G branded non-ionic surfactant referred to as N surfactant, with carbon chain lengths ranging from C12-C14 was also investigated in a similar manner as the triton-x-114, by adding it to P&G's Y anionic surfactant (figure 4.12). As before, the instability completely disappeared when increasing concentrations of the N surfactant from 17 mM – 51 mM was used.

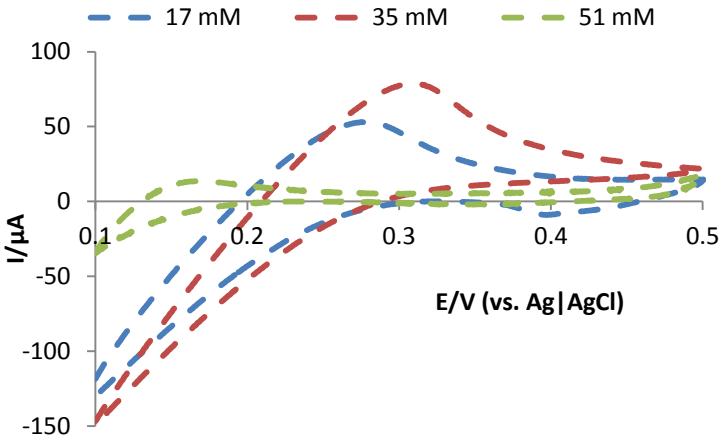

Figure 4.12: CVs for 17 mM – 51 mM of P&G's N (non-ionic) surfactant, at a scan rate of 10 mVs^{-1}.

The stabilisation of the interface observed is due to both, triton-x-114 and P&G's N surfactant adsorbing strongly at the phase boundary and forming a monolayer. Thus, preventing the hydrodynamic movement of the interface and halting the avalanche type transfer of the emulsion droplets. The findings coincided well with Samec and co-workers work on the effect of 10 mmol dm^{-3} of the non-ionic surfactant, sorbitan monooleate, on the suppression of chaotic currents[129,130].

4.11.3 Chronoamperometry (CA)

The presence of interfacial turbulences, indicating adsorption and the onset of emulsification when SDBS concentrations of 1.5 mM, 8 mM and 13.4 mM were added to the aqueous phase was confirmed using the potential –step chronoamperomtry (CA). As the SDBS concentration was increased from 1.5 mM - 13.4 mM, the instability enhanced at the aqueous/surfactant -1,2-DCE interfaces with electrolytes (figure 4.13). The CA potential was stepped from 0 mV to 300 mV and then, it was held at that potential continually for a period of time for each of the surfactant concentrations investigated (figure 4.13).

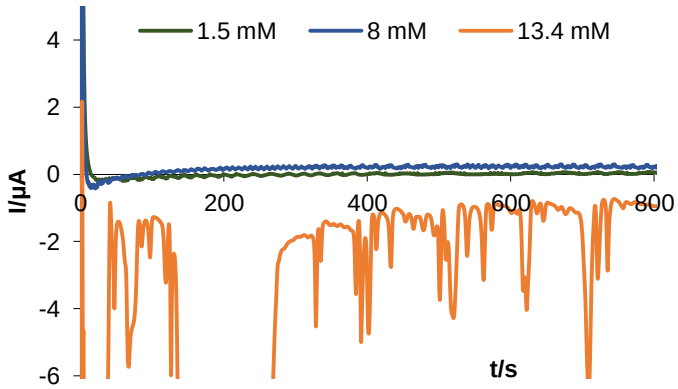

Figure 4.13: Current versus time transient obtained for 1.5 mM, 8 mM and 13.4 mM of SDBS added to the aqueous phase of the water (with LiCl)-1,2-DCE (with TBATPB) system, using CA.

The CA transient obtained as the potential was stepped to 300 mV, clearly showed emulsification effects dominating at a SDBS concentration of 13.4 mM. The results obtained using CA corroborates that the existence of unstable interface is over a limited range of potential difference as identified using the CV.

4.11.4 Conductivity measurements and presence of emulsion droplets

The conductivity measurements obtained for the aqueous/SDBS-1,2-DCE system with electrolytes (red line in figure 4.14) and SDBS surfactant were found to correspond well with the data obtained using CV and CA. It showed that there was a sharp increase in differential conductivity (dκ/dC) from 40 µS/mM to 200 µS/mM as the concentration of SDBS was enhanced to 1.5 mM (red line in figure 4.14 below). This is likely to be due to an increased number of anionic surface active ions being adsorbed at the interface and forming aggregates into micelles as the CMC point has been reached.

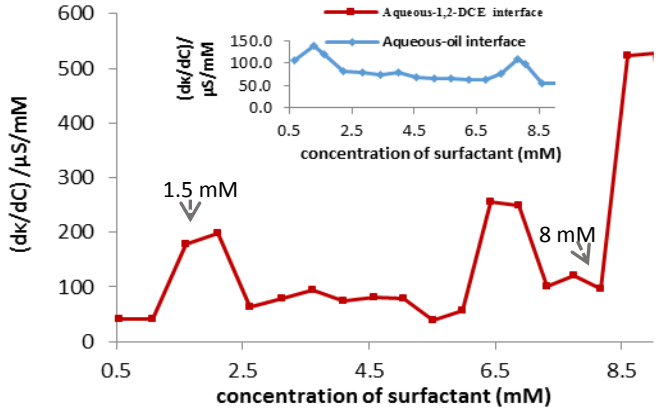

Figure 4.14: Conductivity measurements obtained for the aqueous (with LiCl)-1,2-DCE (with TBATPB) interface (red line) and GTO-water (with LiCl) interface (figure 4.14 inset – blue line). Where, the aqueous phase consists of SDBS.

Above 2.5 mM, the differential conductivity remained constant around 100 µS/mM. This is due to the presence of micelles. Micelles are larger than a monomer and therefore, diffuse slowly through the solution and acts as a less efficient charge carrier/weak electrolyte. Hence, the dκ/dC is significantly small [131]. However, as the concentration of SDBS was further enhanced to 6 - 7 mM, a peak was identified. Following this, a sharp rise in differential conductivity was also observed around 8.5 mM. The initial dκ/dC results obtained agreed with the data presented by Tyowua *et al.*[132], who have shown that in the presence of 5 mM KCl electrolyte and with an increase in the concentration of SDBS surfactant, the differential conductivity is highest at around 1 mM indicating that the CMC for SDBS has been reached. This was then followed by a steep decrease before leveling out due to presence of an increased number of micelles at concentrations of 1 mM – 5 mM. Furthermore, Smet *et al.*[133] has shown using the dynamic light scattering and the computer simulation techniques that the oil solubilisation and Ostwald ripening rate in emulsions of undecane (a liquid alkane hydrocarbon) is enhanced significantly as a result of increased number of micelles and with an increase in the concentration of the SDBS. Based on this finding, it can be suggested that above the CMC level and in the presence of micelles, the mass transport processes such as oil solubilisation and Ostwald ripening is enhanced at the phase boundary for both the water-1,2-DCE/oil systems examined. The conductivity findings therefore reflect that by increasing the concentration of SDBS generates an increased number of micelles which in turn causes faster emulsification and an increase in the size of the emulsion droplets via Ostwald ripening. This was also evident from the images of the emulsion droplets (figure 4.15) captured using the optical microscope, for both the

aqueous/SDBS-1,2-DCE and aqueous/SDBS-GTO systems with and without electrolytes. These phenomena occurring at the phase boundary are also likely to be contributing factors to the interfacial instability as observed using CV and CA.

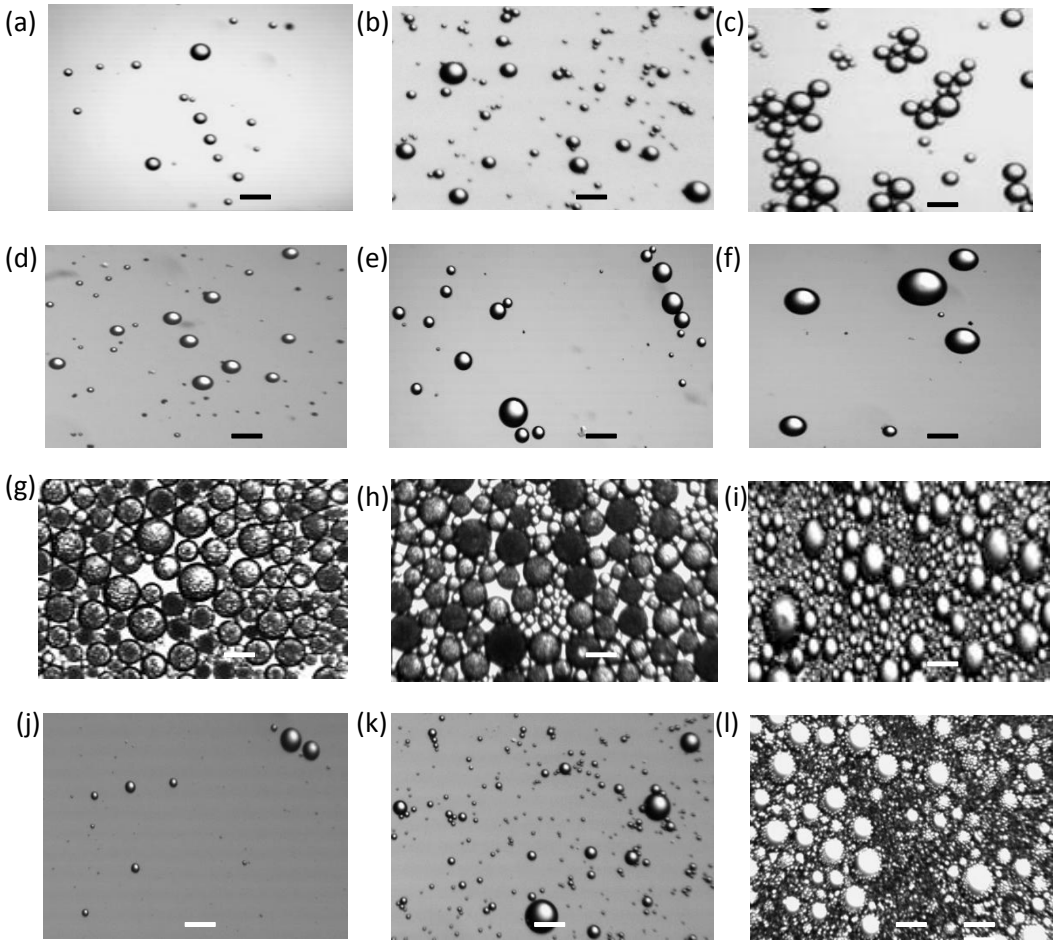

Figure 4.15: Optical microscope images of the emulsion droplets formed when SDBS concentrations of 1.5 mM (left), 8 mM (middle) and 13.4 mM (right) were added to the water phase of the aqueous-1,2-DCE system without electrolyte (a-c), aqueous-GTO system without electrolyte (d-f), aqueous-1,2-DCE system with electrolyte (g-i) and aqueous-GTO system with electrolyte (j-l). Scale bar 105.9 µm.

Furthermore, the addition of increasing concentrations of the SDBS surfactant to the aqueous phase of the GTO-water/electrolyte system (figure 4.14 – blue coloured inset) showed a similar trend as observed for the salt based aqueous/SDBS-1,2-DCE system. A small rise in the dκ from 0.5 mM – 2.2 mM (the CMC point) and between 7 mM - 8.5 mM due to the presence of micellar aggregates and emulsification was observed (figure 4.14 inset). The positions of the peaks for the aqueous with LiCl/SDBS-GTO system however were slightly shifted with increase in concentration of the surfactant compared to the aqueous/SDBS-1,2-DCE system with salts. For the aqueous

(with LiCl) - GTO system, the first peak appeared from 0.5 mM – 2.2 mM and the second peak was identified between 7 mM – 8.5 mM as opposed to 1 mM -2.5 mM and two additional peaks at 6 mM – 7.3 mM and 8 mM observed for the aqueous and 1,2-DCE system with electrolytes, respectively. This is probably due to the shift in the CMC point which in turn is dependent on the type of organic phase used.

4.11.5 Electrocapillary measurements

To further investigate the effect of voltage and surfactant concentration on the chaotic behaviour at the liquid-liquid interfaces, interfacial tension measurements were performed simultaneously with voltage changes on a polarised flat surface. An increasing concentration of the SDBS surfactant was added to the water phase of the aqueous (with LiCl) - 1,2-DCE (with TBATPB) and aqueous (with LiCl) - GTO systems while simultaneously for each concentration, the potential was increased from 0 V – 0.8 V at an interval of 0.2 V using a potentiostat. Each potential applied was kept constant for 100 seconds before the interfacial tension was measured at equilibrium. All measurements were performed at ambient temperature. A series of electrocapillary curves were then plotted for both the aqueous - 1,2-DCE and aqueous - GTO systems with electrolytes, as the SDBS concentration was varied between 0 mM – 13.4 mM. The electrocappilary curves for SDBS concentrations of 1.5 mM, 8 mM and 13.4 mM are included below (figures 4.16a and 4.16b) and compared with the data obtained using CV and conductivity measurements for the aqueous - 1,2-DCE and aqueous - GTO systems with electrolytes. In the electrocapillary plots (figure 4.16), $\Delta\gamma = \gamma_0 - \gamma_\infty$, where γ_0 is the interfacial tension of the interface without SDBS and applied potential (black dashed background curve) and γ_∞ is the interfacial tension following the application of potential and when the stabilisation is reached after 1 minute of adding different concentrations of the surfactant (blue and red coloured lines/curves).

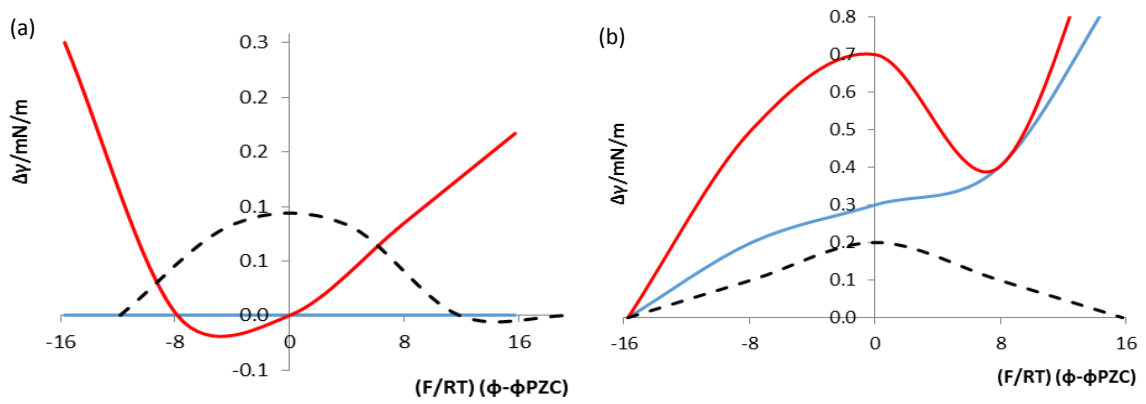

Figure 4.16: Electrocapillary curves showing a change in the interfacial tension against the potential applied for (a) aqueous (with LiCl) -1,2-DCE (with TBATPB) system and (b) GTO -water (with LiCl) system. Where, the aqueous phase consists of 1.5 mM (blue line) and 8 mM (red line) of SDBS. A background curve (dashed black line) representing the aqueous phase of the water-1,2-DCE/ GTO systems with electrolytes and no surfactant added was obtained for comparison.

A symmetric parabolic curve with a negative curvature (dashed black line, figure 4.16) and $\Delta\gamma_{max}$ of 0.1 and 0.2 mN m^{-1} at the point of zero charge, E_{PZC}, were observed in the absence of SDBS surfactant, for the aqueous (with LiCl) -1,2-DCE (with TBATPB) and aqueous (with LiCl) – GTO systems, respectively. The point of zero charge and the potential of electrocapillary maximum was established when a potential of 0.3 V was applied, for both the aqueous-1,2-DCE/GTO systems with electrolytes. At this point, the total amount of free charge in the bulk of adjoining phases i.e. water (w) and organic (o) is equal to zero, for the polarised aqueous (with LiCl)- 1,2-DCE (with TBATPB) and aqueous (with LiCl)- GTO interfaces and, therefore can be defined by the following: $\Gamma^{w,o}_{\mathrm{Li+\ TPB-}} = \Gamma^{o,w}_{\mathrm{Cl-\ TBA+}}$ [134]. The γ_0 obtained for the aqueous-LiCl/1,2-DCE-TBATPB system was 28.2±0.1 mN m^{-1} which is close to the literature value of 28.43±0.13 mN m^{-1} [135]. For the aqueous phase with LiCl/GTO system the γ_0 value measured was 17.3±0.1 mN m^{-1} compared to 31.08 mN m^{-1} for a GTO-saline water (Tris-hydrochloride, 150 mM Sodium chloride) interface[136,137]. For the latter system, the large variation in the interfacial tension is probably due to the type and the concentration of the electrolyte used. Lima *et al.* [138] has shown that when the concentration of NaCl was enhanced from 0-1.5 mol/L in the aqueous phase of the water-hydrocarbon oil system, the interfacial tension of the aqueous electrolyte solution also increased linearly.

Figure 4.16a shows the change in the interfacial tension with potential for the aqueous (with LiCl)/ 1,2-DCE (with TBATPB) system, on addition of the SDBS surfactant to the aqueous phase at concentrations of 1.5 mM (the CMC point) and 8 mM. At 1.5 mM of SDBS, a drastic change is observed with a flattening of the electrocapillary curve. Following this, a positive curve was seen to emerge with a dip shifted negatively to the E_{PZC} point for 8 mM of SDBS, showing the region of instability as the potential was increased between 0.2-0.4 V. At equilibrium, the polarised interface becomes unstable when 8 mM of the SDBS is introduced into the aqueous (with LiCl) -1,2-DCE (with TBATPB) system due to phase boundary potential-dependent partitioning and adsorption of the surface active molecules at the interface. The criterion for such unstable system can be therefore expressed as $(\partial^2\gamma/\partial\Delta_o^w\phi^2)_{T,P,\mu_j} > 0$, which indicate attainment of a positive γ value as a result of spontaneous emulsification and Marangoni effect.

The interfacial tension dip observed also indicates specific adsorption of the anionic surfactant at the interface alongside micellar emulsification. The instability at the phase boundary caused by the adsorption and partitioning effect of the surface active ions and the presence of micelles in turn is overcome by dissipating energy via emulsification and the avalanche type transfer of the emulsion droplets across the phase boundary. These phenomena are also possible causative factors for instability, generating a positive curvature as observed when 8 mM of SDBS was added to the aqueous (with LiCl)/ 1,2-DCE (with TBATPB) system and for producing negative values of the differential capacitance of the double layer in accordance with the Lippmann equation [64]. Beyond the SDBS concentration of 8 mM, the electrocapillary curve was found to be inconsistent and independent of the concentration of the surfactant due to interfacial emulsification.

It is interesting to note the differences between the aqueous (with LiCl)-1,2-DCE (with TBATPB) and aqueous (with LiCl)-GTO systems, where GTO is fully inert oil and there is no (concentration dependent or surface) potential against which the adsorption of electrolytes occur. Furthermore, from figure 4.16b it can be identified that on the addition of 8 mM of the SDBS no positive curvature could be seen as was observed for the aqueous-LiCl/1,2-DCE-TBATPB system (figure 4.16a). For the aqueous-LiCl/GTO system (figure 4.16b), the slope of the electrocapillary curve was seen to gradually increase in the negative potential region of the E_{PZC} until a potential of 0.3 V (E_{PZC}) was applied. At this point, a small dip in the interfacial tension was identified which was then followed by a steep rise in the interfacial tension, for both SDBS concentrations of 1.5 mM and 8mM, respectively. These observations probably indicate the onset of emulsification due to the adsorption of the surfactant molecules from the aqueous phase. The results obtained are reproducible and supported by the optical microscope images in section 4.11.6.

4.11.6 Optical Microscopy

Further qualitative studies were conducted using an optical microscope on the aqueous/SDBS-1,2-DCE and aqueous/SDBS- pure GTO systems with and without salts. An increase in the interfacial instability and emulsification was observed with an increase in the concentration of SDBS surfactant above the CMC level, for all systems (figures 4.17a-4.17d). However, the interfacial fluctuations were found to be more conspicuous in the presence of electrolytes (figures 4.17a and 4.17c). This indicates that the salts probably enhance the adsorption of the

SDBS surfactant and increases the rate of emulsification at the phase boundary, for both the aqueous-SDBS-1,2-DCE/GTO systems with electrolytes.

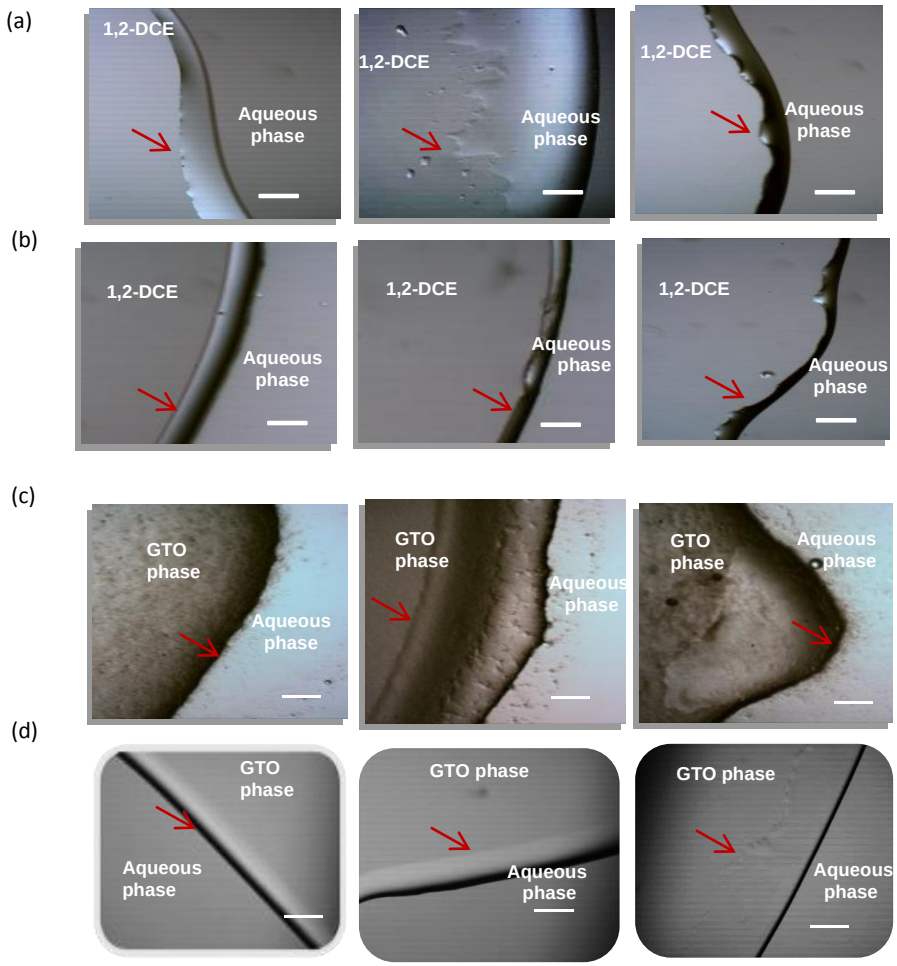

Figure 4.17: Microscope images obtained for the interface between (a) aqueous-1,2-DCE with electrolyte (b) aqueous-1,2-DCE without electrolyte (c) aqueous with electrolyte -GTO and (d) aqueous-GTO without electrolyte systems, after adding SDBS concentrations of 1.5 mM (left), 8 mM (centre) and 13.4 mM (right) to the aqueous phase. Scale bar: 43.4 µm. The microscope images presented are taken after 2 minutes since the addition of different concentrations of SDBS surfactant. The red arrow shows the location of the unstable expanded interface.

From further analysis of the microscopic images (figure 4.17), it can be suggested that the Marangoni effect resulting from the mass transfer and adsorption of solute ions at the phase boundary as well as the change in the interfacial tension induced by the concentration gradient[139] and the emulsification process seems to be more prominent in the presence of electrolytes and at the GTO/aqueous interface (Figures 4.17a and 4.17c). This is not unexpected as (1) the presence of electrolytes results in enhanced transfer of ions across the interface which

results in interfacial turbulence, (2) there is a larger difference in kinematic viscosity between the GTO/aqueous interface compared to the 1,2-DCE/aqueous interface, (3) the interfacial instability is more rapid in systems with lower interfacial tensions such as the aqueous-LiCl/GTO interface where the interfacial tension was measured to be 17.3 mN m^{-1} compared to 28.2 mN m^{-1} for the aqueous-LiCl/1,2-DCE-TBATPB system and (4) the presence of anionic surfactant leads to concentration dependent effect which is observed with increasing concentration of SDBS in the aqueous phase (figure 4.17),′ especially at 8 mM and 13.4 mM[139,50]. Additionally, a time dependent effect is also evident at longer time scales (i.e. after 10 minutes) irrelevant of the type of organic phase used (figures 4.18 and 4.19).

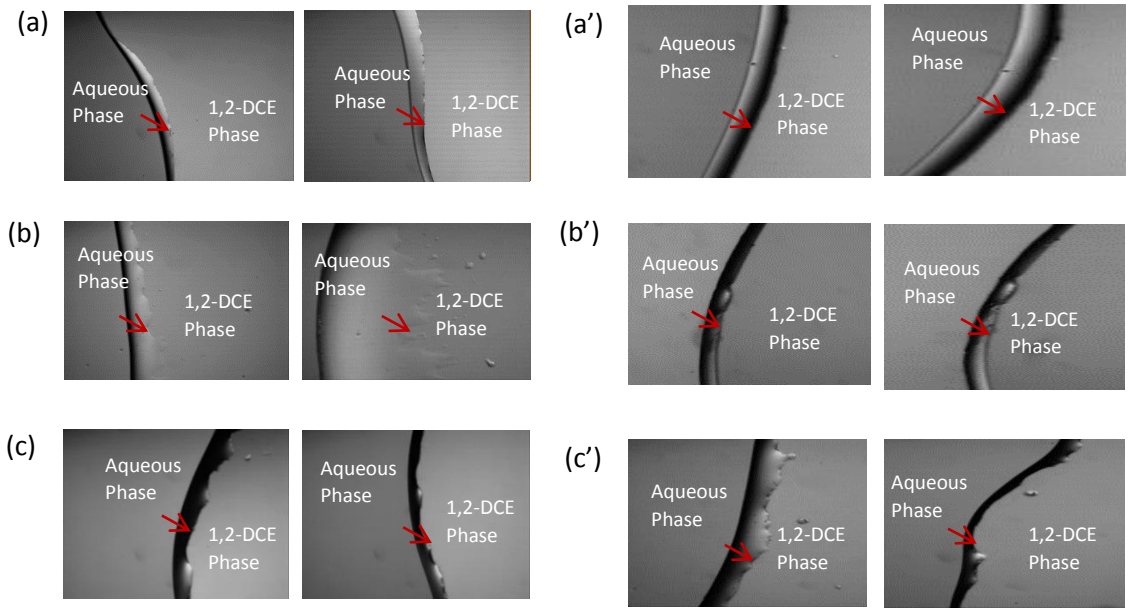

Figure 4.18: Optical microscope images captured after 2 minutes (left) and 10 minutes (right) at SDBS concentrations of (a/a') 1.5 mM, (b/b') 8 mM and (c/c') 13.4 mM for the aqueous (with LiCl)/ 1,2-DCE (with TBATPB) system (left hand side images) and the aqueous / 1,2-DCE system without electrolytes (right hand side images), respectively. The red arrow shows the location of the unstable expanded interface.

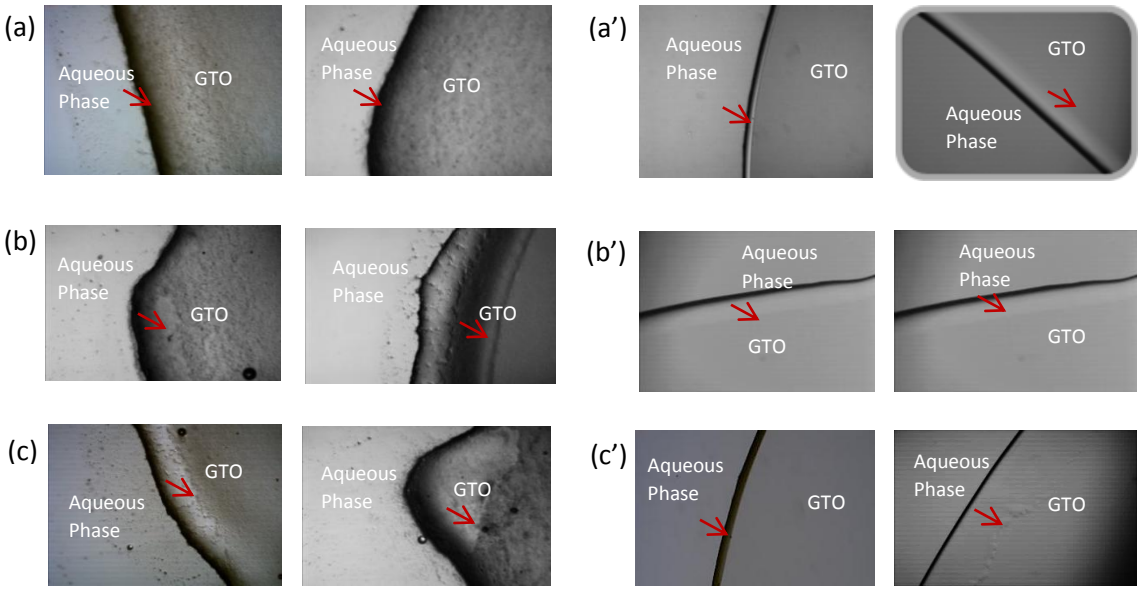

Figure 4.19: Optical microscope images captured after 2 minutes (left) and 10 minutes (right) at SDBS concentrations of (a/a') 1.5 mM, (b/b') 8 mM and (c/c') 13.4 mM for the aqueous (with LiCl)/ GTO system (left hand side images) and the aqueous (without LiCl)/ GTO system (right hand side images), respectively. The red arrow shows the location and the width of the unstable expanded interface.

Overall, it can be suggested that the optical microscopic findings obtained for the SDBS at concentrations of 1.5 mM, 8 mM and 13.4 mM correlated well with the instability results collected using the electrochemical methods, conductivity and electrocapillary measurements. It would be interesting to extend this study to investigate the effect of other factors such as the temperature, ionic strength and pH gradients.

4.11.7 Identification of interfacial crystal formation using optical microscopy

Further investigation of just the aqueous (with 10 mM LiCl) and 1,2-DCE (with 20 mM TBATPB) system using optical microscopy have shown rapid crystallisation at the interface without the need of external potential (figure 4.20a). It was also found that when the SDBS surfactant was added to the water phase of the aqueous (with LiCl) and 1,2-DCE (with TBATPB) system, it did not show any crystal formation however an increase in instability at the interface with an increase in anionic surfactant concentration was observed (figure 4.18).

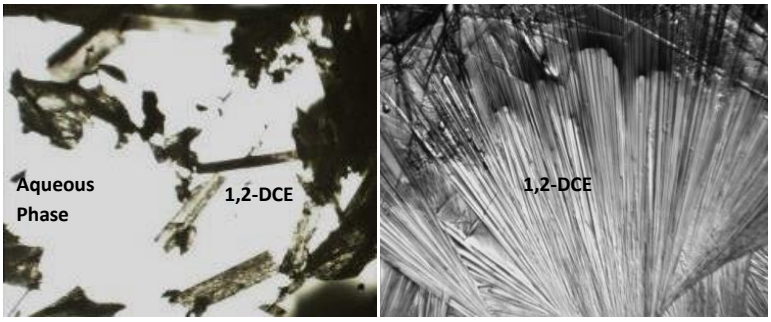

Figure 4.20: (a) powdery/needle-like crystals generated at the aqueous (with LiCl) and 1,2-DCE (with TBATPB) interface and (b) single needle crystals produced at the aqueous (with LiCl)/ triton-x-114/with and without SDBS and 1,2-DCE (with TBATPB) interfaces.

Contrary to figure 4.18, the addition of non-ionic surfactant, triton-x-114, to the aqueous phase of the aqueous (with LiCl and with/without the addition of SDBS) – 1,2-DCE (with TBATPB) system (figures 4.20b and 21) demonstrated that the phase boundary became more unstable and single needle-like crystals were formed at the interface. The crystals are probably produced due to interaction between the excess dehydrated $Li^+/Cl^-/TBA^+/TPB^-$ ions and in the presence of surfactants, fusion of anionic/non-ionic surfactant ions with the salt ions deposited at the phase boundary as a result of competition for water [140].

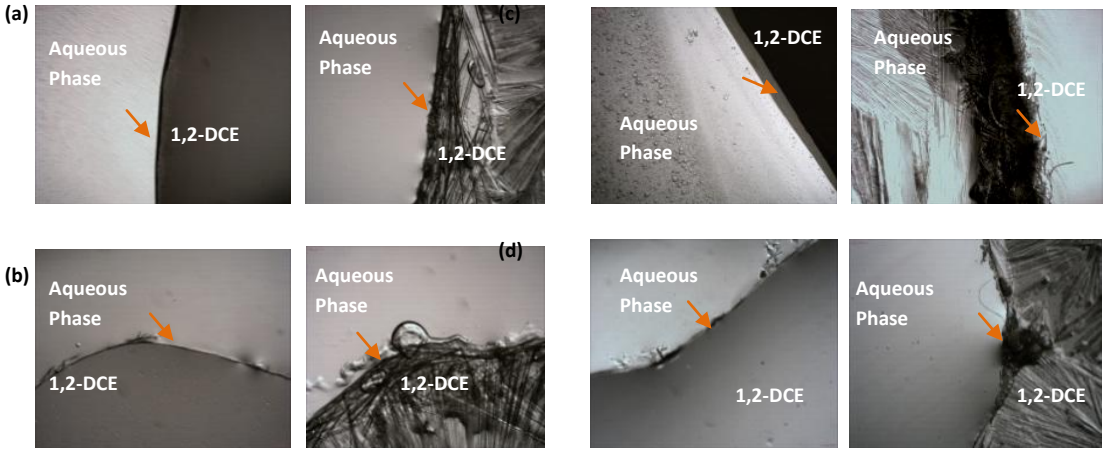

Figure 4.21: Optical microscope images captured for the aqueous (with LiCl)-1,2-DCE (with TBATPB) interface after 2 minutes (left) and after 10 minutes (right) of adding triton-x-114 at concentrations of (a) 48 mM, (b) 83 mM, (c) 114 mM and (d) 48 mM combined with 1.5 mM of SDBS. The orange coloured arrows show the location of the interface.

Moreover, the optical microscope images obtained for the aqueous/SDBS and/or triton-x-114 with electrolytes - GTO systems did not show presence of any crystallites. However, an increase

in the interfacial instability with an increase in the concentration of the surfactants was observed (figure 4.22). The phenomenon was found to be both concentration and time dependent.

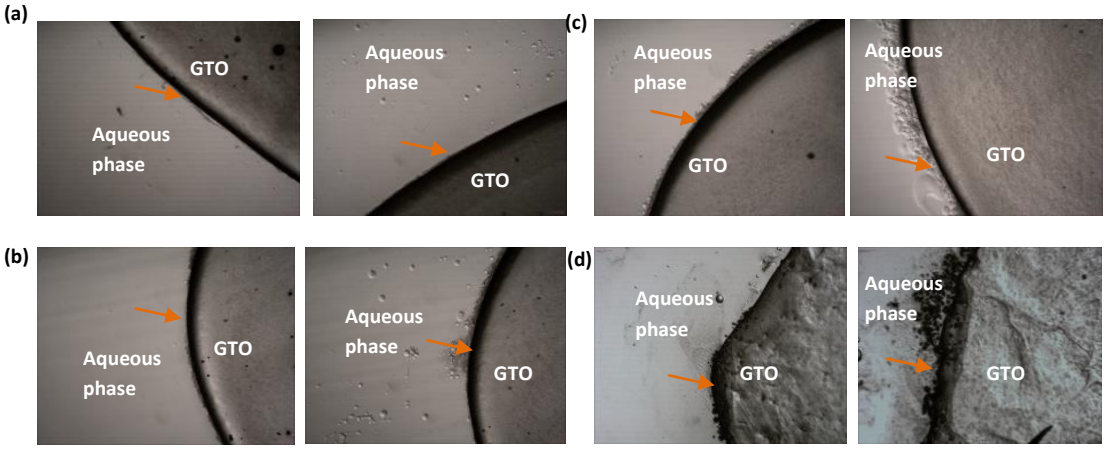

Figure 4.22: Optical microscope images captured for the aqueous (with LiCl)-GTO system after 2 minutes (left) and after 10 minutes (right) at triton-x-114 concentrations of (a) 48 mM, (b) 83 mM, (c) 114 mM and (d) 48 mM combined with 1.5 mM of SDBS. The orange coloured arrows show the location of the interface.

Similar results as SDBS/triton-x-114 was also obtained when P&G's Y and N surfactants were added to the aqueous -1,2-DCE/GTO systems with and without electrolytes. Interfacial instability was observed at the aqueous (with/without LiCl) -1,2-DCE (with/without TBATPB)/GTO interfaces as P&G's Y surfactant was added to the aqueous phase (figures 4.23 , 4.24 and 4.25).

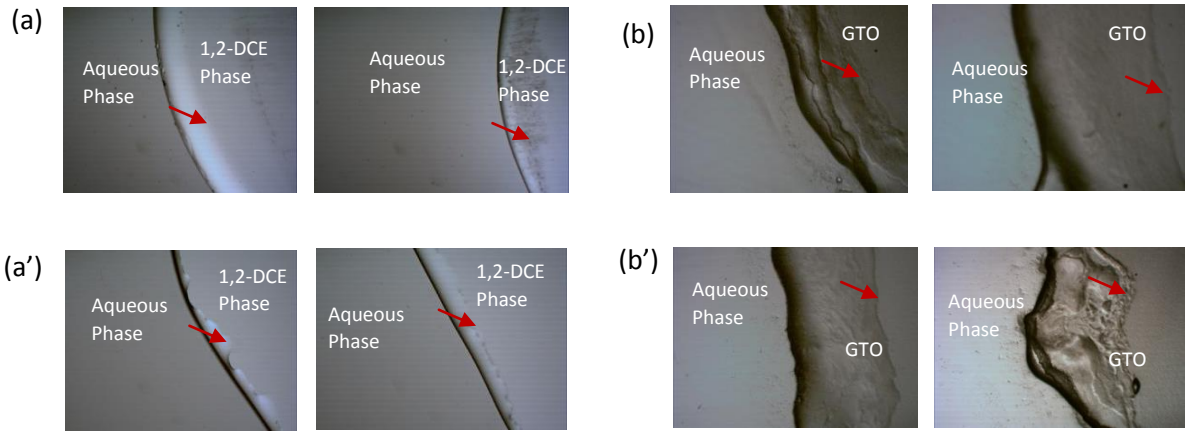

Figure 4.23: Optical microscope images captured after 2 minutes (left) and 10 minutes (right) of adding P&G's Y surfactant at a concentration of 4.2 mM for (a) the aqueous (with LiCl)/ 1,2-DCE (with TBATPB) system, (a') the aqueous / 1,2-DCE system without electrolytes, (b) the aqueous (with LiCl)/ GTO system and (b') the aqueous / GTO system without electrolytes, respectively. . The red arrow shows the location and the width of the unstable expanded interface.

The presence of crystals due to salting-out effect was however observed for only the aqueous (with LiCl)/P&G's N surfactant -1,2-DCE (with TBATPB) systems with and without the addition of P&G's Y surfactant (figures 4.24a and 4.25a).

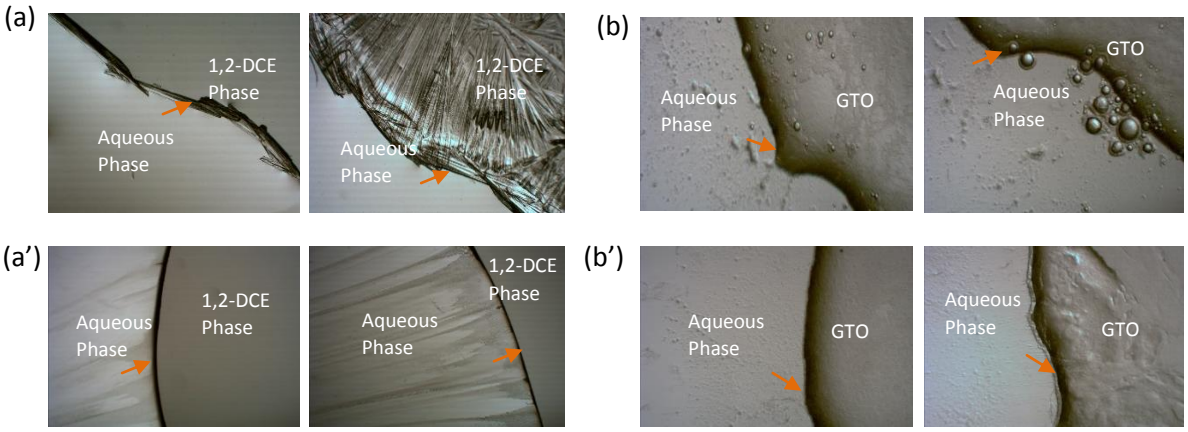

Figure 4.24: Optical microscope images captured after 2 minutes (left) and 10 minutes (right) at P&G's N surfactant concentration of 17 mM for (a) the aqueous (with LiCl)/ 1,2-DCE (with TBATPB) system, (a') the aqueous / 1,2-DCE system without electrolytes, (b) the aqueous (with LiCl)/ GTO system and (b') the aqueous / GTO system without electrolytes, respectively. The orange coloured arrows show the location of the interface.

The aqueous/P&G's N surfactant -1,2-DCE and the aqueous/P&G's Y and N surfactants -1,2-DCE systems without electrolyte did not show any interfacial crystal formation (figures 4.24b and 4.25b). Therefore, confirming that the crystallisation process is triggered by the precipitated salt ions and the reaction is promoted in the presence of surfactants because of ionic association between the precipitated non-ionic/ a mixture of anionic and non-ionic surfactant ions and salt ions at the phase boundary.

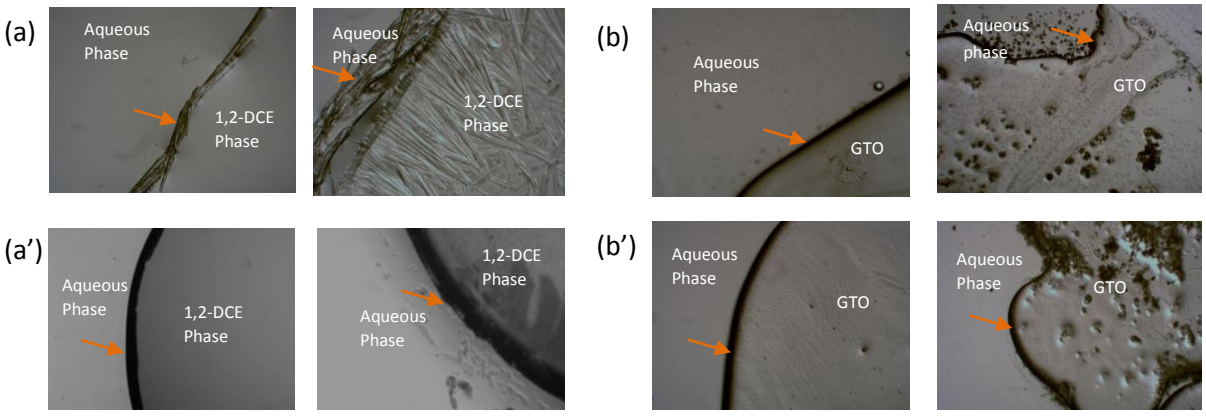

Figure 4.25: Optical microscope images captured after 2 minutes (left) and 10 minutes (right) at P&G's N surfactant concentration of 17 mM and P&G's Y surfactant concentration of 4.2 mM for (a) the aqueous (with LiCl)/ 1,2-DCE (with TBATPB) system, (a') the aqueous / 1,2-DCE system without electrolytes, (b) the aqueous (with LiCl)/ GTO system and (b') the aqueous / GTO system without electrolytes, respectively. The orange coloured arrows show the location of the interface.

4.11.8 Differential Scanning Calorimetry

In depth analysis of the interfacial crystal structures conducted using the Differential Scanning Calorimetry (DSC, appendix figure A1.1) have shown presence of a peak within the temperature range of 226.98 – 238.02 ^{0}C representing the TBATPB electrolyte [141]. Another unknown peak between 177.92- 184.56 ^{0}C was also identified for all of the crystal samples examined labeled as samples S1-S5 (see table 4.1 below and appendix figure A1.1), indicating formation of a new crystalline product which is composed of a mixture of ion-pairs (formed between the excess Li^{+}/Cl^{-} ions and the TBA^{+}/ TPB^{-} ions) and dehydrated surfactant chains. There is also a possibility that the surfactants added may promote faster crystallisation reaction at the phase boundary. The DSC analysis of SDBS (labelled as sample S6) have shown presence of three different peaks at 188.04, 233.40 and 244.76 ^{0}C (see table 4.1 below and appendix figure A1.1), out of which one of the peaks was found to overlap with the peaks that were identified for the crystal samples extracted from the aqueous/LiCl/triton-x-114 and 1,2-DCE/TBATPB system (sample S1), the aqueous/LiCl/SDBS/ triton-x-114 and 1,2-DCE/TBATPB system (sample S2), the aqueous/LiCl/P&G's N surfactant and 1,2-DCE/TBATPB system (sample S3), the aqueous LiCl/P&G's Y/ P&G's N surfactants and 1,2-DCE/TBATPB system (sample S4) and the aqueous/LiCl-1,2-DCE/TBATPB mixture (sample S5). However, since all of the samples consisted of TBATPB and are not composed of SDBS, it demonstrates that the peak within the range of 226.98 – 238.02 ^{0}C is likely to be due to the presence of hydrophobic salt.

Table 4.1: Showing the DSC peak positions and the melting points for the crystals formed at the aqueous (with LiCl) -1,2-DCE (with TBATPB) interface for samples S1-S5.

	Peak 1			
Samples	**Onset temperature/ ^{o}C**	**Max Peak temperature/^{o}C**	**End temperature/ ^{o}C**	**Change in temperature/ ^{o}C**
S1 (aqueous/LiCl/triton-x-114 and 1,2-DCE/TBATPB)	179.78	181.61	183.72	3.94
S2 (aqueous/LiCl/SDBS/ triton -x-114 and 1,2-DCE/TBATPB)	182.27	182.93	184.56	2.41
S3 (aqueous/LiCl/P&G's N surfactant and 1,2-DCE/ TBATPB system)	180.58	181.95	182.82	2.24
S4 (aqueous LiCl/P&G's Y/ P&G's N surfactants and 1,2-DCE/TBATPB system)	182.77	183.58	184.28	1.51
S5 (aqueous/LiCl-1,2-DCE/ TBATPB mixture)	177.92	179.55	184.24	6.32
	Peak 2			
S1	231.35	234.11	235.57	4.22
S2	227.13	232.03	233.93	6.8
S3	226.98	230.14	232.11	5.13
S4	228.86	231.26	233.45	4.59
S5	235.14	236.16	236.72	1.58

By analysing the DSC data (see table 4.1 below and appendix figure A1.1) for samples S1-S5 further, it can be evaluated that the melting points of the crystals for samples S1-S4 are enhanced by a factor of 2-5 ^{0}C compared to the melting temperature of sample S5 crystallites. The difference in the temperature is probably due to the variation in the composition of the crystals. The crystallites for samples S1-S4 probably consist of a mixture of surfactant ions and solute ions as opposed to the crystals extracted from sample S5, which are composed of just a combination of hydrophilic and hydrophobic salt ions.

4.11.9 Mass Spectroscopy

Examination of the crystal samples S1-S4 using the mass spectroscopy (MS) have shown presence of peaks at of mass of 251 atomic mass unit (amu) which was not detected for sample S5 (figure 4.26). This confirms the results obtained using the DSC that the non-ionic/a mixture of anionic and non-ionic surfactants may have been incorporated within the crystal structures. Hence, a different type of crystallite is produced comparing to the crystals extracted from sample S5.

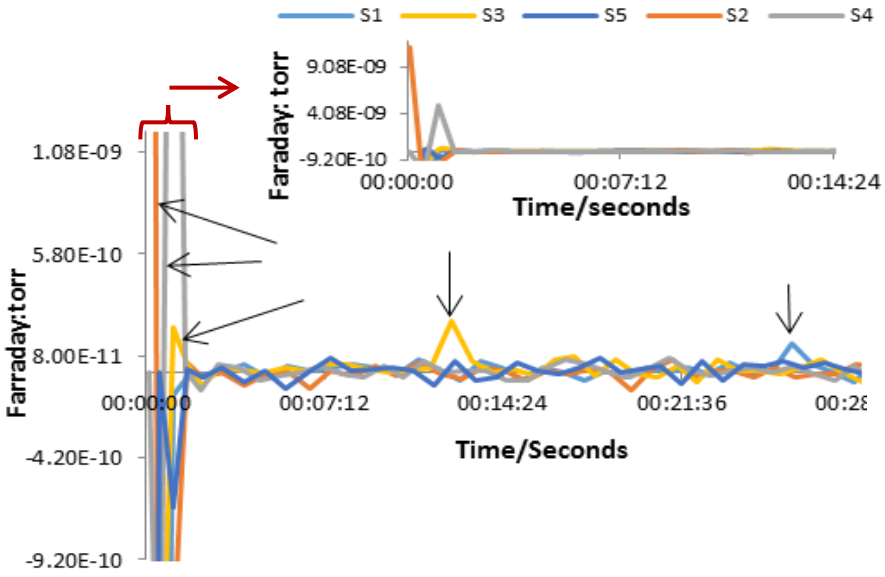

Figure 4.26: Mass spectra obtained for samples S1-S5, at a mass of 251 amu. The black arrows indicate where the peaks are formed. The inset shows close up view of the peaks detected for samples S2 and S4.

From evaluating the results obtained so far using the optical microscope, DSC and mass spectroscopy, it can be suggested that the interfacial crystals are likely to be one of the main factors which prevents the Marangoni-type movement of the phase boundary caused by the adsorption and emulsification processes in the presence of anionic surfactants[21] and therefore, this makes the interface stable.

4.11.10 Fourier transform infrared spectroscopy

The Fourier transform infrared spectroscopy (FTIR) technique was employed to identify the exact composition of the crystal structures. From analysing the FTIR data, it can be observed that both samples S1 (aqueous/LiCl/triton-x-114 and 1,2-DCE/TBATPB) and S3 (aqueous/LiCl/P&G's N surfactant and 1,2-DCE/TBATPB) displayed peaks specific to the non-ionic surfactants as observed for P&G's N surfactant (sample S8) and triton-x-114 when examined on its own (Sample S9) (figure 4.27). The peaks were displayed at the wavenumbers of 1232 cm^{-1}, 1624 cm^{-1}, 1740 cm^{-1} and 2915 cm^{-1} which were not present for sample S5 (aqueous/LiCl-TBATPB/1,2-DCE mixture). This demonstrates that the crystallites extracted from samples S1 and S3 are mainly composed of a fusion of non-ionic surfactant and solute ions.

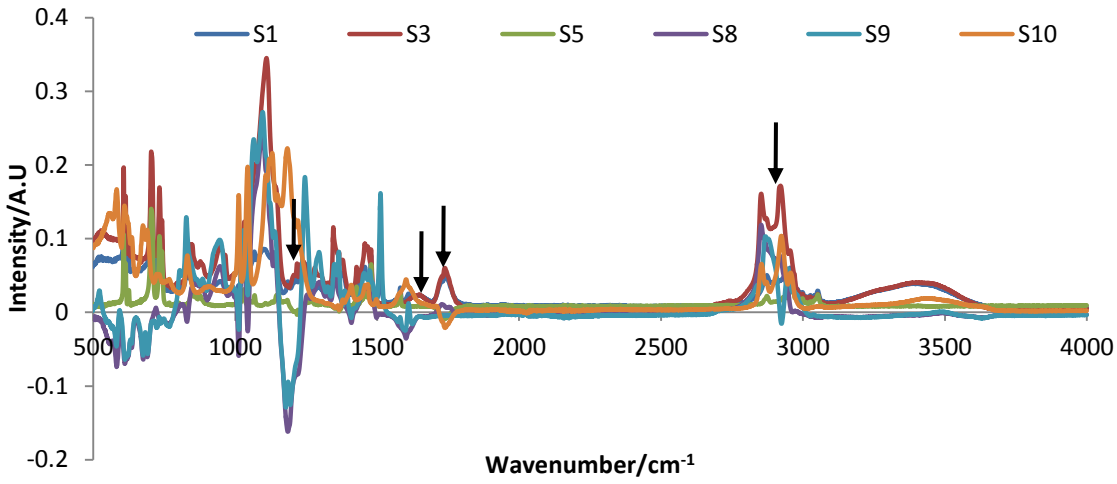

Figure 4.27: FTIR data for samples S1, S3, S5, S8, S9 and S10. The black arrows shows the similarities between sample S1 (aqueous/LiCl/triton-x-114 and 1,2-DCE/TBATPB) and sample S3 (aqueous/LiCl/P&G's N surfactant and 1,2-DCE/TBATPB).

FTIR Analysis of sample S2 (aqueous/LiCl/SDBS/ triton-x-114 and 1,2-DCE/TBATPB) also exhibited one of the peaks at 1624 cm^{-1} (figure 4.28) which represents the non-ionic surfactant, Triton-x-114 (sample S9). It is however unclear from the FTIR data whether or not the SDBS is incorporated within the crystal structures of sample S2, as the peaks representing SDBS (sample S6) were found to overlap with the peaks for the aqueous/LiCl-TBATPB/1,2-DCE mixture (sample S5).

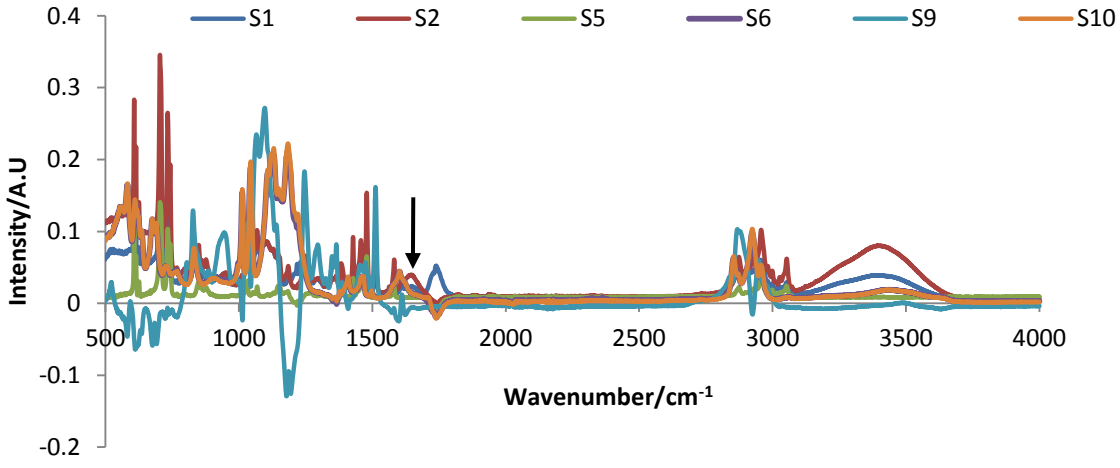

Figure 4.28: FTIR data for samples S1, S2, S5, S6, S9 and S10. The black arrow shows the peak observed for sample S1 (aqueous/LiCl/triton-x-114 and 1,2-DCE/TBATPB) and sample S2 (aqueous/LiCl/SDBS/Triton-x-114 and 1,2-DCE/TBATPB).

The FTIR work was extended to the aqueous/P&G's Y/ P&G's N surfactants and 1,2-DCE system with electrolytes (sample S4) (figure 4.29). However, the data showed that the peaks for P&G's Y (sample S7) and P&G's N surfactants (sample S8) overlapped with the peaks for TBATPB (sample S10) and the aqueous/LiCl-TBATPB/1,2-DCE mixture (sample S5). Thus, it is difficult to determine whether any or both of the surfactants are intertwined within the crystal structures of sample S4 (LiCl/P&G's Y/ P&G's N surfactants and 1,2-DCE/TBATPB system).

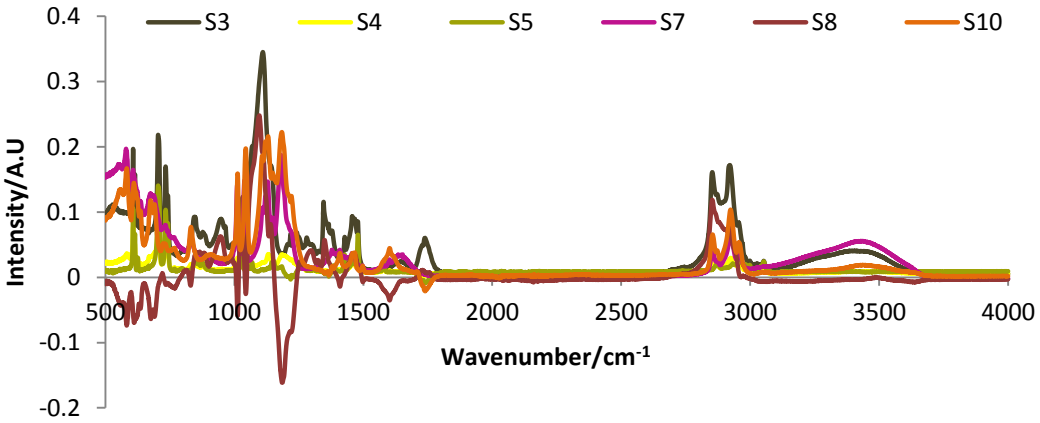

Figure 4.29: FTIR data for samples S3, S4, S5, S7, S8 and S10.

In order to attest the presence of surfactants within the crystallite structures, WAXS was used to undertake further examination on the crystal samples. The WAXS data (figure 4.30) showed that both samples S2 (aqueous/LiCl/SDBS/triton-x-114 and 1,2-DCE/TBATPB) and S4 (aqueous/LiCl/P&G's Y/N surfactants and 1,2-DCE/TBATPB) displayed an additional peak at 2θ value of 31.5/31.6 degree, which is specific to the non-ionic surfactants. However, new peaks at 2θ values of 46.5 and 51.3 degrees for sample S2 and, at 37 and 45.3 degrees for sample S4 were identified when compared to the other samples analysed (figure 4.30).

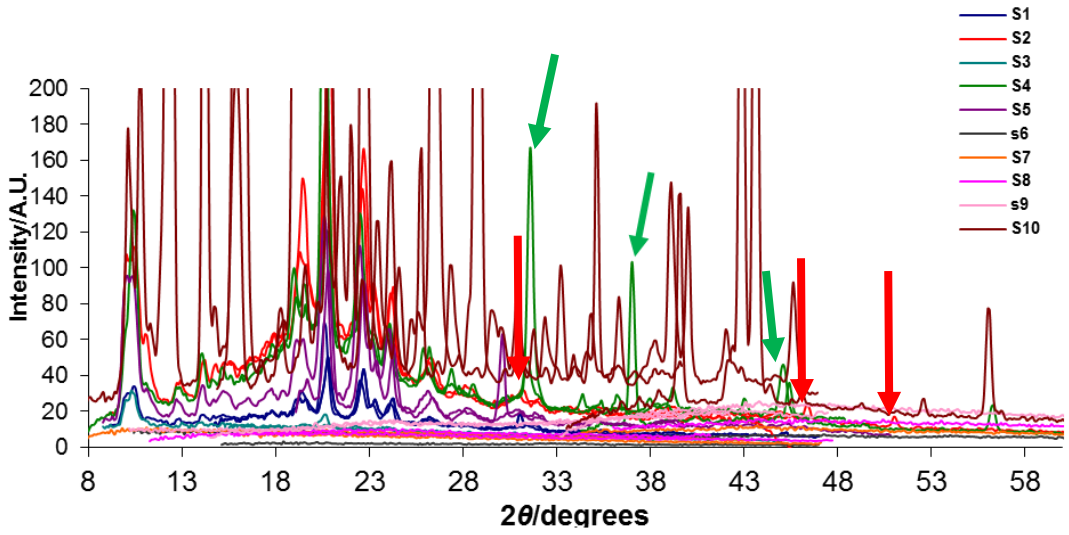

Figure 4.30: WAXS data for all of the crystal samples. The red arrows represent sample S2 (aqueous/LiCl/SDBS/triton-x-114 and 1,2-DCE/TBATPB) and the green arrows represent sample S4 (aqueous/LiCl/P&G's Y surfactant/ P&G's N surfactant and 1,2-DCE/TBATPB).

The new peaks identified for samples S2 and S4 could be because of a mixture of electrolyte and surfactant ions. The differences in the peak positions for both samples are likely to be due to the variation in the molecular structures of P&G's Y/N surfactants and the SDBS/triton-x-114 surfactants. It can be therefore concluded that the WAXS peaks detected coincide well with the results obtained using other techniques such as the DSC, MS and FTIR. By evaluating all the findings it can be concluded that the interfacial crystals are likely to be composed of precipitated electrolyte ions and dehydrated mixture of anionic and non-ionic surfactants.

4.12 Conclusions

The present work undertaken on the SDBS/water – 1,2-DCE/GTO systems using electrochemical techniques and optical microscopy has shown a concentration, time and potential dependent surfactant adsorption and emulsification instability phenomena. Electrochemical studies demonstrated that when the SDBS concentrations of 1.5 mM (CMC point), 8 mM and 13.4 mM were added to the aqueous phase of the water-1,2-DCE system with electrolytes, the reproducible interfacial turbulences were restricted to a limited potential region around the standard ion transfer potential of the surface active ions. The chaotic oscillations however were negated when increasing concentrations (from 8.6 mM – 114 mM) of triton-x-114 were added to the aqueous phase consisting of 13.4 mM of the SDBS surfactant. This was indicative by the reversible ion transfer CVs obtained upon addition of the non-ionic surfactant. Similar interfacial instability as observed with SDBS was also seen when increasing concentration of P&G's Y

(anionic) surfactant (from 4.2 mM – 9.7 mM) were added to the aqueous phase of the water (with LiCl) – 1,2-DCE (with TBATPB) system. The irregular oscillations disappeared when 17 mM – 51 mM of P&G's N (non-ionic) surfactant was added to the aqueous phase composed of P&G's Y surfactant. The electrochemical results obtained for the anionic and non-ionic surfactants above the CMC level, coincided well with the findings reported by Kakiuchi using similar surfactants. Kakiuchi has stated in several papers that the chaotic oscillations caused by the addition of anionic surfactants to the water phase of the aqueous-1,2-DCE interface with electrolytes, as observed using electrochemical techniques were due to surfactant adsorption, spontaneous emulsification and transfer of emulsion particles. However, the electrochemical work undertaken using SDBS and P&G's Y surfactant have demonstrated that above the CMC level micellar emulsification is also a major contributing factor which leads to interfacial instability. In order to confirm the finding other methods and techniques such as conductivity, interfacial tension measurements and optical microscopy were employed.

The simple conductivity measurements and electrocapillary curves have revealed that above the concentration of 8 mM, due to an increased number of micelles and enhanced rate of micellar emulsification, the instability becomes independent of the SDBS concentration and indicates that this phenomenon is closely associated with micellisation and emulsification at the non-polarised interface. Contrary to this, a correlation is observed between the increase in the current with no irregular oscillations and the SDBS surfactant concentration below the CMC point of 1.5 mM. Similar findings to the latter result were reported by Kakiuchi and the co-workers and that the current instability increases with an increase in the concentration of the anionic surfactants such as the alkanesulphonate sodium salts[21]. The increase in the interfacial instability and the presence of emulsion droplets as a result of micellar emulsification at SDBS concentrations of 1.5 mM, 8 mM and 13.4 mM, was visually evident from the optical microscopic images obtained for both the water-1,2-DCE/oil systems with and without electrolytes. However, the interfacial instability was observed to be more pronounced in the presence of electrolytes which indicate salts promote a faster rate of surfactant adsorption and emulsification at the phase boundary comparing to the aqueous-1,2-DCE/GTO systems without salts.

Furthermore, analysis of the aqueous (with 10 mM LiCl) -1,2-DCE (with 20 mM TBATPB) system with and without surfactants using an optical microscope, DSC, MS, FTIR and WAXS have demonstrated presence of crystals at the phase boundary, which are mainly composed of dehydrated salt ions along with surfactant ions (when surfactants are added to the system). Barry *et* al. [112] for aqueous (0.1 M KCl)-1,2-DCE (20 mM TBATPB) system and aqueous (3% NaCl

(w/v))-1,2-DCE (10 mM TBATPB)) system have found that ion pair formation between excess precipitated K^+/Na^+ and TPB^- ions or TBA^+ and TPB^- ions at the interface is probably the cause for crystal formation. However, the major difference between the two systems is that Barry and the co-workers observed presence of crystals at the phase boundary only when a high potential was applied as opposed to the crystals detected at the aqueous (with 10 mM LiCl) -1,2-DCE (with 20 mM TBATPB) interface with/without surfactants in the absence of external potential.

In this study, it was also observed that in the presence of anionic surfactants at the aqueous (with/without LiCl) -1,2-DCE (with/without TBATPB)/oil interfaces, the instability increased with an increase in concentration of the SDBS/P&G's Y surfactants however no crystals were detected at the phase boundary. Contrary to this, both crystal formation and an increase in the interfacial instability with increase in concentration of the non-ionic surfactants were seen for the aqueous/LiCl -1,2-DCE/TBATPB system with triton-x-114 and P&G's N surfactant with and without the addition of SDBS/P&G's Y surfactants. The initiation of the crystallisation reaction at the phase boundary is likely to be due to competition for water between the salt ions and the dehydrated poly(oxyethylene) chains of the non-ionic surfactants, as the electrolytes lead to a reduction in the solubility and cloud point of the surfactants [99]. The formation of clusters at the interface as a result of ionic association between the precipitated surfactant/micelles and electrolyte ions can cause a sufficient decrease in the interfacial Gibbs energy which in turn promotes the occurrence of heterogeneous nucleation and crystallisation processes at the phase boundary[142]. The microscopic images and the data obtained using the MS, DSC and WAXS for samples S2 (aqueous with LiCl/ SDBS/triton-x-114– 1,2-DCE with TBATPB) and S4 (aqueous with LiCl/ P&G's Y/P&G's N surfactants – 1,2-DCE with TBATPB) have overall shown that the crystallites are composed of a mixture of surfactants and salts. This was probably due to the addition of non-ionic (triton-x-114/P&G's N) surfactants to the aqueous phase consisting of anionic (SDBS/P&G's Y) surfactants increasing the competition for water between the anionic surfactant head groups, the non-ionic surfactant chains and the salt ions. Thus, the interaction between the dehydrated surfactant ions and the electrolyte ions initiated the nucleation and crystalline growth process at the phase boundary.

It can be therefore concluded that this phenomenon was only observed with the use of 1,2-DCE solvent as the organic phase and not with the oil phase, which indicate that both the anionic and non-ionic surfactants investigated can be used for detergency application and the effectiveness of the surfactants in removing soil remains unaffected in the presence of other salt based ingredients such as builders which are used in detergent.

4.13 References

1. Carr, C. *Chemistry of the Textiles Industry*. (Springer Science & Business Media, 2012).
2. *Succinates—Advances in Research and Application: 2013 Edition: ScholarlyBrief*. (ScholarlyEditions, 2013).
3. Manning, F. S., (Ph.D.), R. E. T. & Thompson, R. E. *Oilfield Processing of Petroleum: Crude oil*. (PennWell Books, 1995).
4. Tadros, T. F. *Applied Surfactants: Principles and Applications*. (John Wiley & Sons, 2006).
5. Stokes, R. J. & Evans, D. F. *Fundamentals of Interfacial Engineering*. (John Wiley & Sons, 1997).
6. *Trends in Colloid and Interface Science X*. **100,** (Steinkopff, 1996).
7. Hartel, R. W. & Hasenhuettl, G. L. *Food Emulsifiers and Their Applications*. (Springer Science & Business Media, 2013).
8. Hettiarachchy, N. S., Sato, K., Marshall, M. R. & Kannan, A. *Food Proteins and Peptides: Chemistry, Functionality, Interactions, and Commercialization*. (CRC Press, 2012).
9. Gavach, C. in *Biological Aspects of Electrochemistry* (eds. Milazzo, G., Jones, P. E. & Rampazzo, L.) 321–331 (Birkhäuser Basel, 1971). at <http://link.springer.com/chapter/10.1007/978-3-0348-5848-9_28>
10. Gavach, C., Seta, P. & Henry, F. A Study of the Ionic Transfer across an Aqueous Solution Liquid Membrane Interface by Chronopotentiometric and Impedance Measurements. *Bioelectrochem. Bioenerg.* **1,** 329–342 (1974).
11. Gavach, C. & Henry, F. Chronopotentiometric investigation of the diffusion overvoltage at the interface between two non-miscible solutions: I. Aqueous solution-tetrabutylammonium ion specific liquid membrane. *J. Electroanal. Chem. Interfacial Electrochem.* **54,** 361–370 (1974).
12. Samec, Z., Mareček, V. & Weber, J. Charge transfer between two immiscible electrolyte solutions. *J. Electroanal. Chem. Interfacial Electrochem.* **100,** 841–852 (1979).
13. Koryta, J. Electrochemical polarization phenomena at the interface of two immiscible electrolyte solutions. *Electrochimica Acta* **24,** 293–300 (1979).
14. Koryta, J. *et al.* A new model of membrane transport: Electrolysis at the interface of two immiscible electrolyte solutions. *J. Electroanal. Chem. Interfacial Electrochem.* **116,** 61–68 (1980).
15. Koryta, J. Theory and applications of ion-selective electrodes. *Anal. Chim. Acta* **183,** 1–46 (1986).

16. Koryta, J., Vanýsek, P. & Březina, M. Electrolysis with electrolyte dropping electrode: II. Basic properties of the system. *J. Electroanal. Chem. Interfacial Electrochem.* **75,** 211–228 (1977).
17. Amemiya, S. *et al.* Electrochemical Sensing and Imaging Based on Ion Transfer at Liquid/Liquid Interfaces. *Electrochimica Acta* **110,** (2013).
18. Kihara, S., Suzuki, M., Maeda, K., Ogura, K. & Matsui, M. The transfer of anions at the aqueus/organic solutions interface studied by current-scan polarography with the electrolyte dropping electrode. *J. Electroanal. Chem. Interfacial Electrochem.* **210,** 147–159 (1986).
19. Ogura, K., Kihara, S., Suzuki, M. & Matsui, M. Ion transfer at the interface between an aqueous solution in the presence of concentrated salts and an organic solution studied by polarography at the electrolyte solution dropping electrode. *J. Electroanal. Chem.* **352,** 131–151 (1993).
20. Ogawa, T., Shimazaki, H., Aoyagi, S. & Sakai, K. Novel modeling of electrical potential oscillation across a water/octanol/water liquid membrane. *J. Membr. Sci.* **285,** 120–125 (2006).
21. Kakiuchi, T., Nishi, N., Kasahara, T. & Chiba, M. Regular Irregularity in the Transfer of Anionic Surfactant across the Liquid/Liquid Interface. *ChemPhysChem* **4,** 179–85 (2003).
22. Kakiuchi, T., Chiba, M., Sezaki, N. & Nakagawa, M. Cyclic voltammetry of the transfer of anionic surfactant across the liquid–liquid interface manifests electrochemical instability. *Electrochem. Commun.* **4,** 701–704 (2002).
23. Kakiuchi, T., Nishi, N., Kasahara, T. & Chiba, M. Regular Irregularity in the Transfer of Anionic Surfactant across the Liquid/Liquid Interface. *ChemPhysChem* **4,** 179–185 (2003).
24. Kakiuchi, T. Avalanche transfer of charged particles across the electrochemical liquid|liquid interface. *Electrochem. Commun.* **2,** 317–321 (2000).
25. Nakagawa, M., Sezaki, N. & Kakiuchi, T. Fusion of emulsion particles to the polarized 1,2-dichloroethane | water interface. *J. Electroanal. Chem.* **501,** 260–263 (2001).
26. Kasahara, T., Nishi, N., Yamamoto, M. & Kakiuchi, T. Electrochemical Instability in the Transfer of Cationic Surfactant across the 1,2-Dichloroethane/Water Interface. *Langmuir* **20,** 875–881 (2004).
27. Kitazumi, Y. & Kakiuchi, T. Electrochemical Instability in Liquid–Liquid Two-Phase Systems. *Bull. Chem. Soc. Jpn.* **84,** 1312–1320 (2011).
28. Kakiuchi, T. Electrochemical instability of the liquid | liquid interface in the presence of ionic surfactant adsorption. *J. Electroanal. Chem.* **536,** 63–69 (2002).
29. Kitazumi, Y. & Kakiuchi, T. Electrochemical Instability in Liquid–Liquid Two-Phase Systems. *Bull. Chem. Soc. Jpn.* **84,** 1312–1320 (2011).

30. Arai, K., Fukuyama, S., Kusu, F. & Takamura, K. Role of a surfactant in the electrical potential oscillation across a liquid membrane. *Electrochimica Acta* **40,** 2913–2920 (1995).
31. Maeda, K., Nagami, S., Yoshida, Y., Ohde, H. & Kihara, S. Voltammetric elucidation of the process of self-sustained potential oscillation observed with a liquid membrane system composed of water containing cetyltrimethylammonium chloride|nitrobenzene containing picric acid|pure water. *J. Electroanal. Chem.* **496,** 124–130 (2001).
32. McBain, J. W. & Woo, T.-M. Spontaneous Emulsification, and Reactions Overshooting Equilibrium. *Proc. R. Soc. Lond. Ser. Math. Phys. Sci.* **163,** 182–188 (1937).
33. Kakiuchi, T. & Senda, M. Structure of the Electrical Double Layer at the Interface between Nitrobenzene Solution of Tetrabutylammonium Tetraphenylborate and Aqueous Solution of Lithium Chloride. *Bull. Chem. Soc. Jpn.* **56,** 1753–1760 (1983).
34. Kasahara, T., Nishi, N., Yamamoto, M. & Kakiuchi, T. Electrochemical Instability in the Transfer of Cationic Surfactant across the 1,2-Dichloroethane/Water Interface. *Langmuir* **20,** 875–881 (2003).
35. Girault, H. in *Electroanalytical Chemistry* (eds. Bard, A. & Zoski, C.) **20102482,** 1–104 (CRC Press, 2010).
36. Sakka, T., Tanaka, K., Shibata, Y. & Ogata, Y. H. Interfacial tension measurement at a flat liquid–liquid interface under electrochemical instability. *J. Electroanal. Chem.* **591,** 168–174 (2006).
37. Marcus, P. *Corrosion Mechanisms in Theory and Practice, Third Edition*. (CRC Press, 2011).
38. Schmickler, W. & Santos, E. *Interfacial Electrochemistry*. (Springer, 2010).
39. Badiali, J. P. & Goodisman, J. Lippmann equation and the ideally polarizable electrode. *J Phys Chem* **79,** 223–232 (1975).
40. Trojánek, A., Lhotský, A., Mareček, V. & Samec, Z. Limited agreement between the interfacial tension and differential capacity data for the polarised water|1,2-dichloroethane interface. *J. Electroanal. Chem.* **565,** 243–250 (2004).
41. Volkov. *Liquid Interfaces in Chemical, Biological and Pharmaceutical Applications*. (CRC Press, 2001).
42. Daikhin, L. I. & Urbakh, M. What is the origin of irregular current oscillations in the transfer of ionic surfactants across liquid/liquid interfaces? *J. Chem. Phys.* **128,** 014706–014706–8 (2008).
43. Pradines, V., Tadmouri, R., Lavabre, D., Micheau, J.-C. & Pimienta, V. Association, partition, and surface activity in biphasic systems displaying relaxation oscillations. *Langmuir ACS J. Surf. Colloids* **23,** 11664–11672 (2007).

44. Watanabe, A., Higashitsuji, K. & Nishizawa, K. Studies on electrocapillary emulsification. *J. Colloid Interface Sci.* **64,** 278–289 (1978).
45. Kitazumi, Y. & Kakiuchi, T. Potential-Dependent Adsorption of Decylsulfate and Decylammonium Prior to the Onset of Electrochemical Instability at the 1,2-Dichloroethane|Water Interface. *Langmuir* **25,** 8062–8068 (2009).
46. Shahidzadeh, N., Bonn, D. & Meunier, J. A new mechanism of spontaneous emulsification: Relation to surfactant properties. *EPL Europhys. Lett.* **40,** 459 (1997).
47. Pradines, V., Tadmouri, R., Lavabre, D., Micheau, J.-C. & Pimienta, V. Association, partition, and surface activity in biphasic systems displaying relaxation oscillations. *Langmuir ACS J. Surf. Colloids* **23,** 11664–11672 (2007).
48. Kovalchuk, N. M. & Vollhardt, D. Marangoni instability and spontaneous non-linear oscillations produced at liquid interfaces by surfactant transfer. *Adv. Colloid Interface Sci.* **120,** 1–31 (2006).
49. Wojciechowski, K. & Kucharek, M. Interfacial tension oscillations without surfactant transfer. *J. Phys. Chem. B* **113,** 13457–13461 (2009).
50. Sternling, C. V. & Scriven, L. E. Interfacial turbulence: Hydrodynamic instability and the marangoni effect. *AIChE J.* **5,** 514–523 (1959).
51. Miller, C. A. Spontaneous Emulsification Produced by Diffusion — A Review. *Colloids Surf.* **29,** 89–102 (1988).
52. McBain, J. W. & Woo, T.-M. Spontaneous Emulsification, and Reactions Overshooting Equilibrium. *Proc. R. Soc. Math. Phys. Eng. Sci.* **163,** 182–188 (1937).
53. Aoki, K., Li, M., Chen, J. & Nishiumi, T. Spontaneous emulsification at oil–water interface by tetraalkylammonium chloride. *Electrochem. Commun.* **11,** 239–241 (2009).
54. Nishimi, T. & Miller, C. A. Spontaneous Emulsification of Oil in Aerosol-OT/Water/Hydrocarbon Systems. *Langmuir* **16,** 9233–9241 (2000).
55. Uricanu, V. I., Duits, M. H. G., Filip, D., Nelissen, R. M. F. & Agterof, W. G. M. Surfactant-mediated water transport at gelatin gel/oil interfaces. *J. Colloid Interface Sci.* **298,** 920–934 (2006).
56. Srivastava, V. K., Kini, G. & Rout, D. Detergency in spontaneously formed emulsions. *J. Colloid Interface Sci.* **304,** 214–221 (2006).
57. Kaminski, A. & McBain, J. W. Spontaneous Emulsification of Pure Xylene in an Aqueous Solution through Mere Adsorption of a Detergent in the Interface. *Proc. R. Soc. Math. Phys. Eng. Sci.* **198,** 447–454 (1949).

58. Pouton, C. W. Formulation of self-emulsifying drug delivery systems. *Adv. Drug Deliv. Rev.* **25,** 47–58 (1997).
59. Sherwood, T. & Wei, J. Interfacial Phenomena in Liquid Extraction. *Ind. Eng. Chem.* **49,** 1030–1034 (1957).
60. López-Montilla, J. C., Herrera-Morales, P. E., Pandey, S. & Shah, D. O. Spontaneous Emulsification: Mechanisms, Physicochemical Aspects, Modeling, and Applications. *J. Dispers. Sci. Technol.* **23,** 219–268 (2002).
61. Malzert-Fréon, A., Schönhammer, K., Benoît, J.-P. & Boury, F. Interactions between poly(ethylene glycol) and protein in dichloromethane/water emulsions. 2. Conditions required to obtain spontaneous emulsification allowing the formation of bioresorbable poly(d,l lactic acid) microparticles. *Eur. J. Pharm. Biopharm.* **73,** 66–73 (2009).
62. Frazer, A. C., Schulman, J. H. & Stewart, H. C. Emulsification of fat in the intestine of the rat and its relationship to absorption. *J. Physiol.* **103,** 306–316 (1944).
63. Watarai, H., Teramae, N. & Sawada, T. *Interfacial Nanochemistry: Molecular Science and Engineering at Liquid-Liquid Interfaces*. (Springer, 2005).
64. Kakiuchi, T. Electrochemical instability of the liquid|liquid interface in the presence of ionic surfactant adsorption. *J. Electroanal. Chem.* **536,** 63–69 (2002).
65. Kakiuchi, T., Kobayashi, M. & Senda, M. The effect of the electrical potential difference on the adsorption of the hexadecyltrimethylammonium ion at the polarized nitrobenzene-water interface. *Bull. Chem. Soc. Jpn.* **60,** 3109–3115 (1987).
66. Kakiuchi, T. Potential-dependent adsorption and partitioning of ionic components at a liquid | liquid interface. *J. Electroanal. Chem.* **496,** 137–142 (2001).
67. Kakiuchi, T. Potential-dependent adsorption and partitioning of ionic components at a liquid|liquid interface. *J. Electroanal. Chem.* **496,** 137–142 (2001).
68. Shchukin, E. D., Pertsov, A. V., Amelina, E. A. & Zelenev, A. S. *Colloid and Surface Chemistry*. (Elsevier, 2001).
69. Kakiuchi, T. & Senda, M. Structure of the electrical double layer at the interface between nitrobenzene solution of tetrabutylammonium tetraphenylborate and aqueous solution of lithium chloride. *Bull. Chem. Soc. Jpn.* **56,** 1753–1760 (1983).
70. Sakka, T., Tanaka, K., Shibata, Y. & Ogata, Y. H. Interfacial tension measurement at a flat liquid–liquid interface under electrochemical instability. *J. Electroanal. Chem.* **591,** 168–174 (2006).

71. Kitazumi, Y. & Kakiuchi, T. Potential-Dependent Adsorption of Decylsulfate and Decylammonium Prior to the Onset of Electrochemical Instability at the 1,2-Dichloroethane|Water Interface. *Langmuir* **25,** 8062–8068 (2009).
72. Watanabe, A., Matsumoto, M., Gotoh, R. & Tamai, H. Electrocapillary phenomena at oil-water interfaces. *Colloid Polym. Sci.* **221,** 47–52 (1967).
73. Rosen, M. J. & Kunjappu, J. T. *Surfactants and Interfacial Phenomena*. (John Wiley & Sons, 2012).
74. Fainerman, V. B. & Miller, R. Surface Tension Isotherms for Surfactant Adsorption Layers Including Surface Aggregation. *Langmuir* **12,** 6011–6014 (1996).
75. Birdi, K. S. *Handbook of Surface and Colloid Chemistry, Third Edition*. (CRC Press, 2008).
76. Dukhin, S. S., Kretzschmar, G. & Miller, R. *Dynamics of Adsorption at Liquid Interfaces: Theory, Experiment, Application*. (Elsevier, 1995).
77. Mohammadi, H. Mechanistic modeling, design, and optimization of alkaline/surfactant/polymer flooding. (2008). at <http://repositories.lib.utexas.edu/handle/2152/18190>
78. Johal, M. S. *Understanding Nanomaterials*. (CRC Press, 2012).
79. Rosen, M. J. *Surfactants And Interfacial Phenomena*. (John Wiley & Sons, 2004).
80. Lee, Y.-C., Lin, S.-Y. & Liu, H.-S. Role of Equation of State on Studying Surfactant Adsorption Kinetics. *Langmuir* **17,** 6196–6202 (2001).
81. Bockris, J. O., Reddy, A. K. N., Gamboa-Aldeco, M. & Gamboa-Aldeco, M. E. *Modern Electrochemistry*. (Springer Science & Business Media, 2001).
82. Narayanan, R. & Andérez, J. M. *Interfacial Processes and Molecular Aggregation of Surfactants*. (Springer, 2008).
83. Markin, V. S., Volkova-Gugeshashvili, M. I. & Volkov, A. G. Adsorption at Liquid Interfaces: The Generalized Langmuir Isotherm and Interfacial Structure. *J Phys Chem B* **110,** 11415–11420 (2006).
84. Texter, J. *Reactions and Synthesis in Surfactant Systems*. (CRC Press, 2001).
85. Birikh, R. & Rudakov, R. Effect of the adsorption-desorption process intensity on solutal convection near a drop in a horizontal channel. *Fluid Dyn.* **46,** 131–137 (2011).
86. Danov, K. D., Kralchevsky, P. A., Denkov, N. D., Ananthapadmanabhan, K. P. & Lips, A. Dynamics of Adsorption from Micellar Surfactant Solutions at Expanding Fluid Interfaces in Relation to the Emulsification Process. *Chem. Phys.* 3–6 (2006).
87. Industriel, P. Adsorption from Micellar Surfactant Solutions: Nonlinear Theory and Experiment. *Langmuir* **235,** 223–235 (1996).

88. Kresheck, G. C., Hamori, E., Davenport, G. & Scheraga, H. A. Determination of the Dissociation Rate of Dodecylpyridinium Iodide Micelles by a Temperature-Jump Technique1a,b. *J. Am. Chem. Soc.* **88,** 246–253 (1966).
89. Aniansson, E. A. G. & Wall, S. N. Kinetics of step-wise micelle association. *J. Phys. Chem.* **78,** 1024–1030 (1974).
90. Birdi, K. S. *Handbook of Surface and Colloid Chemistry, Fourth Edition*. (CRC Press, 2015).
91. Danov, K. D. *et al.* Adsorption from Micellar Surfactant Solutions: Nonlinear Theory and Experiment. *J. Colloid Interface Sci.* **183,** 223–235 (1996).
92. Goto, T., Maeda, K. & Yoshida, Y. Relationship between interfacial transfer and adsorption-desorption of surface-active bis-ammonium ions at a liquid/liquid interface. *Langmuir ACS J. Surf. Colloids* **21,** 11788–11794 (2005).
93. Donaldson, E. C., Chilingarian, G. V. & Yen, T. F. *Enhanced Oil Recovery, II: Processes and Operations*. (Elsevier, 1989).
94. Kolev, V. L., Danov, K. D., Kralchevsky, P. A., Broze, G. & Mehreteab, A. Comparison of the van der Waals and Frumkin Adsorption Isotherms for Sodium Dodecyl Sulfate at Various Salt Concentrations. *Langmuir* **18,** 9106–9109 (2002).
95. Stellner, K. L. & Scamehorn, J. F. Surfactant precipitation in aqueous solutions containing mixtures of anionic and nonionic surfactants. *J. Am. Oil Chem. Soc.* **63,** 566–574 (1986).
96. Kralchevsky, P. A., Danov, K. D., Broze, G. & Mehreteab, A. Thermodynamics of ionic surfactant adsorption with account for the counterion binding: Effect of salts of various valency. *Langmuir* **15,** (1999).
97. Danov, K. D., Kralchevsky, P. A. & Ananthapadmanabhan, K. P. Micelle–monomer equilibria in solutions of ionic surfactants and in ionic–nonionic mixtures: A generalized phase separation model. *Adv. Colloid Interface Sci.* **206,** 17–45 (2014).
98. Mortada, W. I., Hassanien, M. M. & El-Asmy, A. A. Cloud point extraction of some precious metals using Triton X-114 and a thioamide derivative with a salting-out effect. *Egypt. J. Basic Appl. Sci.* **1,** 184–191 (2014).
99. Komaromy-Hiller, G., Calkins, N. & von Wandruszka, R. Changes in Polarity and Aggregation Number upon Clouding of a Nonionic Detergent: Effect of Ionic Surfactants and Sodium Chloride. *Langmuir* **12,** 916–920 (1996).
100. Nascentes, C. Cloud point formation based on mixed micelles in the presence of electrolytes for cobalt extraction and preconcentration. *Talanta* **61,** 759–768 (2003).
101. Gu, T., Qin, S. & Ma, C. The effect of electrolytes on the cloud point of mixed solutions of ionic and nonionic surfactants. *J. Colloid Interface Sci.* **127,** 586–588 (1989).

102. Gu, T. & Galera-Gómez, P. A. Clouding of Triton X-114: The effect of added electrolytes on the cloud point of Triton X-114 in the presence of ionic surfactants. *Colloids Surf. Physicochem. Eng. Asp.* **104,** 307–312 (1995).
103. Reible, D. D. *Fundamentals of Environmental Engineering*. (CRC Press, 1998).
104. Schmelzer, J. W. P. *Nucleation Theory and Applications*. (John Wiley & Sons, 2006).
105. Hassan, S. A. Computer Simulation of Ion Cluster Speciation in Concentrated Aqueous <b/> Solutions at Ambient Conditions. *J. Phys. Chem. B* **112,** 10573–10584 (2008).
106. Kitayama, A. *et al.* Diffusion behavior in a liquid-liquid interfacial crystallization by molecular dynamics simulations. *J. Chem. Phys.* **131,** 174707 (2009).
107. Kadota, K., Tanida, S., Shirakawa, Y., Shimosaka, A. & Hidaka, J. Production of Asymmetrical Particles in a Crystallization Process Using Liquid–Liquid Interfaces. *J. Chem. Eng. Jpn.* **40,** 217–221 (2007).
108. Hundhammer, B., Solomon, T., Dhawan, S. K., Zerihun, T. & Tessema, M. Ion transfer across the water/nitrobenzene interface facilitated by ion association and precipitation. *J. Electroanal. Chem.* **369,** 275–277 (1994).
109. Caçote, M. H. M., Pereira, C. M., Tomaszewski, L., Girault, H. H. & Silva, F. Ag+ transfer across the water/1,2-dichloroethane interface facilitated by complex formation with tetraphenylborate derivatives. *Electrochimica Acta* **49,** 263–270 (2004).
110. Geblewicz, G., Kontturi, A. K., Kontturi, K. & Schiffrin, D. J. Salting out of hydrophobic ions at immisicble electrolyte interfaces. *J. Electroanal. Chem. Interfacial Electrochem.* **217,** 261–269 (1987).
111. Kontturi, K., Murtomaki, L. & Quinn, B. MONOVALENT CATIONS AT THE WATER/1,2-DICHLOROETHANE INTERFACE. *Acta Chem. Scand.* **50,** 640–642 (1996).
112. Silver, B. R. New approaches to protein crystallization. (University of Warwick, 2013). at <http://webcat.warwick.ac.uk/record=b2669613~S1>
113. Williams, D. F. & Schmitt, W. H. *Chemistry and Technology of the Cosmetics and Toiletries Industry*. (Springer, 1996).
114. Butt, H.-J., Graf, K. & Kappl, M. *Physics and Chemistry of Interfaces*. (John Wiley & Sons, 2003).
115. Troy, D. & Beringer, P. *Remington: The Science And Practice Of Pharmacy*. (Lippincott Williams & Wilkins, 2006).
116. Board, N. *Modern Technology Of Cosmetics*. (National Institute Of Industrial Re, 2004).
117. De, S. & Mondal, S. *Micellur Enhanced Ultrafiltration: Fundamentals & Applications*. (CRC Press, 2012).

118. Jagow, G. ‘von ’ & Schägger, H. *A Practical guide to membrane protein purification*. (Gulf Professional Publishing, 1994).

119. Koshy, L., Saiyad, A. H. & Rakshit, A. K. The effects of various foreign substances on the cloud point of Triton X 100 and Triton X 114. *Colloid Polym. Sci.* **274,** 582–587 (1996).

120. Williamson, K. & Masters, K. *Macroscale and Microscale Organic Experiments*. (Cengage Learning, 2010).

121. Williamson, K. L. & Masters, K. M. *Macroscale and Microscale Organic Experiments*. (Cengage Learning, 2010).

122. Kodali, D. R., Atkinson, D., Redgrave, T. G. & Small, D. M. Structure and polymorphism of 18-carbon fatty acyl triacylglycerols: effect of unsaturation and substitution in the 2-position. *J. Lipid Res.* **28,** 403–413 (1987).

123. Rogers, A. *Industrial Chemistry: A Manual for the Student and Manufacturer*. (Taylor & Francis, 1925).

124. Vanysek, P. & Basaez Ramirez, L. INTERFACE BETWEEN TWO IMMISCIBLE LIQUID ELECTROLYTES: A REVIEW. *J Chil Chem Soc* **53,** 1455–1463 (2008).

125. Ulmeanu, S. M. *et al.* Cyclic voltammetry of highly hydrophilic ions at a supported liquid membrane. *J. Electroanal. Chem.* **530,** 10–15 (2002).

126. Bostrelli, D. V. *Solution Chemistry Research Progress*. (Nova Publishers, 2008).

127. Watarai, H., Teramae, N. & Sawada, T. *Interfacial Nanochemistry: Molecular Science and Engineering at Liquid-liquid Interfaces*. (Springer, 2005).

128. Watarai, H., Teramae, N. & Sawada, T. *Interfacial Nanochemistry: Molecular Science and Engineering at Liquid-Liquid Interfaces*. (Springer Science & Business Media, 2006).

129. Samec, Z. & Kakiuchi, T. in *Advances in Electrochemical Sciences and Engineering* (eds. Gerischer, H. & Tobias, C. W.) **4,** 297–361 (Wiley-VCH Verlag GmbH, 1995).

130. Kakiuchi, T., Chiba, M., Sezaki, N. & Nakagawa, M. Cyclic voltammetry of the transfer of anionic surfactant across the liquid–liquid interface manifests electrochemical instability. *Electrochem. Commun.* **4,** 701–704 (2002).

131. Bucak, S. & Rende, D. *Colloid and Surface Chemistry: A Laboratory Guide for Exploration of the Nano World*. (CRC Press, 2013).

132. Manipulation of Concentration-Conductivity Data of Sodium Dodecyl Sulphate and Sodium Dodecylbenzene Sulphonate in KCl Solution in Relation to Micellisation Parameters. at <http://connection.ebscohost.com/c/articles/89095757/manipulation-concentration-conductivity-data-sodium-dodecyl-sulphate-sodium-dodecylbenzene-sulphonate-kcl-solution-relation-micellisation-parameters>

133. De Smet, Y., Deriemaeker, L. & Finsy, R. Ostwald Ripening of Alkane Emulsions in the Presence of Surfactant Micelles. *Langmuir* **15,** 6745–6754 (1999).

134. Girault, H. H. J. & Schiffrin, D. J. Thermodynamics of a polarised interface between two immiscible electrolyte solutions. *J. Electroanal. Chem. Interfacial Electrochem.* **170,** 127–141 (1984).

135. M. C. Martins, C. M. P. Specific Adsorption of Tetraalkylammonium Cations on the 1,2-Dicloroethane/ Water Interface. *Electrochimica Acta* **50,** (2004).

136. Handa, T., Saito, H. & Miyajima, K. Phospholipid monolayers at the triolein-saline interface: production of microemulsion particles and conversion of monolayers to bilayers. *Biochemistry (Mosc.)* **29,** 2884–2890 (1990).

137. Girault, H. H. in *Modern Aspects of Electrochemistry* (eds. Bockris, J. O., Conway, B. E. & White, R. E.) **25,** 1–62 (Springer US, 1993).

138. Lima, E. R. A., Melo, B. M. de, Baptista, L. T. & Paredes, M. L. L. Specific ion effects on the interfacial tension of water/hydrocarbon systems. *Braz. J. Chem. Eng.* **30,** 55–62 (2013).

139. Agble, D. & Mendes-Tatsis, M. . The prediction of Marangoni convection in binary liquid–liquid systems with added surfactants. *Int. J. Heat Mass Transf.* **44,** 1439–1449 (2001).

140. Hubbard, A. T. *Encyclopedia of Surface and Colloid Science* -. (CRC Press, 2002).

141. VanýSek, P. & BasáEz RamíRez, L. INTERFACE BETWEEN TWO IMMISCIBLE LIQUID ELECTROLYTES: A REVIEW. *J. Chil. Chem. Soc.* **53,** (2008).

142. Callister, W. D. & Rethwisch, D. G. *Fundamentals of Materials Science and Engineering: An Integrated Approach*. (John Wiley & Sons, 2012).

CHAPTER 5

Sol-gel/ferrocenated gold nanoparticle based enzymatic biosensor for glycerol detection

5.1 Biosensors

Biosensors can be defined as self-contained analytical devices which incorporate a biological recognition element in close contact with an appropriate transduction element for the detection of the concentration of activity of the chemical species/analyte (s) in the sample. A typical biosensor includes two steps which are a recognition step and transducing step[1]. In the recognition step the biological recognition element with high selectivity and fast response (such as enzymes, antibodies, antigens, proteins or cell organelles) are responsible for transforming the analyte into chemical or physical signal[2]. The biological element is usually immobilised and it is in direct contact with the transducer that detects the physicochemical changes (for instance, variation in the pH, electron and mass transfer or recognises the analyte in the solution/the atmosphere) and, converts it into electrical signals (figure 5.1)[3]. The measurable physical signal in turn is proportional to the concentration of the analyte[4].

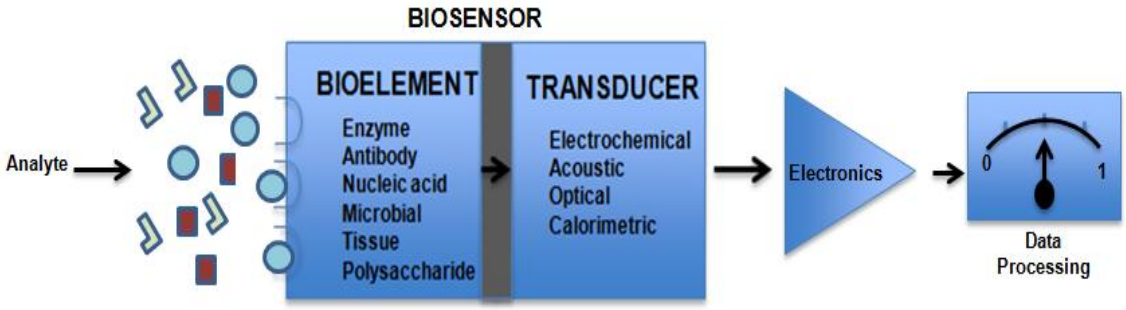

Figure 5.1: schematic diagram of the components and setup of a biosensor[5].

Biosensors research is a fast growing field and it has been predicted that the value of the industry is set to be worth around 17 billion dollars for 2018[6]. These sensors have been found to be useful tool for various applications including the food and beverages[7,8],biotechnological[9,10,11], environmental[12,13], and pharmaceutical market[14,15,16]. The biosensors can be used to attain rapid and continuous measurements in real time for both on-site and remote monitoring for example, of bimolecular interactions. There are numerous

other advantages associated with the application of such inexpensive biosensors and these include high selectivity, sensitivity, specificity and reliability[17].

5.2 Types of sensing element

The method of transduction depends on the type of physiochemical change that results from the sensing element. The biosensing components of the biosensor can be divided into two categories which are catalytic type where the signal is produced after binding of analytes i.e. enzymes, microbes, organelles, cells or tissues without altering the sensor and affinity type which include antibodies, receptors and nucleic acids. In this study, enzymes such as glucose oxidase (GOx) and glycerol dehydrogenase (GDH) were used as the sensing element for the detection of glucose and glycerol substrates below[18].

5.2.1 Enzymes

Enzymes are proteins which has high catalytic activity and selectivity for specific substrates. These biocatalysts have been applied for decades in assays to determine the concentration of a range of analytes from the initial reaction rates. The initial concept of enzymes forming complexes with substrates was first founded in the 19th century and it was Emil Fischer who initially proposed the 'lock and key' model for describing the stereochemical relationship between enzymes and the substrates[19]. Following this, the velocity of the enzyme catalysed reactions and saturation kinetics were explored by Adrian Brown in 1902[20], soon after which in 1903 Victor Henri developed his first mathematical model for defining the enzyme kinetics[21]. Based on the Henri model, in 1913 Leonor Michaelis and Maud Menten derived the enzyme rate equation, that relates the velocity at which the enzymatic process occurs with the substrate concentration, known as the Henri-Michaelis-Menten or Michaelis-Menten equation which is still to this day have been applied extensively in the analysis of enzyme reaction mechanisms[21,22]. In depth analysis of the enzymatic rate of reaction was accomplished by Linus Pauling in 1948 who established that upon molecules tightly binding to the enzyme active site led to the stabilisation of the transition state of the catalysed reaction[23]. Subsequently, in 1958 the 'induced fit model' was introduced by Daniel Koshland to further describe the relationship between the enzyme's affinity for substrate binding and the increase in reaction rate[24]. The possibility of small molecules other than substrates

binding to the enzymatic active site led to the development of the theory of allosteric transitions by Monod, Wyman and Changeux in 1965[25].

It was in the early twentieth century when the enzymatic structure was extensively studied using methods such as the X-ray crystallography. In 1926, James Sumner was the first to publish the crystal structure of a purified and crystallized urease enzyme[26] .Based on Kendrew and Perutz's work on myoglobin protein using the X-ray scattering[27], crystal structures of many enzymes were solved. In most recent years, X-ray diffraction and NMR techniques has been to be useful for various purposes such as to identify the mechanisms of enzyme catalysis and for designing new molecules which can bind to specific sites within the enzymes.

Enzymes have many applications for example, in the medical, pharmaceutical and the food and beverage industries[29]. They can be also applied in stereospecific chemical synthesis and it is widely used as a key ingredient in various consumer products like laundry detergents[30]. The availability of the biomolecules at high purity grade and its re-usability has made the proteins highly ideal for mass production of enzymatic sensors[31]. However, the activities of the enzymes can be affected by factors such as the pH, ionic strength, chemical inhibitors and temperature[32]. Most enzymes denature and lose their activity at temperatures higher than 60 ^{o}C. Enzymes such as oxidases are commonly used for immobilisation on the electrode for the determination of electrochemical properties of the proteins and they are normally coupled to either the electrochemical or fiber optic transducer.

5.3 Types of transducers

Biosensors are classified based on the transducer type which includes optical, acoustic, colorimetric, electrochemical and piezoelectric crystals. The choice of indicator transducer is dependent on the species involved in the particular reaction[21]. In this study the electrochemical biosensor was applied for the detection of specific analytes i.e. glucose and glycerol using GOx and GDH enzymes.

5.3.1 Electrochemical biosensors

Electrochemical biosensors can be used for coloured or opaque samples which cannot be attained using the optical sensors and the response of the substrate binding to the receptors are recorded as an electrical signal. These types of biosensors can be categorised into amperometric, voltammetric, potentiometric, conductivity, capacitance and impedance

biosensors. The amperometric sensors measure the current when an electroactive species is oxidised or reduced at the electrode whilst the potential between the two electrodes are set. If the current however is measured under controlled variation of potential, it is referred to as voltammetry. The peak current generated over a potential range using the voltammetric biosensor is directly proportional to the bulk analyte/electroactive species concentration. The potentiometric sensors on the other hand operate on the principle of charge accumulation of the substrate at the working electrode, in the form of potential and the current remains very low or there is no net current flow[34]. For potentiometric measurements, the concentration and the potential relationship can be expressed by the Nernst equation (equation 5.1)[35].

$$E_{cell} = E^0_{cell} - \frac{RT}{nF} In\, Q \qquad \text{(eq. 5.1)}$$

where, E_{cell} is a constant potential to the cell, n is the charge number and Q is the ratio of charged ions at the anode and the cathode. Furthermore, the conductance biosensors measure the changes in electrical conductivity of the solution/medium between electrodes that could occur for example, due to an enzymatic reaction or it can be used to monitor the variation in conductance of an electrode caused by immobilisation of i.e. enzymes on to the electrode surface. The capacitance/impedance biosensors are normally used to determine the capacity modification/impedimetric response due to presence of an immobilised layer in the electrode surface[36].

5.4 Enzyme biosensors

An enzyme biosensor is analytical device which links the enzyme to a transducer and produces a signal that is proportional the substrate concentration. The transducer then converts the signal into a measureable response and this could be in the form of for example, current, potential or temperature change[37]. The first biosensor which is an enzyme based sensor for measuring glucose level was first developed in 1962 by Clark and Lyons[38]. The biosensor consisted of an external dialysis membrane which trapped the thin layer of GOx enzyme deposited on an oxygen probe. The glucose was determined in proportion to the depletion of oxygen concentration. The stability of the GOx was further improved by Updike and Hicks in 1967 via protein immobilisation in a polyacrylamide gel onto a surface of an oxygen electrode for rapid and quantitative measurement of glucose concentration in biological fluids[39]. Following this, the first commercially available glucose biosensor was made in 1975 based on

Clark and Lyons work and it was known as 'the Yellow Springs Instrument Company analyser' that allowed amperometric detection of hydrogen peroxide resulting from the breakdown of glucose by GOx[40]. However, the analysers can be only used in the clinical laboratories because of its requirement for the usage of expensive platinum electrode. Other problems associated with these oxygen based biosensors include interference from other substrates in the solution such as ascorbic acid or uric acid and variation in the oxygen level present in the solution. Despite the drawbacks, the potential for mass producing biosensors for rapid testing meant that the biosensor market was still emerging[41].

It was in 1984 when the first glucose biosensor using soluble ferrocene carboxylate mediator for glucose monitoring was produced by Cass, where the red-ox mediator acted as an electron acceptor and transferred electrons between the redox centre of the enzyme glucose oxidase in solution and the surface of the working electrode[42]. An amperometric signal was generated as the reduced mediator was formed before it was re-oxidised again at the electrode when a potential was applied[43]. It was observed that the mediators such ferrocene (Fc) and ferrocyanide did not react with the oxygen (O_2) and consequently, no hydrogen peroxide (H_2O_2) was generated. In the 1980s, alongside the mediated biosensors, screen printed electrodes and modified electrodes with membranes were also established, all of which displayed an enhanced sensor performance. The first pen-sized miniature electrochemical biosensor which used glucose dehydrogenase enzyme and pyrroquinolinequinone and ferrocene derivative as a mediator was developed as ExacTech by Medisense Inc. in 1987 for diabetic patients[44]. The amperometric based glucose biosensors were portable and inexpensive which made them ideal for the patient's to self-monitor the blood glucose level at home[45]. In order to increase the rate of electron transfer further between the red-ox centre of the GOx enzyme and the electrode surface, other methods for example, enzyme wiring of GOx by electron conducting red-ox hydrogels, chemical alteration of the GOx enzyme structure with electro-relay groups and the use of nanostructures as electrical connectors were applied. Since the late 90s and early 2000, other forms of glucose sensors such as in –vivo and non-invasive techniques have been constructed and applied. Although, initially 90% of the biosensor work was undertaken on developing glucose sensor, there has been application of this technique in a wide range of niche markets[46]. For instance, Guilbault and Montalvo in 1969 used glass electrodes coupled with urease enzyme to quantify the urea concentration by potentiometry[47]. An amygdaline sensor was also invented which involved coupling of ion selective electrode and betaglucosidase enzyme by Professor G. Rechnitz[48]. Subsequently, due to the numerous advantages of biosensors such as rapid and

real time measurement, reproducibility and reliability as well as its miniature size, low cost, ease of manufacture and replacement of the biological element or the type of transducer which in turn allow selective detection of specific analytes have led to a large-scale commercial success. The biosensors were applicable to a variety of fields which include rapid detection of pathogens in food/drinks to ensure food safety, monitoring crop diseases or level of plant nutrients in agriculture, recognition of pollutants/toxic chemicals in water supply/air/landmass or the level of pesticides/fertilizers for environmental monitoring and for drug discovery or diagnosis of diseases in medicine[49]. Other fields of relevance comprise of biotechnology, science and industrial sectors which involves use of a range of substrates and enzymes for catalyzing a variety of red-ox reactions[50]. The enzyme-substrate catalytic reactions are investigated by measuring the rate of detectable products formed or disappearance of reactants, which in turn is proportional to the analyte concentration. Apart from enzymes other factors such as activators, prosthetic groups and inhibitors can also alter the rate of reaction. Changes in optimal environmental conditions can affect the thermal and chemical stability of the enzymes and this in turn can limit enzyme applicability[51,52].

The glucose sensors for the effective management of diabetes are the largest driving force in the biosensor market while the medical analysis biosensors are the second biggest contributors for the development of the sensor technologies[53]. Research undertaken by Newsguide US in 2009 have revealed that the biosensors market value was set to reach $ 6.1 billion by 2012 and it will continue to expand over the upcoming years as there are increasing applications for biosensors due to growing population leading to a rise in chronic diseases such as diabetes and it is also required for environmental monitoring. The market for the environmental biosensors is also rapidly mounting as evident by the growth in Germany alone, contributing $ 32.7 million to this biosensor industrial sector[54,55].

5.5 Types of enzyme electrodes

An enzyme electrode is usually composed of a dialyser, enzyme reactor and a detector[56]. There are different types of enzyme electrodes which have been established over the years. The oxygen electrode was initially developed as a glucose biosensor which was later modified for the detection of H_2O_2 and it is the most widely applied transducer in biosensors. The electrode potential for this specific electrode is kept at low as possible and a redox substrate or electron mediator is manipulated to prevent electrochemical interferences, allow the electrodes to be used in oxygen free solution and enhance the electrode's selectivity[57]. The

covalent binding/adsorption or the addition of the enzymes and mediator into carbon paste electrodes on the other hand has been reported to produce alternative effective glucose sensors[58]. By wiring specific parts of enzymes such as the $FADH_2$/FAD centers of the GOx or glucose dehydrogenase with an osmium complex to the carbon electrode, sensors for glucose have been initially pioneered by Heller which was then applied for the detection of other substrates like H_2O_2 and NAD(P)H[59,60].

Other electrodes such as the ion selective electrode have been used to determine the rate of enzymatic activity by potentiometric measurement of the product generated. The most common ion selective electrode is the glass electrode which has been used for pH measurement and also, for monitoring enzymatic reactions[61]. On the contrary, the metal oxide transducers i.e. the antimony oxide, palladium oxide or iridium oxide electrodes coupled with immobilised enzymes have been manipulated for enzymatic reactions due to its enhanced mechanical stability comparing to the ion selective probes[62]. In this study, amperometric based carbon electrodes have been used as enzymatic biosensors as they are simple to use and the sensors can be applied to attain a much wider detection limit comparing to potentiometric electrodes.

5.5.1 Amperometric enzyme electrodes

Electrodes are commonly used in either a potentiostatic mode or an amperometric mode. Amperometric electrodes measure the electrochemical activity by relating it with a quantity of current which in turn can be directly associated with the concentration of the species of interest. The electrodes used are usually composed of platinum, gold, silver, stainless steel or carbon materials which are inert at the potentials where electrochemical reaction occurs. These kind of electrodes can be made more selective by electrochemical or non-electrochemical modification[63]. There are 2 types of amperometric enzyme electrodes: unmediated and mediated[64]. The unmediated reactions typically involve enzymes such as oxireductases which can produce electroactive species. These small molecules can then be monitored using electrode sensors amperometrically without the need of a mediator. The unmediated amperometric enzyme electrodes have a range of desirable applications which include detection of millimolar to micromolar concentration of analyte where the sample matrix is complicated[65].

The mediated reactions on the other hand involve use of enzymes such as oxidases and electron acceptors/mediators to shuttle electrons between the redox centre of the enzyme

(where the cofactor is situated) and the working electrode. In this study, the mediation process constituted of an initial oxidation step where interaction of the glucose/glycerol substrate with the oxidised form of GOx/glycerol dehydrogenase (GDH) enzyme leads to formation of the gluconolactone/ dihydroxyacetone product and reduced form of the enzyme(s). Following this, the active form of the enzyme(s) is then regenerated by the transfer of an electron to the oxidised form of the ferrocenated gold nanoparticle (FcAuNP) mediator which in turn produces the reduced form of the FcAuNP mediator. Finally, the diffusion of the electron from the reduced FcAuNP to the electrode surface generates an electrolytic current which is then detected using electrochemical techniques such as cyclic voltammetry (figure 5.2)[66].

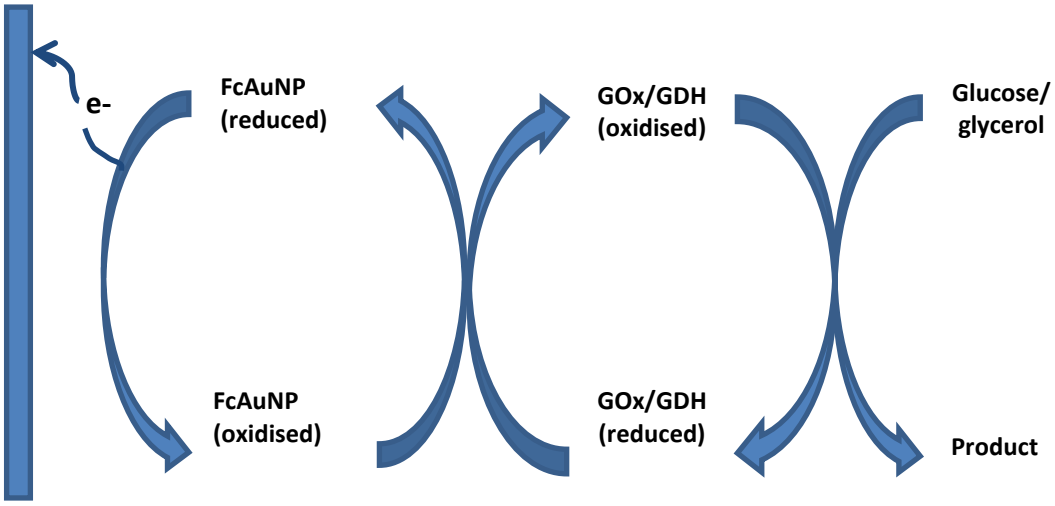

Figure 5.2: mediated enzymatic electrode based reaction[67,68].

There are a range of other compounds apart from FcAuNP that can be used as mediators for example, organic dyes, cytochromes, ferrocene and ferricyanide. The reaction involving a mediator based enzymatic biosensor generally follows the EC' mechanism. The mechanism includes a reversible electron transfer (E) step followed by a catalytic process (C'). This can be represented by the following kinetic scheme (scheme 5.1)[69].

$$R + e^- \rightleftharpoons O;$$

$$Z + O \xrightarrow{k_{cat}} R + Y$$

Scheme 5.1: kinetic of the EC' mechanism[69].

Where, *R*, is the reduced mediator regenerated from *O*; *O*, is the oxidised mediator; *Z*, is the component which regenerates R and it is in the process converted to final product Y; and K*cat,* is the catalytic rate constant[69]. The type of mediator required should react rapidly with enzyme, exhibit heterogeneous kinetics or possess a low overpotential for regeneration. Overpotential can be defined as the potential which is required for driving a reaction beyond the equilibrium potential[66]. The mediator also needs to be stable at different pH, temperature and redox state. The electrode used for construction of an enzymatic biosensor is usually made of platinum, gold or carbon[70].

5.6 The methods of enzyme immobilisation

For repeat use of enzymes in analytical devices and to attain advantages such as enzyme sensitivity, functional stability and high activity, the biocatalysts can be attached to the electrode via a variety of techniques comprised of both physical and chemical methods[71]. Physical immobilisation involves enzyme adsorption to water insoluble carriers or surfaces and entrapment of enzyme in water insoluble polymeric gels or by using selective membranes. The chemical immobilisation on other hand includes covalent coupling and intermolecular cross-linking of the biomolecules[72]. The details of the different methods which have been applied in the enzymatic study are outlined below.

5.6.1 Adsorption

Adsorption of the enzymes at the electrode surface is more preferable as it is the easiest to perform, less expensive and the detrimental effect on activity and selectivity is minimal[73,74]. This process does not require any specific condition or chemicals that can cause the enzyme to denature. The adsorption process usually involves an aqueous solution containing the biocatalysts to be kept in constant contact with the active surface of the electrode for a defined period of time. The biomolecules which are not adsorbed are then removed via washing. The only disadvantage associated with this method is that the protein adsorption process is reversible which means that the enzymes can detach for instance, if exposed to change in pH, ionic strength, substrate concentration or temperature[75].

5.6.2 Gel entrapment

Gel entrapment is a widely preferred method of immobilisation and it prevents the enzymes from diffusing into the reaction mixture by trapping it in a polymeric gel. Simultaneously, it allows small substrate, products or effector molecules to penetrate through the gel network whilst retaining the enzyme. The advantage associated with this method is that the biomolecules are not covalently attached to the matrix which in turn averts enzyme denaturation [76]. The most common matrices used for this process are hydrogels which includes alginate, carageenan, collagen, cellulose triacetate, polyacrylamide, gelatin, agar, silicone rubber and poly (vinyl alcohol)[77]. This was the chosen method for enzyme immobilisation in this study. Sol-gel mixture was used to entrap the enzyme(s) before drop-casting it on to the electrode surface for use. A dialysis membrane was also manipulated to hold firmly the sol-gel/enzyme mixture in a fixed position on the active area of the macroelectrode.

5.6.3 Membrane

An external membrane permeable to a specific analyte can be used to: (1) enhance the selectivity of the physicochemical detector, (2) protect the biological sensing element against mechanical stresses and (3) provide support for the biological element and diffusion control of the analyte. Its thickness, pore size and charge can be manipulated to allow particular analyte (s) to reach the surface of the transducer, to control the rate of the reagents and exclude interfering molecules from reaching the reaction layer[78]. After permeation through the membrane into the enzyme layer, the analyte (s) are converted into detectable species. The enzyme membrane is characterised by enzyme loading which encompasses the enzymatic kinetics and mass transport. The loading process is vital for the response characteristics and the stability of the sensor. The choice of enzyme on the other hand is important for the selectivity of the measurement[79].

The amperometric enzyme kinetics where the enzyme is entrapped in a membrane can be defined by Albery and Barlett equation (equation 5.2) below[80]:

$$\frac{S_\infty}{j} = \frac{1}{k_h}\left[1 + \frac{S_\infty}{k_m}\left(1 - \frac{j}{k_s S_\infty}\right)\right] \qquad \text{(eq.5.2)}$$

where, S_∞ is the bulk substrate concentration, j is the flux, k_h is the heterogeneous rate constant and k_m is the Michaelis-Menten constant for homogeneous enzyme kinetics.

5.7.~~1~~ Kinetic model for interfacial lipolysis

The interfacial lipolysis reaction at the oil-water interface involves complex equilibrium between the adsorption and desorption processes, conformational changes and catalytic mechanisms. This can be represented in terms of the Michaelis-Menten kinetic model[95]. The first step involves fixation of the water-soluble enzyme to the oil – water interface via a reversible adsorption-desorption mechanism. Initially, the physical adsorption process leads to generation of a favorable energetic state of the enzyme (E*) and it also causes the lid at the active site to open. The activated enzyme then binds a substrate (S) such as triglycerides at the interface and forms an enzyme-substrate complex (E*S) which is then hydrolysed to release products (P). At the same time, adsorbed enzyme (E*) is regenerated via the pseudo Michaelis-Menten catalytic step (figure 5.3)[96].

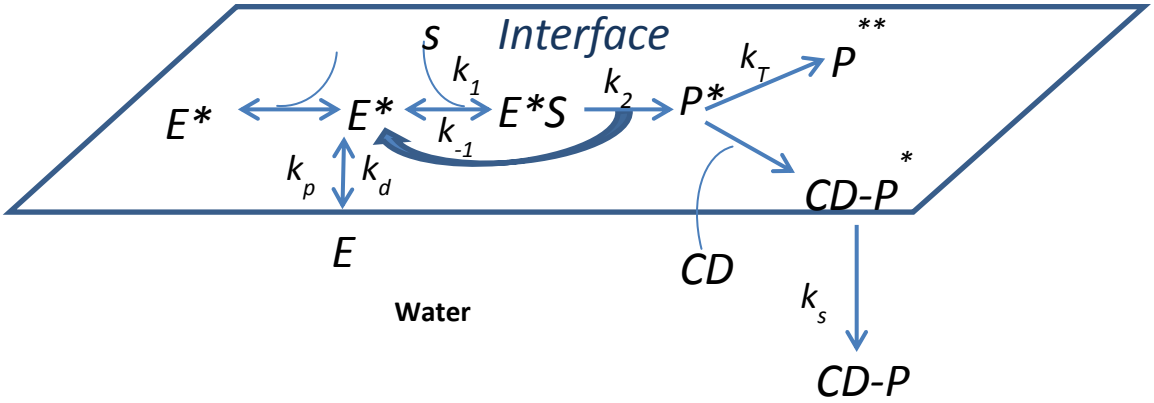

Figure 5.3: General model of Michaelis – Menten Kinetics model describing interfacial lipolysis[96].

In the above kinetics model (figure 5.3), E^* is the energetically favorable enzyme; *S* is the substrate; E^*S is the enzyme-substrate complex; P^* is the reaction product; P^{**} is the soluble product*; CD* is an example of the lipolytic product acceptor used to solubalise the insoluble products at the interface via complex formation *CD-P*, k_1 is the kinetic constant associated with binding of substrate to enzyme; k_{-1} is the kinetic constant associated with dissociation of substrate from the complex, k_p is the kinetic constant associated with the adsorption of enzyme onto the interface, k_d is the kinetic constant associated with desorption of enzyme from the interface, k_T is the kinetic constant for reaction product formation, k_s is the rate

constant for insoluble product complex formation and K_2 also known as k_{cat} is the kinetic constant associated with catalysis. This particular constant (K_2 or k_{cat}) is the turnover number which estimates the rate of product formation [97].

The above model can be adapted to various interfacial structures such as monolayers at the oil-water interface, micelles and oil-in-water emulsions. By assuming that the surface concentration of the substrate remains constant during hydrolysis of short and medium-chain lipids, a simplified model of the enzymatic reaction can be derived (figure 5.4).

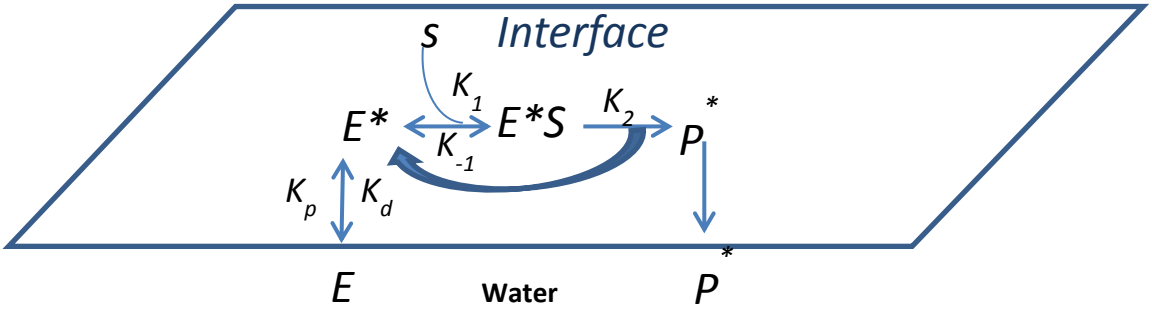

Figure 5.4: Hydrolysis of short- and medium- chain lipids with soluble reaction products[96].

The rate of an enzyme catalysed reaction,*v*, for a fixed enzyme concentration can be defined by the Michaelis-Menten formula (equation 5.12)[98]. The step by step derivation of the Michaelis-Menten equation can be found below[99].

It can be stated from the Michaelis-Menten model that:

$$the\ rate\ of\ E*S\ complex\ formation\ = k_1\,[E]\,[S] \qquad \text{(eq. 5.3)}$$

$$and,\ \ the\ rate\ of\ breakdown\ of\ E*S\ =\ (k_{-1}+\ k_2)\,[ES] \qquad \text{(eq. 5.4)}$$

Under the steady-state conditions, it can be assumed that the rate of formation is equal to the rate of breakdown of the *E*S* complex, which can be represented by equation 5.5 below:

$$k_1\,[E][S]\ =\ (k_{-1}+\ k_2)\,[E*S] \qquad \text{(eq. 5.5)}$$

By rearranging equation 5.5, we obtain:

$$[E][S]/[E*S] =\ (k_{-1}+\ k_2)/\ k_1 \qquad \text{(eq. 5.6)}$$

The equation 5.6 can be simplified by defining a new constant, K_m

$$K_m = (k_{-1} + k_2)/ k_1 \quad \text{(eq. 5.7)}$$

The rate constant, $k_m \approx k_{-1}/ k_1$ *if* $k_2 << k_{-1}$ (which indicates that the formation of product is the rate limiting step). If k_{-1} and k_1 are larger than k_2, k_2 can be referred to as k_{cat}. The k_{cat}/K_m ratio can be used to assess the tendency of the enzyme-substrate complex to dissociate or form product[100]. By substituting equation 5.6 with equation 5.7 gives equation 5.8 below.

$$[E * S] = [E][S]/ K_m \quad \text{(eq. 5.8)}$$

Furthermore, given that the concentration of the enzyme present is lower than that of the substrate, it can be assumed that the concentration of unoccupied enzymes *[E]* is equal to the total enzyme concentration $[E]_T$ minus the concentration of the *E*S* complex *[E*S].*

$$[E] = [E]_T - [E * S] \quad \text{(eq. 5.9)}$$

By substituting the above equation 5.9 in equation 5.8 produces equation 5.10:

$$[E * S] = [E]_T - [E * S]\,[S]\,/K_m \quad \text{(eq. 5.10)}$$

By solving the equation 5.10 for *[E*S]*, it gives:

$$[E * S] = [E]_T[S] / [S] + K_m \quad \text{(eq. 5.11)}$$

The initial catalytic rate of the substrate-enzyme reaction, *v*, can be expressed as equal to the product of *[E*S]* and the kinetic constant associated with catalysis process *(k_2).* Whereas, the maximum rate, V_{max} , is attained when all the enzyme catalytic sites are saturated with the substrate and therefore, *[E*S]* = $[E]_T$ and it can be expressed as: $V_{max} = k_2[E]_T$ [102]. By substituting this expression into the above equation 5.11, generates the Michaelis-Menten equation (equation 5.12):

$$v = \frac{V_{max}\,[S]}{k_m + [S]} \qquad \text{(eq. 5.12)}$$

The K_m value is also referred to as the true dissociation constant for the enzyme-substrate binary complex and it can be used to determine the stability of the complex. This parameter can be defined as the concentration of the substrate *[S]* at which the initial rate, *v*, is half of the maximum velocity (V_{max}) of an enzyme catalysed reaction, at equilibrium (figure 5.5). The V_{max} corresponds to the rate at which all the enzymes are fully occupied by the substrate in the catalysis process, given that there is a presence of high concentration of the substrate used. The attainment of a low k_m and a high V_{max} value is ideal for an effective enzymatic biosensor[101].

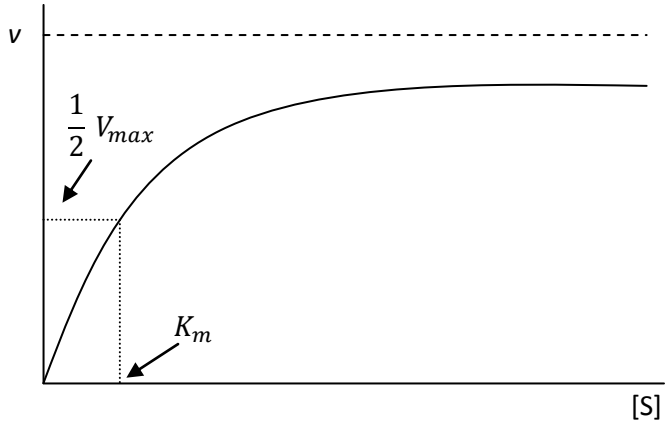

Figure 5.5: The Michaelis-Menten saturation plot for an enzyme catalytic reaction[102].

The Michaelis-Menten plot (figure 5.5) and the Michaelis-Menten formula (equation 5.12) primarily demonstrate that a first order process and the initial reaction rate enhances with the substrate concentration given that *[S]* is low and *[S]* < K_m. Following this, as the rate becomes constant and independent of the substrate concentration when *[S]* is high and *[S]* > K_m, a second-order reaction takes place and at this point, *v* = V_{max}. When *[S]* =K_m, then *v* = V_{max} [½] [102].

Apart from the Michaelis-Menten model for substrate-enzyme catalytic reaction, a Verger *et al.* model can be adapted to illustrate the scooting and hopping mode of enzyme action. The scooting mode can be defined as the kinetic situation whereby the enzyme molecules are restrained to the interface over many catalytic cycles and the characteristic time of enzyme partitioning is larger than the time required for catalysis step to complete. As a result, better catalytic efficacy and enzymatic rate can be achieved. In contrast, hopping mode occurs when the enzyme molecules desorbs from the interface. This leads to lower catalytic efficiency and

a reduction in the enzymatic rate.[103] However, since the enzyme activity and the partitioning of the enzyme between the aqueous and lipid interface are difficult to measure simultaneously using both the Verger *et al.* and the Michaelis-Menten models, kinetic information such as the k_{cat} (kinetic constant associated with catalysis), Km (Michaelis-Menten constant) and K_i (inhibition constant) values therefore cannot be obtained via these systems. Thus, the kinetic parameters can be alternatively determined by rearranging the Michaelis-Menten equation in the form of straight line (y = mx +c) models i.e. using the Lineweaver – Burk and Hanes-Woolf plots[104].

5.8 Glycerol dehydrogenase

Glycerol dehydrogenase (GDH) can be extracted from a number of different organisms such as bacteria[105], yeast[106] and mammals[107]. These enzymes are classified into groups depending upon the site of oxidation of the glycerol and the nature of coenzyme required. In anaerobic environment, many microorganisms use the glycerol as a carbon source via the coupled oxidative and reductive pathways. The utilisation of glycerol in such way is catalysed by GDH which in turn leads to formation of dihydroxyacetone with concomitant reduction of the coenzyme NAD^+ to NADH (scheme 5.2) [108]. The dihydroxyacetone is then phosphorylated by dihydroxyacetone kinase before entering the glycolytic pathway for further degradation[109].

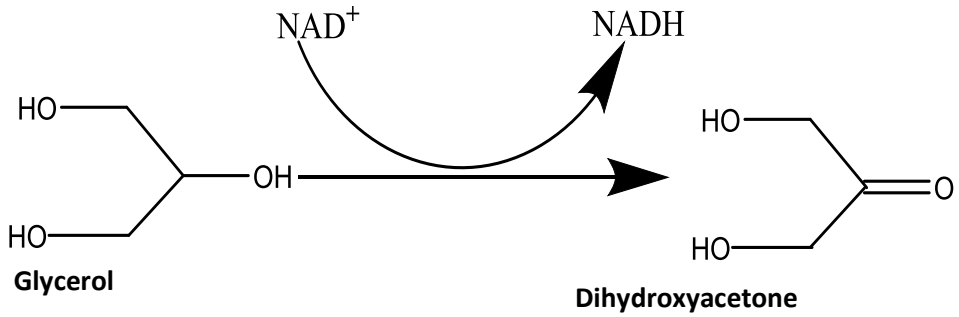

Scheme 5.2: Glycerol oxidation pathway[108].

The enzymes consist of a Zn^{2+} dependent polypeptide chain as the proteins require a divalent metal ion for catalysis[110]. The single polypeptide chain is made up of 370 residues and exists as a homooctamer in the solution[111]. The GDH subunit is composed of components such as 9 β strands, 14 α helices as well as a number of loops all of which together fold into 2 domains that are separated by a deep cleft. The active site of the enzymes lies in the cleft with the catalytic zinc ion playing a role in stabilizing an alkoxide intermediate (figure 5.6) [112].

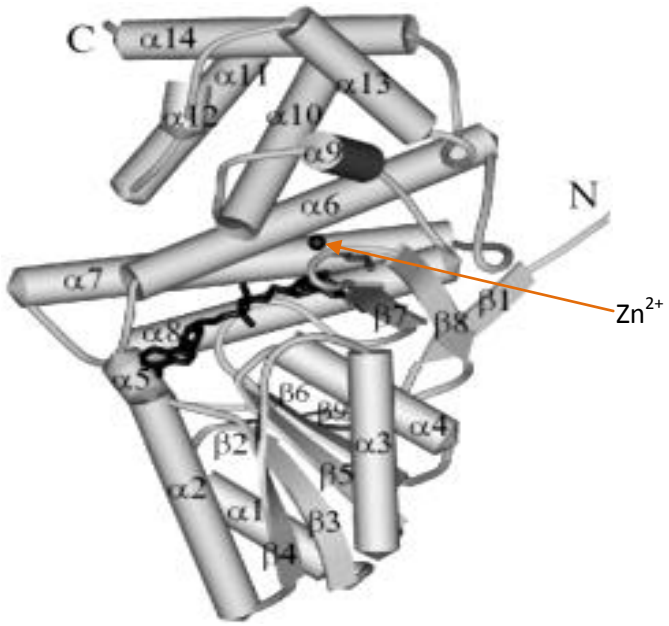

Figure 5.6: Stereo representation of α helices and β strands for GDH subunit along with the presence of Zn^{2+} ion (grey sphere) in the middle (Ruzheinikov *et al*, 2001) [108].

Both, the NAD and glycerol binding sites are found to be in the vicinity of the catalytic Zn^{2+} ion present in the GDH complex. The metallo-enzyme displays maximum activity between pH 6.0-8.5[113]. In the presence of the GDH enzyme, glycerol is oxidised by NAD^+. The NADH produced as a result is then oxidised by the mediator which in turn is reduced in the process.

5.9 NAD^+/NADH dependent dehydrogenases

In the amperometric enzyme electrode, the NAD^+/NADH coenzymes usually shuttles between the enzyme and the electrode and therefore, plays a vital part in a range of redox reactions involving various types of enzymes such as dehydrogenases and flavin bound diaphorase[114]. The NADH dependent enzymatic reactions occur by an ordered bisubstrate mechanism. The initial step involves the oxidised form of the coenzyme (NAD^+) to bind to the apoenzyme (enzyme without bound cofactor) which leads to formation of holoenzyme. The holoenzyme then binds to the substrate and reaction takes place between the bound coenzyme and substrate. This in turn is followed by the dissociation of the product and reduced coenzyme (NADH) to complete the catalytic cycle[115]. The NADH produced is then reoxidised to form NAD^+ at the working electrode. This can be represented by the following scheme 5.3.

$$NADH \xrightarrow{-2e^- - H^+} NAD^+$$

Scheme 5.3: Step for oxidation of the reduced NADH coenzyme[116].

The oxidation and reduction processes of the cofactor are controlled by the presence of redox species. The current flowing at the working electrode is then related to the concentration of the substrate present. For NADH –dependent dehydrogenases based reactions both the enzyme and coenzyme need to be present at the electrode. In order to ensure this both the enzyme and the coenzyme are for example, entrapped using a membrane[117].

5.10 Diaphorase

Diaphorase (DP) enzymes are ubiquitous class of flavoprotein (consists of iron-sulphur centres) and they can be obtained from various bacteria[118], plants[119] and mammalian organs[120]. These enzymes are involved in catalysing the reduction of various redox species via electron transfer from NADH. As a result, the mediator acts as a hydrogen acceptor (from the reduced form of di- and tri-phophopyridine nucleotides such as NADH) and leads to production of enzymatically active NAD^+ [121]. This can be represented in the form of scheme 5.4.

$$\mathbf{NADH + H^+ + OXIDISED\ ACCEPTOR \longleftrightarrow NAD^+ + REDUCED\ ACCEPTOR}$$

Scheme 5.4: Step for oxidation of the reduced NADH coenzyme[121].

The catalytic function of the enzyme as stated above makes the DP based electrodes useful for detecting substrates of various NADH/NAD^+ coupled enzymes[122].

5.11 Lineweaver –Burk plot

The Lineweaver –Burk plot or the double reciprocal plot are usually used to obtain important enzymatic kinetic data such as the K_m and V_{max} values. It was developed in 1934 and it is generated by taking the reciprocal of both parts of the Michaelis-Menten equation (equation

5.12) that can be represented in the form of a straight line with the equation y = mx + c (equation 5.13)[123].

$$\frac{1}{V} = \frac{K_m}{V_{max}}\frac{1}{[S]} + \frac{1}{V_{max}} \qquad \text{(eq. 5.13)}$$

When the linear equation is plotted in the form of Lineweaver –Burk plot, the y – intercept is equivalent to $1/V_{max}$ and the x-intercept represents $-1/K_m$ while the slope is equal to K_m/V_{max} as can be observed in the graph below (figure 5.7)[124].

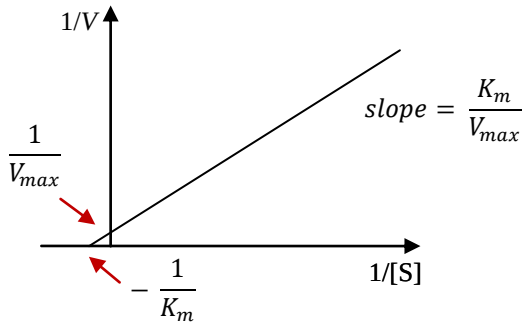

Figure 5.7: Lineweaver-Burk plot[124].

The Lineweaver-Burk plot is the simplest method of attaining enzymatic kinetic information. However, the disadvantage associated with this plot is that since it is a double reciprocal graph, the errors can be significant as the experimental values taken into account for calculating the K_m value are likely to be overemphasised when a low substrate concentration is analysed[125].

5.12 Mediators

Over the years, mediators have been used to overcome drawbacks associated with biosensors such as slow electron exchange and electrode fouling. The effect of oxygen (O_2) as a mediator was initially investigated using GOx enzyme by Clark *et al.* in 1962, a metalloflavoenzyme consisting of two flavin adenine dinucleotide (FAD) and two iron components, which is the most commercially used enzyme for construction of glucose sensors for self-monitoring diabetics. The findings have revealed that due to inconsistency in the level of ambient oxygen concentration at the enzyme sensing site, the amount of H_2O_2 produced and detected as it is reduced at the electrode was ambiguous. The glucose oxidation reaction

occurring at the electrode in the presence of GOx enzyme and where oxygen was used as the mediator is illustrated in scheme 5.5 below[128].

$$Glucose + GOx(FAD) + 2H^+ \longrightarrow \textit{gluconolactone + GOx(FADH}_2\textit{)}$$
$$GOx(FADH_2) + O_2 \longrightarrow GOx(FAD) + H_2O_2$$
$$H_2O_2 \longrightarrow O_2 + 2H^+ + 2e^- \textit{ (at electrode surface)}$$

Scheme 5.5: showing enzymatic oxidation of glucose in the presence of GOx and O_2[128].

In order to overcome the limitation of varying O_2 concentration as observed with the first-generation amperometric glucose biosensors, 'second-generation' electrodes were developed by Cass *et al.* in 1984 which involved the use of Fc derivatives such as ferrocene carboxylic acid as the mediator in the place of O_2 [129]. The reaction involving enzymatic oxidation of glucose in the presence of GOx and Fc can be represented by scheme 5.6 below[130]:

$$Glucose + GOx(FAD) + 2H^+ \longrightarrow \textit{gluconolactone + GOx(FADH}_2\textit{)}$$
$$GOx(FADH_2) + 2Fc^+ \longrightarrow GOx(FAD) + 2Fc + 2H^+$$
$$2Fc \longrightarrow 2Fc^+ + 2e^- \textit{ (at electrode surface)}$$

Scheme 5.6: showing enzymatic oxidation of glucose in the presence of GOx and Fc[130].

Another type of second-generation biosensor involving wired enzyme electrodes for glucose measurements was made by Heller *et al.* in 1987. The GOx enzyme was wired on to the electrode surface with an elongated and flexible hydrophilic redox polymer which can easily bind with the enzyme. Thus, it drastically decreased the distance between the redox center of the polymer and the FAD part of the enzyme. As a result, the electrons were transferred via the polymer film between the GOx enzyme and electrodes and, a fast response and a high current output was obtained without the loss of mediators in the process[131].

5.13 Gold nanoparticles as mediators

Metal based nanoparticles have been found to be often used in both non-enzymatic and enzymatic reactions and they are an integral part of biosensor design because of its ability act as an efficient re-dox mediator. Different types of nanoparticles for example, gold and gold-

platinum alloy, nanoparticles are widely used in the design of electrochemical biosensors and in biofuels[132]. The nanostructures in recent years were found to have various applications in different fields such as the biomedical sciences, optics, electronics, energy storage, magnetism and electrochemistry[133]. Current publications have demonstrated that the nanoparticles can be successfully combined with enzymes to modify electrodes which have been of interest in the biotechnology and bioanalytical chemistry industries. Gold nanoparticles (AuNPs) are now used as the most common model for various interfacial studies since the surface chemistry of these nanostructures in interfacial processes is well known[134]. The AuNPs also have been found to improve the performance of biosensors significantly due to its beneficial characteristics such as large surface area, exceptional biocompatibility and the ability to act as an excellent red-ox mediator[135]. The AuNP based biosensors for evaluating glucose oxidase activity has been explored extensively over the years which revealed that these nanoparticles are capable of minimising the insulating effect of the protein shell and therefore, allowing direct electron transfer without any interference[136]. The AuNPs were modified using *Fc* to generate an even more effective re-dox mediator which enhances electron mediation between the electrode and the enzyme re-dox center, leading to an increase in the rate of enzyme reaction and a faster time response for detecting specific substrates is also achieved.

5.14 Immobilisation of AuNPs and enzymes on electrode surface

Li *et* al.[137] and Bharathi *et* al.[138] have stated that the immobilisation of the AuNPs and the GOx enzyme on the surfaces of gold and indium tin oxide based electrodes displayed a fast electron transfer between the enzyme redox centre and the sol-gel/AuNP based electrode and it also demonstrated an enhanced stability. Chang *et* al.[139] on the other hand have reported that the AuNP modified glassy carbon macroelectrodes showed a glucose detection limit ranging from 0.1 mM to 25 mM and an increase in sensitivity and stability was also observed using the cyclic and linear voltammetry techniques, whilst the free form of GOx enzyme was added to the 0.5 M of sulfuric acid aqueous solution. In contrary, it was established that the immobilisation of the AuNPs along with the GOx enzyme on the carbon electrode led to instability and a decrease in the selectivity of the enzyme for the glucose substrate. In order to overcome this problem, a sol-gel matrix composed of FcAuNPs and GOx/GDH enzymes were drop-casted on to the surfaces of the glassy carbon macroelectrodes and SPEs to examine the activities of the GOx and GDH enzymes. The sol-gel silicate matrix was used to

attain chemical inertness, physical rigidity, permeability and thermal stability which are required to fabricate a well-functioned enzymatic biosensor[140].

5.15 Methods/Techniques used

5.15.1 Cyclic voltammetry

In this chapter, cyclic voltammetry has been used to qualitatively determine the change in current with increase in concentration of the analyte and also, to calculate Km values for GOx and GDH enzymes (more information on CV can be found in the experimental methodology chapter).

5.15.2 Chronoamperometry

Chronoamperometry (CA) has been used in this chapter to confirm the data obtained using CV for the GOx, GDH and lipase enzymes. More information on CA can be found in the method chapter.

5.15.3 Wide angle-X-ray scattering

Wide angle-X-ray scattering (WAXS) has been used to determine the crystalline structure of the sol-gel/FcAuNP mixture and to characterise the nanoparticles by analysing the Bragg peaks scattered at wide angles due to coherent scattering from the crystalline lattice planes (more information on WAXS can be obtained from the experimental methodology chapter).

5.15.4 Environmental scanning electron microscope

Environmental scanning electron microscope (ESEM) in this study was used to evaluate the size range of the sol-gel/FcAuNP mixture particles. A 0.3 µL of the sol-gel/FcAuNP mixture was gently sonicated for 30 minutes to ensure the particles were separated before drop-casting the solution onto a silica wafer and analysing it using ESEM. More information on ESEM can be found in the experimental methodology chapter.

5.15.5 Transmission electron microscopy

Transmission electron microscopy (TEM) has been applied to identify the FcAuNPs dispersed within the sol-gel matrix which in turn is used to immobilise the enzyme(s) and the mediator

to the working carbon electrode. More information on TEM can be found in the in the experimental methodology chapter.

5.15.6 Screen printed electrodes

Screen printed electrodes (SPEs) have been modified using sol-gel and FcAuNPs to investigate the GOx, GDH and lipase enzyme activity**.** More information about the sol-gel process and the method followed for preparing the sol-gel/FcAuNP based SPEs as biosensors can be found in the experimental methodology chapter).

5.16 Characterisation of sol-gel/ FcAuNP mixture for the biosensor

The sol-gel/FcAuNP mixture was characterised using ESEM and WAXS techniques (figure 5.8). The sizes of the sol-gel particles mixed with FcAuNPs were determined to be within the range of 239 – 842 nm, using ESEM (figure 5.8a). The average sol-gel/FcAuNP particle size was determined to be 440 nm.

(a)

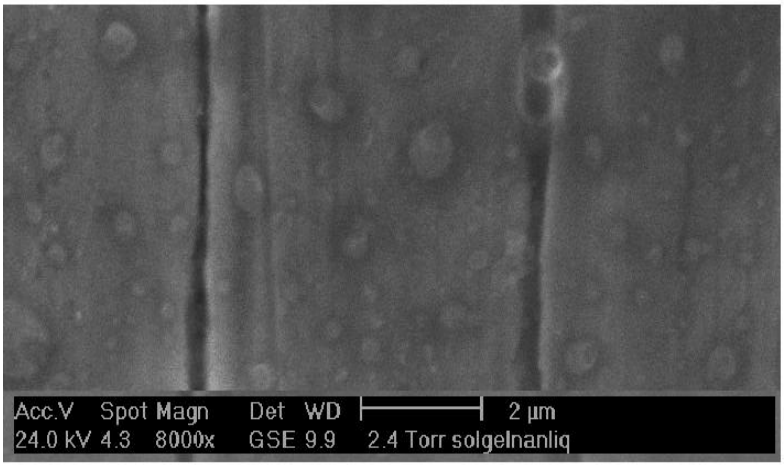

(b)

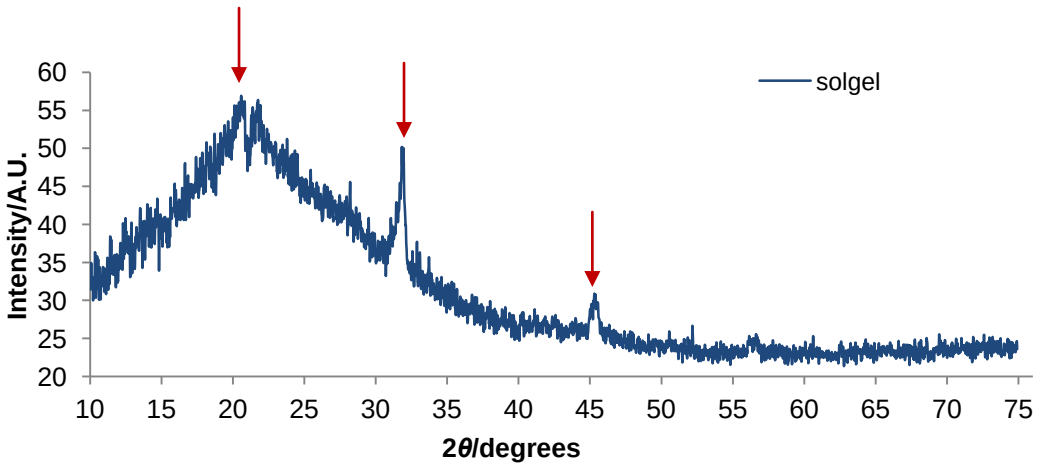

(c)

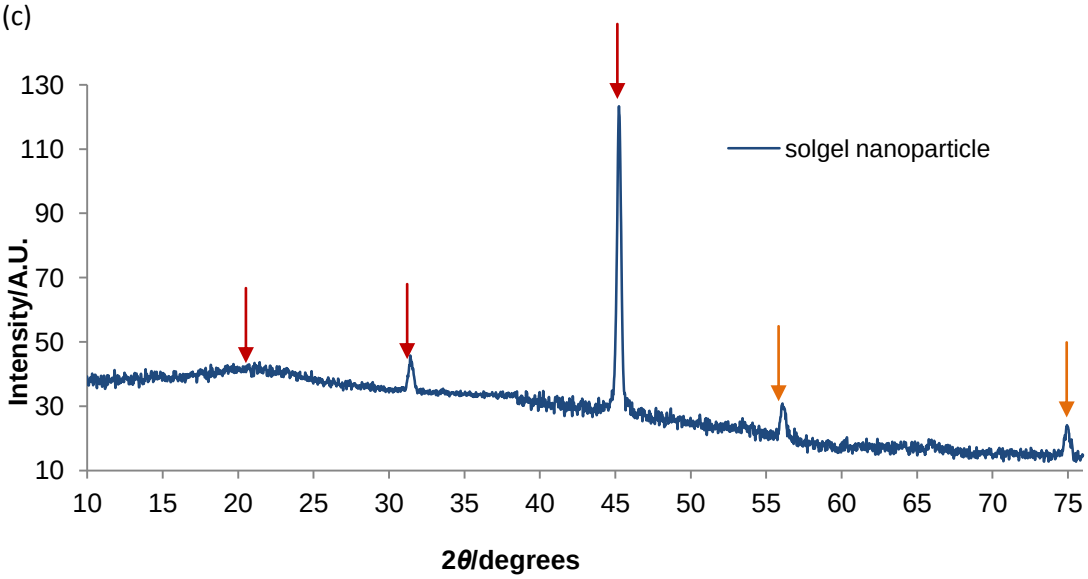
130
110
90
70
50
30
10
Intensity/A.U.
10 15 20 25 30 35 40 45 50 55 60 65 70 75
2θ/degrees
solgel nanoparticle

(d)

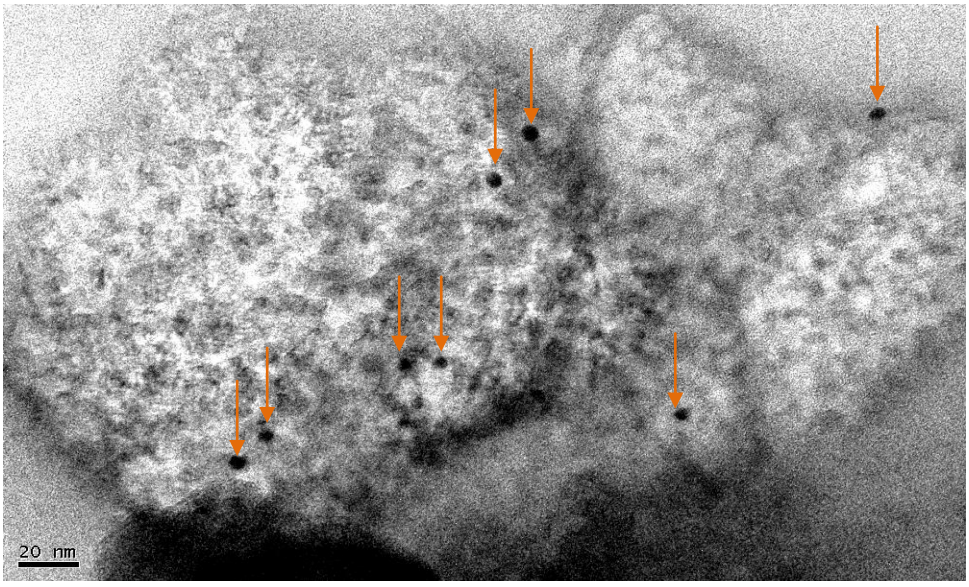
20 nm

(e)

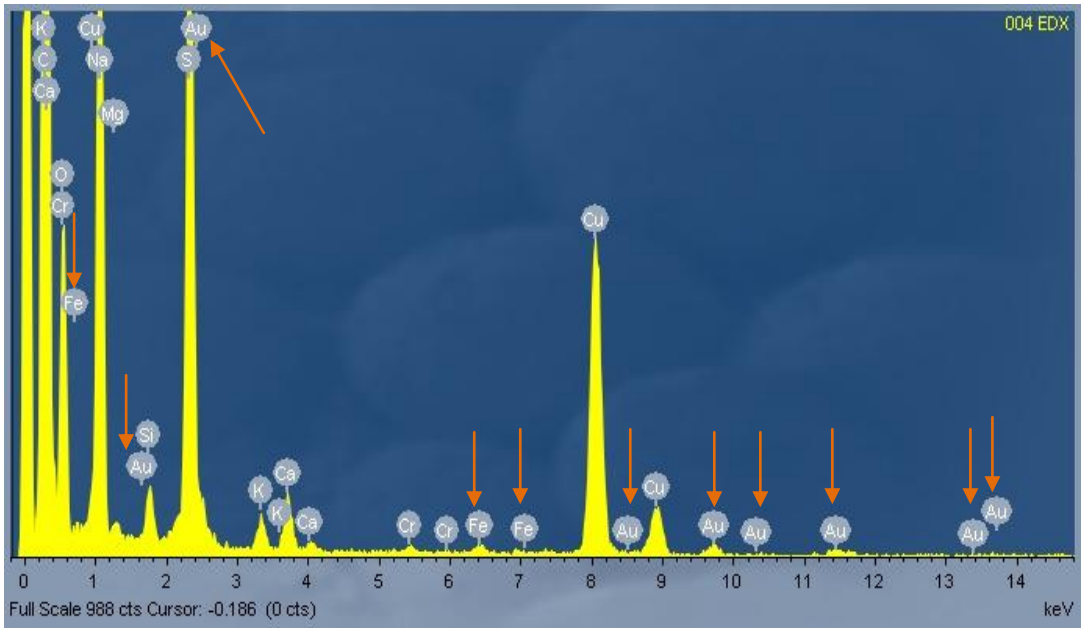

Figure 5.8: (a) ESEM images of the different sizes of the sol-gel/FcAuNP, (b) WAXS data for the sol -gel particles , (c) WAXS data for sol –gel/FcAuNP, (d) TEM image of the sol-gel/FcAuNP matrix and (e) EDX analysis of the of the sol-gel/FcAuNP matrix . The red arrows in figures 5.8b and 5.8c indicate WAXS peaks which belong to the sol-gel mixture and the orange arrows represent peaks and images specific to FcAuNPs in figures 5.8c-5.8e.

Furthermore, the WAXS analysis of the dried sol-gel/FcAuNP mixture has shown presence of peaks specific to the sol-gel mixture at 2θ values of 20^{o}, 32^{o} and 45^{o} (figures 5.8a and 5.8b). Additional peaks corresponding to FcAuNPs, which are added and mixed with the sol-gel solution, were identified at 2θ of 56^{o} and 74^{o} (figure 5.8c). The peak at 45^{o} as observed for the sol-gel particles could be also due to the presence of the modified gold nanoparticles[144]. TEM analysis of the sol-gel/FcAuNP matrix also displayed presence of spherical shaped FcAuNPs with average diameter of 5.74 nm dispersed within and around the sol-gel clusters (figure 5.8d), which in turn was confirmed using the EDX coupled to the TEM. Elemental analysis of the sol-gel/FcAuNP matrix has demonstrated the presence of ferrocene (Fc) and gold (Au) particles corresponding to FcAuNPs (figure 5.8e).

5.17 Results and Discussion

5.17.1 Sol-gel/ FcAuNP/GOx based enzymatic macroelectrode

The sol-gel and FcAuNP based macroelectrode biosensor was used to initially investigate the activity of the standard GOx enzyme in pH7 buffer solution using cyclic voltammetry and choronoamperometry techniques. GOx was chosen as the standard because it is one of the most well studied enzymes and its kinetic data such as the Km value for a similar system to which is investigated in this chapter can be easily found and compared.

Li *et* al.[137] and Bharathi *et* al.[138] have stated that the immobilisation of the AuNPs and the GOx enzyme on the surfaces of gold and indium tin oxide based electrodes displayed a fast electron transfer between the enzyme redox centre and the sol-gel/AuNP based electrode and it also demonstrated an enhanced stability. Chang *et* al.[139] on the other hand have reported that the AuNP modified glassy carbon macroelectrodes showed a glucose detection limit ranging from 0.1 mM to 25 mM and an increase in sensitivity and stability was also observed using the cyclic and linear voltammetry techniques, whilst the free form of GOx enzyme was added to the 0.5 M of sulfuric acid aqueous solution. In contrary, it was established that the immobilisation of the AuNPs along with the GOx enzyme on the carbon electrode led to instability and a decrease in the selectivity of the enzyme for the glucose substrate. In order to overcome this problem, a sol-gel matrix composed of FcAuNPs and enzymes were drop-casted on to the surfaces of the glassy carbon macroelectrodes and SPEs to examine the activities of the GOx and GDH enzymes. The sol-gel silicate matrix was used to attain chemical inertness, physical rigidity, permeability, mechanical and thermal stability which are required to fabricate a well-functioned enzymatic biosensor[140,145,146]. FcAuNPs were manipulated to enhance the conductivity and the electron transfer kinetics at the electrode/solution interface.

The cyclic voltammograms (CVs) obtained for the immobilised sol-gel/FcAuNP biosensor while the GOx enzyme and glucose were added to the pH7 buffer solution showed a decrease in the current with increase in the concentration of the glucose (figures 5.9a and 5.9c) contrary to the CVs collected for the immobilised sol-gel/FcAuNPs/GOx enzymatic biosensor (figures 5.9b and 5.9d) which demonstrated a rise in current with increase in glucose concentration. The solution and immobilised enzymes were compared to identify the most effective method for the attainment of enzyme stability and maximum efficiency. The glucose concentration for both systems involving GOx was increased by adding successive aliquots of the substrate in the buffer solution. After the addition of each aliquot of glucose, the solution

was gently swirled and left for a short period of time to reach equilibrium before a measurement was taken using CV.

The background CVs for both the solution and immobilised enzymes without the addition of glucose have shown presence of an oxidation peak which is generated due to the mediator (figures 5.9a and 5.9b). As the glucose concentration was enhanced for the system with GOx enzyme in solution, no correlation was observed between current and the substrate. However, for the immobilised GOx enzyme system, a rise in current of the oxidation peak with increase in glucose concentration was detected using CV, when compared to the background. This indicates that the GOx enzyme is more stable and it is capable of catalysing glucose oxidation reaction for longer without being deactivated by other compounds such as products of reaction in the buffer solution.

For both systems, the CV data was plotted in the form of current versus glucose concentration graphs (figure 5.9c). The current data was obtained from the oxidation peaks at -1.3 V for GOx in solution and at 0 V for the immobilised GOx enzyme. From the figure 5.9c (orange squares), a steep rise in the current was observed as the concentration of glucose was increased up to 3 mM. Beyond this point, as the glucose concentration was enhanced from 3-5 mM a steady state current was observed using the immobilised sol-gel/FcAuNP/GOx enzymatic biosensor, indicating the attainment of enzyme saturation. It is also a characteristic of an enzyme catalytic reaction (figure 5.9c).

(a)

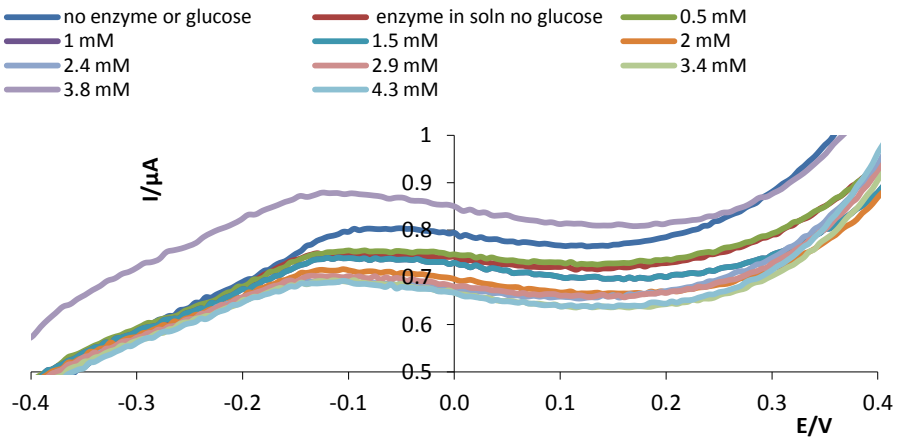

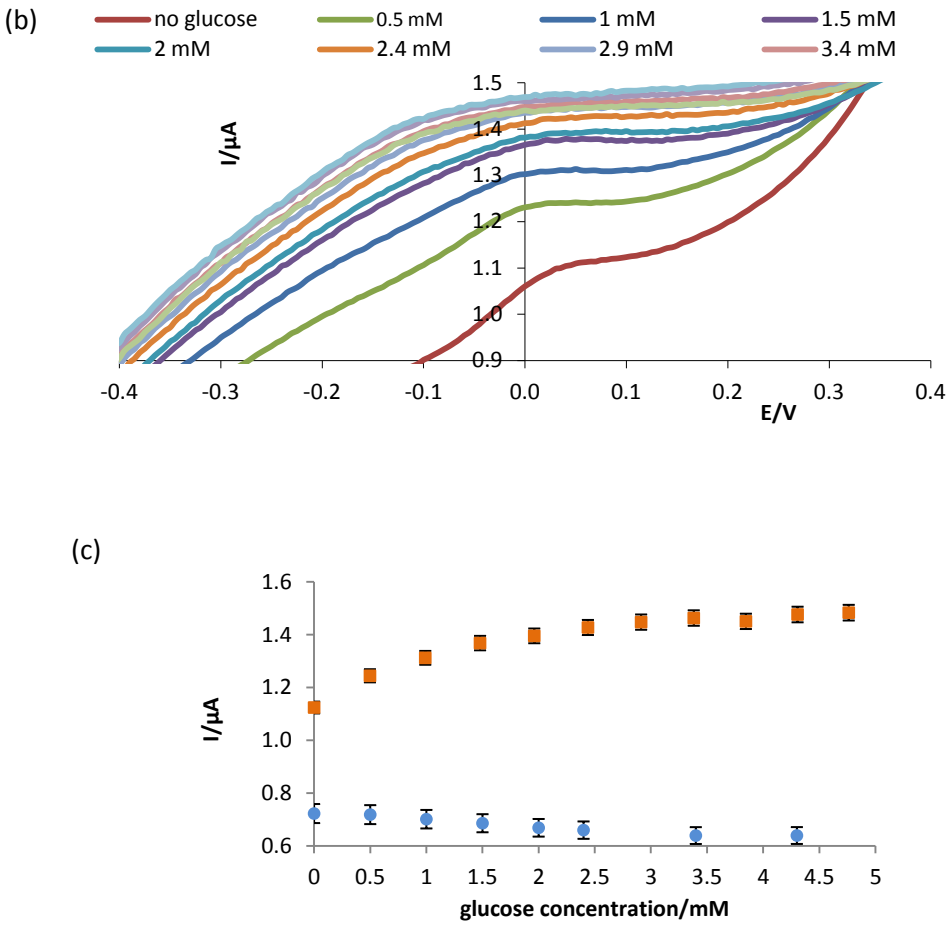

Figure 5.9: (a) CVs for GOx in solution, (b) CVs for immobilised sol-gel/FcAuNP/GOx enzymatic carbon macroelectrode and (c) shows the change in current against glucose concentration plot for GOx in solution (blue circles) and for immobilised sol-gel/FcAuNP/GOx enzymatic macroelectrode (orange square).

The current against time transient (figure 5.10) reflect the same findings as obtained using the CV for the drop-casted sol-gel/FcAuNP/GOx based biosensor. The results demonstrate that the enzyme efficiency and electron mediation increases when the GOx enzyme is immobilised on the surface of the carbon electrode.

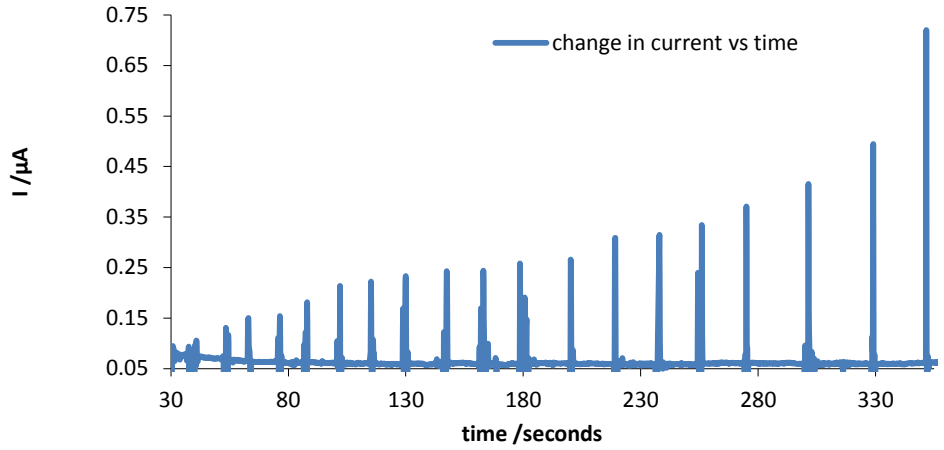

Figure 5.10: showing CA for immobilised sol-gel/FcAuNP/GOx enzymatic carbon macroelectrode.

The efficacy of the immobilised GOx enzyme in converting glucose into gluconic acid was expressed in the form of Michaelis constant (km) value which in turn was determined using the Lineweaver-Burk plot (figure 5.11) below. The km value was calculated to be 1.5 $\pm$ 0.01 mM for the immobilised solgel/FcAuNP/GOx enzymatic carbon macroelectrode (see appendix table A2.1) which is much lower than the literature value of 7.4 mM as stated for an immobilised AuNP/GOx/graphite based biosensor in sodium phosphate buffer solution[147].

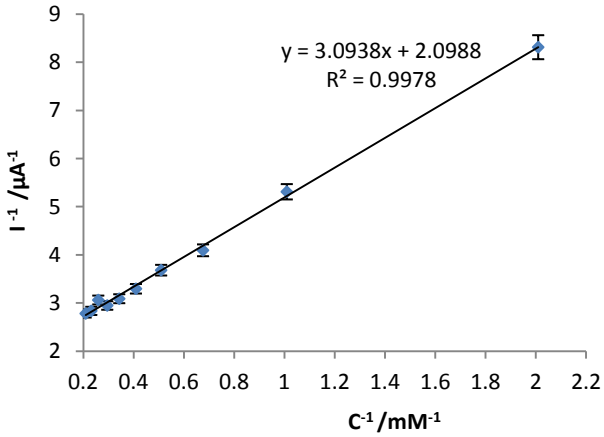

Figure 5.11: Lineweaver-Burk plot showing the reciprocal of change in current against the reciprocal of glucose concentration. The graph was plotted using the CV data obtained for the immobilised sol-gel/FcAuNP/GOx carbon macroelectrode.

Furthermore, GOx enzyme immobilised in platinum nanoparticles (PtNP) and mesoporous carbon matrix followed by fixation on the surface of the carbon electrode using gelatin and also, by cross-linking it with glutaraldehyde have been reported to exhibit a much higher km value of 10.8 mM, with a linear response to glucose concentration within the range of 0.04-

12.2 mM. Further modification of the PtNP/mesoporous carbon matrix/GOx based bioelectrode with a Nafion film displayed interference from the electroactive compounds to the glucose response as the glucose concentration was enhanced to 5.6 mM[148].

5.17.2 Sol-gel/ FcAuNP/NAD^+- dependent DP and GDH multi- enzymatic macroelectrode and - SPE

The procedure for developing the immobilised sol-gel/FcAuNP/GOx enzyme based biosensor was repeated by replacing the GOx enzyme with NAD^+ - dependent DP and GDH enzymes. The current measured using the immobilised sol-gel/FcAuNP/ NAD^+ - dependent DP and GDH enzymatic bioelectrode was plotted against the glycerol concentration, which showed a similar trend as identified with the immobilised sol-gel/FcAuNP/GOx based biosensor (figure 5.12a). It was established that the current response increased with a rise in the glycerol concentration upto 2 mM (figures 5.12a, 5.12b and 5.12c – green circles). The chronoamperometry technique was found to be much more sensitive than the CV and it revealed that the modified enzymatic biosensor can detect glycerol concentration upto 7 mM and an anodic current response is attained within 11.4 seconds (figure 5.12b).

(a)

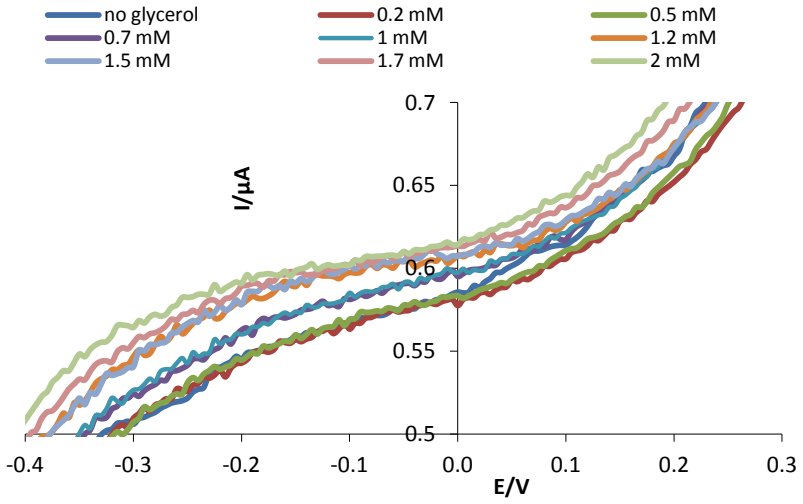

(b)

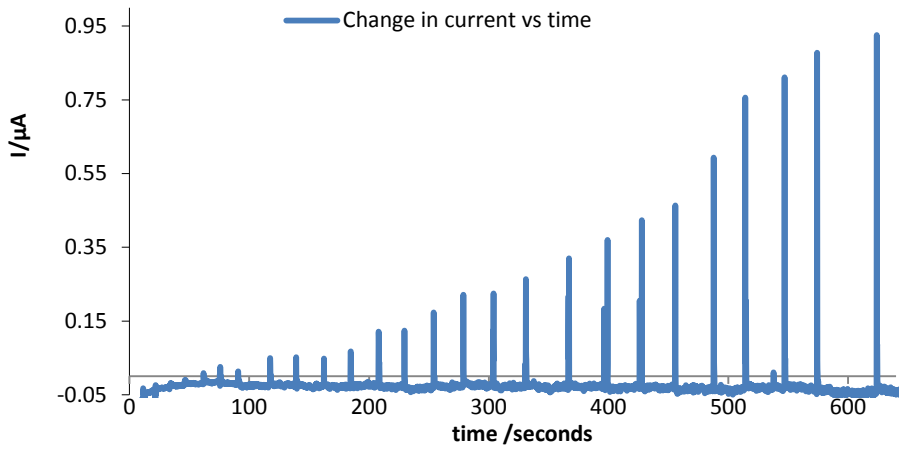

(c)

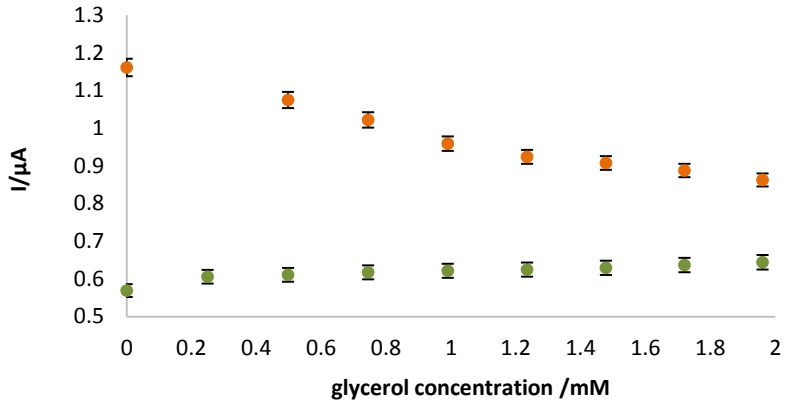

Figure 5.12: (a) CVs obtained at a scan rate of 50 mVs^{-1} for the immobilised sol-gel/FcAuNP/NAD^+- dependent DP and GDH enzymatic macroelectrode, (b) CA obtained for the immobilised sol-gel/FcAuNP/NAD^+- dependent DP and GDH enzymatic macroelectrode and (c) change in current against glycerol concentration graph for the GDH in solution (orange circles) and the immobilised sol-gel/FcAuNP/NAD^+ - dependent DP and GDH enzymatic macroelectrode (green circles) plotted using CV data from figure 5.12a and 5.13.

The narrow concentration range detected using the sol-gel/FcAuNP/ NAD^+- dependent DP and GDH multi-enzymatic macroelectrode indicate that the GDH has slightly lower stability comparing to the GOx enzyme leading to prompt denaturation. The reaction mecahnism that is likely to occur at the electrode surface after the application of a forward potential is outlined below in scheme 5.6[149].

$$Glycerol + NAD^{+} \overset{GDH}{\leftrightharpoons} dihydroxyacetone + NADH + H^{+} \quad \text{(Step 1)}$$

$$H^{+} + NADH + FcAuNP_{(ox)} \overset{DP}{\leftrightharpoons} FcAuNP_{(red)} + NAD^{+} \quad \text{(Step 2)}$$

$$FcAuNP_{(red)} \xrightarrow[\text{Amperomeric measurement, E, 0.300 V}]{} FcAuNP_{(ox)} \quad \text{(Step 3)}$$

Scheme 5.6: shows the reaction mechanism occurring at the surface of the immobilised sol-gel/FcAuNP/ NAD^{+} - dependent DP and GDH multi-enzymatic working electrode.

It was also observed that when the GDH enzyme and glycerol were present in solution, the effectiveness of the GDH enzyme in biotransformation of the glycerol into dihydroxyacetone product was reduced (figure 5.13 b (orange circles) and figure 5.14).

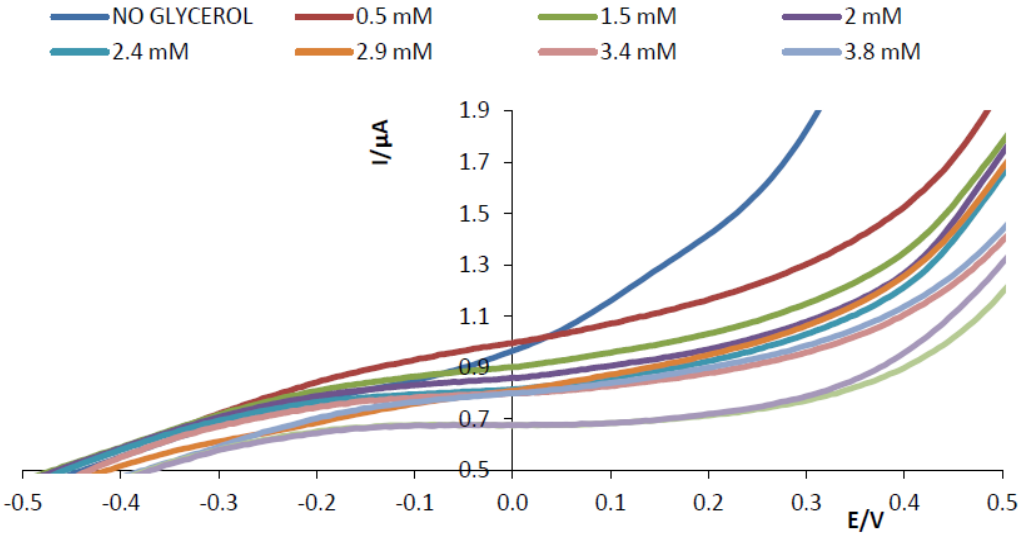

Figure 5.13: CVs obtained using the sol-gel/FcAuNP based macroelectrode while glycerol, NAD^{+} - dependent DP and GDH enzymes were added to the buffer solution.

The results obtained using the immobilised sol-gel/FcAuNP/ NAD^{+}- dependent DP and GDH multi-enzymatic macroelectrode was found to coincide well with the CVs collected using the immobilised sol-gel/FcAuNP/ NAD^{+} - dependent-DP and GDH based SPE (figure 5.14a). A similar trend in the linear response range was obtained as observed with the modified GDH macroelectode and an increase in current with an increase in the concentration of glycerol was identified with the modified SPEs (figures 5.14a and 5.14b).

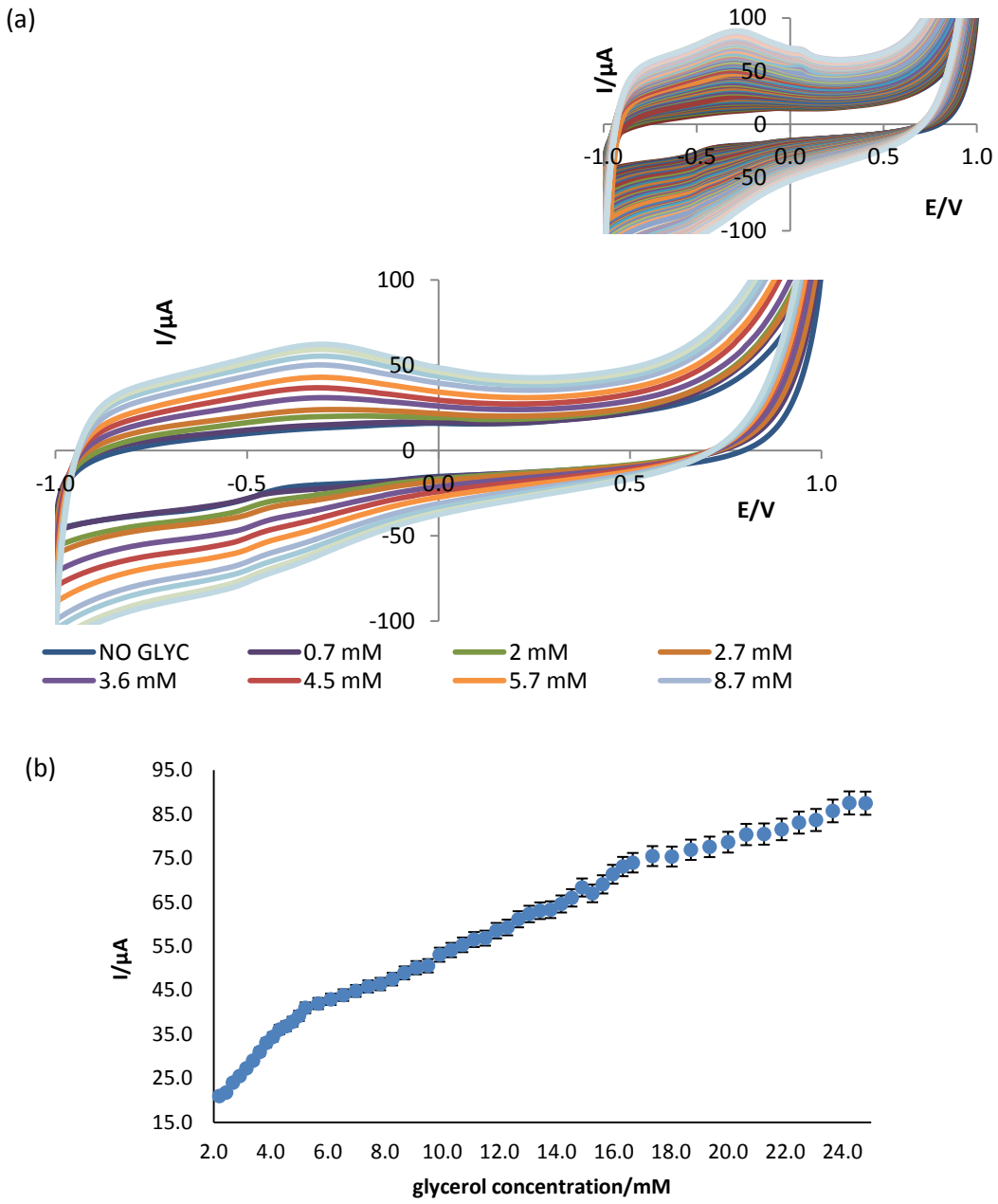

Figure 5.14: (a) CVs for glycerol concentration ranging from 0.7 mM – 12.7 mM (with inset showing CVs for 0.2 mM to 24.8 mM of glycerol concentration) and (b) current versus glycerol concentration graph plotted using CV data, for the immobilised sol-gel/FcAuNP/NAD^+ - dependent DP and GDH enzymatic SPE.

The current response of the modified NAD^+ - dependent DP and GDH enzymatic SPE (figure 5.14b) was found to increase 100 fold compared to the results obtained using the immobilised sol-gel/FcAuNP/NAD^+ - dependent DP and GDH enzymatic macroelectrode (figure 5.13c– green circles). This demonstrates that the modified SPE can exhibit enhanced sensitivity and improved signal to noise ratio in comparison to the modified macroelectrode. As a result, the

incorporation of FcAuNPs, NAD^+ cofactor and the enzymes in the sol-gel matrix enable efficient electron transfer and easy access of the substrate to the enzymes immobilised on the surface of the carbon SPE. From figure 5.14a inset and 5.14 b , it can be established that the immobilised sol-gel/FcAuNP/ NAD^+ - dependent DP and GDH enzymatic SPE is capable of detecting a wide range of glycerol concentration from 0.2 mM to 24.8 mM and a correlation coefficient of 0.9988 was also attained (figure 5.15b). Furthermore, a Km value of 4.9 $\pm$ 0.01 mM was established for the immobilised sol-gel/FcAuNP/ NAD^+ - dependent DP and GDH enzymatic-carbon macroelectrode in comparison to 5.4 $\pm$ 0.01 mM for the immobilised sol-gel/FcAuNP/ NAD^+ - dependent DP and GDH enzymatic SPE. The values were determined from the Lineweaver –Burk graphs (figures 5.15a-5.15b and see appendix table A2.2) shown below and were found to be lower than the literature value of 9.9 mM, which in turn was obtained using an immobilised GDH enzyme cross-linked with gluteraldehyde on the surface of a graphite electrode[150]. A lower km indicates that the immobilised sol-gel/FcAuNP/ NAD^+ - dependent DP and GDH enzyme based biosensors has a higher affinity for glycerol and requires a lower concentration of the substrate to attain the maximum rate of reaction.

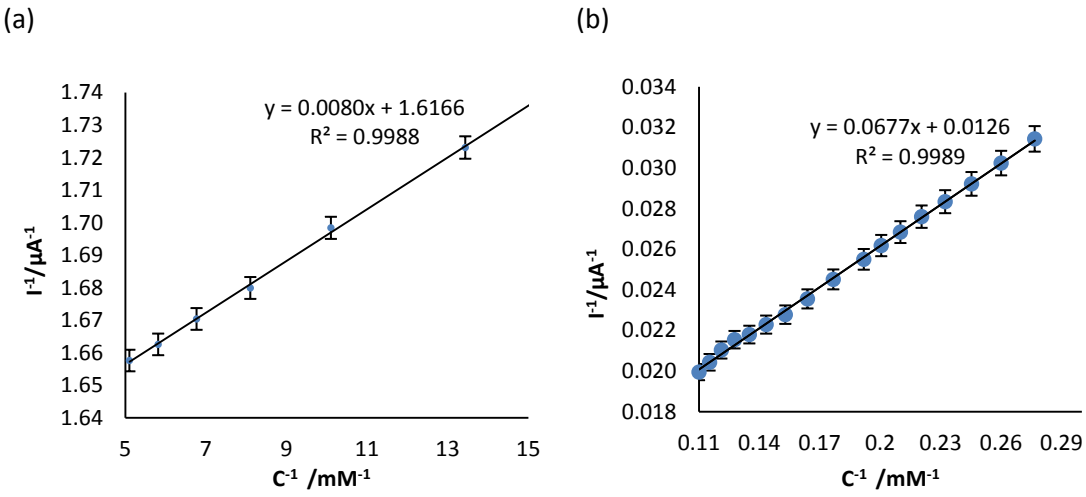

Figure 5.15: Lineweaver-Burk plots showing the reciprocal of change in the current against the reciprocal of glycerol concentration for (a) immobilised sol-gel/FcAuNP/ NAD^+ - dependent DP and GDH multi-enzymatic -carbon macroelectrode and (b) immobilised sol-gel/FcAuNP/ NAD^+ - dependent DP and GDH enzymes based SPE. The graphs were plotted from the CV data obtained using an immobilised sol-gel/FcAuNP/NAD^+ - dependent DP and GHD enzymatic - carbon macroelectrode and –SPE.

From further literature review, it was found that the biosensors constructed using GDH enzyme combined with phenazine methosulphate mediator, with and without cross-linking the protein with gluteraldehyde before immobilising the mixture on the surface of the carbon

electrode showed high km values of 12.1 mM and 33.5 mM respectively, in 0.05 M of potassium buffer solution at pH 7.3[151]. In another report, co-immobilisation of the lipase and the GDH enzymes using cerium oxide nanoparticles and multi-wall carbon nanotubes on a glassy carbon electrode combined with the fast Fourier transformation continuous cyclic voltammetry (FFTCCV) technique in a flow injection analysis system, demonstrated a response time of less than 25 seconds, a detection limit of 5.4 mM for the glycerol substrate and an initial sensitivity of 95.2% was also achieved which however gradually decreased over time due to a loss in the catalytic activity[152]. Thus, this confirms that the sol-gel based biosensors exhibit improved performance, higher enzymatic activity and selectivity for a specific analyte depending on the particular enzyme examined compared to other biosensors available to this date.

The Lineweaver-Burk plots obtained for the immobilised sol-gel/FcAuNP/ NAD^+ - dependent DP and GDH enzymatic-SPE using the CV data (figure 5.15a and 5.15b) showed linearity with high R^2 values of greater than 0.99. This signifies that the immobilised GHD enzymes follow the Michaelis-Menten model and it is also a characteristic expected of an enzyme catalysis-controlled amperometric biosensor[102]. Similar results were also obtained using the immobilised sol-gel/FcAuNP/GOx enzyme which displayed a linear line with R^2 value greater than 0.99.

5.17.3 Sol-gel/ FcAuNP/NAD^+- dependent DP and GDH multi- enzymatic – SPE in the presence of lipase and GTO in solution

Furthermore, from the CVs (figure 5.16a) collected using the sol-gel/FcAuNP/NAD^+ - dependent DP and GDH based enzymatic- SPE in the presence of lipase and GTO in solution, a linear increase in the current with an increase in the concentration of GTO was observed, up to 1.5 mM. Beyond this point, the current response declined as the concentration of GTO was enhanced above 1.5 mM, which was clearly reflected using CA and in the current versus GTO concentration graphs plotted using CV and CA data (figures 5.16a and 5.16b). This indicates that the detection limit for glycerol product generated from lipolysis of GTO was probably restricted due to competitive inhibition caused by the binding of increased amount of insoluble lipolytic products at the enzyme active sites and therefore, leading to deactivation of the lipase enzymes[153].

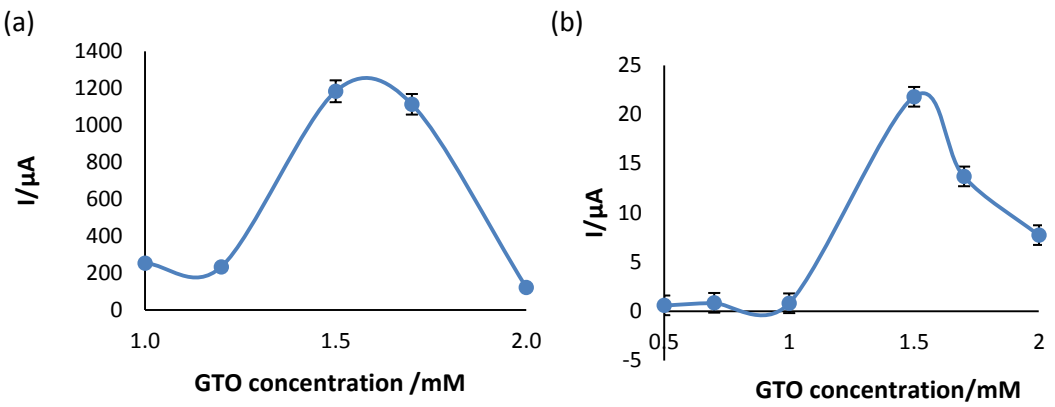

Figure 5.16: shows the change in current against GTO concentration using the data from (a) CVs and (b) CA, for the immobilised sol-gel/FcAuNP/ NAD^+ - dependent DP and GDH enzymatic SPE biosensor, in the presence of lipase and GTO in solution.

The lipase enzyme inhibition can be minimised for example, by immobilising the enzyme using sol-gel/FcAuNP matrix which should enhance the stability of the enzyme as observed with GOx and GDH enzymes by only allowing the triacylglyceride substrate molecules to reach and access the active site of the lipase and therefore, prevent chemical deactivation[154].

All of the above experiments were repeated twice and the results from the replicates reflected a similar trend as observed initially, that immobilisation leads to enhanced stability of the enzymes as opposed to the proteins in its free form in solution. This is because immobilising the enzymes in a sol-gel matrix only allows specific substrates to access the binding site and prevents other by-products/products from deactivating the proteins. A standard error for the km values was calculated by taking into account of the km values from the repeats and by applying the following equation 5.16:

$$SE = \frac{s}{\sqrt{n}} \qquad \text{(eq. 5.16)}$$

Where, *SE* is the standard error of the mean, *s* is the standard deviation of the mean and *n* is the number of repeats.

5.18 Conclusions

The study involving immobilised sol-gel/FcAuNP/enzymatic-biosensors have demonstrated a fast time response and an enhanced sensitivity and selectivity for specific substrates. These

characteristics make these bioelectrodes ideal devices for a range of biocatalyst and biotechnological applications compared to other feasible enzymatic biosensors available.

It was established that when the GOx and GDH enzymes were in solution and not immobilised with the sol-gel and FcAuNPs on to the electrodes, the current reduced with an increase in the concentration of glucose and glycerol substrates, respectively. This indicates a decrease in the enzyme activity. However, when both the GOx and the GDH enzymes were immobilised along with the sol-gel/ FcAuNP (and NAD^+ - dependent DP for the GDH biosensors) on to the surfaces of carbon electrodes, it was observed that the current increased with an increase in glucose/glycerol concentration, respectively. This demonstrates that the immobilised enzymatic biosensors enhance electron mediation between the re-dox center of the enzymes and the electrodes, leading to increased rate of enzymatic reaction. Furthermore, it was deduced that the enzymatic-biosensors have exhibited low Km values of 1.5 $\pm$ 0.01 mM (for the immobilised sol-gel/ FcAuNPs/GOx enzymatic- carbon macroelectrode biosensor), 4.9 $\pm$ 0.01 mM (for the immobilised sol-gel/ FcAuNPs/ /NAD^+ - dependent DP and GDH enzymatic - carbon macroelectrode based biosensor) and 5.4 $\pm$ 0.01 mM (for the immobilised sol-gel/ FcAuNPs/ /NAD^+ - dependent DP and GDH enzymatic SPE based biosensor) compared to the literature values of 7.4 mM (for an immobilised AuNPs/GOx enzymatic-biosensor)[147] and 9.9 mM (for an immobilised GDH enzymatic biosensor)[150], respectively. The sol-gel/ FcAuNPs/ NAD^+ - dependent DP and GDH based enzymatic- SPE was found to detect glycerol concentration ranging between 0.2 mM to 24.8 mM and exhibit a fast response time as well as a high correlation coefficient of 0.9903 was also attained. The simple yet cost effective and easily disposable miniature bioelectrodes displayed other desirable characteristics such as reusability, reproducibility, real time monitoring and higher specificity for the substrates. Overall, it can be suggested that the wiring of the FcAuNPs, which are used as mediators, along with the enzymes in a sol-gel matrix on the electrode surface led to an enhanced electron transfer and increased enzyme activity comparing to the other mediators used. This is probably because of the surface curvature of the AuNPs (1) modified with self-assembled monolayers (SAMS) of ferrocene headgroups which allows a favourable shift in redox potentials and (2) has a dramatic effect on the interaction between the headgroups of the SAMS. For example, the ferrocene headgroups of the SAMS for small NPs are further apart which leads to less electrostatic repulsion and an amplification in electron transfer[141].

In the presence of lipase and GTO in solution, it was observed that the sol-gel/ FcAuNP/NAD^+ - dependent DP and GDH based enzymatic- SPEs demonstrated an increase in

current with an increase in the GTO concentration upto 1.5 mM as a result of lipolysis. Beyond this point, the current was seen to decrease with a rise in GTO concentration. This suggests that the glycerol detection limit is probably restricted as a result of competitive inhibition by the insoluble lipolytic products present in the buffer solution [154].

By comparing the results obtained for the lipase enzyme in solution with the data collected for both the immobilised GOx and GDH enzymatic electrodes, it can be identified that there is an increase in current with an increase in substrate concentration, until a specific concentration is attained at which the current reaches a plateau due to enzyme saturation, for the immobilised GOx and GDH sensors. On the other hand, the current was observed to decrease drastically as the GTO concentration was enhanced above 1.5 mM in the presence of lipase enzyme in buffer. This indicates that the lipase enzyme in its free form in solution is likely to be deactivated via the by-products/products present and therefore, leading to a decrease in the lipase enzyme activity and efficacy.

Based on the findings observed using immobilised GOx/GDH enzymatic biosensors, it can be suggested that the drawbacks associated with the lipase enzyme in solution can be overcome by trapping the protein in a sol-gel/FcAuNP mediator based matrix. This should allow the lipase enzyme to remain stable without premature deactivation and increase enzyme efficiency. The method can be therefore applied for example, to determine the effectiveness of different types of lipase enzymes, which are widely used in detergent formulation for removing soils.

5.19 References

1. Grieshaber, D., MacKenzie, R., Vörös, J. & Reimhult, E. Electrochemical Biosensors - Sensor Principles and Architectures. *Sensors* **8,** 1400–1458 (2008).
2. Herrera-López, E. J. in *Lipases and Phospholipases* (ed. Sandoval, G.) **861,** 525–543 (Humana Press, 2012).
3. Sadana, A. *Biosensors: Kinetics of Binding and Dissociation Using Fractals*. (Elsevier, 2003).
4. Colegate, S. M. & Molyneux, R. J. *Bioactive Natural Products: Detection, Isolation, and Structural Determination, Second Edition*. (CRC Press, 2007).
5. Herrera-López, E. J. Lipase and phospholipase biosensors: a review. *Methods Mol. Biol. Clifton NJ* **861,** 525–543 (2012).

6. Leonardo, P. C. *Development of an Electrochemical Biosensor Platform and a Suitable Low-Impedance Surface Modification Strategy*. (KIT Scientific Publishing, 2014).

7. Mutlu, M. *Biosensors in Food Processing, Safety, and Quality Control*. (CRC Press, 2010).

8. Alocilja, E. C. & Radke, S. M. Market analysis of biosensors for food safety. *Biosens. Bioelectron.* **18,** 841–846 (2003).

9. Velasco-Garcia, M. N. & Mottram, T. Biosensor Technology addressing Agricultural Problems. *Biosyst. Eng.* **84,** 1–12 (2003).

10. Tothill, I. E. Biosensors developments and potential applications in the agricultural diagnosis sector. *Comput. Electron. Agric.* **30,** 205–218 (2001).

11. Lammers, F. & Scheper, T. in *Thermal Biosensors, Bioactivity, Bioaffinitty* (eds. Bhatia, P. K. et al.) 35–67 (Springer Berlin Heidelberg, 1999). at <http://link.springer.com/chapter/10.1007/3-540-49811-7_2>

12. Lüdi, H., Garn, M. B., Bataillard, P. & Widmer, H. M. Flow injection analysis and biosensors: Applications for biotechnology and environmental control. *J. Biotechnol.* **14,** 71–79 (1990).

13. Dennison, M. J. & Turner, A. P. F. Biosensors for environmental monitoring. *Biotechnol. Adv.* **13,** 1–12 (1995).

14. Mascini, M. & Tombelli, S. Biosensors for biomarkers in medical diagnostics. *Biomarkers* **13,** 637–657 (2008).

15. Yang, V. C. & Ngo, T. T. *Biosensors and Their Applications*. (Springer Science & Business Media, 2000).

16. Gil, E. de S. & Melo, G. R. de. Electrochemical biosensors in pharmaceutical analysis. *Braz. J. Pharm. Sci.* **46,** 375–391 (2010).

17. Taylor, R. F. & Schultz, J. S. *Handbook of Chemical and Biological Sensors*. (CRC Press, 1996).

18. Hasan, A. *et al.* Recent Advances in Application of Biosensors in Tissue Engineering. *BioMed Res. Int.* **2014,** (2014).

19. Copeland, R. A. *Enzymes: A Practical Introduction to Structure, Mechanism, and Data Analysis*. (John Wiley & Sons, 2004).

20. Stein, R. L. *Kinetics of Enzyme Action: Essential Principles for Drug Hunters*. (John Wiley & Sons, 2011).

21. *Encyclopedia of Food and Health*. (Academic Press, 2015).

22. Snape, A., Papachristodoulou, D., Elliott, W. H. & Elliott, D. C. *Biochemistry and Molecular Biology*. (OUP Oxford, 2014).

23. Steed, J. W. & Atwood, J. L. *Supramolecular Chemistry*. (John Wiley & Sons, 2013).

24. Ainsworth, S. *Steady-state enzyme kinetics*. (University Park Press, 1977).

25. Jackson, M. B. *Molecular and Cellular Biophysics*. (Cambridge University Press, 2006).

26. Nelson, D. L. & Cox, M. M. *CourseSmart International E-Book for Principles of Biochemistry*. (Palgrave Macmillan, 2013).

27. Soler, L., Trizio, E., Nickles, T. & Wimsatt, W. *Characterizing the Robustness of Science: After the Practice Turn in Philosophy of Science*. (Springer Science & Business Media, 2012).

28. Carey, C. W. *American Scientists*. (Infobase Publishing, 2006).

29. Rao, D. G. *Introduction to Biochemical Engineering*. (Tata McGraw-Hill Education, 2010).

30. El-Mansi, E. M. T., Bryce, C. F. A., Demain, A. L. & Allman, A. R. *Fermentation Microbiology and Biotechnology, Second Edition*. (CRC Press, 2006).

31. Ruso, J. M. & Piñeiro, Á. *Proteins in Solution and at Interfaces: Methods and Applications in Biotechnology and Materials Science*. (John Wiley & Sons, 2013).

32. Illanes, A. *Enzyme Biocatalysis: Principles and Applications*. (Springer Science & Business Media, 2008).

33. Rai, M., Gade, A., Gaikwad, S., Marcato, P. D. & Durán, N. Biomedical applications of nanobiosensors: the state-of-the-art. *J. Braz. Chem. Soc.* (2012). doi:10.1590/S0103-50532012000100004

34. Gs, S., Cv, A. & Mathew, B. B. Biosensors: A Modern Day Achievement. *J. Instrum. Technol. J. Instrum. Technol.* **2,** 26–39 (2014).

35. Buerk, D. G. *Biosensors: Theory and Applications*. (CRC Press, 1995).

36. *Food Protected Designation of Origin: Methodologies and Applications*. (Elsevier, 2013).

37. Mulchandani, A. in *Enzyme and Microbial Biosensors* **6,** 3–14 (Humana Press, 1998).

38. Córcoles, E. P. & Boutelle, M. G. *Biosensors and Invasive Monitoring in Clinical Applications*. (Springer Science & Business Media, 2013).

39. Vestergaard, M. C., Kerman, K., Hsing, I.-M. & Tamiya, E. *Nanobiosensors and Nanobioanalyses*. (Springer, 2015).

40. Ratner, B. D., Hoffman, A. S., Schoen, F. J. & Lemons, J. E. *Biomaterials Science: An Introduction to Materials in Medicine*. (Academic Press, 2012).

41. Yoo, E.-H. & Lee, S.-Y. Glucose biosensors: an overview of use in clinical practice. *Sensors* **10,** 4558–4576 (2010).

42. Bartlett, P. N. *Bioelectrochemistry: Fundamentals, Experimental Techniques and Applications*. (John Wiley & Sons, 2008).

43. Malhotra, B. D. & Turner, A. *Advances in Biosensors: Perspectives in Biosensors*. (Elsevier, 2003).

44. Giardi, M. T. & Piletska, E. *Biotechnological Applications of Photosynthetic Proteins: Biochips, Biosensors and Biodevices*. (Springer Science & Business Media, 2007).

45. Turner, A. P. F., Chen, B. & Piletsky, S. A. In Vitro Diagnostics in Diabetes: Meeting the Challenge. *Clin. Chem.* **45,** 1596–1601 (1999).

46. Hillery, A. M., Lloyd, A. W. & Swarbrick, J. *Drug Delivery and Targeting: For Pharmacists and Pharmaceutical Scientists*. (CRC Press, 2003).

47. Bouroushian, M. *Electrochemistry of Metal Chalcogenides*. (Springer Science & Business Media, 2010).

48. Malcovati, P., Baschirotto, A., d'Amico, A. & Di, C. N. *Sensors and Microsystems: AISEM 2009 Proceedings*. (Springer Science & Business Media, 2010).

49. Palchetti, I. & Mascini, M. in *Sensors and Microsystems* (eds. Malcovati, P., Baschirotto, A., d'Amico, A. & Natale, C.) 15–23 (Springer Netherlands, 2010). at <http://link.springer.com/chapter/10.1007/978-90-481-3606-3_2>

50. Mohanty, S. P. & Kougianos, E. Biosensors: a tutorial review. *IEEE Potentials* **25,** 35–40 (2006).

51. Zhang, X., Ju, H. & Wang, J. *Electrochemical Sensors, Biosensors and Their Biomedical Applications*. (Academic Press, 2007).

52. Scheller, F. W., Lisdat, F. & Wollenberger, U. in *Bioelectronics* (eds. Willner, I. & Katz, E.) 99–126 (Wiley-VCH Verlag GmbH & Co. KGaA, 2005). at <http://onlinelibrary.wiley.com/doi/10.1002/352760376X.ch4/summary>

53. Newman, J. D. & Setford, S. J. Enzymatic biosensors. *Mol. Biotechnol.* **32,** 249–268 (2006).

54. Sadana, A. *Binding and Dissociation Kinetics for Different Biosensor Applications Using Fractals*. (Elsevier, 2006).

55. Sadana, A. & Sadana, N. *Handbook of Biosensors and Biosensor Kinetics*. (Elsevier, 2010).

56. Willner, I. & Katz, E. *Bioelectronics: From Theory to Applications*. (John Wiley & Sons, 2006).

57. Wang, J. Electrochemical Glucose Biosensors. *Chem. Rev.* **108,** 814–825 (2008).

58. Stefan, R.-I. *Electrochemical Sensors in Bioanalysis*. (CRC Press, 2001).

59. Heller, A. Electrical connection of enzyme redox centers to electrodes. *J. Phys. Chem.* **96,** 3579–3587 (1992).

60. Polsky, R., Brozik, S. M., Xiao, X., Holland, J. T. & Webster, J. G. in *Wiley Encyclopedia of Electrical and Electronics Engineering* (John Wiley & Sons, Inc., 1999). at <http://onlinelibrary.wiley.com/doi/10.1002/047134608X.W8194/abstract>

61. Campbell, M. *Sensor Systems for Environmental Monitoring*. (Springer Science & Business Media, 1997).

62. Scheller, F. & Schubert, F. *Biosensors*. (Elsevier, 1991).

63. Srinivasan, S. *Bioelectrochemistry*. (Springer, 1985).

64. Togawa, T., Tamura, T. & Oberg, P. A. *Biomedical TRANSDUCERS and INSTRUMENTS*. (CRC Press, 1997).

65. *Biosensors: A Practical Approach*. (IRL Press, 1990).

66. Banica, F.-G. *Chemical Sensors and Biosensors: Fundamentals and Applications*. (John Wiley & Sons, 2012).

67. Cass, A. E. G. *Biosensors: a practical approach*. (IRL Press at Oxford University Press, 1990).

68. Davis, G. Electrochemical techniques for the development of amperometric biosensors. *Biosensors* **1,** 161–178 (1985).

69. Montenegro, M. I., Queirós, M. A. & Daschbach, J. L. (John L. *Microelectrodes: Theory and Applications*. (Springer, 1991).

70. Hiratsuka, A. *et al.* Electron transfer mediator micro-biosensor fabrication by organic plasma process. *Biosens. Bioelectron.* **21,** 957–964 (2005).

71. Hui, Y. H. *Food Biochemistry and Food Processing*. (John Wiley & Sons, 2008).

72. Karunakaran, C., Bhargava, K. & Benjamin, R. *Biosensors and Bioelectronics*. (Elsevier, 2015).

73. Lojou, É. & Bianco, P. Application of the electrochemical concepts and techniques to amperometric biosensor devices. *J. Electroceramics* **16,** 79–91 (2006).

74. Cosnier, S. Electropolymerization of amphiphilic monomers for designing amperometric biosensors. *Electroanalysis* **9,** 894–902 (1997).

75. Mohamad, N. R., Marzuki, N. H. C., Buang, N. A., Huyop, F. & Wahab, R. A. An overview of technologies for immobilization of enzymes and surface analysis techniques for immobilized enzymes. *Biotechnol. Biotechnol. Equip.* **29,** 205–220 (2015).

76. Sassolas, A., Hayat, A. & Marty, J.-L. Enzyme immobilization by entrapment within a gel network. *Methods Mol. Biol. Clifton NJ* **1051,** 229–239 (2013).

77. Datta, S., Christena, L. R. & Rajaram, Y. R. S. Enzyme immobilization: an overview on techniques and support materials. *3 Biotech* **3,** 1–9 (2013).

78. Guisan, J. M. *Immobilization of Enzymes and Cells*. (Springer Science & Business Media, 2006).

79. Bard, A. J., Inzelt, G. & Scholz, F. *Electrochemical Dictionary*. (Springer Science & Business Media, 2012).

80. Albery, W. J., Bartlett, P. N. & Cass, A. E. Amperometric enzyme electrodes. *Philos. Trans. R. Soc. Lond. B. Biol. Sci.* **316,** 107–119 (1987).

81. Ghosh, P. *Colloid and Interface Science*. (PHI Learning Pvt. Ltd., 2009).

82. Panaiotov, I., Ivanova, M. & Verger, R. Interfacial and temporal organization of enzymatic lipolysis. *Curr. Opin. Colloid Interface Sci.* **2,** 517–525 (1997).

83. Verger, R., Mieras, M. C. E. & Haas, G. H. de. Action of Phospholipase A at Interfaces. *J. Biol. Chem.* **248,** 4023–4034 (1973).

84. Holmes, R. M. *A Cell Biologist's Guide to Modeling and Bioinformatics*. (John Wiley & Sons, 2007).

85. Berg, J. M., Tymoczko, J. L. & Stryer, L. The Michaelis-Menten Model Accounts for the Kinetic Properties of Many Enzymes. (2002). at <http://www.ncbi.nlm.nih.gov/books/NBK22430/>

86. Silverman, R. B. *The Organic Chemistry of Enzyme-catalyzed Reactions*. (Academic Press, 2002).

87. Lieberman, M., Marks, A. D., Smith, C. M. & Marks, D. B. *Marks' Essential Medical Biochemistry*. (Lippincott Williams & Wilkins, 2007).

88. Marangoni, A. G. *Enzyme Kinetics: A Modern Approach*. (John Wiley & Sons, 2003).

89. Sonesson, A. W., Brismar, H., Callisen, T. H. & Elofsson, U. M. Mobility of Thermomyces lanuginosus lipase on a trimyristin substrate surface. *Langmuir ACS J. Surf. Colloids* **23,** 2706–2713 (2007).

90. Purich, D. L. *Contemporary enzyme kinetics and mechanism*. (Academic Press, 1996).

91. Fang, B., Niu, J., Ren, H., Guo, Y. & Wang, S. Mechanistic Study of Manganese-Substituted Glycerol Dehydrogenase Using a Kinetic and Thermodynamic Analysis. *PLoS ONE* **9,** e99162 (2014).

92. Yamada-Onodera, K., Yamamoto, H., Emoto, E., Kawahara, N. & Tani, Y. Characterisation of Glycerol Dehydrogenase from a Methylotrophic Yeast, Hansenula polymorpha Dl-1, and its Gene Cloning. *Acta Biotechnol.* **22,** 337–353 (2002).

93. Mráček, T., Drahota, Z. & Houštěk, J. The function and the role of the mitochondrial glycerol-3-phosphate dehydrogenase in mammalian tissues. *Biochim. Biophys. Acta* **1827,** 401–410 (2013).

94. Ruzheinikov, S. N. *et al.* Glycerol Dehydrogenase: Structure, Specificity, and Mechanism of a Family III Polyol Dehydrogenase. *Structure* **9,** 789–802 (2001).

95. Forage, R. G. & Lin, E. C. DHA system mediating aerobic and anaerobic dissimilation of glycerol in Klebsiella pneumoniae NCIB 418. *J. Bacteriol.* **151,** 591–599 (1982).

96. Mallinder, P. R., Pritchard, A. & Moir, A. Cloning and characterization of a gene from Bacillus stearothermophilus var. non-diastaticus encoding a glycerol dehydrogenase. *Gene* **110,** 9–16 (1992).

97. Burke, J. *et al.* Purification, crystallization and quaternary structure analysis of a glycerol dehydrogenase S305C mutant from Bacillus stearothermophilus. *Acta Crystallogr. D Biol. Crystallogr.* **57,** 165–167 (2001).

98. Han, J.-S. & Ishikawa, K. Active site of Zn2+-dependent sn-glycerol-1-phosphate dehydrogenase from Aeropyrum pernix K1. *Archaea* **1,** 311–317 (2005).

99. Spencer, P., Bown, K. J., Scawen, M. D., Atkinson, T. & Gore, M. G. Isolation and characterisation of the glycerol dehydrogenase from Bacillus stearothermophilus. *Biochim. Biophys. Acta* **994,** 270–279 (1989).

100. Siljegovic V., Boschetti A., Spichiger U.E., Guggisberg D. & Koch H. A Nad/nadh-dependent dehydrogenase from Pseudomonas putida acting on salbutamol. *Biotechnol. Lett.* **20,** 667–671 (1998).

101. Silverman, R. B. *Organic Chemistry of Enzyme-Catalyzed Reactions, Revised Edition*. (Academic Press, 2002).

102. Hancock, G. & Compton, R. G. *Applications of Kinetic Modelling*. (Elsevier, 1999).

103. Hassan, R. Y. A. & Bilitewski, U. A viability assay for Candida albicans based on the electron transfer mediator 2,6-dichlorophenolindophenol. *Anal. Biochem.* **419,** 26–32 (2011).

104. Minton, N. P. & Clarke, D. J. *Clostridia*. (Springer Science & Business Media, 2013).

105. Baltscheffsky, M. *Current Research in Photosynthesis: Proceedings of the VIIIth International Conference on Photosynthesis Stockholm, Sweden, August 6–11, 1989*. (Springer Science & Business Media, 2013).

106. King, T. E., Mason, H. S. & Morrison, M. *Oxidases and Related Redox Systems: Proceedings of the Third International Symposium on Oxidases and Related Redox Systems, held in the State University of New York at Albany, USA*. (Elsevier, 2013).

107. Benoît Limoges, D. M. Electrochemistry of immobilized redox enzymes: kinetic characteristics of NADH oxidation catalysis at diaphorase monolayers affinity immobilized on electrodes. *J. Am. Chem. Soc.* **128,** 2084–92 (2006).

108. Purich, D. L. & Allison, R. D. *The Enzyme Reference: A Comprehensive Guidebook to Enzyme Nomenclature, Reactions, and Methods*. (Academic Press, 2003).

109. Traut, T. W. *Allosteric Regulatory Enzymes*. (Springer Science & Business Media, 2007).

110. Atkins, P. & Paula, J. de. *Atkins' Physical Chemistry*. (OUP Oxford, 2014).

111. Owusu-Apenten, R. *Introduction to Food Chemistry*. (CRC Press, 2004).

112. Nagodawithana, T. & Reed, G. *Enzymes in Food Processing*. (Elsevier, 2013).

113. Murzin, D. Y. & Salmi, T. *Catalytic Kinetics*. (Elsevier, 2005).

114. Bartlett, P. N. *Bioelectrochemistry: Fundamentals, Experimental Techniques and Applications*. (John Wiley & Sons, 2008).

115. Meyers, R. A. *Synthetic Biology*. (John Wiley & Sons, 2015).

116. Bronzino, J. D. *Medical Devices and Systems*. (CRC Press, 2006).

117. Shivani, S. *Handbook of Research on Diverse Applications of Nanotechnology in Biomedicine, Chemistry, and Engineering*. (IGI Global, 2014).

118. Ramanaviciene, A. *et al.* Spectrophotometric evaluation of gold nanoparticles as red-ox mediator for glucose oxidase. *Sens. Actuators B Chem.* **137,** 483–489 (2009).

119. C. Charcosset, S. B. Membrane techniques for the preparation of nanomaterials: nanotubes, nanowires and nanoparticles – A review. 15–23 (2007).

120. Zhou, J., Ralston, J., Sedev, R. & Beattie, D. A. Functionalized gold nanoparticles: synthesis, structure and colloid stability. *J. Colloid Interface Sci.* **331,** 251–262 (2009).

121. Putzbach, W. & Ronkainen, N. J. Immobilization Techniques in the Fabrication of Nanomaterial-Based Electrochemical Biosensors: A Review. *Sensors* **13,** 4811–4840 (2013).

122. Pumera, M. *Nanomaterials for Electrochemical Sensing and Biosensing*. (CRC Press, 2014).

123. Li, Y., Schluesener, H. J. & Xu, S. Gold nanoparticle-based biosensors. *Gold Bull.* **43,** 29–41 (2010).

124. Bharathi, S. & Nogami, M. A glucose biosensor based on electrodeposited biocomposites of gold nanoparticles and glucose oxidase enzyme. *Analyst* **126,** 1919–1922 (2001).

125. Chang, G. *et al.* Gold nanoparticles directly modified glassy carbon electrode for non-enzymatic detection of glucose. *Appl. Surf. Sci.* **288,** 524–529 (2014).

126. Du, D., Chen, S., Cai, J. & Zhang, A. Electrochemical pesticide sensitivity test using acetylcholinesterase biosensor based on colloidal gold nanoparticle modified sol–gel interface. *Talanta* **74,** 766–772 (2008).

127. Wang, J. *Analytical Electrochemistry*. (John Wiley & Sons, 2006).

128. Lund, H. & Hammerich, O. *Organic Electrochemistry*. (CRC Press, 2001).

129. Zutshi, K. *Introduction to Polarography and Allied Techniques*. (New Age International, 2006).

130. Long, N. N. *et al.* Synthesis and optical properties of colloidal gold nanoparticles. *J. Phys. Conf. Ser.* **187,** 012026 (2009).

131. Zub, Y. L. & Kessler, V. G. *Sol-Gel Methods for Materials Processing: Focusing on Materials for Pollution Control, Water Purification, and Soil Remediation*. (Springer Science & Business Media, 2008).

132. Jerónimo, P. C. A., Araújo, A. N. & Conceição B.S.M. Montenegro, M. Optical sensors and biosensors based on sol–gel films. *Talanta* **72,** 13–27 (2007).

133. Tang, W., Li, L., Wu, L., Gong, J. & Zeng, X. Glucose Biosensor Based on a Glassy Carbon Electrode Modified with Polythionine and Multiwalled Carbon Nanotubes. *PLoS ONE* **9,** (2014).

134. El-Ansary, A. Nanoparticles as biochemical sensors. *Nanotechnol. Sci. Appl.* 65 (2010). doi:10.2147/NSA.S8199

135. Winartasaputra, H., Kuan, S. S. & Guilbault, G. G. Amperometric enzymic determination of triglycerides in serum. *Anal. Chem.* **54,** 1987–1990 (1982).

136. Joshi, R. *Biosensors*. (Gyan Publishing House, 2006).

137. I. Lapenaite, B. K. Properties and analytical application of PQQ-dependent glycerol dehydrogenase from Gluconobacter sp. 33. *Anal. Chim. Acta* **549,** 140–150 (2005).

138. Ganjali, M. R. *et al.* FFT Continuous Cyclic Voltammetry Triglyceride Dual Enzyme Biosensor Based on MWCNTs-CeO2 Nanoparticles. *Int J Electrochem Sci* **5,** 1422–1433 (2010).

139. Bengtsson, G. & Olivecrona, T. Lipoprotein lipase. Mechanism of product inhibition. *Eur. J. Biochem. FEBS* **106,** 557–562 (1980).

140. Kosugi, Y. & Suzuki, H. Functional immobilization of lipase eliminating lipolysis product inhibition. *Biotechnol. Bioeng.* **40,** 369–374 (1992).

141. Browne, K. P. & Grzybowski, B. A. Controlling the Properties of Self-Assembled Monolayers by Substrate Curvature. *Langmuir* **27,** 1246–1250 (2011).

CHAPTER 6

Soiled fabrics washed using P&G's C24E3S surfactant

6.1 Review of Polymorphism

Polymorphism in molecular crystals has attracted the attention of many researchers from different scientific discipline over the years. Polymorphism is when a substance can exist in two or more crystalline phases and exhibit different physical and chemical properties as the compound adopts different conformations or packing arrangements in a crystal lattice[1]. Scientists have been aware of the existence of polymorphism since the 1820s. It was the pioneering work of Malkin *et al*. on the different melting behaviour of triacylglycerides due to polymorphism, which was investigated using powder X-ray diffraction, that led to the understanding of the structure and physical properties of fat crystals[2]. Further to this, the nomenclature proposed by Lutton *et al*. in 1950, based on the short spacing structural information obtained for triacylglycerides using powder X-ray diffraction has been extensively used worldwide to characterise the different types of polymorphs. Factors such as the packing arrangement of hydrocarbon chains of the triacylglycerides and the layered structure composed of the same series of acyl chains were taken into account for derivation of the nomenclature[3]. The subcell and layered structures of fat polymorphs corresponds to short and long Bragg spacings when analysed using the X-ray diffraction method. The long spacings are affected by the chain length of the fatty acids which makes up the triacylglyceride molecules, and importantly, the angle of tilt. The long spacing values can be therefore used to identify different types of polymorphs for the same fatty acid. The short spacings, on the other hand, are independent of the chain length of the fatty acids and can be used to characterise the polymorphs [4]. Since the late 19th Century, as well as X-ray diffraction, other methods such as NMR have been used to study molecular mobility within the polymorphic structure. Vibrational Spectroscopy (VS) has also been used to determine fat polymorphism and Atomic force spectroscopy (AFM) has been applied to investigate the structure of triacylglerides [5].

A substance can also exist in various other forms for instance, as a pseudo polymorph, hydrate or amorphous solid[6]. In 1965, Walter McCrone introduced the term pseudo polymorphism to describe crystalline solvates consisting of stoichiometric or non-stoichiometric quantity of a solvent[7]. If the bound solvent is water then the crystalline molecules are referred to as hydrates[8]. Amorphous solids on the other hand are formed as a

result of disordered arrangement of molecules without an obvious lattice structure [9]. Polymorphs of the same compound can arise due to two main factors and these are (1) different packing arrangement whilst retaining the same conformation (which is referred to as packing polymorphism) and (2) packing into different structures due to different molecular conformations (which is termed as conformational polymorphism)[10]. As a result, molecules have different arrangements in the unit cell of its crystals and such compounds can display various chemical, physical, mechanical, thermodynamic and kinetic properties[11]. Examples include chemical reactivity, solubility, dissolution rate, melting behaviour, hardness and stability which are all dependent on the structure of the polymorphic crystals [12]. The formation of polymorphic phases during crystallisation often follows Ostwald's rule of stages. This emperical rule states that the least thermodynamically stable polymorph with highest free energy is formed first on crystallisation of solution or melt. The polymorphic forms than undergo successive transformation until the most stable polymorph is formed [13]. External factors such as seeding, pressure and temperature change can be used to override Ostwald's law to select a specific fat polymorph [14]. In this project, the different types and structures of fat polymorphs formed at room temperature and at 20^{o}C, with and without fabrics, are investigated using techniques such as small-angle X-ray scattering(SAXS), wide-angle X-ray scattering(WAXS) and atomic force spectroscopy (AFM).

6.2 Structure of Fats

Most naturally produced fats are widely used in food products such as chocolate and margarine. These fats are composed of a combination of various triacylglycerols, which are in turn is made up of triesters of fatty acids with glycerol[15]. The melting, crystallisation characteristics and packing arrangement of the triacylglycerols (TAG) are affected by the type of fatty acids, the degree of saturation as well as the position and chain length of the fatty acids. The acyl group of the TAG can pack in 2 possible structures: tuning fork (the fatty acid chains in position 1 and 3 are located alongside each other whilst the one in position 2 remains unpaired) shown in figure 6.1a and chair (the acyl chain in position 2 aligns with the one in either position 1 or 3) shown in figure 6.1b [16].

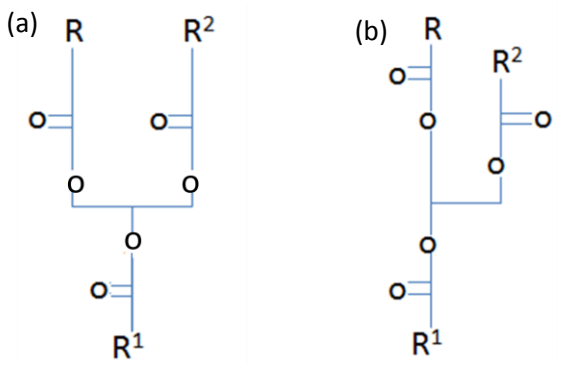

Figure 6.1: (a) tuning fork and (b) chair conformation.[17]

Where, R_1, R_2 and R_3 are fatty acid chains. These configurations are packed in either double or triple chain length manner in the crystal planes which can be observed using techniques such as powder X-ray diffraction (figure 6.2). The quarto- and hexa-chain length structures can be also observed in asymmetrical saturated triacylglycerides [18].

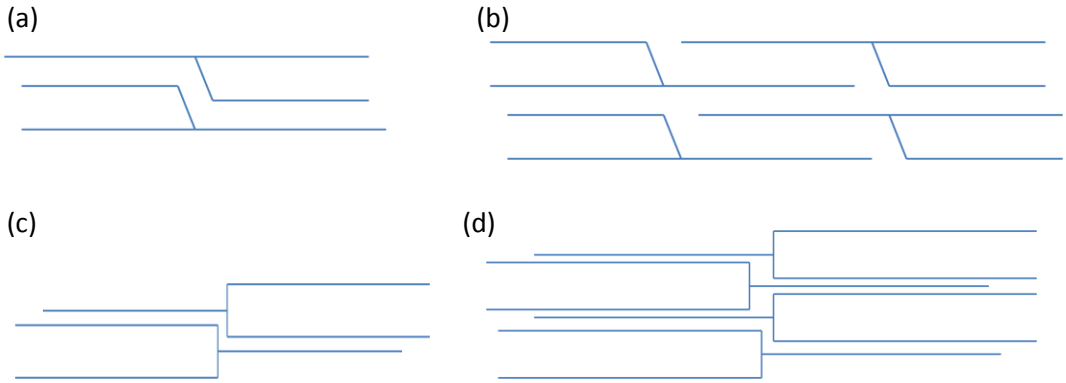

Figure 6.2: The double and triple chain length of the chair (a and b) and tuning fork (c and d) structure of fat[19].

These chain length arrangements can be identified by long spacings between the crystal planes and also, the details about the structures of different polymorphs i.e. the interchain distances can be determined from short spacings within the planes, using the X-ray diffraction technique [20].

Fatty acids are a form of carboxylic acids which are obtained from either animals or vegetable fats or oils [21]. These fatty acids are produced by alkaline hydrolysis of fats and are composed of a hydrocarbon chain which is linked to a carboxylic acid group. The chain length can vary between 4 to 30 carbons and it can be either linear or kinked. Unsaturated fat

consists of triglycerides with unsaturated fatty acids. The unsaturated fatty acids contain carbon and hydrogen atoms which are linked together by double bonds and can exist in cis or trans form. As the unsaturated fatty acids disturb the close packing of the triglycerides it leads to formation of kinks in the chain (figure 6.3c). Consequently, unsaturated fats such as oils exist as liquid at lower temperature [22]. Saturated fat on the other hand consists of triglycerides with a high content of saturated fatty acids that do not contain any double bonds. Such fats have linear chain with even number of carbons, appear as a solid at room temperature and have higher melting points (figure 6.3b) [23].

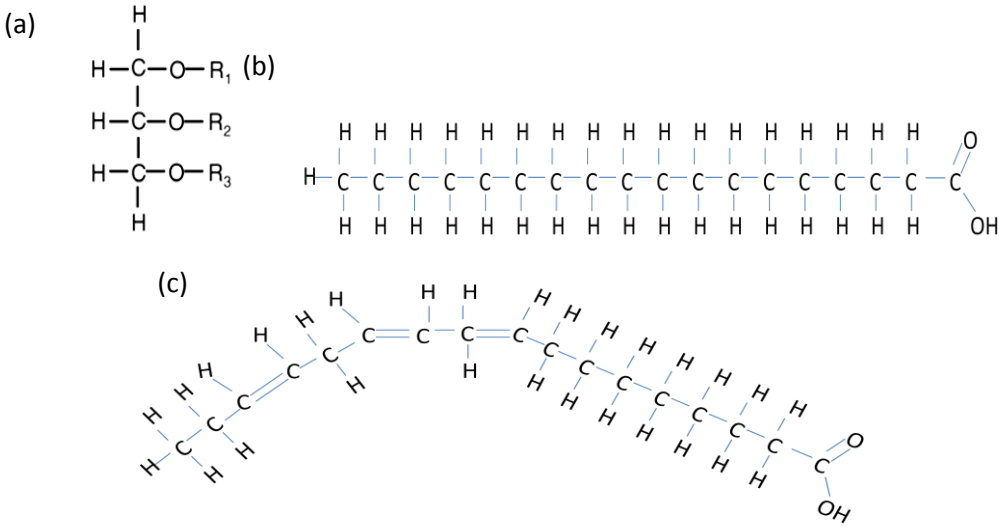

Figure 6.3: molecular structure of (a) a triacylglyceride (R_1, R_2 & R_3 are fatty acids) (b) a saturated fatty acid - Stearic acid & (c) an unsaturated fatty acid – Linolenic acid [23].

Lard is an example of fat which consists of both saturated fatty acids such as palmitic, stearic and myristic acid, as well as unsaturated fatty acids for example, oleic, linoleic and palmitoleic acid [24].

6.3 Lard

Lard is a fat obtained by rendering fatty tissue of the hog/domestic pig. Natural lard has a waxy texture type of characteristic and exhibits unsatisfying bakery qualities. These undesirable features are overcome by fat blending or interesterification in making commercial shortenings. The composition of lard varies with the hog's food. However, it mainly consists of a few long-chain major fatty acids such as saturated fatty acids like palmitic (24%) and stearic (14%) acids as well as unsaturated fatty acids for example, oleic (41%) and linoleic (10%) acids. The oleic acid is mostly found in the 1-and 3- position of glycerol while

the palmitic acid is esterified in the 2-position of glycerol. Other fatty acids include myristic acid, myristoleic acid, palmitoleic acid, α-linolenic acid, arachidic acid, eicosenoic acid and eicosadienoic acid [25]. Lard exhibits different polymorphic crystals after melting, cooling and slowly increasing the temperature (table 6.1).

Table 6.1: SAXS and WAXS characteristics of the various types of polymorphs for lard[26,27].

Polymorph	Crystal System/Chain packing & chain length structure	Melting Point /°C	Unit cell	Unit cell dimensions	Unit Cell Characteristics	SAXS Characteris-tics/Å	WAXS Characteris-tics/Å
α	Hexagonal arrangement (H), double chain	15-20	α = β = 90°, γ = 120°	a=b, c≠a, c≠b	Acyl groups oriented at 90 ° to the plane of the glycerol group	48.2	4.18
β'_1	Orthorhombic and perpendicular ($O_\perp$), double or triple chain	25-27	α = β= γ = 90°	a≠b≠c	Acyl groups are tilted 68-70 ° from the plane of the glycerol group	35.1	3.95 , 3.83 & 4.14
β'_2	Pseudo- Orthorhombic, double or triple chain	25-27	α = γ = 90° β ≠ 90°	a≠b≠c	Acyl groups are tilted 68-70 ° from the plane of the glycerol group	43.8	4.3 & 4.4
β	Triclinic and parallel ($T_{//}$), Double or triple chain	35-45	α≠ β ≠ γ ≠ 90°	a≠b≠c	Acyl groups are tilted 50-70° from the plane of the glycerol group	43.8	(3.6 -3.9), 4.6

The 2-palmitooleostearin (13%) and 2-palmitodiolein (19%) are the two major triacylglycerols of lard. The major trisaturated triacylglycerol is 2- palmitodistearin which varies between 2-10%. Lard consists of fewer triacylglycerols compared to many other fats yet it still exhibits complex thermal properties [27].

6.4 Triglycerides

Triglycerides (TAGS) display a complex monotropic polymorphism. This means it can lead to formation of various polymorphic crystals depending on the following factors: the type of fatty acid chains esterified to the glycerol, the crystallisation procedure such as the melt, cooling or solvent mediation and sample purity[28]. The crystals are composed of triglyceride layers and the thickness of these layers depends on the length and insaturation of the fatty acids, as well as the angle of tilt with respect to the basal planes produced as a result of the methyl end groups. The layer thicknesses, also referred to as long spacings, can be

determined using the Small Angle X-ray Scattering (SAXS) method at $0 < q < 0.9$ Å^{-1} , where $q = 4\pi\sin\theta/\lambda$, θ is half the scattering angle and λ is the X-ray wavelength, whereas the packing of the aliphatic chains is characterised by short spacings at $0.9 < q < 1.8$ Å^{-1} using the Wide Angle X-ray Scattering (WAXS) technique[29]. The crystalline transformation to a more stable polymorph is an irreversible process. The various types of polymorphs are obtained by melting the fat followed by crystallisation (via the processes of nucleation and growth) leading to generation of the more stable polymorphic species (figure 6.4) [30].

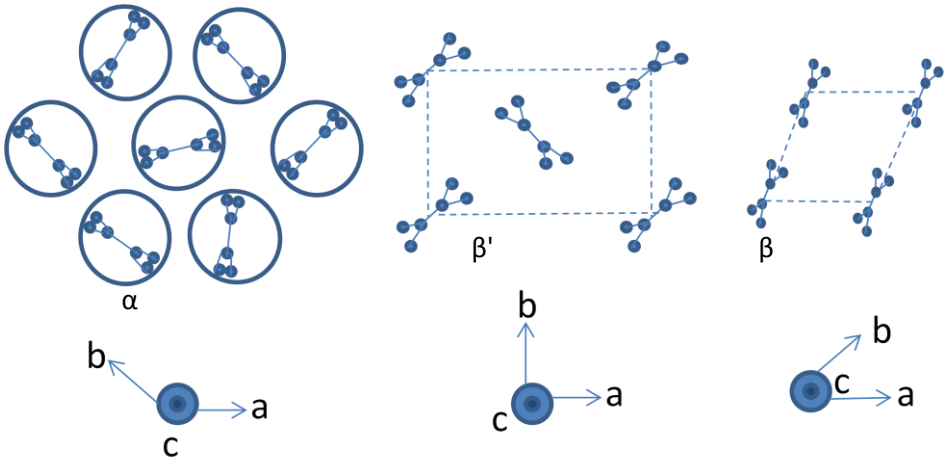

Figure 6.4: Schematic representation of the chain packings of long chain triglycerides (a) Hexagonal packing (least thermodynamically stable) (b) Orthorhombic packing and (c) Triclinic packing (most thermodynamically stable) [31].

The most stable polymorphic crystal is the β form which exhibits a triclinic packing and has the lowest Gibbs energy at a higher temperature above 35 °C - 45 °C. At temperatures lower than 35 °C the β' polymorphs can be identified with an intermediate Gibbs energy and orthorhombic packing arrangement. Whereas, fast cooling after melt leads to formation of α crystals displaying hexagonal packing and has the highest Gibbs energy. The three metastable crystallines melt successively and the liquid recrystallises instantly into the next metastable form[32].

6.5 Polymorphism of fats

The fat crystal forms can be categorised into 3 main types of polymorphs which are α, β' and β (figure 6.5) [33].

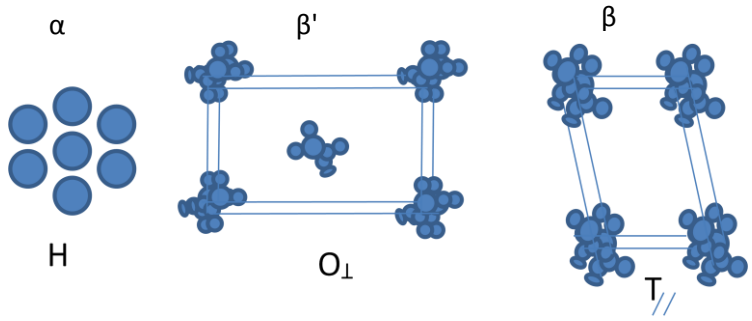

Figure 6.5: Structures of the 3 main types of fat polymorphs [33].

The different types of polymorphs are obtained from melting the fat followed by crystallisation. The α-form is formed upon moderate to high cooling rate after melting. The β' polymorphs on the other hand are produced via slow cooling and when the temperature is raised slightly higher than the melting point of α form. At a much slower cooling rate and just above the melting temperature of β' polymorph, β crystals are found to crystallise as these high melting components of fat solidify at an earlier stage[34]. Alongside the rate of cooling, other factors such as variation in the chain length of the fatty acids and the thermal history can also influence the polymorphic behaviour[35]. The different melting points and characteristics of the polymorphs can be identified by techniques such as XRD.

6.6 Types of polymorphism

There are 2 types of polymorphism which exist in lipids and these are enantiotropic and monotropic polymorphism. Enantiotropic polymorphism occurs when each of the fat polymorphs is thermodynamically stable over a particular range of temperature and pressure. Monotropic polymorphism on the other hand results in when there is only one thermodynamically stable polymorph at all temperatures and pressures. Change in conditions, i.e. altering the temperature over a period of time, leads to transformation of less stable polymorphs to more stable ones with the lowest Gibbs energy (figure 6.6)[28].

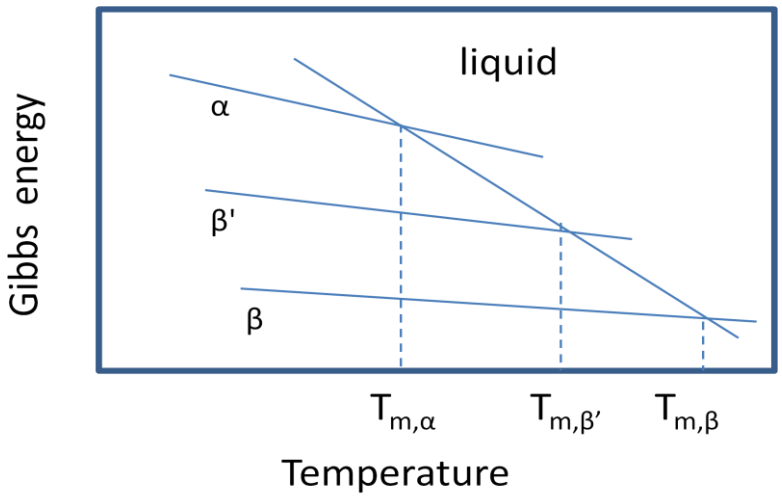

Figure 6.6: Gibbs free energy against temperature relationship for the 3 different types of polymorphic forms of TAGs. Where, T_m is the melting temperature [28].

The ability of triacylglycerol molecules to pack in various crystalline arrangements allows the various fat polymorphs to exhibit different melting temperatures. Due to their monotropic nature and according to Ostwald's rule, the less stable polymorph, which in this case is α, with the least dense crystal packing, low melting point and largest Gibbs energy value is formed first. Followed by the β'-form, which has an intermediate Gibbs energy being thermodynamically more unstable than β. The transition from vertical structured α polymorph to tilted β' form occurs as a result of the hydrocarbon chains subsiding or possibly due to conformational change of the glycerol molecule. This transformation route takes place at a much higher rate during melting process than supercooling. As the phase change process continues, the most stable polymorph which is the β-form with the most dense crystal packing, highest melting point and lowest Gibbs energy is produced. Interpolymorphic conversion of β polymorph to β'-form and β'-form to α polymorph is not possible as it is thermodynamically unfavorable. At equilibrium, when the change in Gibbs energy (ΔG) is zero, the melting temperature, T_m, can be defined in terms of the ratio of enthalpy, ΔH_m, and entropy, ΔS_m , of melting (equation 6.1) [36].

$$T_m = \left(\frac{\Delta H_m}{\Delta S_m}\right) \qquad \text{(eq. 6.1)}$$

The ΔH_m and ΔS_m are influenced by factors such as hydrogen bonding, crystal packing and intermolecular interactions [37].

6.7 The crystallisation process

Crystallisation can be defined as the first order transition of molecular aggregates from the liquid to the solid phase, which results in the formation of a crystal lattice. This phenomenon is a multi-step process which involves nucleation and then crystal growth including Ostwald ripening of the crystals. Nucleation determines the initial formation of crystals from molecules or ions and crystal growth establishes the crystal size. Following this, other processes such as secondary nucleation can occur.

All of the processes above are dependent on the degree of supersaturation and the change in free energy. Supersaturation can be referred to as a solution containing more of a component than can be within it when it is at equilibrium with a bulk crystal at that temperature. Supersaturation is the ratio of the fraction of solute in the supersaturated solution to the amount of solute in a saturated solution at the same temperature. The relationship between supersaturation and spontaneous crystallisation process can be represented in the form of concentration against temperature diagram/solubility curve (figure 6.7)[38].

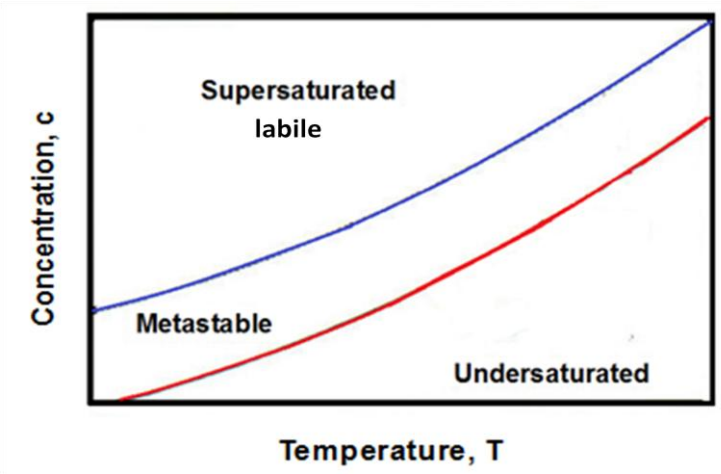

Figure 6.7: showing change in solubility of a compound with concentration and temperature[38].

Solutions with concentration lower than the red solubility curve at a specific temperature are considered as undersaturated. This means in such solutions any crystals present will redissolve. The metastable region in the diagram arises due to crystal growth being possible on pre-existing crystals, e.g. crystal seeds, or on surfaces at which small aggregates can absorb and grow to become crystal nuclei; however nucleation within the bulk phase does not occur. In the supersaturated region, the concentration of the solution is well above the

solubility curve. Consequently spontaneous nucleation as well as crystal growth processes can occur[39].

6.7.1 Kinetics and thermodynamics of crystallisation of fat

The thermodynamic driving force for the crystallisation process of a component, *i*, is the chemical potential difference ($\Delta\mu_i$) between the liquid ($\Delta\mu_i^L$) and solid ($\Delta\mu_i^S$) phase (equation 6.2) [40].

$$\Delta\mu_i = \Delta\mu_i^L - \Delta\mu_i^S = \Delta\mu_{i,0} + RT\,In\left(\frac{\gamma_i^L x_i^L}{\gamma_i^S x_i^S}\right) \qquad \text{(eq. 6.2)}$$

Where, γ_i is the activity coefficient for *i*, x_i is the mole faction of *i* and $\Delta\mu_{i,0}$ *is* the chemical potential difference of the pure component i in the respective phases. For the crystallisation of one or more components from a melt, supercooling is required. Supercooling refers to the degree by which the sample has been cooled with respect to the melting temperature of the crystallised sample. This produces a thermodynamic driving force and a chemical potential for formation of a nuclei. It can be expressed in the form of equation 6.3 [40,41].

$$\Delta\mu_i \cong \Delta H_{m,i}\left(T_{m,i} - T/T_{m,i}\right) \qquad \text{(eq. 6.3)}$$

Where, $\Delta H_{m,i}$ is the enthalpy of melting of pure component *i*, *T* is the sample temperature and $T_{m,i}$ is the melting temperature of component *i*. Equation 6.3 assumes that $\Delta H_{m,i}$ is independent of temperature. The crystallisation driving force for a fat system consisting of multi component TAGS in the liquid phase which has similar size and structure, can be defined by equation 6.4 where, $x_i^{L,eq}$ is the saturation composition and it is assumed that $x_i^{L,eq} \approx x_i^L \approx 1$ [42].

$$\Delta\mu_i \cong RT\,In\left(\frac{x_i^L}{x_i^{L,eq}}\right) \qquad \text{(eq. 6.4)}$$

6.8 Nucleation of crystals

During fat crystallisation from the melt, the triacylglycerol molecules form into ordered lamella-like structures which then act as a precursor to the formation of different

polymorphic crystals; this is nucleation. In order for this to occur, the fat system has to overcome the nucleation energy barrier, ΔG^* (figure 6.8) [43].

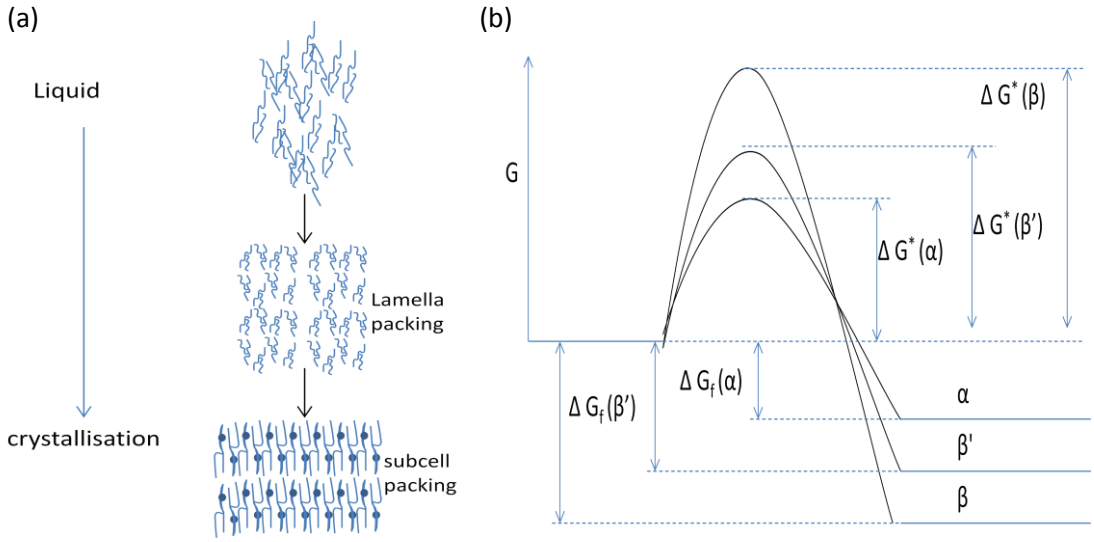

Figure 6.8: (a) ordering of TAGS & (b) energy barrier of the 3 main types of polymorphs as a transition from liquid to solid phase occurs.

In Figure 6.8, ΔG^* is the Gibbs energy barrier for nucleation from the liquid phase and ΔG_f is the Gibbs energy difference between the supercooled liquid phase and the macroscopic solid phase for each of the α, β and β' polymorphs[43]. Factors such as diffusion rates and interaction of fat molecules with one another can affect the kinetic properties of the ordering process in the liquid and solid phases as well as influence the type of polymorph crystal that will form as a result of crystallisation (see types of polymorphism section 6.6). Specific crystals can be also selectively grown by altering the conditions for example, by controlling the shear stress and tempering during the processes[43].

The process of nucleation initiates as a result of clustering and aggregation of molecules or ions to a stable size in a supersaturated melt, solution or vapour. The critical nucleus is defined as the nucleus size at which there is equal probability of the nucleus growing or dissolving (figure 6.9) [45].

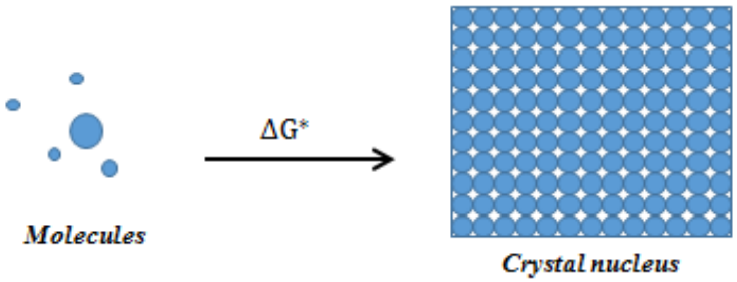

Figure 6.9: Schematic representation of nucleation process. Where, ΔG^* is the Gibbs energy of nucleation.

The different arrangements of the stable aggregates during nucleation lead to formation of polymorphs. Production of specific type of polymorph is dependent on factors such as intermolecular bonding, molecular conformation and lattice energy [46]. Primary nucleation can be defined as the process of initial crystal formation in a system that does not contain any crystalline matter of that chemical species. The nucleus of a crystal is formed due to molecules interacting with one another via forces such as hydrogen bonding, dispersion forces and van der waals interaction. As a result, clusters of particles formed in the system gain attractive lattice interactions and this in turn leads to a decrease in Gibbs free energy. However this decrease in free energy due to bulk crystal interactions is more than offset initially by the increase in free energy due to the need to create a crystal-liquid interface of free energy γA, where A is the interfacial area and γ is the interfacial tension. Once a critical radius (r^*) is achieved, however, a critical nucleus is formed where the energy increase of creating extra interface is balanced by the energy decrease in forming more of the new crystal phase [47]. When the critical radius is exceeded, particles become stable and tend to undergo spontaneous crystal growth leading to formation of crystal polymorphs (figure 6.10). The critical radius is dependent on the pressure, temperature, solvent and supersaturation [48].

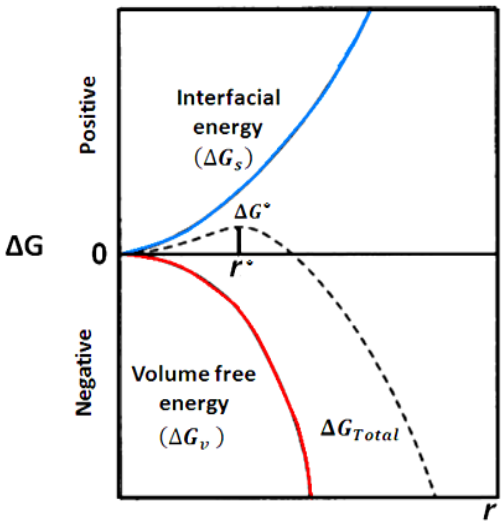

Figure 6.10: Changes in nucleation energy (ΔG) with the radius of nucleus (r). Where, ΔG_s is the energy increase due to creating the surface, ΔG_v is the energy decrease coagulating atoms to form clusters and ΔG^* is the critical free energy [48].

6.8.1 Nucleation process of fat and the kinetics and thermodynamics of nucleation

Volmer's nucleation mode[49] suggests that the possibility of cluster formation during nucleation is dependent on the attainment of critical cluster size with mean radius, r^*. The total free energy of a cluster (ΔG_{total}) is equal to volume free energy and surface free energy (equation 6.5). The activation energy barrier for nucleation, ΔG^*, from solution can be expressed in the form of equation 6.6 for a spherical nucleus[50].

$$\Delta G_{Total} = \Delta G_s + \Delta G_v = 4\pi r^2\gamma + \left(\frac{-4\pi r^3 kTIn\sigma}{3\nu}\right) \quad \text{(eq. 6.5)}$$

$$\Delta G^* = \left[\frac{16\pi\nu^2}{3(kTIn\sigma)^2}\right] \quad \text{(eq. 6.6)}$$

Where, ΔG^* is the energy increase in creating the surface, ΔG_v is the energy decrease coagulating atoms/molecules to form clusters, r is the mean radius of the cluster, k is Boltzmann's constant, T is the absolute temperature, γ is the interfacial free energy between the nucleus and the supersaturated solution, σ is the supersaturation ratio (which is the ratio of solute concentration to saturated solution for an ideal solution) and ν is the molecular volume. Primary nucleation can be subdivided into two categories: homogeneous and heterogeneous nucleation. Homogeneous nucleation occur as a result of spontaneous formation of a nuclei from a clear bulk solution whereas heterogeneous nucleation takes

place at the interfaces or surfaces due to foreign particles which increases the rate of nucleation [51]. Secondary nucleation on the other hand is formation of nuclei induced by the collision between existing particles, such as crystals from the primary nucleation in a supersaturated solution or crystal seeds which can be added deliberately. Increasing shear rate can also lead to faster formation of the most stable polymorph from a less stable one [52].

The formation of nuclei is the initial process of solid phase formation. Nucleation can take place from a solution or from a melt for a fat system. The Gibbs energy of the system alters as a result of decrease of free energy per unit volume arising from enthalpy of fusion and increase of the surface energy due to surface tension. For formation of spherical nuclei via homogeneous nucleation from the melt the Gibbs free energy (ΔG_{hom}) can be expressed in the form of equation 6.7 [53].

$$\Delta G_{hom} = \Delta G_v V + \Delta G_s A = \frac{4}{3}\pi r^3 \Delta G_v + 4\pi r^2 \sigma \qquad \text{(eq. 6.7)}$$

Where, ΔG_s is the energy increase due to surface tension, ΔG_v is the free energy of condensation per unit volume, *r* is the mean radius of cluster, σ is surface energy (which is the ratio of solute concentration to saturated solution), V and *A* are the volume and surface area of the cluster. The Gibbs energy of the system *(*ΔG_{hom}) increases with radius until the nucleation energy barrier (ΔG^*_{hom}) is reached at the critical radius size (r^*). Any clusters with radius larger than the critical radius, ($r^* = -\frac{2\sigma}{\Delta G_v}$), decrease in free energy and becomes stable. The critical free energy or the activation energy barrier of nucleation from melts can be expressed in terms of equation 6.8 [54].

$$\Delta G_{hom^*} = \frac{16\pi\sigma^3 V_m^2 T_m^2}{3\,(\Delta H_m \Delta T)^2} \qquad \text{(eq. 6.8)}$$

Where, V_m is the molar volume of clusters, $\Delta T = T_m - T$ *is t*he supercooling, ΔH_m is the enthalpy of melting and T_m *i*s the melting temperature. There are also various other barriers due to diffusion of molecules with the appropriate conformation to the interface between the bulk and the growing nucleus. The conformation and diffusion barriers, *(*$-\Delta G_{diff^*}$), which the molecules need to overcome in order to interact with the growing surface of the nucleus and these can be related to the frequency of nuclei formation, J_{hom}, by equation 6.9 [55].

$$J_{hom} = \frac{NkT}{h} exp\left(\frac{-\Delta G_{diff^*}}{kT}\right) \exp\left(\frac{-\Delta G_{hom^*}}{kT}\right) \quad \text{(eq. 6.9)}$$

Where, *k* is Boltzmann's constant, *h* is Planck's constant, *N* is the number of molecules and *T* is the absolute temperature. The rate of diffusion of the molecules decreases as the temperature is reduced and the viscosity of the solution is increased. As the molecules overcome the conformation barrier and comes in contact with the nuclei, it results in loss of entropy from the system.

Heterogeneous nucleation in the fat crystallisation process, on the other hand, is initiated due to factors such as walls of a container, impellers, the presence of lipids like mono or diglycerides or dust molecules acting as nucleation sites. The decrease in the interfacial energy required to form the critical nucleus in heterogeneous nucleation causes the activation energy barrier for this process to be lower than that of homogeneous nucleation. Heterogeneous nucleation can be defined as the product of homogeneous nucleation and a function of the contact angle (θ) between the nucleus, foreign substrate and the liquid phase. If the surface of the foreign particle is flat and the nucleus is cap-shaped, then the activation free energy for heterogeneous nucleation can be expressed as a function of the activation free energy for homogeneous nucleation (equation 10) [56].

$$\Delta G_{het} = \Delta G_{hom} * f(\theta) \quad \text{(eq. 6.10)}$$

$$\textit{Where, } f(\theta) = \frac{1}{4}(2 + \cos\theta)(1 - \cos\theta)^2 \quad \text{(eq. 6.11)}$$

Secondary nucleation in a fat system can occur as a result of the components from growing crystals acting as seeds for further crystallisation. Triaclyglycerol seeds consisting of unsaturated fatty acids with higher melting points can be used at this stage to control the polymorphic crystallisation of fats [57].

6.9 The morphology of fats

The term morphology or habit can be defined as the overall shape of a crystal. The competitive growth of crystal surfaces can affect the morphology or habit of the solid phase. The variation of surface roughness affects the growth rate of the different planes of crystals, with the flattest crystal faces growing the slowest. These slowest growing crystal faces dominate the morphology and can have large surface areas. Crystals can be classified into 3

types of habits: prismatic (elongated crystals thicker than needles), acicular (long and needle like thinner than prismatic crystals) and tabular (flat-plate like crystals) (figure 6.11) [58].

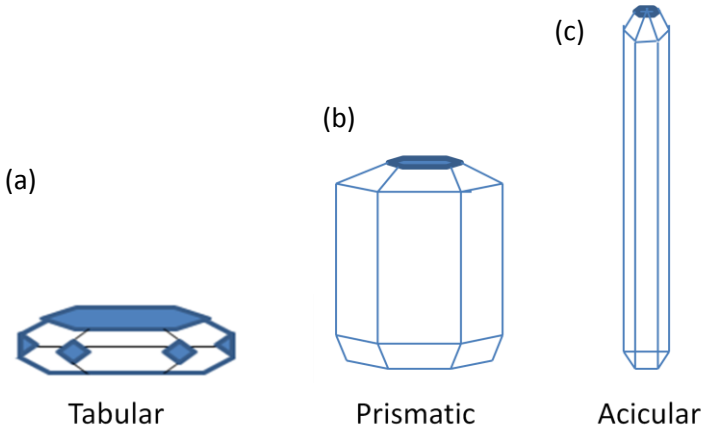

Figure 6.11: Examples of crystal habits [58].

In fat polymorphism, α crystals are likely to be thin and have small crystalline structure, β' crystals on the other hand has a needle-like morphology (less than 5 µm) and β polymorphs are much larger and have a plate-like shape[59].

6.10 Types and Structures of surfactants in colloidal system

Surfactants can be defined as amphiphilic or amphipathic compounds. This means that such substances consist of a hydrophilic head that has affinity for a polar solution and a hydrophobic chain with affinity for non-polar solutions (figure 6.12). The polar or ionic head groups in the aqueous environment interact with one another via dipole-dipole and ion-dipole interactions [60].

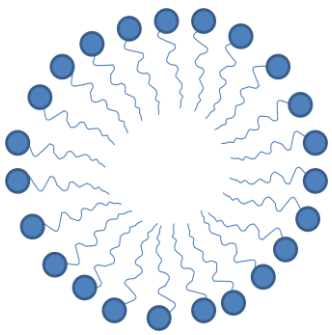

Figure 6.12: Surfactant molecules with a hydrophilic moiety and a hydrophobic chain forming a micelle [61].

There are 4 main types of surfactants which are classified according to the charge of the hydrophilic head group. These are anionic (negatively charged polar head group), non-ionic, amphoteric or zwitterionic (the hydrophilic moiety can be positively or negatively charged depending on the condition) and cationic (positively charged polar head group) surfactants [62].

In liquid-liquid systems, the surfactant molecules are concentrated at the interface between the two immiscible phases which decreases the interfacial tension of the phase boundary. There are 3 main types of detergency mechanisms; one of which involves the surface active agents functioning by forming micellar aggregates, when a critical micelle concentration (CMC) is reached with increase in concentration of the surfactant. The micelles surround the stain particles and break them down into smaller fragments. This in turn allows removal of dirt and grease from the surfaces i.e. fabrics (detergency mechanisms are discussed in depth in section 6.13). The CMC of a surfactant can be affected by variables such as temperature, pressure and increasing hydrocarbon chain length of apolar groups. For instance, the CMC for ionic surfactants has been found to decrease in the presence of electrolytes (which reduces the strength of electrostatic repulsions between the surfactants' charged headgroups) and increase with decrease in charge of the counterions present in solution, since this decreases the screening ability of the counterions [63]. Micelles can exist in two forms which are oil-in-water micelles and water-in-oil micelles. In aqueous solution, the hydrophilic heads are in contact with the surrounding polar environment whilst sequestering the hydrophobic tail regions in the micellar core to form oil-in-water micelles. In non-polar solvents however, exposing the hydrophilic head group moieties to the solvent is energetically unfavourable so this causes the hydrophilic head groups to be in the micellar core and the hydrophobic chains to point away from the centre and into the solvent. Droplet microemulsions are swollen micelles in which the micellar core contains a liquid immiscible with the continuous liquid phase. The size of microemulsion droplets can be altered by varying the oil to surfactant and water to surfactant ratios for inverse and reverse micellar systems [64].

6.11 Thermodynamics and kinetics of surfactants

The solubility of ionic surfactants increases with temperature until it reaches the CMC, at a specific temperature. At this point the CMC and the surfactant solubility are equal which is referred to as the Krafft or critical micelle temperature. The solid hydrated surfactant,

micelles and monomers exist in equilibrium at this Krafft point. Beyond the Krafft temperature, surfactants form micelles at concentrations above its CMC [65]. Surfactants with ionic or highly polar head groups and long straight alkyl chains have high Krafft temperatures. Non-ionic surfactants on the other hand do not exhibit a Krafft point as the solubility decreases with temperature. Instead, after reaching a transition temperature known as the cloud point the non-ionic surfactants lose its surface active properties due to the formation of micellar aggregates which separate and cause the dispersion to become turbid [66,67].

The overall Gibbs energy for micelle formation in a surfactant based system is mainly affected by the electrostatic and hydrophobic effects. The hydrophobic Gibbs energy (or transfer Gibbs energy), ΔG_t^o, can be defined as the Gibbs energy for the process of transferring the hydrocarbon solute from the hydrocarbon solvent to an aqueous phase (equation 6.12) [67].

$$\Delta G_t^o = (a - bn_c)RT \qquad \text{(eq. 6.12)}$$

Where, a and b are constants for a specific hydrocarbon chain and n_c is the number of carbon atoms in the chain. The transfer Gibbs energy can also be defined in terms of entropy and enthalpy (equation 6.13) [67].

$$\Delta G_t^o = \Delta H_t^o - T\Delta S_t^o \qquad \text{(eq. 6.13)}$$

Where, ΔH_t^o is the enthalpy of transfer and ΔS_t^o is the entropy of transfer. The transfer of the hydrocarbon solute into the aqueous medium causes the hydrogen bonds between the water molecules to break and form differently structured water molecules known as icebergs around the hydrophobic chain. This leads to an increase in the Gibbs energy and a decrease in the entropy [68].

6.12 Surfactants used in detergency

Surfactants are most widely used as cleaning agents in laundry and cleaning products. These active agents have different properties depending on the ratio of hydrophilic and hydrophobic groups. For instance, as the hydrophobicity of the surfactant increases, the solubility of it in the aqueous phase decreases whilst the solubility in oil increases [69]. Since

1954, the degree of hydrophilicity and hydrophobicity of a surfactant has been characterised using the Griffin method known as the hydrophilic- hydrophobic balance or HLB. This involves use of a scale ranging from 0 (extremely lipophilic) to 20 (extremely hydrophilic surfactant). The HLB system is a good indicator for identifying the emulsification behaviour of surfactants and for selecting appropriate types of surfactant for particular applications i.e. as emulsifiers, detergents and wetting agents. The surface active compounds with good oil solubility tend to produce water-in-oil emulsions whereas, surfactants which are more hydrophilic form oil-in-water emulsions [70].

The main types of surface active agents which are used for commercial cleaning purposes are alcohol ethoxylates, alkyl ethoxylated sulphates and linear alkylbenzene sulphonates. The detergent analysed in this project is composed of 4 different types of surfactants. These are linear alkylbenzene sulphonate (anionic), alkyl ethoxylates (non-ionic), ethoxylated alkyl sulphate (anionic) and alkyl carboxylate (anionic).

6.12.1 Linear Alkylbenzene Sulphonates

Linear Alkylbenzene Sulphonates (LAS) are highly water soluble surface active agents. Such surfactants are mostly used in detergent formulation and household cleaning products. These compounds are synthesised by Friedel-Craft alkyation of benzene followed by sulphonation of the aromatic ring (figure 6.13) at the para-position of the hydrocarbon chain [71].

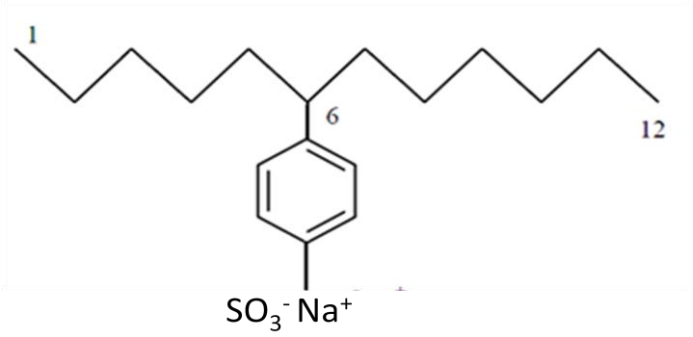

Figure 6.13: Structure of LAS [72].

The carbon chain length of LAS can vary between C_{10} to C_{14} and the position of the benzene group can also be altered. This results in formation of 26 isomers of LAS. Such surfactants exist in the form of anionic surfactants in solution [72].

6.12.2 Alkyl Ethoxylates

Alkyl ethoxylates (AEs) are a type of non-ionic surfactant which is widely used in various household cleaning applications. These surface active agents are composed of an aliphatic hydrocarbon chain connected to one or more ethoxylate groups. The alkyl chain length of AE consists of 12-15 carbons (figure 6.14) [73].

$$\mathbf{RO - (CH_2 - CH_2O)_n - H}$$

Figure 6.14: Structure of an AE. Where, R is the alkyl chain length consisting of 12-15 carbons and n is the ethoxylated chain length of 1 – 20 [73].

AEs are usually removed from the environment by aerobic and anaerobic biodegradation once it enters the wastewater treatment system.

6.12.3 Ethoxylated Alkyl Sulphates

Ethoxylated Alkyl Sulphates (AESs) are a type of anionic surfactant which consists of a long alkyl chain length of 12 to 18 carbons bound to a variable length ethoxylated chain which in turn is connected to a sulphate group (figure 6.15) [74].

$$\mathbf{CH_3(CH_2)_x\,(CH_2)_yOSO_3^-}$$

Figure 6.15: Structure of an AES [74].

The properties of these surfactants are affected by the alcohol chain length and the polar head moiety. These compounds are more hydrophilic than the sulphonates as it consists of an addition oxygen atom[74].

6.12.4 Alkyl Carboxylate

Most carboxylates including Alkyl Carboxylate (AC) are widely used as soaps. These surfactants are alkali metal salts of fatty acids which are obtained from oils using

saponification. This process involves neutralisation of alkali or addition of salt to the glycerol by-product. ACs consists of a mixture of fatty-acid hydrocarbon chain lengths with high levels of even numbered carbon atoms (figure 6.16) [76].

$$\mathbf{CH_3(CH_2)_xCOONa}$$

Figure 6.16: Structure of AC [76].

Where, x = 16-36. Pure long chain soaps exist as anhydrous crystals or crystal hydrates at room temperature and also, as viscous semisolids in the presence of water. Such compounds can exhibit higher solubility in polar and aqueous based solvents[76].

6.13 The mechanisms of detergency on soiled fabrics

Fabric detergency can be defined as a process involving interaction between aqueous detergent solutions, soils and fabric surfaces. Due to the surfactants' ability to adsorb at both fabric-water and soil-water interfaces it acts as an effective soil remover. The efficiency of the surface active agents is affected by several factors and these include the weave of the fabrics, types and quantity of soils on the materials as well as fabric pretreatments i.e. the presence of a dye can complicate removal of contaminants from the surface. The composition of the fabrics is also one of the main aspects that determine the mechanism via which soils can be removed using surfactant. For example, oily soils are removed by the means of a roll-up mechanism from the cotton fabrics, since these fabrics consist of rough and inconsistent structured hydrophilic fibers. In contrast, emulsification is the prevalent method of oily soil elimination from polyester, which is composed of identical cylindrical-shaped hydrophobic fibers [77].

Over the past 20 years, detergent solutions consisting of various components including enzymes, surfactants and builders have been developed for eliminating soils effectively from fabrics. Each of the components when combined together has been proven to significantly increase the rate of soil removal from fabrics. For example, builders function by precipitating the divalent ions from water which are in turn also responsible for formation of complexes and increasing interactions between the fabrics and the soil [78]. Lipases, on the other hand, hydrolyse triglycerides into three fatty acids and glycerol, which are more easily removed. Hence, lipase enzymes aid surfactants in removing soils from the fabrics [79].

Surfactants are the key ingredient for detergent formulations. These surface active agents function via three main mechanisms of oily soil removal: roll-up, emulsification or necking and solubilisation [80]. The roll-up process involves lowering of the fabric surface-water interfacial tension by the deposition of surfactant molecules at this interface which then increases the contact angle between the soil molecules and the fabric interface. This relationship can be expressed in terms of equation 6.14 [81].

$$\cos\theta = \frac{\gamma_{ws} - \gamma_{os}}{\gamma_{ow}} \qquad \text{(eq. 6.14)}$$

Where, γ_{ws} is the interfacial tension between the surfactant solution and solid substrate (the fabric), γ_{os} is the interfacial tension between the oil (the soil) and solid substrate and γ_{ow} is the interfacial tension between the surfactant solution and oil. For instance, anionic surfactants adsorb on the fabric with their negatively charged head groups facing the detergent solution and it acts by reducing the interfacial tension between the surface active agent molecules and the solid substrate. This method is effective for removal of soil from more hydrophilic fabrics such as cotton which swells when the material comes in contact with water and as a result, releases the oily particles from the fibres (figure 6.17) [82].

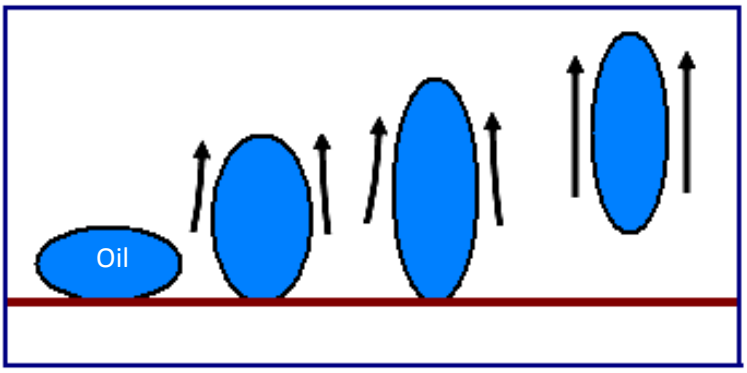

Figure 6.17: Roll up mechanism due to fabric wetting [82].

On the other hand, emulsification involves reduction of the interfacial tension at the oil-water interface. During this process the contact angle between the soil and the surface remains constant and the outer segments of soils are incorporated in small emulsion droplets (figure 6.18). In the presence of high levels of polar soil components, liquid crystals form due to interaction between the soil constituents and the oil-water surface. The intermediate phase is then agitated to produce fragments which are emulsified in the detergent solution. Factors

such as the ratio of polar and non-polar components of the oil substrate, electrolyte concentration and temperature can affect this mechanism [83].

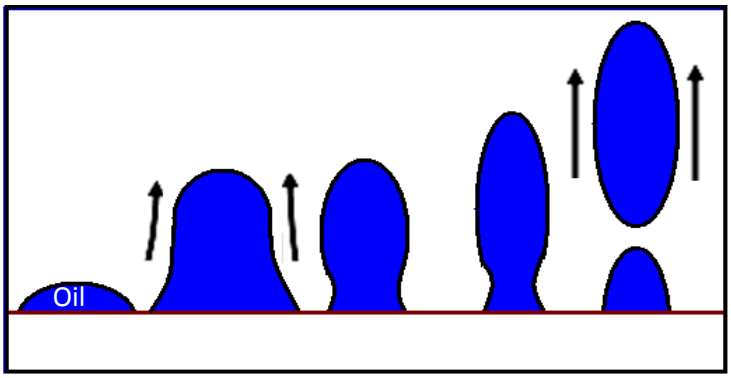

Figure 6.18: Emulsification mechanism as a result of soil-water interfacial tension reduction [83].

Another effective mechanism via which soils are removed from fabrics is solubilisation. This involves micelles breaking down the soils into smaller fragments when there is an excess surfactant relative to oil present (figure 6.19). The rate of such a mechanism is affected by the isotropic or liquid crystalline form of the surfactant-rich phases. Such phases solubilise soils either directly or by interacting with soils to form a microemulsion which in turn is emulsified under specific conditions. This process can be identified when non-ionic surfactants are above their cloud point [27]. The key issue with lard, however, is that it is not liquid at the lower wash temperatures, which may seriously hinder the 3 detergency mechanisms of roll-up, emulsification and solubilisation.

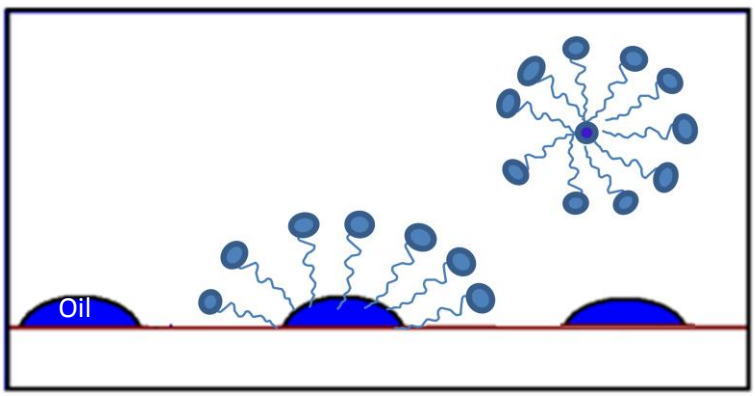

Figure 6.19: Solubilisation mechanism of an oil droplet in the presence of surfactants.

6.14 Techniques for fat analysis

The techniques which have been used to analyse fats such as the lard and glycerol trioleate as well as the soiled fabrics before and after wash using P&G's C24E3S surfactants, are described below.

6.14.1 Wide angle X-ray scattering

WAXS was used to analyse the crystal structures of lard with change in temperature, fabrics and detergent surfactant. More information on WAXS can be found in the Experimental Methodology chapter.

6.14.2 Small angle X-ray scattering

The small angle X-ray scattering (SAXS) technique was used to analyse the crystal structures of lard with change in temperature, fabrics and detergent/surfactant. More information on SAXS can be found in the Experimental Methodology chapter.

6.14.3 Atomic force microscopy

Atomic force microscopy (AFM) has been was used to investigate how the structure of the lard changes with variation in temperature. More information on AFM can be found in the Experimental Methodology chapter.

6.14.4 Laser diffraction particle sizing technique

The laser diffraction particle sizing technique has been employed to determine the size distribution of the lard globules produced after wash and when left in wash solution. More information on this technique can be found in the Experimental Methodology chapter.

6.15 Results and Discussion

6.15.1 SAXS and AFM data for lard - exposed to uncontrolled (room temperature) and controlled (20 ^{o}C) condition

Lard was initially used as the fat model instead of other fat substrates such as the glycerol trioleate or glycerol tristearate because it's composed of a range of triglycerides, making it more problematic and difficult to remove from the fabrics. An as-received lard sample provided by P&G was initially melted at a temperature of 55 °C and this was verified by the SAXS intensity versus 2θ, dark blue line in figure 6.20 not showing any peaks. Following this, the melted lard was super-cooled and then slowly heated up to 40 °C. This showed the presence of α, β' and β polymorphs with d-spacing values of 49.0 Å (2θ= 1.8°), 34.2-35.4 Å (2θ= 2.5 to 2.6) and 43.4 Å (2θ= 2°), respectively (calculations are included in appendix table A3.1), at the temperatures of -10 °C, -20 °C and 10 °C. The results suggest that upon super-cooling after initially melting the lard, the least densely packed α crystals with the largest Gibbs energy were formed, along with the more stable β' and β crystals, and so all three forms were detected by SAXS until the temperature was raised above the melting point of the α polymorph, which was 15 °C. Following this, the SAXS peaks for only the β' and β polymorphic crystals with lower Gibbs energy and greater thermodynamic stability were visible with increase in temperature up to 30 °C. As the temperature was further enhanced to 40 °C, just the presence of the most stable β polymorph was identified, indicating that the lard follows monotropic behaviour with change in temperature [27].

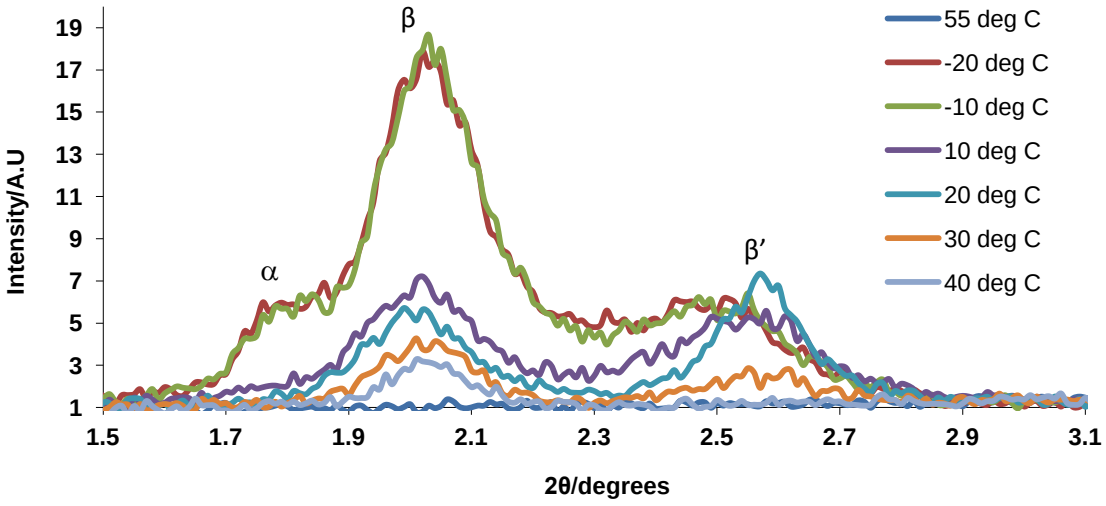

Figure 6.20: SAXS results for lard with change in temperature.

The gradual polymorphic transformation with increase in temperature was also evident using the AFM. By using this technique a clear change in shape of the lard sample with change in

temperature was observed (Figure 6.21). It was seen that at the lower range of temperatures (≤ 15 °C), a globular fat structure was identified whilst at higher temperature (≥ 15 °C) a clear phase transition indicated by the formation of vertical pleated sheet like structures representing the β polymorphs was detected.

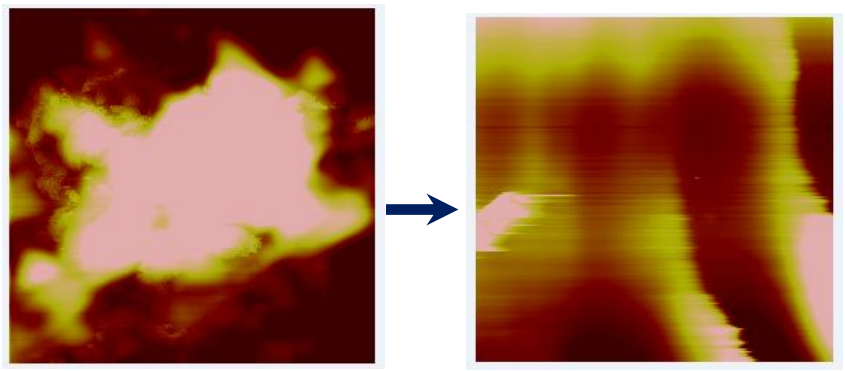

Globular α crystals at ≤ 15 °C. Vertical pleated sheet like βcrystals at > 15 °C.

Figure 6.21: Change in the shape of lard with increase in temperature after complete melt, analysed using the AFM.

6.15.2 SAXS analysis of unsoiled and soiled cotton, polyester and polycotton fabrics

SAXS analysis of the fabrics (cotton, polycotton and polyester) on their own, and with lard melted and kept at 55 °C did not show the presence of any peaks (figure 6.22).

(a)

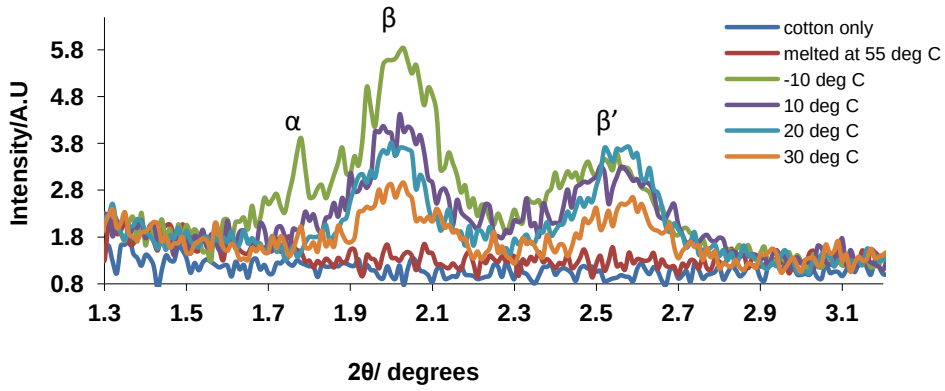

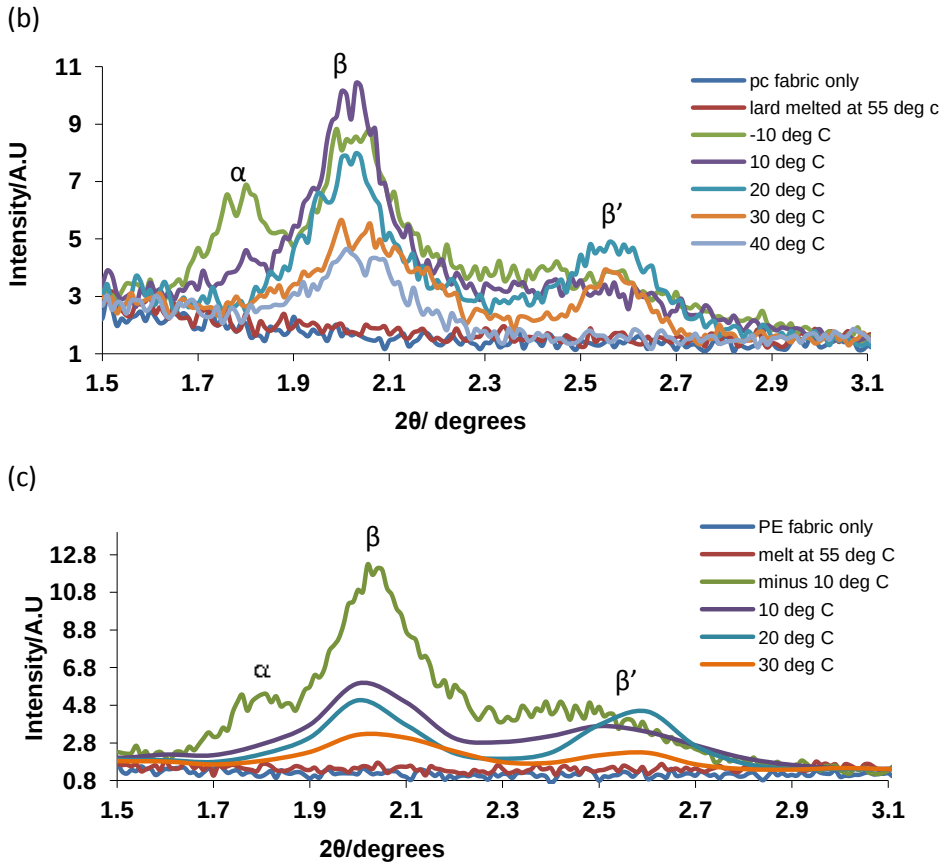

Figure 6.22: SAXS results for soiled (a) cotton (b) polycotton and (c) polyester, with change in temperature.

As the temperature was decreased rapidly down to -10 ^{o}C after melting, the presence of all the polymorphs were detected using SAXS with d-spacing values of 49.0 Å (α), 35-36.3 Å (β'_1) and 43.4-45.5 Å (β'_2/β) on all the fabrics. For the different types of soiled fabrics analysed it was observed that with a continuous increase in temperature to 20 ^{o}C and 30 ^{o}C, only the Bragg peaks for β'_1 and β'_2/β polymorphs were identified. A decreased α peak with d-spacing value of 49.0 Å was observed for the soiled polycotton fabric swatch exposed to 10 ^{o}C, showing that some α-crystals have not yet melted whereas for the soiled cotton and polyester, the α-crystals appear to have all melted at this temperature. The persistence of some α-crystals at 10 ^{o}C on the soiled polycotton sample is most likely to be due to these crystals having a larger size.

6.15.3 SAXS data for unsoiled and soiled fabrics after exposure to room temperature and at a constant temperature of 20 °C

Analysis of the different types of unsoiled fabrics did not show any SAXS diffraction peaks (figure 6.23a). After applying a high concentration (78 mg/L) of Jupiler detergent solution to the fabrics and partial drying at 20 °C overnight, diffraction peaks with d-spacing values ranging from 32.5-34.6 Å were observed for all the fabric swatches (figure 6.23b). This clearly signifies that the scattering peaks detected are due to the partially dried detergent alone.

(a)

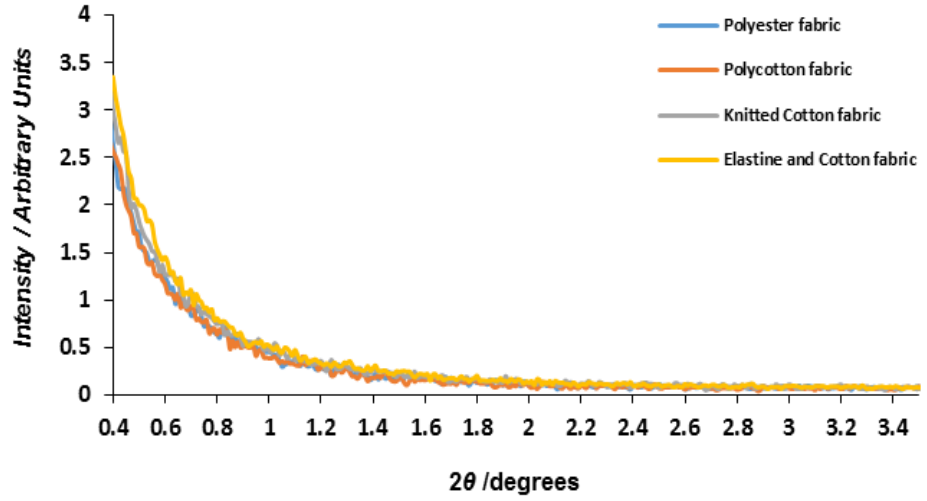

(b)

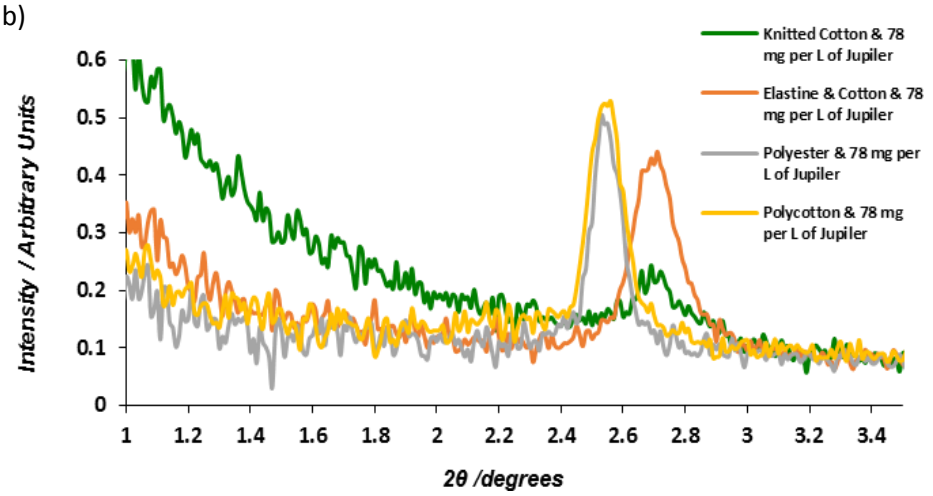

(c)

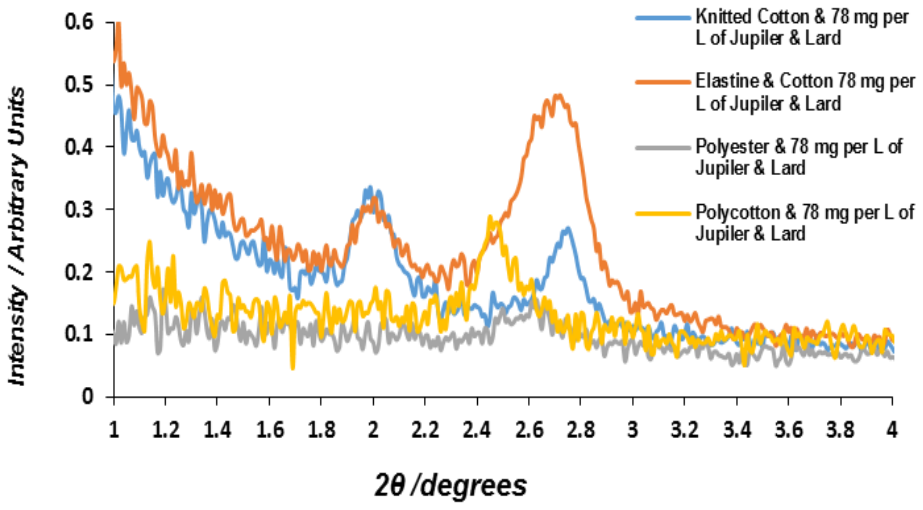

Figure 6.23: Intensity against 2θ values for fabrics (a) without lard (b) with 78 mg/L of detergent and without lard & (c) with detergent and lard, measured using SAXS.

Furthermore, similar results as obtained for fabrics with 78 mg/L of detergent were also gathered from examining the unsoiled fabrics with a range of detergent concentrations using SAXS (table 6.2). After lard was deposited on fabrics containing the detergent solution and left to dry overnight, SAXS analysis of the fabric swatches showed additional diffraction peaks with a d-spacing value between 44.0 Å -44.2 Å (table 6.2), demonstrating existence of the β'_2 or β polymorphs.

Table 6.2: d-spacing values for the unsoiled and the soiled fabrics after various concentrations of the detergent solution have been applied and dried at 20 ^{o}C.

Fabric type d-spacing value for fabrics	Polyester	Polycotton	Knitted Cotton	Elastine & Cotton
with 78 mg/L of detergent after drying and without lard/ Å	34.6	34.5	32.5	32.5
with 40 mg/L of detergent after drying and without lard/ Å	33.2	31.9	32.6	32.5
with 20 mg/L of detergent after drying and without lard/ Å	32.8	32.1	32.2	32.6
with 78 mg/L of detergent after drying and with lard/ Å	32.7	36.1	32.6, 32.0,44.0	32.7, 44.0
with 40 mg/L of detergent after drying and with lard/ Å	44.2	44.2	32.8, 44.2	32.7, 44.0
with 20 mg/L of detergent after drying and with lard/ Å	31.9	32.2	32.4,44.0	31.9

By analysing the results from table 6.2, it can be evaluated that the lard was present on the knitted cotton fabric for all the detergent concentration range applied. It was also detected

on all the other types of fabrics when 40 mg/L of the detergent was used. For the 20 mg/L and 78 mg/L detergent concentrations used, the presence of lard polymorphs was not always evident. The results obtained indicate that although the lard was spread as evenly as possible on the fabrics, some areas of the fabrics were still likely to have more lard than other areas. It is also possible that initial exposure of the lard on the soiled fabrics to the detergent solution during the drying process at 20 ^{o}C have removed the small amount of lard present via one or more combinations of detergency functionalities. These include roll up mechanism for soil removal from cotton based fabrics, emulsification for eliminating fat from the polyester fabric and solubilisation for soil eradication from fabrics when exposed to high detergent concentration. In the presence of excess surfactant and when a CMC has been reached, micelles can form, which in turn can break down the fat substrates into smaller molecules.

6.15.4 WAXS data obtained for fat exposed to a constant temperature of 20^{o}C

The results obtained using WAXS on lard in its solid form showed the presence of orthorhombic and pseudo orthorhombic β′-polymorphs with d-spacing values of 3.8 Å and 4.2 Å respectively, when the Bragg peaks were analysed. The peak detected at 4.2 Å could be also possibly due to formation of α crystals. However, this is highly unlikely as the temperature used was above the melting point of α polymorph. Furthermore, a peak at 4.5 Å representing the β polymorph was also detected (figure 6.24).

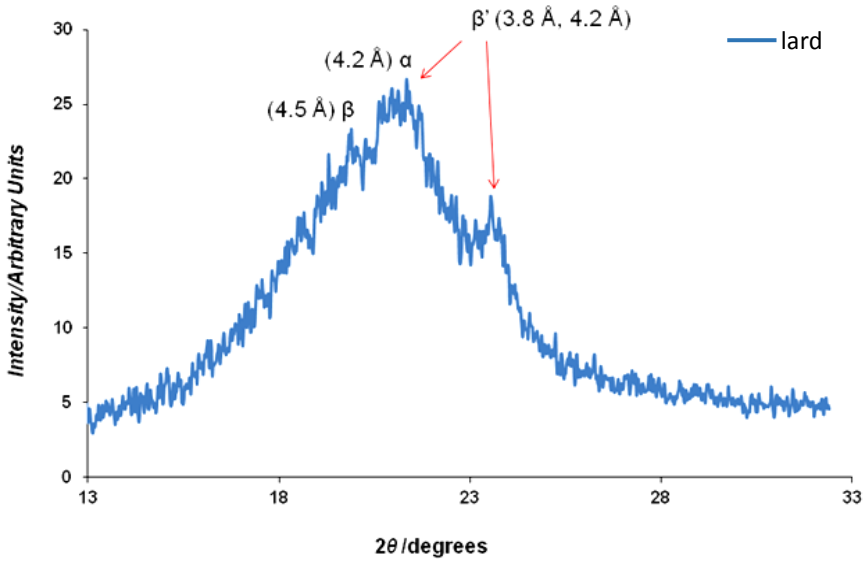

Figure 6.24: Intensity against 2θ values for lard, measured using WAXS.

The results obtained for lard using WAXS and SAXS coincides with the data reported by Kalnin *et al.* [27], which shows that at a temperature of 20 °C both β' and β polymorphs are present. This is because β'/ β crystals have a higher melting point than 20 °C, which is required to break down the ordered and stable lamella structure.

6.15.5 WAXS data for unsoiled and soiled fabrics after constant heating at a temperature of 20 °C

WAXS analysis of the different types of fabrics showed overlap between the d-spacing values obtained for the fabrics (table 6.3 and figure 6.1a) and the lard on its own (figure 6.24).

Table 6.3: WAXS characteristics of the different types of fabrics used.

Fabric type	WAXS Characteristics/ d-spacing Literature values/Å[27]	WAXS Characteristics Experimental values/Å
Polyester	3.4,3.8, 5.1	3.4, 3.8, 4.9
Knitted Cotton	2.6, 3.9, , 4.3, 5.4, 6.0	2.6, 3.8, 4.3
Polycotton	3.4 , 3.8	3.4,3.8
Elastine & Cotton	3.8, 4.3	3.8

From figure A3.1 in the appendix, the high intensity WAXS peaks at 3.8-3.9 Å and 4.3 Å for the different types of fabrics with lard (appendix figure A3.1b) compared to the fabrics on its own (appendix figure A3.1a) suggests that the β' polymorphs are formed and present at the temperature of 20°C. Further to this, the soiled fabrics exposed to uncontrolled room temperature of 20 °C $\pm$ 2 °C overnight also displayed high intensity peaks at the 2θ regions of 20° and 23° in contrast with the intensities for clean swatches of fabrics. This confirms the existence of the β' polymorphs at the temperature of 20 ($\pm$ 2) °C (table 6.4).

Table 6.4: d-spacing values for soiled fabrics (under controlled and uncontrolled conditions), areas of fabrics without direct lard deposition/with detergent and soiled fabric samples without detergent solution.

Fabric type	Polyester	Polycotton	Knitted Cotton	Elastine & Cotton
d-spacing value for fabrics with lard at 20 °C/ Å	3.5, 3.8, 4.25	3.9, 4.24	2.6, 3.9, 4.15, 5.3	2.6, 3.9, 5.9
d-spacing value for fabrics with lard at room temperature/ Å	3.5, 3.8	4.0, 4.26	2.6, 3.9, 5.8	2.6, 3.9, 4.2, 5.2
d-spacing value for fabrics with lard and without detergent after ageing for 30 days at room temperature/ / Å	3.8, 3.5, 4.2	3.8, 4.2	2.6, 3.8	3.8, 4.2
d-spacing value for fabrics areas without lard and with detergent after 30 days at room temperature / Å	3.5, 3.8, 5.0	4.3, 4.5, 6.1	2.5, 4.1,4.3, 6.1	2.6, 3.9, 4.3, 5.4, 6.1

In a separate experiment, by exposing the soiled samples at room temperature of 20 $\pm$ 2 ^{o}C for 30 days, showed presence of thermodynamically stable β' polymorphs indicated by the high intensity scattering peaks with d-spacing values of 3.8 Å and 4.2 Å. This demonstrates that the lard polymorphs follow monotropic behaviour. This was also reflected in the WAXS analysis of the areas of the aged fabrics consisting of detergent solution only and where the lard was not deposited directly (table 6.4). The fat was found to spread as a result of initial melting of the lard at 60 ^{o}C and cooling at 20 ^{o}C. Thus, it can be suggested that the fat components have liquefied at high temperature and diffused across the fibers of the fabrics before crystallising.

6.15.6 WAXS analysis of the detergent solution

The WAXS analysis of the dried detergent solution has shown formation of a broad amorphous peak within the 2θ range of 18 to 37 degrees (figure 6.25).

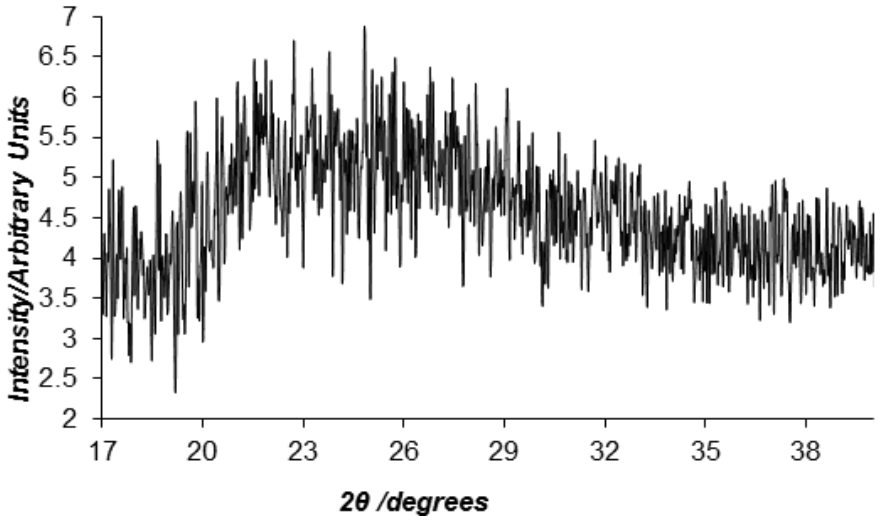

Figure 6.25: Showing a broad amorphous peak for the detergent solution.

By applying a range of detergent concentration to all the different types of fabrics and then, allowing the swatches to dry overnight (table 6.5 and appendix A3.2a, A3.2c, A3.2e, A3.2g and A3.2i) before WAXS analysis was carried out, have shown presence of WAXS scattering peaks corresponding to d-spacing values around 3.8 Å - 3.9 Å and 4.2 Å – 4.3 Å. The peaks are probably due to the structure of the fabrics used, confirmed by the WAXS values obtained earlier for unsoiled fabric swatches in table 6.5.

Table 6.5: d-spacing values for unsoiled fabrics consisting of various concentrations of the detergent solution.

Fabric type **d-spacing value**	**Polyester**	**Polycotton**	**Knitted Cotton**	**Elastine & Cotton**
with 78 mg/L of detergent after drying and without lard/ Å	3.5, 3.8, 4.7	2.6, 3.9	3.5, 3.8, 4.9	2.6, 3.9, 4.2, 5.2
with 40 mg/L of detergent after drying and without lard/ Å	3.4, 3.8, 4.8	2.6, 3.9, 4.3	3.5, 3.9	2.6, 3.9, 4.2
with 20 mg/L of detergent after drying and without lard/ Å	3.4,3.8,4.8	2.6, 3.9, 4.3	2.6, 3.5, 3.9, 5.0	2.6, 3.9, 4.3
with 10 mg/L of detergent after drying and without lard/ Å	3.5,3.8,4.8	2.6,3.9,4.2,5.3	2.6,3.5,3.8,5.0	2.2,2.6,3.9,4.4,5.2,5.6
with 5 mg/L of detergent after drying and without lard/ Å	3.5,3.9,5.0	3.5,3.8,4.7	2.6,3.5,3.8,5.0	2.6,3.0,3.9,4.3,5.2,5.3
with 1 mg/L of detergent after drying and without lard/ Å	3.5,3.8,4.9	2.6,3.9,4.2,5.3	3.4,3.8	2.6,3.8,4.2,5.2

Furthermore, the results obtained for fabrics containing detergent and lard showed intensity peaks with d-spacing values between 3.8 Å-3.9 Å and 4.1 Å-4.3 Å (table 6.6 and appendix figures A3.2b, A3.2d, A3.2f, A3.2h and A3.2j). However, due to overlap between the fabric and the lard WAXS intensity peaks, it is difficult to determine whether the β' polymorphs were eradicated from the fabrics via one or a combination of detergency mechanisms.

Table 6.6: d-spacing values for soiled fabrics consisting of various concentrations of the detergent solution.

Fabric type d-spacing value	Polyester	Polycotton	Knitted Cotton	Elastine & Cotton
with 78 mg/L of detergent after drying and lard/ Å	2.4, 3.8	2.6, 3.9,5.2	3.4, 3.8, 4.9	2.6, 3.9, 4.1
with 40 mg/L of detergent after drying and lard/ Å	3.8	2.6, 3.8	3.4, 3.8	2.6, 3.8, 4.2
with 20 mg/L of detergent after drying and lard/ Å	3.5,4.1,5.0	3.9, 4.1	3.4, 3.9, 4.9	2.6, 3.8
with 10 mg/L of detergent after drying and lard/ Å	3.8,4.2,4.7	3.5, 3.9, 4.2,4.5	2.6,3.9,4.2	2.6,3.8,4.2
with 5 mg/L of detergent after drying and lard/ Å	3.5,3.8,5.0	3.9,4.1	2.6, 3.9,5.4	3.8,4.2,5.2
with 1 mg/L of detergent after drying and lard/ Å	3.4,3.9,4.9	3.4,3.8	2.6, 3.9,4.2,5.1	3.8,4.3,5.2

6.15.7 Ageing experiment

The ageing experiments carried out on the soiled cotton, polycotton and polyester fabrics showed presence of only the β and β' polymorphs at the temperatures of -10 ^{o}C, 10 ^{o}C, 20 ^{o}C and 30 ^{o}C (appendix figures A3.3, A3.4 and A3.5). The SAXS intensities from the analysis of the different types of soiled fabrics was found to differ when the data collected for day 1, day 3 and day 5 of ageing samples were compared. This could be due to limitations associated with the experiments such as the fabric pieces (1 cm x 1 cm) were cut out from different fabric swatches for day 1, day 3 and day 5 of SAXS analysis rather than using the same swatch for SAXS investigation over the period of 5 days. Other factors such as instrumental error can also affect the results. In a separate experiment, after melting the lard on a number of soiled cotton, polycotton and polyester fabric swatches and cooling the samples down to 10 ^{o}C, the soiled fabric pieces were left to age for 1 hour and 4 hours before analysis was undertaken using the SAXS technique. From the data obtained, it was observed that the intensities of the Bragg peaks for β'_1 and β'_2/β polymorphs were almost two to three times higher after 4 hours

of ageing compared to the intensities after just 1 hour for the soiled, polycotton polyester fabrics (figure 6.26).

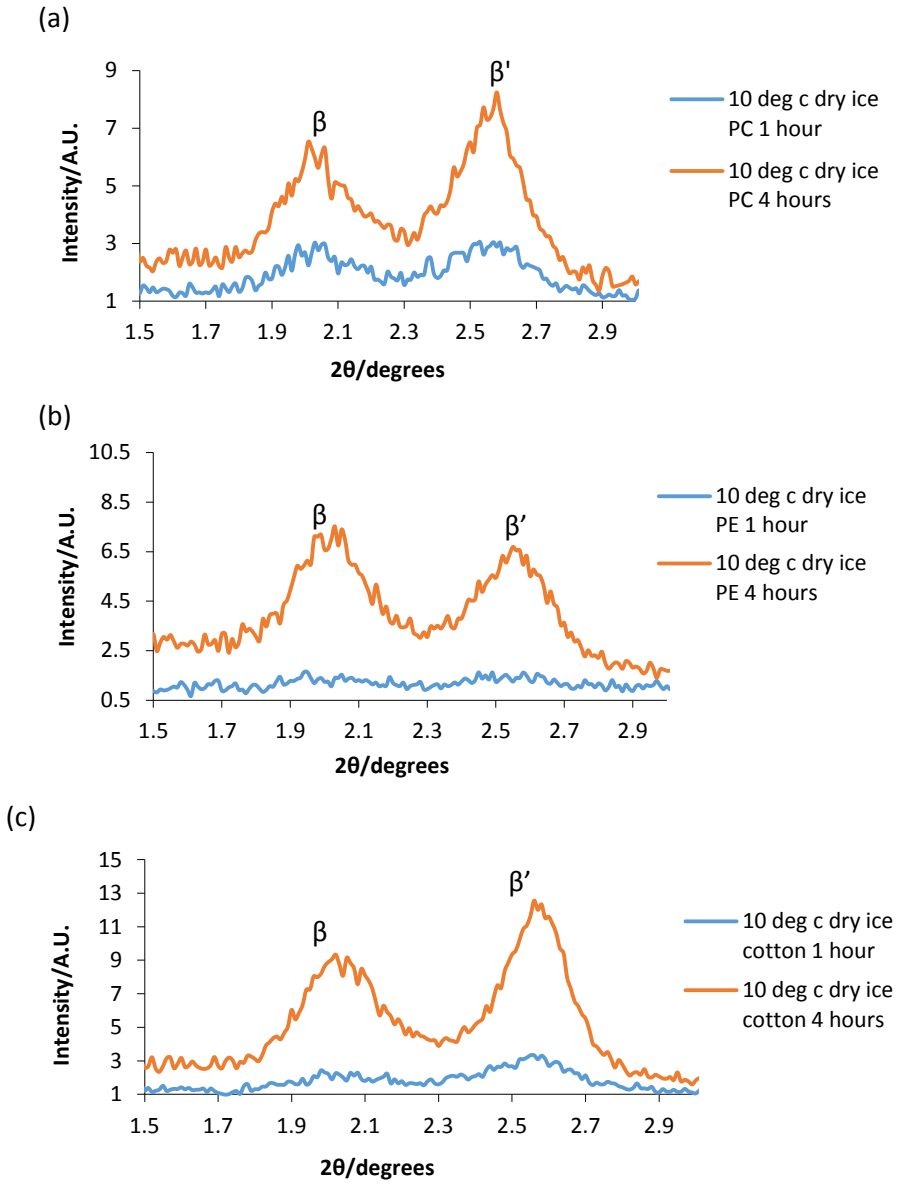

Figure 6.26: SAXS data obtained for (a) polycotton/pc (b) polyester/PE and (c) cotton/C fabrics after 1 hour and 4 hours of ageing, at a temperature of 10 °C.

Overall, from evaluating the SAXS results it can be suggested that even after a small period of time, the most thermodynamically stable β'_1 and β'_2/β polymorphs are present on the variety of soiled fabrics even at a lower temperature of 10 °C.

6.15.8 Wash experiments

For the wash experiments, C24E3S surfactant which is one of the main anionic surfactants used in P&G's Jupiler detergent formulation was applied. A range of different types of soiled fabric swatches (i.e. cotton, polycotton, polyester and elastine/cotton) were washed with a high concentration C24E3S surfactant (50 mg/ mL), above its CMC level at which micellar formation can be clearly detected using SAXS (figure 6.27). This procedure was repeated using a lower C24E3S surfactant concentration (0.7 mg/mL – below the CMC). In all cases after washing the soiled fabrics at 20 ^{o}C, 30 ^{o}C and 40 ^{o}C, the presence of thermodynamically stable β'_1 and β'_2/β polymorphs were detected using SAXS (appendix figures A3.6 and A3.7).

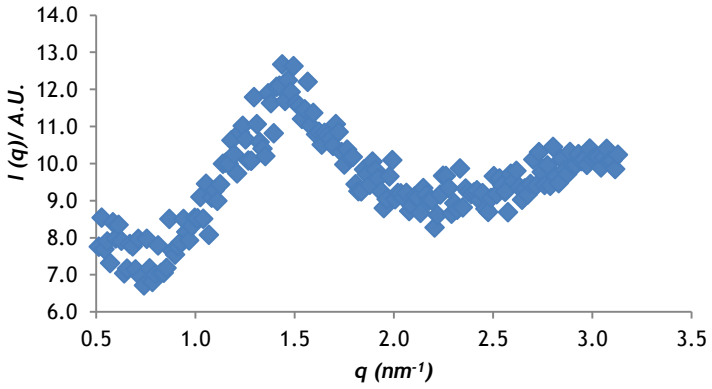

Figure 6.27: I (q) versus q graph showing formation of a peak due to the presence of micelle at C24E3S surfactant concentration of 50 mg/ mL.

The initial experiments using a high concentration of the C24E3S surfactant were undertaken only with the cotton and the polycotton fabrics. The range of fabric types used was then extended to polyester and elastine/cotton for the next two set of experiments involving the application of a low surfactant concentration and then no surfactant. An extensive variation in the SAXS intensities was observed for all of the washed soiled fabrics from the low surfactant wash experiment when compared to the high surfactant wash results. This could be due to limitations as mentioned above such as different fabric swatches were used for each wash experiment and for the SAXS analysis. Other factors like the position of the SAXS beam not focused on the same area of all the washed fabrics can also affect the results. The wash experiments where no surfactant was applied could not be analysed due to the SAXS equipment not working and it needed to be repaired. Consequently, the SAXS intensity results could not be obtained. However, the % lard removal was determined from the wash

without surfactant and compared with the data collected from the high and low surfactant experiments in section 6.15.9.

6.15.9 Quantification of lard removal

The average quantity of lard removed after washing the different types of soiled fabrics under varied wash conditions using 50 mg/mL of the C24E3S surfactant, ranged between 6% - 35% for polycotton and 21% - 36 % cotton (table 6.7 below) across the different wash temperatures. This indicates that a larger amount of lard was removed from cotton fabric compared to the polycotton fabric. It is probably due to the polar lard components trapped in the cotton fibers being removed by the aqueous based (polar) detergent solution during the washing process.

It was also observed that when one specific fabric type was exposed to different drying temperatures and washed at temperatures of either 20 ^{o}C, 30 ^{o}C or 40 ^{o}C, in average more lard was removed from both the cotton and polycotton fabrics at a higher wash temperature of 40 ^{o}C than at 20 ^{o}C and 30 ^{o}C (table 6.7). This was expected as 40 ^{o}C is close to the melting point of the most stable β polymorphs (see table 6.1 in section 6.3) and therefore, the fats are likely to softer at this temperature, making it easier to wash the soils from the fabrics. The average % lard removal value for each fabric type (cotton (C), polycotton (PC) and polyester (PE)) washed at a specific temperature (20 ^{o}C, 30 ^{o}C or 40 ^{o}C) was calculated using formula 6.1 and by taking into account of the % of lard removed from fabric swatches exposed to/ dried at temperatures of 10 ^{o}C /10 ^{o}C, 10 ^{o}C /20 ^{o}C, 20 ^{o}C /20 ^{o}C and 30 ^{o}C /30 ^{o}C, respectively. By applying the formula 6.1 below, the average % of lard removed for polycotton swatches washed at 40 ^{o}C (PC W40) which is used as an example here, was determined.

$$Average\ \%\ lard\ removed\ for\ PC\ W40 = \frac{[(\%\ lard\ removed\ at\ 10\ ^{o}\mathrm{C}/10\ ^{o}\mathrm{C}) + (\%\ lard\ removed\ at\ 10\ ^{o}\mathrm{C}/20\ ^{o}\mathrm{C}) + (\%\ lard\ removed\ at\ 20\ ^{o}\mathrm{C}/20\ ^{o}\mathrm{C}) + (\%\ lard\ removed\ at\ 30\ ^{o}\mathrm{C}/30\ ^{o}\mathrm{C})]}{4}$$

Formula 6.1: The average % lard removal for different types of washed soiled fabrics under different wash conditions has been determined using this formula.

For the wash experiments, a higher concentration of the C24E3S surfactant was deliberately used to ensure formation of micelles and to compare the level of lard removal to that of obtained using a low surfactant concentration (below the CMC level) and no surfactant at all.

Table 6.7: showing the average % lard removal from the different types of washed fabric swatches when C24E3S surfactant concentrations of 50 mg/mL, 0.7 mg/mL and none were added.

Fabric type	Average % lard removal		
	High surfactant (50 mg/mL)	**Low surfactant** (0.7 mg/mL)	**No surfactant**
Average PC W40	35± 1.2	63 ± 1.5	60 ± 2.1
Average C W40	36 ± 1.4	65 ± 1.3	62 ± 1.4
Average PE W40	-	71 ± 0.7	64 ± 0.5
Average PC W30	10 ± 2.4	54 ± 1.9	46 ± 1.7
Average C W30	21 ± 1.4	56 ± 1.3	53 ± 2.2
Average PE W30	-	61 ± 2.1	54 ± 1.5
Average PC W20	6 ± 2.1	52 ± 0.8	40 ± 2.0
Average C W20	22 ± 2.2	57 ± 1.1	46 ± 1.3
Average PE W20	-	55 ± 2.1	48 ± 2.4

It can be evaluated from the results in table 6.7 that the polyester fabric swatches demonstrated greater efficiency in removing soil both in the presence (0.7 mg/mL of C24E3S) and absence of the detergent compared to the cotton and polycotton fabrics. This could be because polyester fabrics consist of hydrophobic uniform cylindrical fibers which can cause the soils to attach to the fabric surfaces in thinner layers [84,85]. Therefore, making it easier to remove fats via agitation and also, the fats are readily accessible for the surfactant to act upon via emulsification as a result of localized micellar formation when 0.7 mg/mL of the C24E3S surfactant is added. It can be also deduced that even when no surfactant was added, the polyester fabric swatches exhibited the maximum % lard removal after washing due to the hydrophobic nature of the polyester fabric making the lard available on the surface which can be removed via agitation created by the rotation of the propellers during the wash. Furthermore, it can be stated that the cotton fabrics demonstrated higher % soil removal than the polycotton under all wash conditions. Polycotton is made up of a blend of cotton and polyester fibers which are intertwined in a hybrid fashion. The more efficient cleaning of the cotton compared to polycotton could be due to the cotton fabric being composed solely

of hydrophilic fibers which when in contact with the detergent solution leads to swelling of the fibers and an increase in the hydrophilicity [86]. This in turn aids in the exclusion of soils from the cotton fabrics via the roll-up mechanism because the lard will have a higher contact angle, θ, with the fabric when in aqueous solution. This specific detergency mechanism, along with the agitation produced by the tergotometer propellers, is found to be more effective in soil elimination from cotton than from the polycotton fabrics. It can be therefore concluded that the pure hydrophobic polyester and the hydrophilic cotton are proven to be most efficient in eradicating soil than the polycotton under different wash conditions, with and without surfactant.

The results obtained from the wash experiments with different concentrations of the C24E3S surfactant and no surfactant at all have shown that a high concentration of the surfactant remove a reduced amount of lard from all the fabrics under different wash conditions when compared to the low concentration of the surfactant and no surfactant added (table 6.7). The high surfactant concentration solution, which is above the CMC and so contains micelles, can remove lard by a solubilisation mechanism, which lower surfactant concentrations below the CMC cannot. Consequently, the reduced amount of lard removal when using the high surfactant concentration solution is likely to be due to initial solubilisation of only the triglycerides with low melting point, which can be easily removed from the surfaces of the fabrics, whilst a more resistant fat layer consisting of triglycerides with high melting point has probably remained behind on the fabrics and is then harder to eradicate. Furthermore, when the % lard removal data for all the washed fabrics exposed to a low C24E3S surfactant concentration was compared with the results obtained for the washed fabrics with soils only and no surfactant, it was observed that a higher amount of lard was removed when a low concentration of the surfactant was used. This indicates that agitation produced by the propeller combined with surfactant mechanisms such as emulsification and roll-up for removing lard from polyester and cotton fabrics, respectively, are the most effective mechanisms for lard removal. Hence, low surfactant concentration are probably more effective in eliminating solid soils, such as lard, from all the fabrics compared to the high surfactant concentrations (where the additional solubilisation mechanism leaves behind a more detergent-resistant solid film) or agitation on its own when no surfactants is added and so the roll-up and emulsification mechanisms cannot operate. All the results from the wash experiments show that, as expected, there is enhanced fat eradication from the fabrics at a higher wash temperature of 40 ^{o}C than at 20 ^{o}C (table 6.7).

Analysis of the wash water collected from the wash cycle involving soiled fabrics exposed to different wash conditions and application of a high concentration (50 mg/mL) of the C24E3S was undertaken using the laser diffraction particle sizing technique, in order to determine the % volume range of the fat globules which were removed from the fabrics during wash (table 6.8 and appendix figure A3.8).

Table 6.8: showing the soiled fabric conditions from which the wash water was extracted and the diameter range of the fat globules obtained.

Soiled Fabrics denoted by Exposure/dry/wash temperature / ^{o}C	**Particle diameter range of the fat globules / μm**
20 20 20 (%volume)	2-40
30 30 30 (%volume)	1.66 – 39.8

Further analysis of the fat globules using WAXS have shown that the fat globules exist as β' and β polymorphs (figure 6.28). This coincides well with the data collected for the washed soiled fabrics using SAXS which clearly demonstrated the presence of lard in the form of β' and β polymorphs.

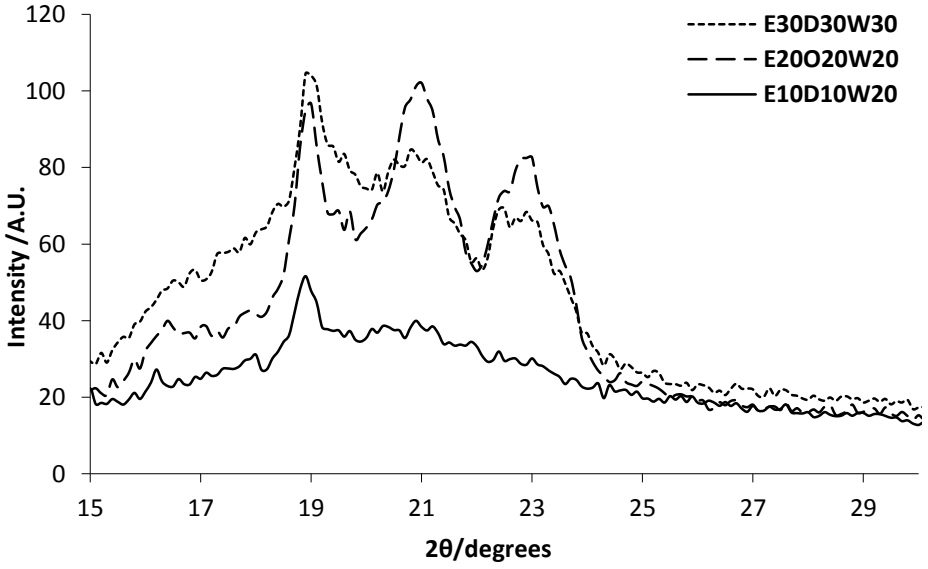

Figure 6.28: WAXS data for the fat globules obtained from the wash water when a high concentration (50 mg/mL) of the C24E3S surfactant was applied.

6.16 Conclusions

Initial investigations carried out using the SAXS technique on lard after melting it at 55 ^{o}C and then supercooling before gradually increasing the temperature have shown the presence of α, β' and β polymorphs with d-spacing values of 49.0 Å, 35.4 Å and 43.4 Å respectively, at the temperatures of -10 ^{o}C, -10 ^{o}C and 20 ^{o}C. As the temperature was raised to 30 ^{o}C, the β' and β polymorphs with lower Gibbs energy than α crystals were detected. Following this, only the most stable β polymorph with higher melting point than the β' polymorph was identified at the temperature of 40 ^{o}C. The transformation from the least stable polymorph to highest stable polymorphic crystal was also confirmed by the change in shape of the lard from globular (α polymorph) to pleated sheet like structure (β'/β polymorphs), with increase in temperature using AFM.

Furthermore, SAXS analysis of the dried detergent solution (ranging between 20 mg/L – 78 mg/L) on unsoiled fabrics revealed a diffraction peak ranging between the d-spacing values of 32.5-34.6 Å. Lard was applied to the fabrics with different concentrations of the detergent solution which were dried overnight at 20 ^{o}C before SAXS analysis was carried out. The results demonstrated presence of the β'_2/β polymorphs on some of the swatches of fabrics, indicated by the d-spacing value between 44.0 Å -44.2 Å. Some of the soiled fabric swatches with detergent and added lard however did not show SAXS evidence of any lard crystals. This could be due to the areas of the fabrics analysed probably composed of a minute amount of lard which when initially coming in contact with the surfactant solution during the drying process has been instantaneously broken down into smaller particles via one or more combination of surfactant mechanisms. The lard structure was also investigated using the WAXS technique, which revealed that the lard at a temperature of 20 ^{o}C can be detected in its stable β' and β polymorphic forms with d-spacing values of 3.8 Å, 4.2 Å and 4.5 Å, respectively. This is because both β' and β crystals have a low Gibbs energy and a higher melting point than 20 ^{o}C. Additionally, WAXS analysis of the different types of fabrics showed overlap between the d-spacing values for the fabrics (table 6.3 and appendix figure A3.1a) and the lard on its own (figure 6.26). In a separate experiment, soiled fabric samples were left at room temperature of 20 $\pm$ 2 ^{o}C for 30 days before WAXS analysis was carried out, which showed scattering peaks with d-spacing values of 3.8 Å and 4.2 Å even in areas of the fabrics where lard was not deposited directly demonstrating the presence of β' polymorphs (table 6.4). This could be due to the initial melting of the lard at 60 ^{o}C allowing the fat

components to liquefy and diffuse across the fibers of the fabrics before crystallising as a result of supercooling to 20 ^{o}C.

The WAXS technique was further used to investigate the structure of the dried out detergent solution. The results showed formation of a broad amorphous peak within the 2θ range of 18 ^{O} to 37^{O}. Following this, a range of detergent concentrations were applied to all of the unsoiled fabrics and then the swatches were left to dry overnight. The WAXS analysis of the fabrics stained with the detergent showed presence of scattering peaks corresponding to d-spacing values around 3.8 Å - 3.9 Å and 4.2 Å – 4.3 Å (appendix figures A3.2a, A3.2c, A3.2e, A3.2g and A3.2i). The peaks identified are probably due to the structure of the fabrics used (table 6.4 and appendix figure A3.1a). In addition, the results obtained for the fabrics containing different concentrations of the detergent solution and lard (appendix figures A3.2b, A3.2d, A3.2f, A3.2h and A3.2j) showed presence of peaks with d-spacing value between 3.8 Å-3.9 Å and 4.1 Å-4.3 Å. However, since there was an overlap between the d-spacing value for the fabrics and the lard, SAXS was used to undertake further investigation on the soiled fabrics, with and without exposure to the detergent solution.

The SAXS analysis of the soiled cotton, polycotton and polyester fabrics showed presence of only the β’ and β polymorphs at the temperatures of -10 ^{o}C, 10 ^{o}C, 20 ^{o}C and 30 ^{o}C after 1 day, 3 days and 5 days of ageing (appendix figures A3.3, A3.4 and A3.5). The SAXS intensities of the soiled fabrics subjected to ageing however was found to vary randomly. This could be due to limitations such as the fabric pieces (1 cm x 1 cm) were cut out from different swatches rather than the same swatch for SAXS analysis on day 1, day 3 and day 5. In a separate experiment, the lard was melted and then applied on cotton, polycotton and polyester fabric swatches before cooling the samples down to 10 ^{o}C. The soiled swatches were then left to age for 1 hour and 4 hours before SAXS analysis was undertaken which in turn revealed that the intensities of the Bragg peaks for β'_1 and β'_2/β polymorphs at 2θ values of 2^{o} and 2.6 ^{o} respectively were almost two/three times higher after 4 hours of ageing compared to just 1 hour for the soiled cotton, polycotton and polyester fabrics (figure 6.26), indicating transformation of amorphous lard into β and β' polymorphs.

Following the ageing experiment, soiled cotton, polycotton, polyester and elastine/cotton fabrics were washed with a high concentration of C24E3S surfactant (50 mg/mL - above the CMC level), a low C24E3S surfactant concentration (0.7 mg/mL – below the CMC) and no surfactant at all. The presence of thermodynamically stable β'_1 and β'_2/β polymorphs were detected on the different types of soiled fabrics after wash with a low and a high level of C24E3S surfactant (appendix figures A3.6 and A3.7), using SAXS. The initial wash experiment

using a high concentration of the C24E3S surfactant was undertaken with just the soiled cotton and polycotton fabrics for comparison. Other types of fabrics i.e. cotton/elastine and polyester were then used alongside cotton and polycotton for the next two set of experiments (involving the application of a low surfactant concentration and no surfactant at all). However, due to limitations such as the use of different fabric swatches for each wash experiments and the SAXS beam was not focused at a fixed area on all the fabric swatches which have resulted in random variation in the SAXS intensities as observed for the low and high surfactant wash experiments. Hence, the intensity data collected for each fabric type could not be compared reliably. The washed soiled fabrics collected after wash without surfactant could not be analysed using SAXS because of the SAXS equipment not working.

Nonetheless, from all the wash experiments (with low and high surfactant and without surfactant) the quantity of lard removed and the fabric types which are most efficient in removing soils with and without the addition of low and high concentrations of C24E3S surfactant solution were determined. For the highest surfactant concentration of 50 mg/mL, it was identified that more lard was removed from the cotton fabric than the polycotton after washing. This was probably due to the attraction between the polar lard components and the hydrophilic cotton fibers, making the low melting point triglycerides available for the aqueous based (polar) detergent solution to eliminate via solubilisation. Additionally, the % of lard removed was found to be lower when a high C24E3S surfactant concentration was used comparing to low concentration or no surfactant added. This is likely to be because of the presence of a more resistant fat layer composed of unsaturated triglycerides with high melting point which is polymerised on to the fabric surfaces and therefore, harder to remove by solubilisation, roll-up, emulsification and agitation. It was also observed that on average more lard was eradicated from both the cotton and polycotton fabrics at a higher wash temperature of 40 ^{o}C than at 20 ^{o}C and 30 ^{o}C. This was predicted as 40 ^{o}C is closer to the melting point of the β polymorph and therefore, it is likely that at this temperature the fats are softer. Thus, the soils are more easily washed away from the fabrics at 40 ^{o}C when in contact with detergent solution and exposed to agitation generated by the tergotometer propellers.

Furthermore, from the results obtained for wash experiments with low concentration of the C24E3S surfactant and no surfactant added, it was identified that the polyester fabric swatches were more effective in removing soil under both conditions compared to the cotton and polycotton fabrics. This could be due to the polyester fabrics being composed of hydrophobic fibers which allow the lard to bind on to the fabric surface and produce thinner

layers spread over more of the fabric and therefore, the fats are more easily removed via agitation and at low surfactant concentration, by the emulsification mechanism. The % of lard removed using the low surfactant concentration was found to be higher compared to the other wash conditions, which indicate that a combination of detergency mechanisms such as emulsification and roll-up combined with agitation may be the most efficient method for eradicating solid soils from fabrics; in contrast, the solubilsation mechanism that can operate at high surfactant concentrations was detrimental to lard removal. Thus, it can be evaluated that agitation generated by the rotation of the propellers has a vital role in increasing the rate of soil removal from the cotton (under high surfactant concentration wash conditions) and the polyester (under low surfactant concentration or no surfactant wash conditions).

The results from the low surfactant and no surfactant wash experiments reflected the findings from high surfactant concentration wash experiments, that most of the soil from the different types of fabrics was eliminated when a high wash temperature of 40 ^{o}C was used compared to 20 ^{o}C and 30 ^{o}C. This is because at 40 ^{o}C more of the most stable and difficult to remove β polymorphs are likely to be softer as this specific wash temperature is close to the melting point of the β crystals. The softer fats are less likely to bind to the fabrics firmly and therefore, are more easily eradicated when exposed to the detergent solution and agitation during the wash experiments.

Additionally, using the laser diffraction particle sizing technique the particle diameter range was determined to be within 1.66 – 40 μm, for the β' and β polymorphic fat globules extracted from the wash water collected for soiled fabrics exposed, dried and washed at temperatures of 20 ^{o}C and 30 ^{o}C while a high concentration (50 mg/mL) of the C24E3S surfactant was applied (table 6.8 and appendix figure A3.8).

6.17 References

1. Bernstein, J. Crystal growth, polymorphism and structure-property relationships in organic crystals. *J. Phys. Appl. Phys.* **26,** B66–B76 (1993).
2. Lutton, E. S. The Polymorphism of Tristearin and Some of its Homologs. *J. Am. Chem. Soc.* **67,** 524–527 (1945).
3. Lutton, E. S. & Jackson, F. L. The Polymorphism of Synthetic and Natural 2-Oleyldipalmitin. *J. Am. Chem. Soc.* **72,** 3254–3257 (1950).
4. Gibon, V., Durant, F. & Deroanne, C. Polymorphism and intersolubility of some palmitic, stearic and oleic triglycerides: PPP, PSP and POP. *J. Am. Oil Chem. Soc.* **63,** 1047–1055 (1986).

5. Bociek, S. M., Ablett, S. & Norton, I. T. A13C-NMR study of the crystal polymorphism and internal mobilities of the triglycerides, tripalmitin and tristearin. *J. Am. Oil Chem. Soc.* **62,** 1261–1266 (1985).
6. Giron, D. Monitoring of Polymorphism – From Detection to Quantification. *Eng. Life Sci.* **3,** 103–112 (2003).
7. Gabbott, P. *Principles and Applications of Thermal Analysis*. (John Wiley & Sons, 2008).
8. Myerson, A. *Handbook of Industrial Crystallization*. (Butterworth-Heinemann, 2002).
9. Bernstein, J. *Polymorphism in Molecular Crystals*. (OUP Oxford, 2007).
10. Brittain, H. G. *Polymorphism in Pharmaceutical Solids, Second Edition*. (CRC Press, 2009).
11. Yu, L., Reutzel-Edens, S. M. & Mitchell, C. A. Crystallization and Polymorphism of Conformationally Flexible Molecules: Problems, Patterns, and Strategies. *Org. Process Res. Dev.* **4,** 396–402 (2000).
12. Lee, A. Y., Erdemir, D. & Myerson, A. S. Crystal polymorphism in chemical process development. *Annu. Rev. Chem. Biomol. Eng.* **2,** 259–280 (2011).
13. Nývlt, J. The Ostwald Rule of Stages. *Cryst. Res. Technol.* **30,** 443–449 (1995).
14. Sato, K. Solidification and phase transformation behaviour of food fats — a review. *Lipid - Fett* **101,** 467–474 (1999).
15. Rosen, J. & Gothard, L. Q. *Encyclopedia of Physical Science*. (Facts On File, Incorporated, 2010).
16. Riegel, E. R. & Kent, J. A. *Riegel's Handbook of Industrial Chemistry*. (Springer Science & Business Media, 2003).
17. Taylor, M. S. Stabilisation of water-in-oil emulsions to improve the emollient properties of lipstick. (University of Birmingham, 2011).
18. Sato, K. & Ueno, S. in *Bailey's Industrial Oil and Fat Products* (ed. Shahidi, F.) (John Wiley & Sons, Inc., 2005).
19. Jacobsberg, B. & Oh Chuan Ho. Studies in palm oil crystallization. *J. Am. Oil Chem. Soc.* **53,** 609–617 (1976).
20. Metin, S. & Hartel, R. W. in *Bailey's Industrial Oil and Fat Products* (ed. Shahidi, F.) (John Wiley & Sons, Inc., 2005).
21. Wang, F.-S. & Lin, C.-W. Contribution of Particle Sizes and Particle Size Distributions in Crystalline Fractionation of Lard. *J. Agric. Food Chem.* **43,** 785–790 (1995).
22. Hoeger, W. & Hoeger, S. *Lifetime Physical Fitness and Wellness: A Personalized Program*. (Cengage Learning, 2014).

23. Himawan, C., Starov, V. M. & Stapley, A. G. F. Thermodynamic and kinetic aspects of fat crystallization. *Adv. Colloid Interface Sci.* **122,** 3–33 (2006).
24. Erickson, D. R. *Edible Fats and Oils Processing: Basic Principles and Modern Practices : World Conference Proceedings*. (The American Oil Chemists Society, 1990).
25. Belitz, H.-D., Grosch, W. & Schieberle, P. *Food Chemistry*. (Springer Science & Business Media, 2009).
26. Florence, A. T., Attwood, D. & Attwood, D. *Physicochemical Principles of Pharmacy*. (Pharmaceutical Press, 2011).
27. Kalnin, D., Lesieur, P., Artzner, F., Keller, G. & Ollivon, M. Systematic investigation of lard polymorphism using combined DSC and time-resolved synchrotron X-ray diffraction. *Eur. J. Lipid Sci. Technol.* **107,** 594–606 (2005).
28. Avramov, I., Rüssel, C. & Avramova, K. Conditions for metastable crystallization from undercooled melts. *J. Non-Cryst. Solids* **337,** 220–225 (2004).
29. MacMillan, S. D. *et al.* In Situ Small Angle X-ray Scattering (SAXS) Studies of Polymorphism with the Associated Crystallization of Cocoa Butter Fat Using Shearing Conditions. *Cryst. Growth Des.* **2,** 221–226 (2002).
30. Moran, D. P. *Fats in Food Products*. (Springer Science & Business Media, 2012).
31. Mazzanti, G., Marangoni, A. G. & Idziak, S. H. J. Modeling of a two-regime crystallization in a multicomponent lipid system under shear flow. *Eur. Phys. J. E Soft Matter* **27,** 135–144 (2008).
32. Mohos, F. *Confectionery and Chocolate Engineering: Principles and Applications*. (John Wiley & Sons, 2010).
33. Ghotra, B. S., Dyal, S. D. & Narine, S. S. Lipid shortenings: a review. *Food Res. Int.* **35,** 1015–1048 (2002).
34. Stuart, B. H. *et al.* Characterization of the triacylglycerol crystal formation in adipose tissue during a vehicle collision. *J. Forensic Sci.* **52,** 938–942 (2007).
35. Garti, N. *Crystallization and Polymorphism of Fats and Fatty Acids*. (Taylor & Francis, 1988).
36. van Mechelen, J. B., Peschar, R. & Schenk, H. Structures of mono-unsaturated triacylglycerols. I. The beta1 polymorph. *Acta Crystallogr. B* **62,** 1121–1130 (2006).
37. Katritzky, A. R. *et al.* Perspective on the Relationship between Melting Points and Chemical Structure. *Cryst. Growth Des.* **1,** 261–265 (2001).
38. Pethrick, R. A. *Polymer Structure Characterization: From Nano to Macro Organization in Small Molecules and Polymers*. (Royal Society of Chemistry, 2013).

39. Hartel, R. W. *Crystallization in Foods*. (Springer, 2001).
40. Meldrum, F. C. & Cölfen, H. Controlling mineral morphologies and structures in biological and synthetic systems. *Chem. Rev.* **108,** 4332–4432 (2008).
41. Groza, J. R. & Shackelford, J. F. *Materials Processing Handbook*. (CRC Press, 2007).
42. De Loos, T. *et al.* in *Fat Crystal Networks* **20044541,** 481–709 (CRC Press, 2004).
43. Dickinson, E. & McClements, D. J. *Advances In Food Colloids*. (Springer Science & Business Media, 1995).
44. Himawan, C., Starov, V. M. & Stapley, A. G. F. Thermodynamic and kinetic aspects of fat crystallization. *Adv. Colloid Interface Sci.* **122,** 3–33 (2006).
45. Cerdeira, M. *et al.* Nucleation behavior of blended high-melting fractions of milk fat as affected by emulsifiers. *Eur. J. Lipid Sci. Technol.* **107,** 877–885 (2005).
46. Oxtoby, D. W. in *Advances in Chemical Physics* (eds. Prigogine, I. & Rice, S. A.) **70,** 263–296 (John Wiley & Sons, Inc., 1988).
47. Lyklema, J. *Fundamentals of Interface and Colloid Science: Soft Colloids*. (Academic Press, 2005).
48. Mitchell, B. S. *An Introduction to Materials Engineering and Science for Chemical and Materials Engineers*. (John Wiley & Sons, 2004).
49. Hilfiker, R. *Polymorphism: In the Pharmaceutical Industry*. (John Wiley & Sons, 2006).
50. Alcock, C. B. *Thermochemical Processes: Principles and Models: Principles and Models*. (Butterworth-Heinemann, 2000).
51. Rao, N. P., Preminger, G. M. & Kavanagh, J. P. *Urinary Tract Stone Disease*. (Springer Science & Business Media, 2011).
52. Fox, P. F. & McSweeney, P. L. H. *Advanced Dairy Chemistry Volume 2: Lipids*. (Springer, 2006).
53. Dhanaraj, G., Byrappa, K., Prasad, V. & Dudley, M. *Springer Handbook of Crystal Growth*. (Springer Science & Business Media, 2010).
54. Marangoni, A. G. & Narine, S. S. *Physical Properties of Lipids*. (CRC Press, 2002).
55. Turnbull, D. & Fisher, J. C. Rate of Nucleation in Condensed Systems. *J. Chem. Phys.* **17,** 71 (1949).
56. Gunstone, F. D., Harwood, J. L. & Dijkstra, A. J. *The Lipid Handbook with CD-ROM, Third Edition*. (CRC Press, 2007).
57. Walstra, P. in *The Colloid Science of Lipids* (eds. Lindman, B. & Ninham, B. W.) **108,** 4–8 (Steinkopff, 1998).
58. Mullin, J. W. *Crystallization*. (Butterworth-Heinemann, 2001).

59. Marangoni, A. & Wright, A. in *Handbook of Functional Lipids* (ed. Akoh, C.) **20053857,** 135–162 (CRC Press, 2005).
60. Texter, J. *Reactions And Synthesis In Surfactant Systems*. (CRC Press, 2001).
61. Maibach, H. I. *Toxicology of Skin*. (CRC Press, 2001).
62. Myers, D. *Surfactant Science and Technology*. (John Wiley & Sons, 2005).
63. Sun, Y.-P. *Supercritical Fluid Technology in Materials Science and Engineering: Syntheses: Properties, and Applications*. (CRC Press, 2002).
64. Gu, T. & Sjöblom, J. Surfactant structure and its relation to the Krafft point, cloud point and micellization: Some empirical relationships. *Colloids Surf.* **64,** 39–46 (1992).
65. Tadros, T. F. *Applied Surfactants: Principles and Applications*. (John Wiley & Sons, 2006).
66. Schramm, L. L. *Surfactants: Fundamentals and Applications in the Petroleum Industry*. (Cambridge University Press, 2000).
67. Silvério, S. C., Rodríguez, O., Teixeira, J. A. & Macedo, E. Gibbs free energy of transfer of a methylene group on {UCON + (sodium or potassium) phosphate salts} aqueous two-phase systems: Hydrophobicity effects. (2010).
68. Armstrong, J. *General, Organic, and Biochemistry: An Applied Approach*. (Cengage Learning, 2014).
69. Choudhury, A. K. R. *Textile Preparation and Dyeing*. (Science Publishers, 2006).
70. Akyüz, M. Ion-pair extraction and GC–MS determination of linear alkylbenzene sulphonates in aqueous environmental samples. *Talanta* **71,** 471–478 (2007).
71. Oude, N. T. de. *Detergents*. (Springer, 2013).
72. McAvoy, D. C. *et al.* Removal of alcohol ethoxylates, alkyl ethoxylate sulfates, and linear alkylbenzene sulfonates in wastewater treatment. *Environ. Toxicol. Chem.* **17,** 1705–1711 (1998).
73. Zoller, U. *Handbook of Detergents, Part E: Applications*. (CRC Press, 2008).
74. Gallup, D. L., Curiale, J. A. & Smith, P. C. Characterization of Sodium Emulsion Soaps Formed from Production Fluids of Kutei Basin, Indonesia. *Energy Fuels* **21,** 1741–1759 (2007).
75. Zoller, U. *Handbook of Detergents: Applications*. (CRC Press, 2008).
76. Miller, C. A. & Raney, K. H. Solubilization—emulsification mechanisms of detergency. *Colloids Surf. Physicochem. Eng. Asp.* **74,** 169–215 (1993).
77. Dillan, K. W., Goddard, E. D. & Mckenzie, D. A. Examination of the parameters governing oily soil removal from synthetic substrates. *J. Am. Oil Chem. Soc.* **57,** 230–237 (1980).
78. Aehle, W. *Enzymes in Industry*. (John Wiley & Sons, 2008).

79. Sonesson, A. W., Callisen, T. H., Elofsson, U. M. & Brismar, H. Imaging the Detergency of Single Cotton Fibers with Confocal Microscopy: the Effect of Surfactants and Lipases. *J. Surfactants Deterg.* **10,** 211–218 (2007).
80. Dillan, K. W. Factors affecting oil/water interfacial tension in detergent systems: Nonionic surfactants and nonpolar oils. *J. Am. Oil Chem. Soc.* **61,** 1278–1284 (1984).
81. Obendorf, S. K. & Borsa, J. Lipid soil removal from cotton fabric after mercerization and carboxymethylation finishing. *J. Surfactants Deterg.* **4,** 247–256 (2001).
82. Dillan, K. W., Goddard, E. D. & McKenzie, D. A. Oily soil removal from a polyester substrate by aqueous nonionic surfactant systems. *J. Am. Oil Chem. Soc.* **56,** 59–70 (1979).
83. Rosen, M. J. & Kunjappu, J. T. *Surfactants and Interfacial Phenomena*. (John Wiley & Sons, 2012).
84. Adanur, S. *Wellington Sears Handbook of Industrial Textiles*. (CRC Press, 1995).
85. Goswami, B. C., Anandjiwala, R. D. & Hall, D. *Textile Sizing*. (CRC Press, 2004).
86. Broze, G. *Handbook of Detergents: Properties*. (CRC Press, 1999).

CHAPTER 7

Conclusions & Further work

7.1 Conclusions

The main conclusion which can be derived from the systematic studies of emulsification at an ITIES is that it can give realistic insights into a wide range of applications for surfactant adsorption and emulsification. For the SDBS/water – 1,2-DCE/GTO systems, use of electrochemical techniques and optical microscopy has demonstrated occurrence of a concentration, time and potential dependent surfactant adsorption and emulsification instability at the interfaces. It was observed that there was an increase in current without any irregular oscillations as the SDBS surfactant concentration was gradually increased in the aqueous phase of the water (with LiCl) – 1,2-DCE (with TBATPB) system, below the CMC point of 1.5 mM. On the other hand, the electrochemical studies on SDBS concentrations of 1.5 mM (CMC point), 8 mM and 13.4 mM added to the aqueous phase of the water-1,2-DCE system with electrolytes have shown presence of reproducible interfacial instability within a limited potential region around the standard ion transfer potential of the surface active ions. The chaotic fluctuations however were negated when increasing concentrations of triton-x-114 were added to the aqueous phase consisting of 13.4 mM of the SDBS surfactant. Similar irregular oscillations to those observed for SDBS were also identified with P&G's Y (anionic) surfactant which again disappeared when P&G's N (non-ionic) surfactant was added to the aqueous phase composed of P&G's Y (anionic) surfactant. Furthermore, conductivity and electrocapillary measurements of the aqueous (with LiCl) – 1,2-DCE (with TBATPB)/GTO systems, have shown that above 8 mM of SDBS the instability became independent of the SDBS concentration due to presence of increased number of micelles and enhanced rate of micellar emulsification at the non-polarised interfaces. By further investigating the aqueous-1,2-DCE/oil systems, with and without electrolytes, using an optical microscope has revealed an increase in the interfacial instability and presence of emulsion droplets due to micellar emulsification at SDBS concentrations of 1.5 mM, 8 mM and 13.4 mM. The findings were confirmed using CV, conductivity and electrocapillary methods. The interfacial instability was also found to be more prominent in the presence of electrolytes, which suggests that the electrolytes promote a faster rate of surfactant adsorption and emulsification at the aqueous (with LiCl)-1,2-DCE (with TBATPB)/GTO interfaces compared to the aqueous-1,2-DCE/GTO

systems without salts. By further exploring the transfer and adsorption behaviour of the anionic surface active ions electrochemically and optically, a deeper understanding of the ubiquitous phenomena associated with the unstable interfaces, such as the occurrence of spontaneous emulsification with the change in phase boundary potential at the oil-water interface will emerge [1].

Further analysis of the aqueous (with 10 mM LiCl) -1,2-DCE (with 20 mM TBATPB) interface using optical microscopy, DSC, MS, FTIR and WAXS techniques has demonstrated the presence of crystals at the phase boundary, which are mainly composed of electrolyte ions mixed with anionic/non-ionic surfactant (in the presence of surfactant in the system). Analysis of the aqueous (with/without LiCl) -1,2-DCE (with/without TBATPB)/oil phase boundaries using an optical microscope has revealed an increase in the interfacial instability with an increase in concentration of the SDBS/P&G's Y surfactants, although no crystals were detected. Contrary to this, for the aqueous/LiCl -1,2-DCE/TBATPB system with triton-x-114 and P&G's N surfactant with and without the addition of SDBS/P&G's Y surfactants has shown formation of crystals at the interfaces. This is probably due to competition for water between the salt ions and the dehydrated poly(oxyethylene) chains of the non-ionic surfactants, as the electrolytes cause a decrease in the solubility and cloud point of the surfactants[2]. The findings as obtained using an optical microscope were confirmed using DSC, MS and FTIR methods. WAXS on the other hand, has shown that the crystals are probably composed of a mixture of electrolyte ions and both anionic and non-ionic surfactants, indicated by the presence of new peaks at 2θ values of 46.5^{o} and 51.3^{o} for the aqueous/LiCl/SDBS/triton-x-114 and 1,2-DCE/TBATPB system and at 37^{o} and 45.3^{o} for the aqueous/LiCl/P&G's Y/N surfactants and 1,2-DCE/TBATPB system. This crystallisation study gives an insight into how non-ionic/a mixture of anionic and non-ionic surfactants behaves in different organic phases, in the presence of salts. The crucial findings on the mode of interaction between the surfactants and the electrolytes can be advantageous for improving various industrial processes such as crude oil recovery[3] and for retrieval of surfactants from surfactant based separation reactions[4].

Following the characterisation of different types of anionic and non-ionic surfactants at the oil/1,2-DCE-aqueous interfaces, initial investigations were undertaken on lard using the SAXS technique, which showed that after melting the lard at a temperature of 55 ^{o}C, followed by supercooling and then steadily increasing the temperature again, led to formation of α, β' and β polymorphs with d-spacing values of 49.0 Å, 35.4 Å and 43.4 Å, respectively, at the temperatures of -10 ^{o}C, -20 ^{o}C and 10 ^{o}C. On a further increase in temperature to 30 ^{o}C, lard

exhibited the presence of both β' and β polymorphs, however, as the temperature was continually raised to 40 °C, only the most stable β polymorph with higher melting point than the β' polymorphs was identified. The transformation from the least stable polymorph (α polymorph) to highest stable polymorphic crystals (β'/β polymorphs) was confirmed using AFM.

SAXS analysis of the lard applied on fabrics with different concentrations of the detergent solution and then left to dry overnight at 20 °C has shown the presence of β'_2/β polymorphs with d-spacing values between 44.0 Å -44.2 Å on some of the swatches of fabrics. However, the rest of the soiled fabric swatches with detergent investigated did not show any discernible polymorphic crystals. This could be because the areas of the soiled fabrics analysed probably consisted of small amount of lard which when coming in contact with the detergent solution probably has broken down to form smaller particles via surfactant adsorption and emulsification processes, in the presence of excess surfactant and micelles during the drying process. Lard on its own was also analysed using WAXS which showed that at a temperature of 20 °C, it exists in β' and β polymorphic forms (with high melting points) which was indicated by the presence of WAXS peaks with d-spacing values of 3.8 Å, 4.2 Å and 4.5 Å, respectively. WAXS analysis of the different types of fabrics on the other hand has revealed an overlap between the d-spacing values for the fabrics and the lard. In a separate experiment, by exposing partly soiled fabric samples on which melted lard has been applied, at a room temperature of 20 $\pm$ 2 °C for 30 days, the presence of β' polymorphs was evident by the high intensity WAXS peaks with d-spacing values of 3.8 Å and 4.2 Å, in areas of the fabrics where lard was not deposited directly. This was probably due to melting of the lard at 60 °C causing the fat components with low melting point to liquefy and diffuse across the fibers of the fabrics before crystallising at the temperature of 20 °C. WAXS analysis of soiled fabric swatches exposed to 20 °C for a period of 30 days also demonstrated presence of β' crystals indicating this is indeed the most stable polymorph at this temperature.

The WAXS technique was further used to investigate the structure of the partly dried detergent which showed formation of a broad amorphous peak within the 2θ range of 18° to 37°. Following this, analysis of the fabrics stained with the detergent solution showed presence of scattering peaks corresponding to d-spacing values of 3.8 Å - 3.9 Å and 4.2 Å – 4.3 Å, which are likely to be due to the structures of the fabrics. In addition, the results obtained for the fabrics containing different concentrations of the detergent solution and lard showed an overlap between the d-spacing values for the fabrics and the lard. SAXS was therefore used to undertake further investigation on the soiled fabrics, with and without the addition of

the detergent solution as it did not exhibit any overlap between the peaks for the fabrics and the lard. SAXS analysis of soiled fabric samples after 1 day, 3 days and 5 days of ageing at the temperatures of -10 ^{o}C, 10 ^{o}C, 20 ^{o}C and 30 ^{o}C showed presence of β' and β polymorphs however the SAXS intensities were found to fluctuate as a result of limitations such as the fabric pieces (1 cm x 1 cm) were cut out from different swatches of fabrics for the SAXS study.

Additionally, the lard was melted and then applied to cotton, polycotton and polyester fabric swatches before exposing the samples to a temperature of 10 ^{o}C and leaving them to age for 1 hour and 4 hours. The SAXS intensities of the Bragg peaks for β'_1 and β'_2/β polymorphs at 2θ values of 2^{o} and 2.6^{o} respectively were found to be almost two/three times higher after 4 hours of ageing than just 1 hour, which signified the occurrence of polymorphic transitions into most stable forms over time. Following this, soiled cotton, polycotton, polyester and elastine/cotton fabrics were washed with 50 mg/mL (above the CMC level) of C24E3S, 0.7 mg/mL (below the CMC) of C24E3S and no surfactant at all. The wash experiment with 50 mg/mL of C24E3S surfactant was undertaken with just the soiled cotton and polycotton fabrics whereas other types of fabrics i.e. cotton/elastine and polyester were used alongside cotton and polycotton for the wash experiments involving application of 0.7 mg/mL of C24E3S and no surfactant at all. The SAXS results for all the wash experiments showed the presence of β'_1 and β'_2/β polymorphs on all the different types of washed soiled fabrics. However, inconsistency in the SAXS intensities was also observed for all the washed soiled fabrics due to limitations such as use of different fabric swatches for each wash experiment. The washed soiled fabrics from the wash experiment without the addition of surfactant could not be analysed using SAXS because the equipment was not working at that time and needed to be repaired.

Furthermore, from the quantity of lard removed under all wash conditions, it can be deduced that the application of 0.7 mg/mL of C24E3S was most effective in removing soils as a result of a mixture of detergency mechanisms such as emulsification and roll-up combined with agitation. At a higher surfactant concentration of 50 mg/mL, it is likely that the triglycerides with low melting points were removed by solubilisation, leaving behind a resistant fat layer on the fabric surface which was then only partially removed over time via emulsification process, roll-up mechanism and agitation as evidenced by the low % of lard removal. It was also identified that more lard was removed from the cotton fabric swatches than the polycotton when 50 mg/mL of C24E3S was applied. This was probably due to the attachment of more polar lard components to the hydrophilic cotton fibers, allowing easy access of the aqueous based (polar) surfactant solution to the soils which were then removed

via solubilisation and roll-up mechanisms along with agitation. Furthermore, from the wash experiments for low concentration of the C24E3S surfactant, and no surfactant at all, it was established that the polyester fabric swatches were more effective in removing soil compared to the other types of fabrics. This was because polyester fabrics consist of hydrophobic fibers to which the hydrophobic lard can bind onto and form a thin fat layer on the fabric surface. Thus, when the soiled polyester fabrics came in contact with the surfactant solution, the lard was easily accessed and eliminated via micellar emulsification and roll-up processes in combination with agitation.

For all the wash experiments, it was also observed that, on average more lard was removed from all the soiled fabrics at a higher wash temperature of 40 ^{o}C than at 20 ^{o}C and 30 ^{o}C. This was expected as 40 ^{o}C is closer to the melting point of the β polymorph and therefore, the fats are likely to be softer at this temperature. Consequently, the soils were more easily washed away from the fabrics in the presence of the surfactant solution and also, due to agitation generated by the tergotometer propellers. By using laser diffraction particle sizing technique, analysis of the β' and β polymorphic fat globules collected from the wash water samples for soiled fabrics exposed, dried and washed at temperatures of 20 ^{o}C and 30 ^{o}C while a high concentration (50 mg/mL) of the C24E3S surfactant was applied, have shown that the diameter range for the fat droplets varied between 1.66 – 40 μm.

The activity of enzymes such as GDH and lipase, which is another component of the detergent, was investigated using enzymatic biosensors and electrochemical methods in order to determine the quantity of glycerol produced. The immobilised sol-gel/FcAuNP/enzymatic-biosensors constructed have shown enhanced sensitivity and selectivity as well as a fast time response compared to other feasible enzymatic biosensors available to date. Both, the GOx and GDH enzymes when immobilised with sol-gel and FcAuNPs on the surfaces of the carbon electrodes have exhibited K_m values of 1.5 $\pm$ 0.01 mM (for the immobilised sol-gel/ FcAuNP/GOx enzymatic- carbon macroelectrode), 4.9 $\pm$ 0.01 mM (for the immobilised sol-gel/ FcAuNP/ /NAD^+ - dependent DP and GDH enzymatic - carbon macroelectrode) and 5.4 $\pm$ 0.01 mM (for the immobilised sol-gel/ FcAuNP/ /NAD^+ - dependent DP and GDH enzymatic - SPE) compared to the literature values of 7.4 mM (for an immobilised AuNP/GOx enzymatic-biosensor)[5] and 9.9 mM (for an immobilised GDH enzymatic biosensor)[6], respectively. The sol-gel/ FcAuNP/ NAD^+ - dependent DP and GDH based enzymatic- SPE also demonstrated a wide glycerol concentration detection limit, ranging between 0.2 mM to 24.8 mM; with a fast response time of 11.4 seconds and a high correlation coefficient of 0.9903 was also achieved.

It was observed that in the presence of lipase and GTO in solution, the sol-gel/ FcAuNP/NAD^+ - dependent DP and GDH based enzymatic- SPEs displayed an increase in current with an increase in the GTO concentration up to 1.5 mM. Beyond this point, the current rapidly decreased with increase in GTO concentration as a result of competitive inhibition caused by the presence of lipolytic products in the buffer solution[7]. The lipase enzyme inhibition can be minimised for example, by immobilising the enzyme onto the surface of the carbon electrode and therefore, enhancing its stability against chemical deactivation. Overall, the immobilised sol-gel/ FcAuNP/NAD^+ dependent DP and GDH enzymatic – SPEs have displayed many desirable characteristics which include higher sensitivity and selectivity. The modified biosensors are inexpensive and simple to use which makes these biosensors ideal for glycerol quantification in industries such as the medical[8], food [9] and biofuel[10] sectors.

7.2 Further work

The liquid-liquid interface combined with electrochemical methods can be used to extend the investigation of the effect of other types of surfactants which make up the detergent solution; these methods can be also applied to explore in depth the possible mechanisms that might occur at the water-organic interface in the presence of all the surfactants that constitute the detergent solution. The impedance technique can be employed to establish the thickness of the monolayer formed in the presence of non-ionic surfactant at the liquid-liquid phase boundary.

Furthermore, the enzymatic biosensor study can be repeated by immobilising the lipase enzyme on to the surface of the working electrode using sol-gel/FcAuNP matrix along with the NAD^+ - dependent DP and GDH enzymes. The results can be then compared with the CVs and CAs obtained for the lipase enzyme in solution and the findings can used to determine how effectively the immobilised lipase enzyme works in the presence of triglycerides. By calculating the Km value for the immobilised sol-gel/FcAuNP/ NAD^+ - dependent DP and GDH/lipase enzymatic biosensor and comparing it to the literature, it can be also evaluated whether the immobilised lipase enzyme has a lower or higher affinity for the triglyceride substrate.

The wash experiments undertaken using C24E3S surfactant needs to be repeated and the SAXS intensities of the fabric swatches after wash can be then measured and compared by focusing the beam spot on the same area of the all the swatches. The priority for further work on the wash study would be to repeat the wash experiments using other surfactant components of P&G's Jupiler detergent solution and compare the results with the data

obtained for the C24E3S surfactant in order to determine which of the surfactants is most effective for removing soils from the soiled fabrics under different wash conditions. The effect of all the surfactants combined together, with and without the addition of lipase enzyme, can be also investigated using the SAXS and WAXS techniques to evaluate whether the surfactants, the lipase enzyme or/and agitation is most efficient for removing soils from the different types of fabrics. However, determining the most effective method for removing the resistant fat layer composed of triglycerides with high melting point, from the fabrics would be the most important but challenging aspect of this work.

7.3 References

1. Kitazumi, Y. & Kakiuchi, T. Electrochemical Instability in Liquid–Liquid Two-Phase Systems. *Bull. Chem. Soc. Jpn.* **84,** 1312–1320 (2011).
2. Komaromy-Hiller, G., Calkins, N. & von Wandruszka, R. Changes in Polarity and Aggregation Number upon Clouding of a Nonionic Detergent: Effect of Ionic Surfactants and Sodium Chloride. *Langmuir* **12,** 916–920 (1996).
3. Okandan, E. *Heavy Crude Oil Recovery*. (Springer Science & Business Media, 2012).
4. Scamehorn. *Surfactant - Based Separation Processes*. (CRC Press, 1989).
5. Tang, W., Li, L., Wu, L., Gong, J. & Zeng, X. Glucose Biosensor Based on a Glassy Carbon Electrode Modified with Polythionine and Multiwalled Carbon Nanotubes. *PLoS ONE* **9,** (2014).
6. Joshi, R. *Biosensors*. (Gyan Publishing House, 2006).
7. Kosugi, Y. & Suzuki, H. Functional immobilization of lipase eliminating lipolysis product inhibition. *Biotechnol. Bioeng.* **40,** 369–374 (1992).
8. Castillo, J. *et al.* Biosensors for life quality: Design, development and applications. *Sens. Actuators B Chem.* **102,** 179–194 (2004).
9. Eftekhari, A. Glycerol biosensor based on glycerol dehydrogenase incorporated into polyaniline modified aluminum electrode using hexacyanoferrate as mediator. *Sens. Actuators B Chem.* **80,** 283–289 (2001).
10. Hájek, M., Skopal, F. & Machek, J. Determination of free glycerol in biodiesel. *Eur. J. Lipid Sci. Technol.* **108,** 666–669 (2006).

Appendix

A1 - Surfactant characterisation at the liquid-liquid interface

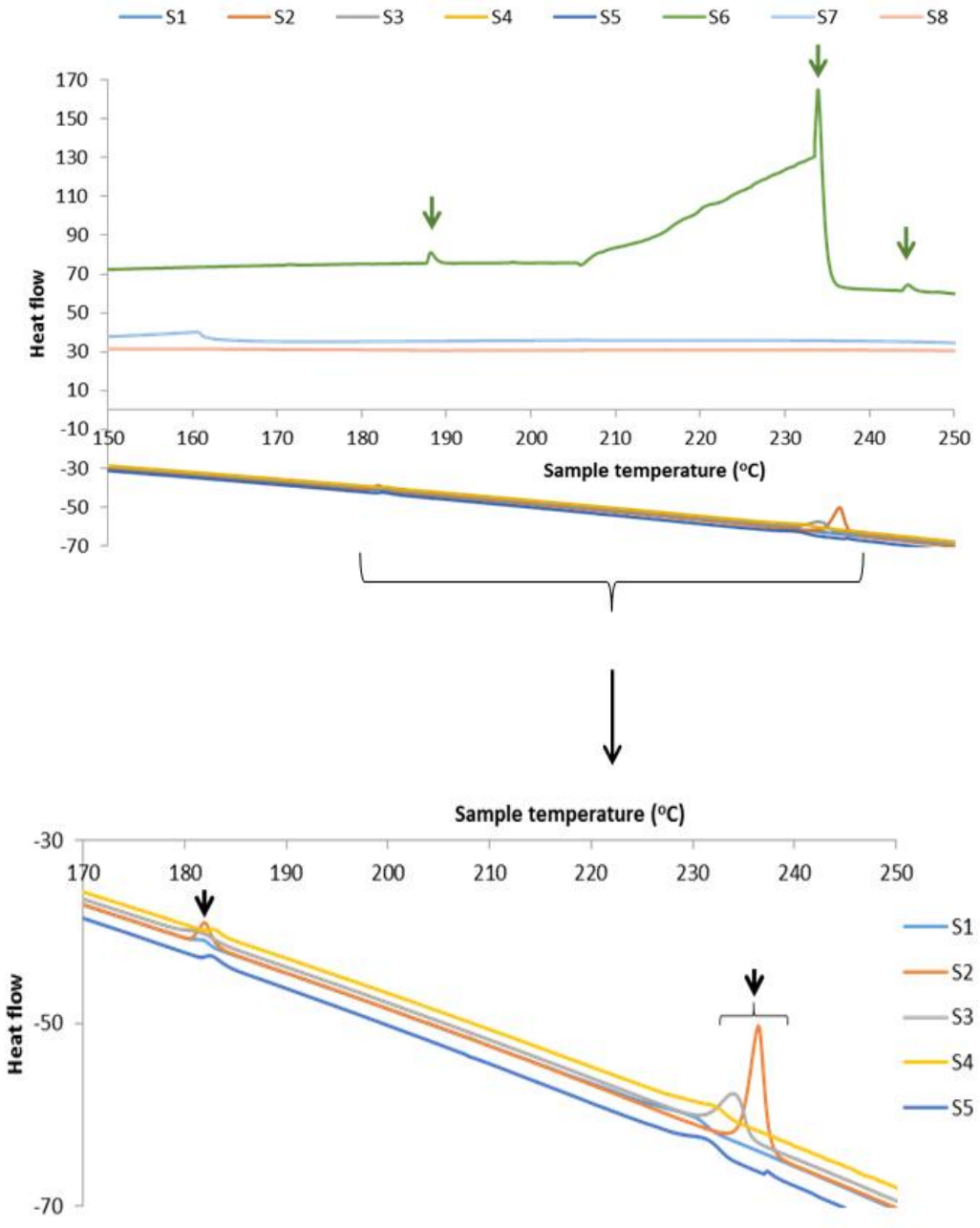

Figure A1.1: DSC data for all the crystal samples S1-S8. Where, sample S1 is the aqueous/LiCl/Triton-x-114 and 1,2-DCE/TBATPB system, sample S2 is the aqueous/LiCl/SDBS/ Triton-X-114 and 1,2-DCE/TBATPB system, sample S3 is the aqueous/LiCl/P&G's N surfactant and 1,2-DCE/TBATPB system, sample S4 is the aqueous LiCl/P&G's Y/ P&G's N surfactants and

1,2-DCE/TBATPB system, sample S5 is the aqueous/LiCl-1,2-DCE/TBATPB mixture and sample S6 is the SDBS . The green arrows show the melting points for sample S6 and the black arrows displays the melting points for samples S1-S5.

A2 - Sol-gel/ferrocenated gold nanoparticle based enzymatic biosensor for glycerol detection

Table A2.1: shows the calculations for the K_m value of the immobilised sol-gel/ FcAuNP/ GOx enzymatic carbon macroelectrode.

Parameters	Calculation	Values
intercept	-	2
imax = 1/intercept	1/2.00	0.5 µAmps
Slope = gradient of the graph	-	3
Km = imax *slope	0.5 * 3	**1.5 mM**

Table A2.2: shows the calculations for the K_m values of the immobilised sol-gel/ FcAuNP/DP and GDH enzymatic-carbon macroelectrode and -SPE.

	Calculation	
Parameters	**Immobilised sol-gel/ FcAuNP/DP and GDH enzymatic-carbon macroelectrode**	**Immobilised sol-gel/ FcAuNP/DP and GDH enzymatic-SPE**
intercept	2	0.0125
imax = 1/intercept	0.5	80
Slope = gradient of the graph	7. 96	0.0683
Km = imax *slope	**3.9 (mM)**	**5.5 (mM)**

A3 - Soiled fabrics washed using C24E3S surfactant

Table A3.1: showing d-spacing values for α, β' and β polymorphs after melting the lard at 55 ^{o}C, super-cooling it – 20 ^{o}C and re-heating it up to 40 ^{o}C.

2theta/deg	2theta/rad	sin(theta)	Q/Angstrom^-1		d/nm	d/ Angstrom	Polymorphs	Temperature/ ^{o}C
2.03	0.03543	0.017714	1.445473	14.45473	4.346804	43.46804	β'2/β	-10, -20, 10, 20, 30 and 40
1.8	0.031416	0.015707	1.281714	12.81714	4.902174	49.02174	α	-10, -20 and 10
2.49	0.043459	0.021728	1.772971	17.72971	3.543873	35.43873	β'1	- 10 and - 20
2.54	0.044331	0.022164	1.808567	18.08567	3.474123	34.74123	β'1	10
2.58	0.045029	0.022513	1.837044	18.37044	3.42027	34.2027	β'1	20 and 30

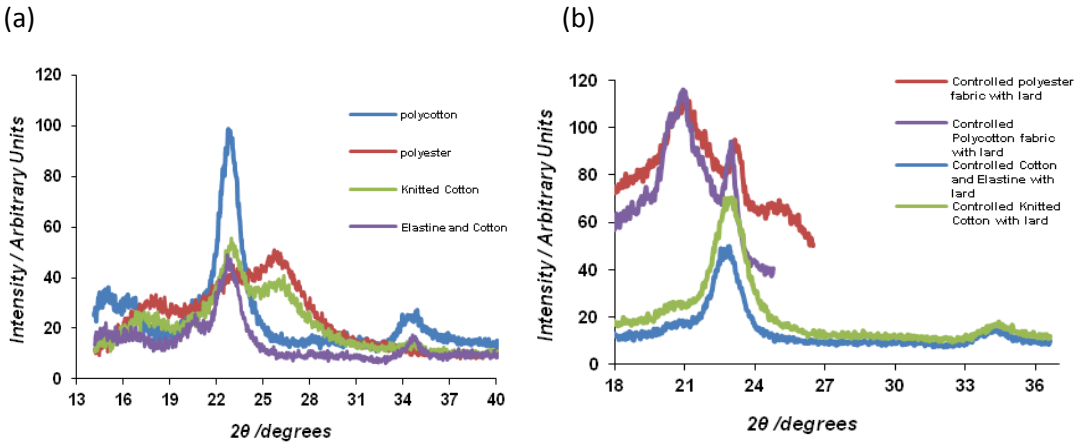

Figure A3.1: WAXS data for (a) different types of fabrics and (b) fabrics with lard.

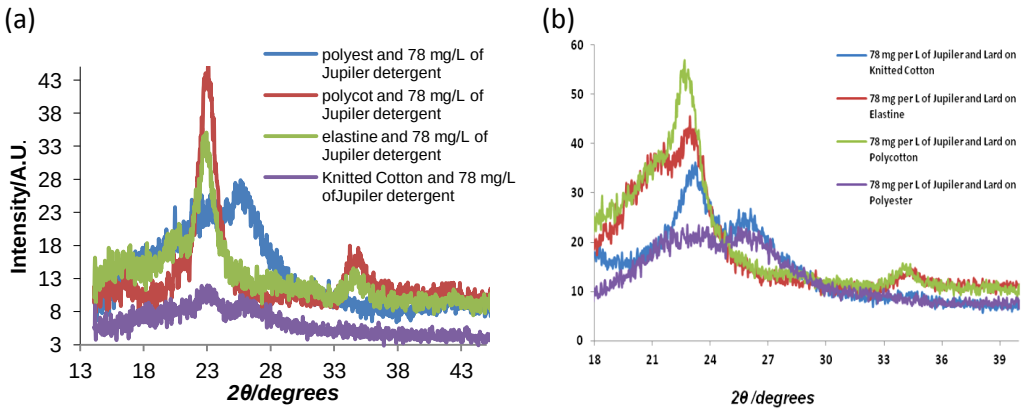

(c)

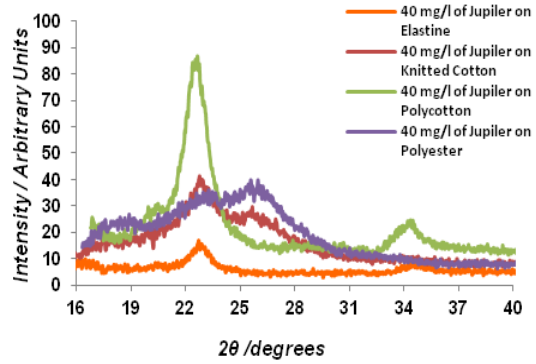
Intensity / Arbitrary Units
2θ /degrees
40 mg/l of Jupiler on Elastine
40 mg/l of Jupiler on Knitted Cotton
40 mg/l of Jupiler on Polycotton
40 mg/l of Jupiler on Polyester

(d)

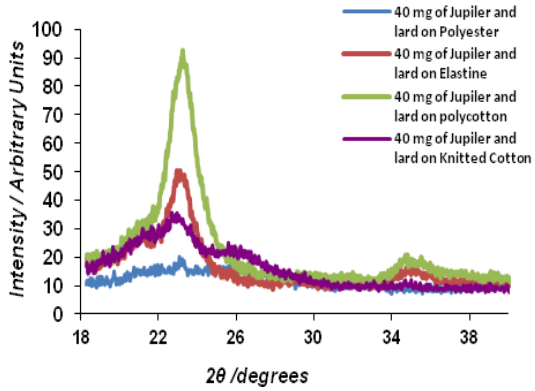
Intensity / Arbitrary Units
2θ /degrees
40 mg of Jupiler and lard on Polyester
40 mg of Jupiler and lard on Elastine
40 mg of Jupiler and lard on polycotton
40 mg of Jupiler and lard on Knitted Cotton

(e)

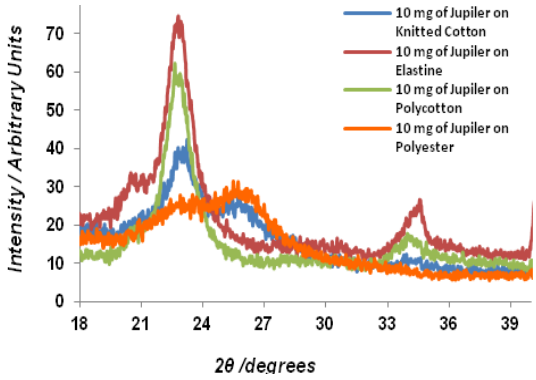
Intensity / Arbitrary Units
2θ /degrees
10 mg of Jupiler on Knitted Cotton
10 mg of Jupiler on Elastine
10 mg of Jupiler on Polycotton
10 mg of Jupiler on Polyester

(f)

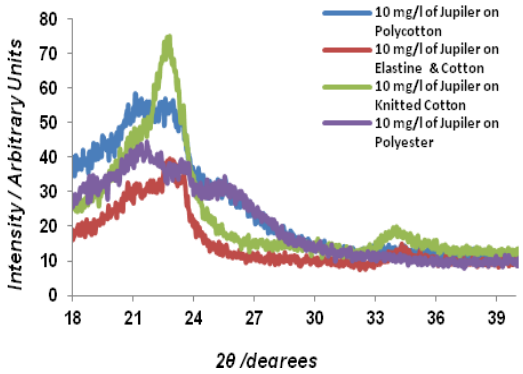
Intensity / Arbitrary Units
2θ /degrees
10 mg/l of Jupiler on Polycotton
10 mg/l of Jupiler on Elastine & Cotton
10 mg/l of Jupiler on Knitted Cotton
10 mg/l of Jupiler on Polyester

(g)

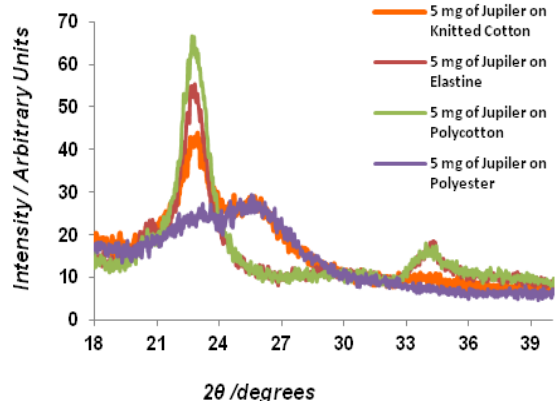
Intensity / Arbitrary Units
2θ /degrees
5 mg of Jupiler on Knitted Cotton
5 mg of Jupiler on Elastine
5 mg of Jupiler on Polycotton
5 mg of Jupiler on Polyester

(h)

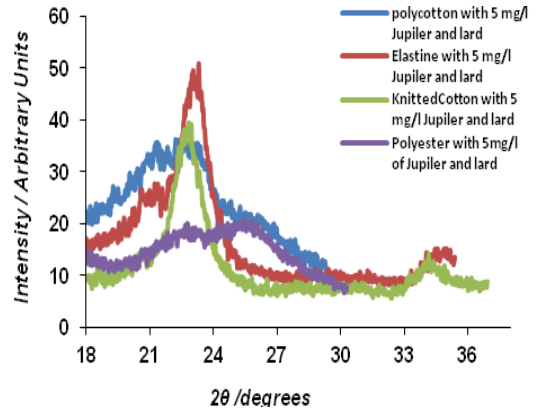
Intensity / Arbitrary Units
2θ /degrees
polycotton with 5 mg/l Jupiler and lard
Elastine with 5 mg/l Jupiler and lard
KnittedCotton with 5 mg/l Jupiler and lard
Polyester with 5mg/l of Jupiler and lard

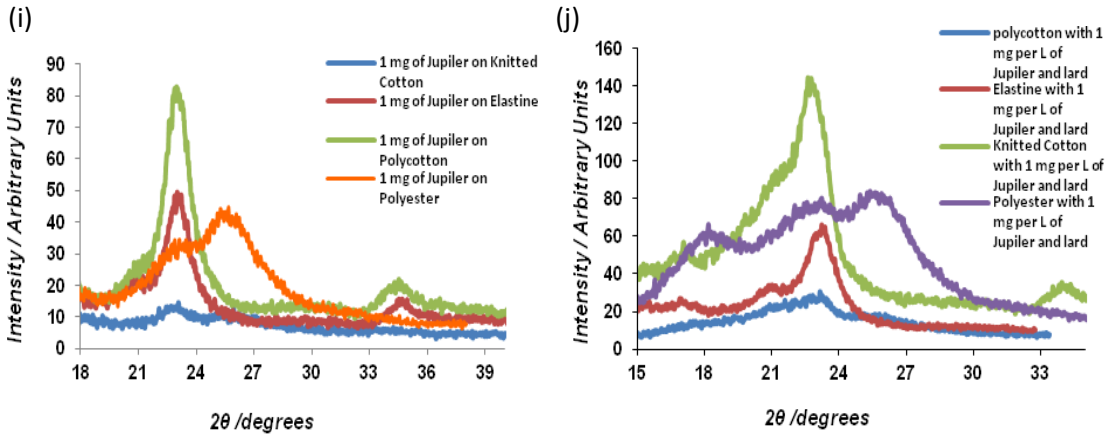

Figure A3.2: WAXS analysis of fabrics with (a) 78 mg/L detergent, (b) 78 mg/L detergent and lard, (c) 40 mg/L detergent, (d) 40 mg/L detergent and lard, (e) 10 mg/L detergent, (f) 10 mg/L detergent and lard (g) 5 mg/L detergent (h) 5 mg/L detergent and lard, (i) 1 mg/L of detergent and (j) 1 mg/L of detergent and lard.

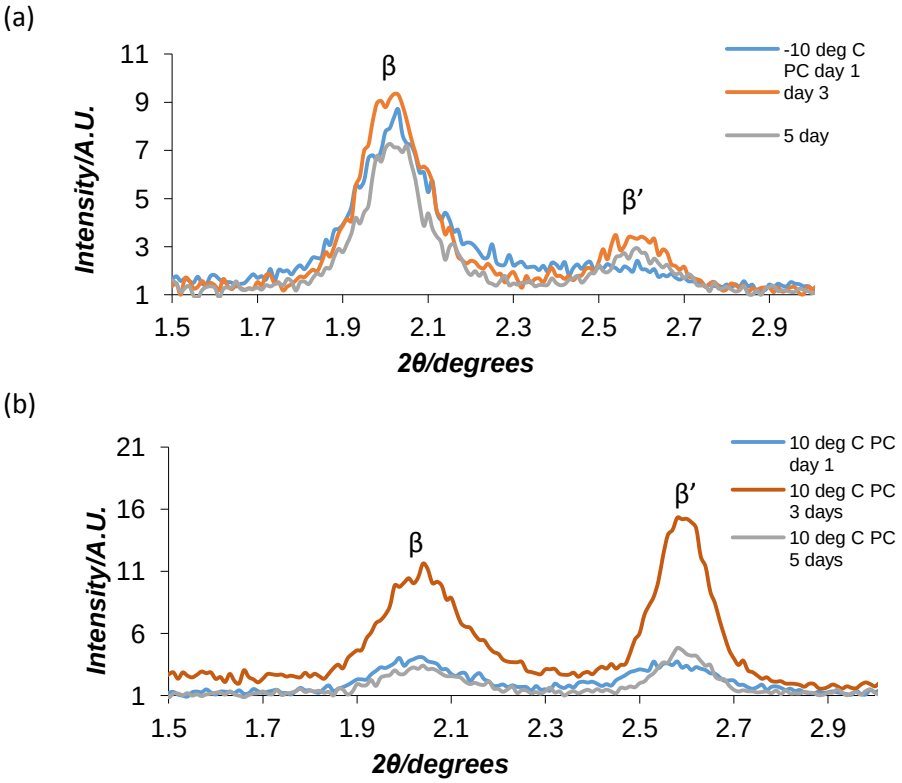

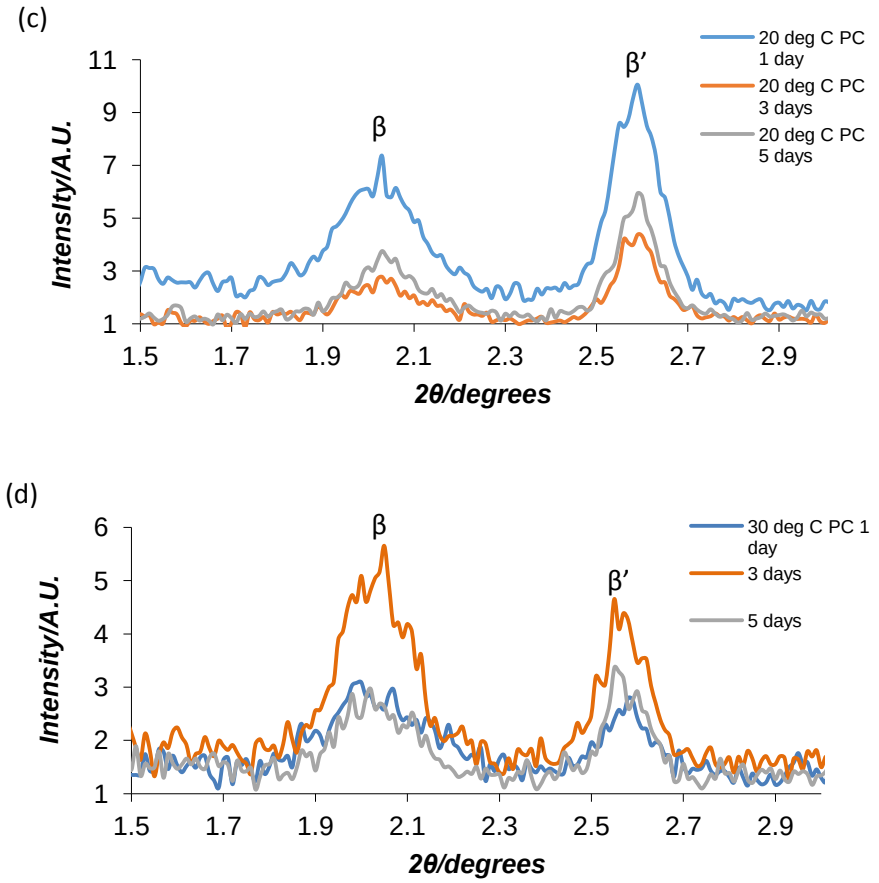

Figure A3.3: SAXS data for soiled polycotton (PC) fabrics obtained at temperatures of (a) -10 °C (b) 10 °C (c) 20 °C and (d) 30 °C over a period of 5 days.

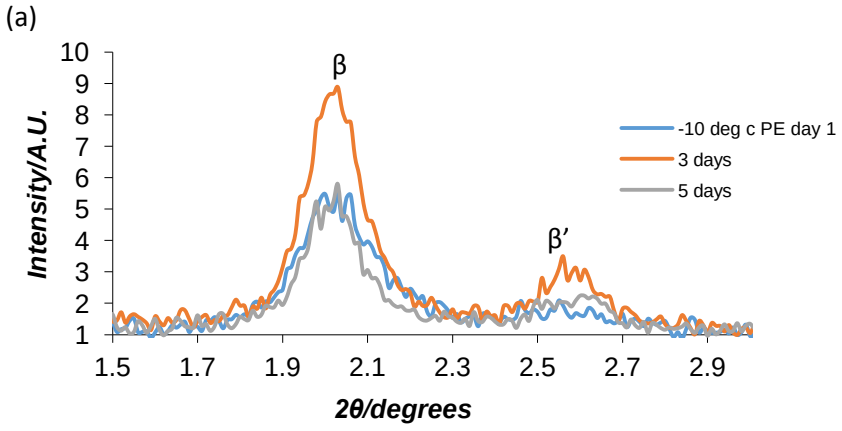

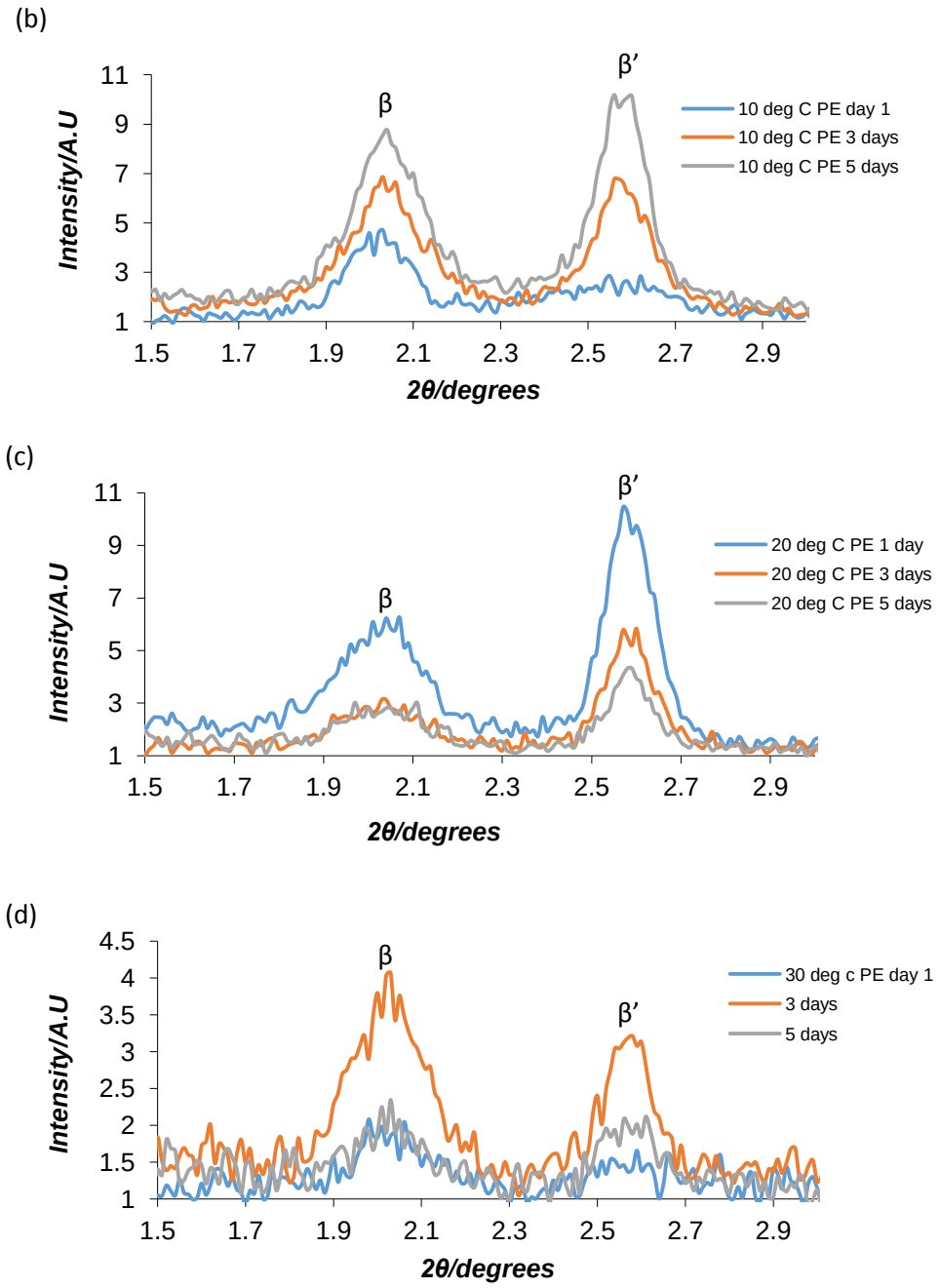

Figure A3.4: SAXS data for soiled polyester (PE) fabrics obtained at temperatures of (a) -10 °C (b) 10 °C (c) 20 °C and (d) 30 °C over a period of 5 days.

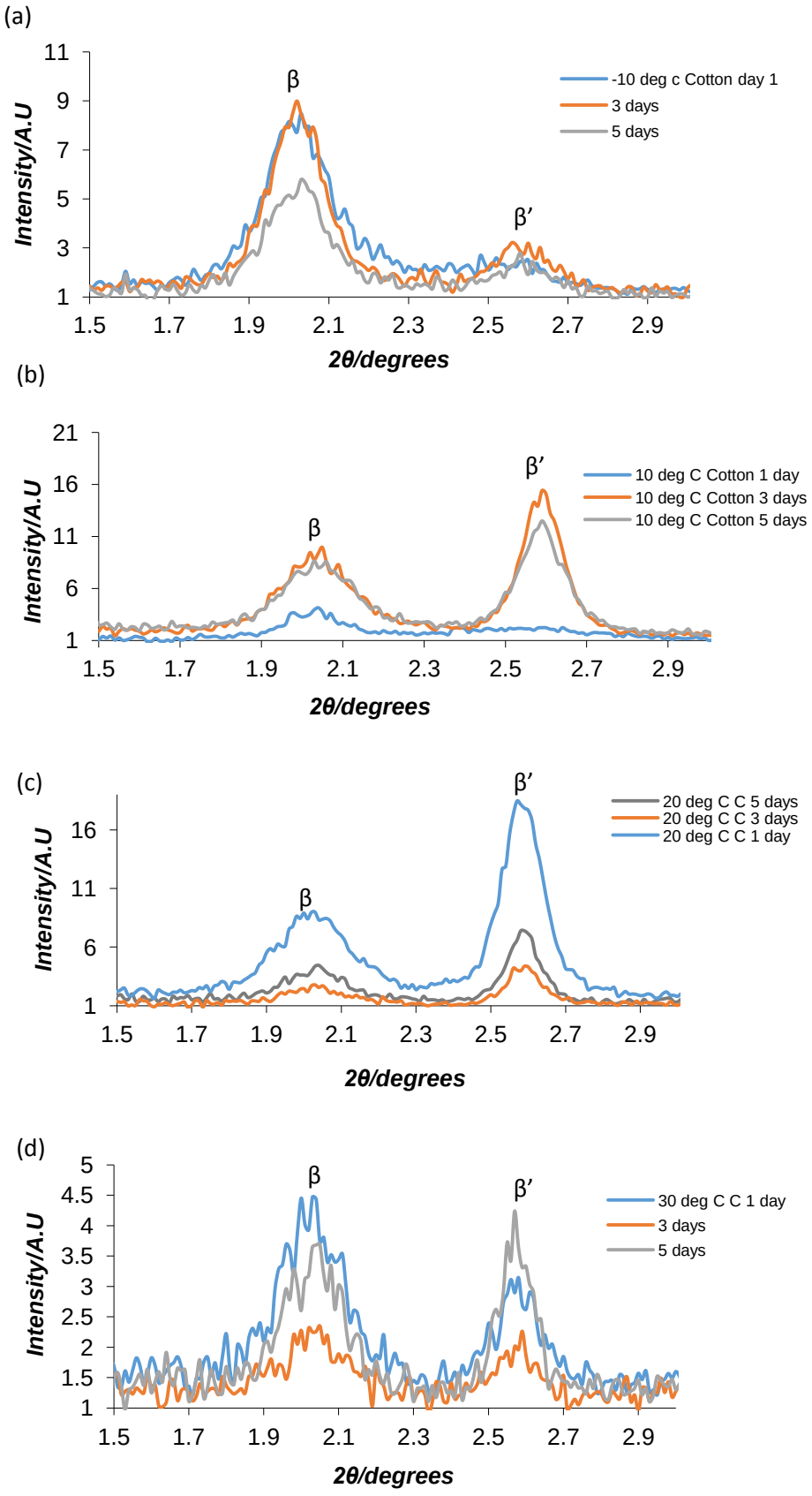

Figure A3.5: SAXS data for soiled cotton (C) fabrics obtained at temperatures of (a) -10 °C (b) 10 °C (c) 20 °C and (d) 30 °C over a period of 5 days.

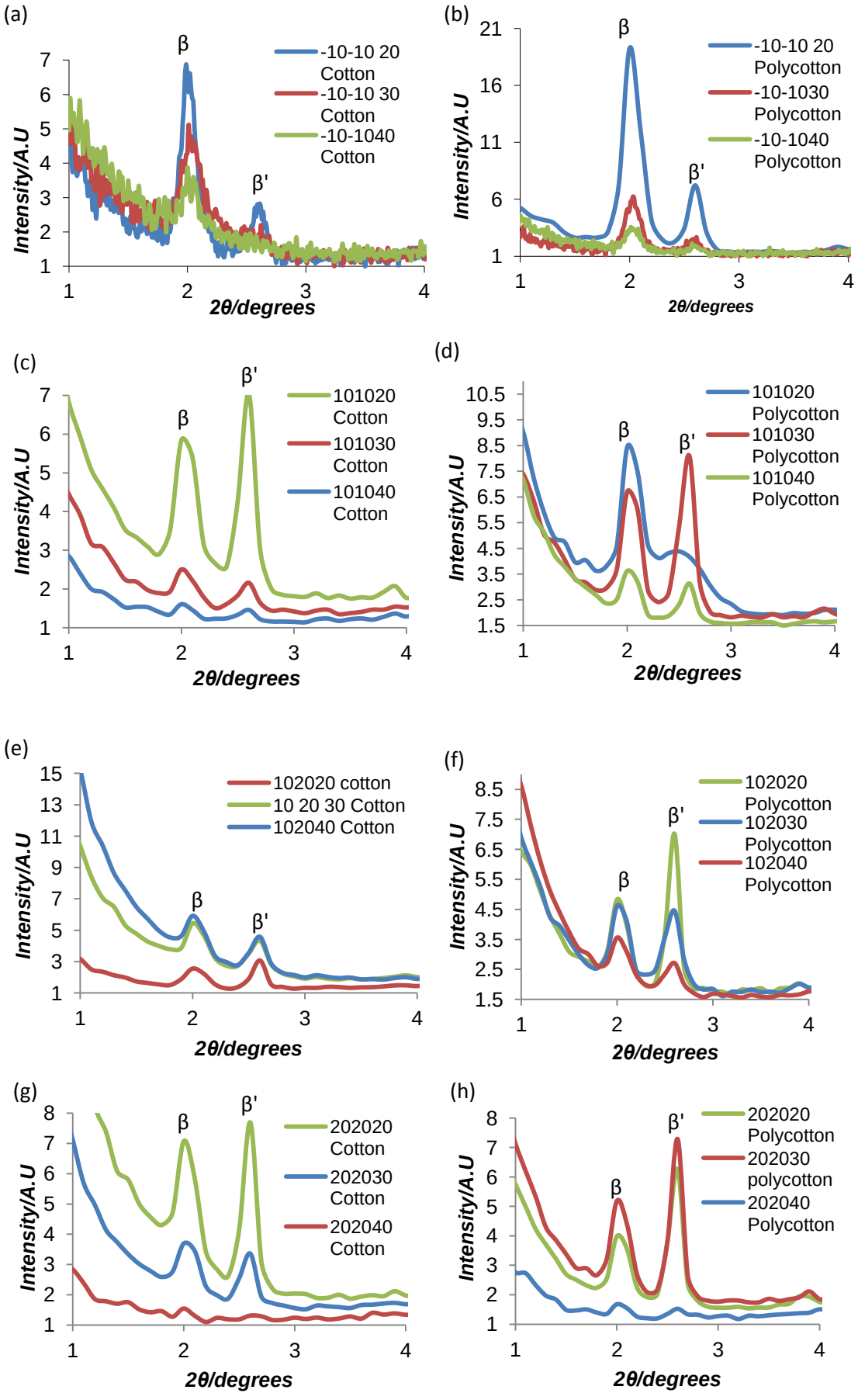
(a)
β
β'
-10-10 20 Cotton
-10-10 30 Cotton
-10-1040 Cotton
Intensity/A.U
2θ/degrees
(b)
β
β'
-10-10 20 Polycotton
-10-1030 Polycotton
-10-1040 Polycotton
Intensity/A.U
2θ/degrees
(c)
β
β'
101020 Cotton
101030 Cotton
101040 Cotton
Intensity/A.U
2θ/degrees
(d)
β
β'
101020 Polycotton
101030 Polycotton
101040 Polycotton
Intensity/A.U
2θ/degrees
(e)
β
β'
102020 cotton
10 20 30 Cotton
102040 Cotton
Intensity/A.U
2θ/degrees
(f)
β
β'
102020 Polycotton
102030 Polycotton
102040 Polycotton
Intensity/A.U
2θ/degrees
(g)
β
β'
202020 Cotton
202030 Cotton
202040 Cotton
Intensity/A.U
2θ/degrees
(h)
β
β'
202020 Polycotton
202030 polycotton
202040 Polycotton
Intensity/A.U
2θ/degrees

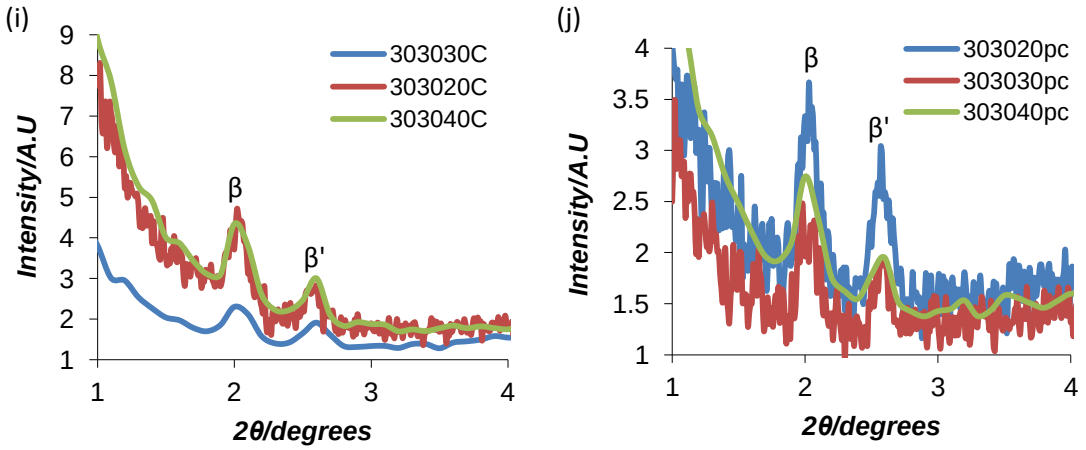

Figure A3.6: SAXS data obtained for soiled cotton (a), (c), (e), (g) and (i) and, for soiled polycotton (b), (d), (f), (g) and (h) swatches exposed, dried and washed at different temperatures, while a high concentration (50 mg/mL) of C24E3S surfactant was applied.

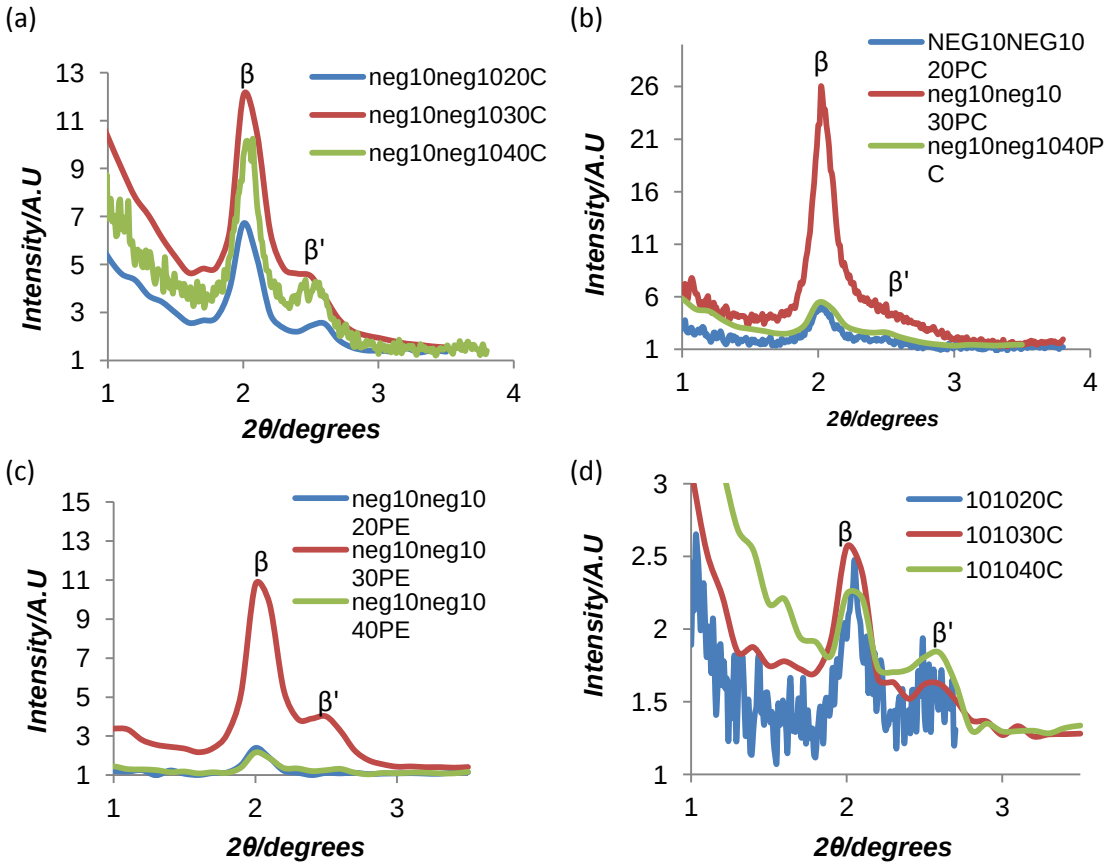

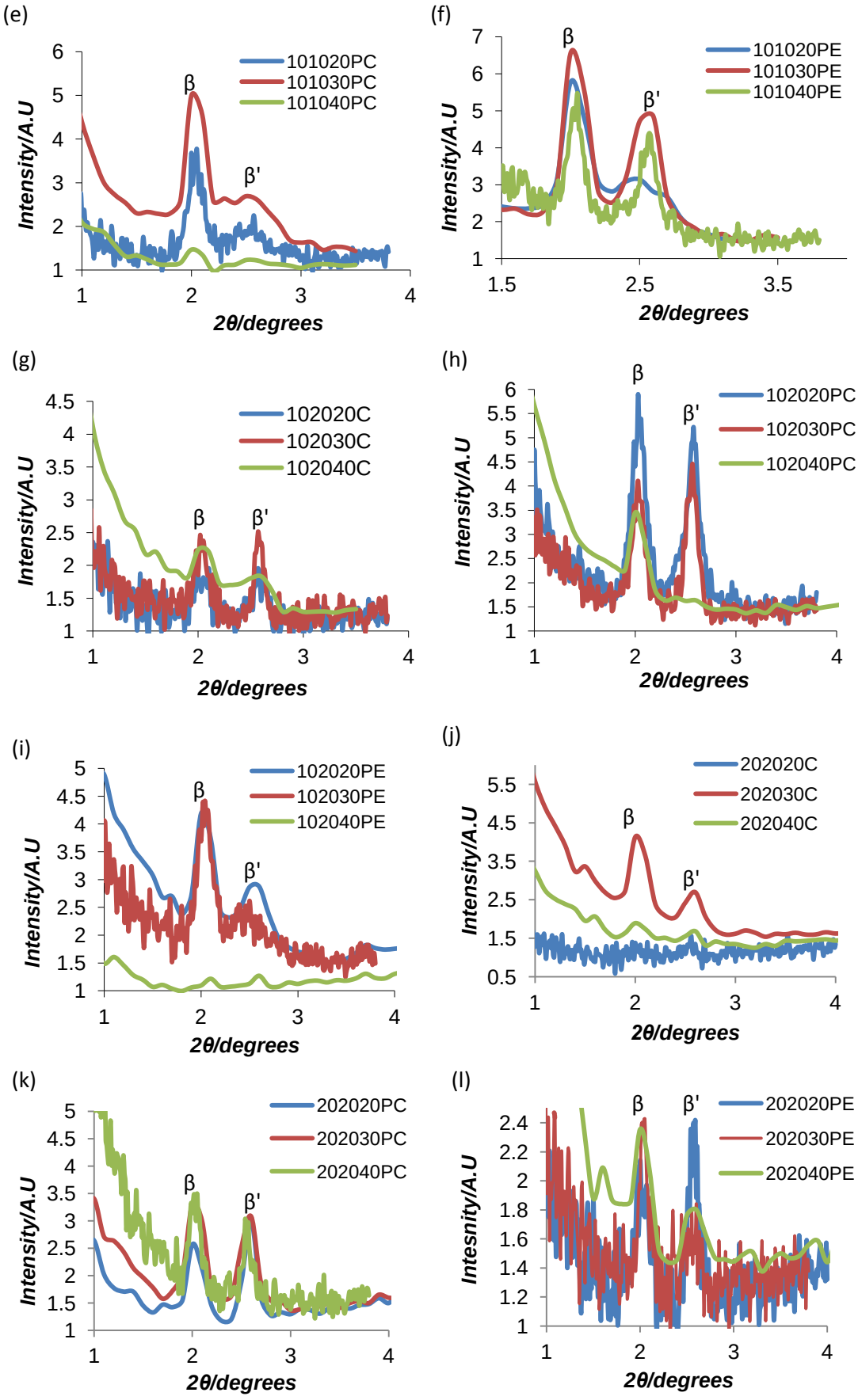
(e)
101020PC
101030PC
101040PC
β
β'
Intensity/A.U
2θ/degrees
(f)
101020PE
101030PE
101040PE
β
β'
Intensity/A.U
2θ/degrees
(g)
102020C
102030C
102040C
β
β'
Intensity/A.U
2θ/degrees
(h)
102020PC
102030PC
102040PC
β
β'
Intensity/A.U
2θ/degrees
(i)
102020PE
102030PE
102040PE
β
β'
Intensity/A.U
2θ/degrees
(j)
202020C
202030C
202040C
β
β'
Intensity/A.U
2θ/degrees
(k)
202020PC
202030PC
202040PC
β
β'
Intensity/A.U
2θ/degrees
(l)
202020PE
202030PE
202040PE
β
β'
Intesnity/A.U
2θ/degrees

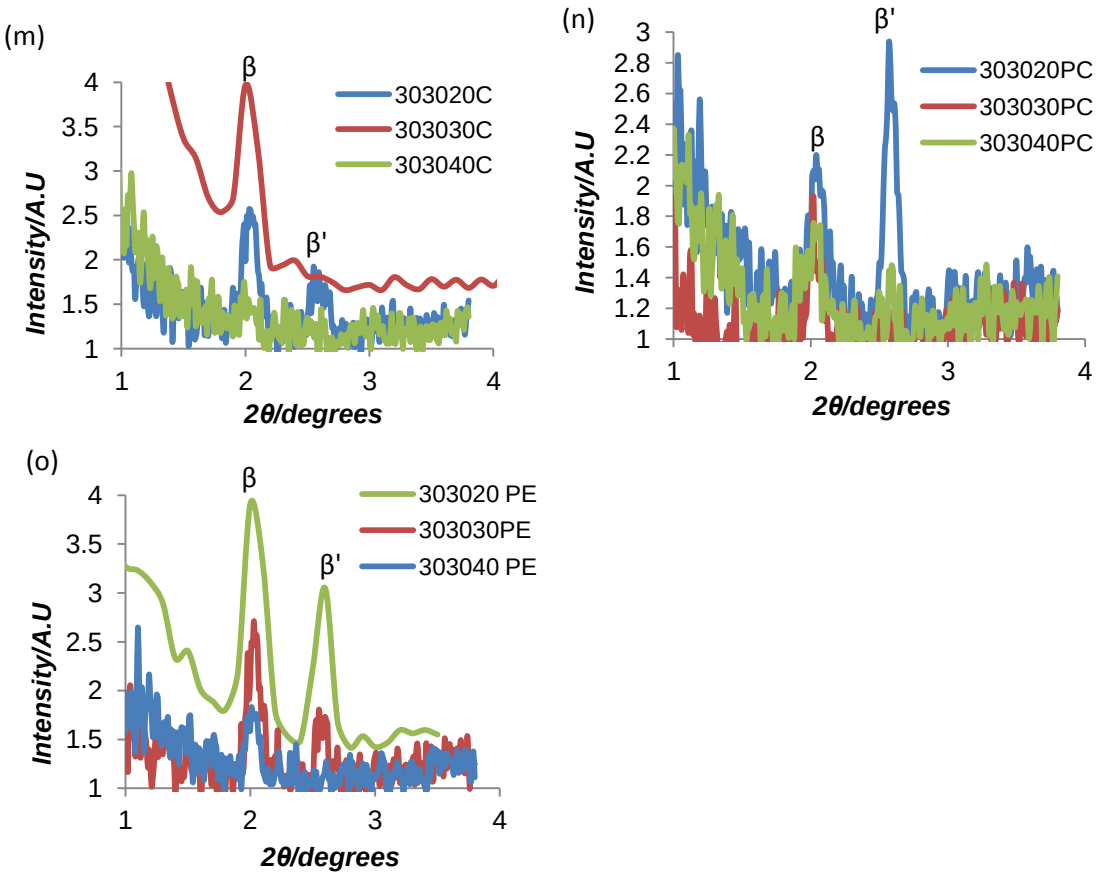

Figure A3.7: SAXS data obtained for cotton (a), (d), (g), (j) and (m), for polycotton (b), (e), (h), (k) and (n) and, for polyester (c), (f), (i), (l) and (o) exposed, dried and washed at different temperatures, while a low concentration (0.7 mg/mL) of C24E3S surfactant was applied.

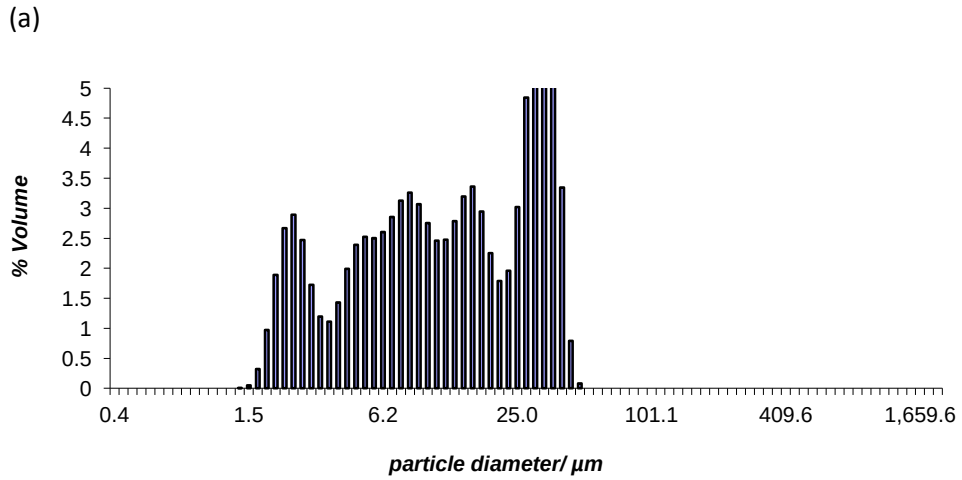

(b)

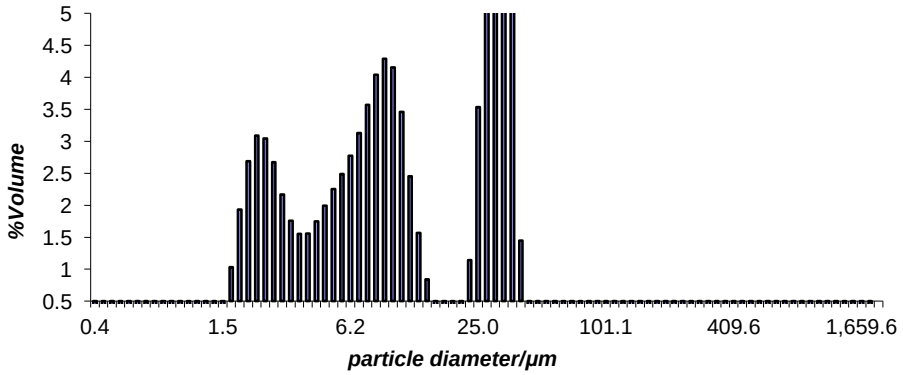

Figure A3.8: % volume data for fat globules collected from wash water extracted from wash conditions where the soiled fabric swatches are exposed, dried and washed at temperatures of (a) 20 ^{o}C and (b) 30 ^{o}C, when a concentration of 50 mg/mL of the C24E3S surfactant was applied.